MPHIL

Superimposed-Fft/Ifft For Sar And Other Microwave Measurement Applications

Abdul-Latif, Omar

Award date:
2015

Awarding institution:
University of Bath

SUPERIMPOSED-FFT/IFFT FOR SAR AND OTHER MICROWAVE MEASUREMENT APPLICATIONS

Omar M. Abdul-Latif

A thesis submitted for the degree of Master of Philosophy

University of Bath

Department of Electrical and Electronics Engineering

February 2015

……

Abstract

Synthetic Aperture Radar (SAR) is a method of constructing high resolution images from radar transmissions. SAR is widely used in a broad range of applications, including satellite imaging and remote sensing, ground penetrating radar and medical imaging. The response of radar systems often suffer from high sidelobe level resulting in resolution degradation. These sidelobes are caused by band-limited property of measured signal. One technique to reduce sidelobes is windowing, but this has a broadening effect on the main-lobe. The proposed technique of superimposition (SI) attempts to reduce sidelobes while enhancing the resolution as oppose to broadening the target's main-lobe as caused by many conventional techniques. Furthermore, the superimposition technique preserves the amplitude of the targets' main-lobe while conventional sharpening techniques tend to distort it in one way or another. Results show minimal resolution loss, noteworthy sidelobe reduction and negligible distortion of peak position and amplitude from the original spectrum. SAR images generated by the Superimposed Fast Fourier Transform (SI-FFT) showed significant enhancement in focus when compared to the images generated by using the standard Fourier Transform method using the same data set, with negligible extra computational requirement. Moreover, two new techniques of superimposition are presented in this thesis: Repetitive Superimposition (RSI) and Normalized Superimposition (NSI). Results have shown significant improvement in sidelobe suppression even when compared to the standard superimposition results and more importantly, it also have shown noticeable reduction in both additive and multiplicative noise. What's more, these techniques have also been applied to other microwave measurement techniques, mainly in Vector Network Analyzer (VNA) and Ground Penetrating Radar (GPR) where superimposed Inverse Fourier Transform (SI-IFFT) is developed and utilized for simulation and measurement and produced results are as impressive as in SI-FFT.

List of Abbreviations and Symbols

Technical Term	**Abbreviations**	***Symbols***
Additive White Gaussian Noise	AWGN	
Antenna Gain		G
Antenna Length		l
Azimuth Resolution		ρ_a
Azimuth Time		η
Backscattering Coefficient		σ^0
Bandwidth		B
Chirp Rate		k_r
Co-polarized Correlation Coefficient		CCC
Conjugate of Signal (S)		S^*
Depression Angle		θ
Dirac-Delta Function		$\delta(n)$
Direct Digital Synthesizer	DDS	
Disciple	dB	
Distance Travelled by Sensor		L_{sa}
Fast Fourier Transformation	FFT	
Filtered Backprojection	FBP	
Frequency Modulated Continuous Wave	FMCW	
Ground Penetrating Radar	GPR	
Height of Sensor from Ground		H
Impulse Response		$h(t)$
Initial Frequency		f_0
Integrated Sidelobe Ratio	ISLR	
Inverse Fast Fourier Transformation	IFFT	
Linear Frequency Modulation	LFM	
Linear Range Walk Correction	LRWC	
Low Noise Amplifier	LNA	
Low Pass Filter	LPF	
Matched Filter	MF	
Multiple Signal Classification	MUSIC	
Normalized Superimposition	NSI	
Peak Sidelobe Ratio	PSLR	
Point Spread Function	PSF	
Point Target Response	PTR	
Power at Antenna		P
Pulse Duration		T
Pulse Repetition Frequency	PRF	
Range Cell Migration	RCM	
Range Difference		Δr
Rate of Change of Frequency in Chirp		A
Real Aperture Radar	RAR	

Relative Dielectric Constant		ϵ_r
Relative Permeability		μ_r
Repetitive Superimposition	RSI	
Resolution in Time		ρ_t
Signal Phase		
Signal-to-Noise Ratio	SNR	
Slant Range Resolution		ρ_r
Spatially Variant Apodization	SVA	
Speed of Light		C
Step Frequency Continuous Wave	SFCW	
Synthetic Aperture Radar	SAR	
Target distance from Radar		R
Time Difference		Δt
Truncation Ratio		K
Two-way Time of Flight to the Target		τ
Vector Network Analyzer	VNA	
Voltage Controlled Oscillator	VCO	
Wave Length		λ

Table of Contents

Table of Figures

Chapter I: Introduction

1. Introduction

RADAR is an acronym for ‘‘**RA**dio **D**etection **A**nd **R**anging’’. It is a system that uses electromagnetic waves to identify the range, altitude, or speed of both moving and fixed objects. Radar is an important technology due to its all-weather, day night capability of detecting, locating and imaging. It consists of a transmitter that emits radio waves propagated at the speed of light, which are reflected by the target and detected by a receiver placed normally at the same location as the transmitter. Knowing the speed of the signal, the range is calculated by measuring the time it takes for the signal to travel from the transceiver and back. Radars can be either fixed or moving. Airborne or Spaceborne radar is an example of moving radars [1].

Imaging radar is a special type of radar and it was originally developed for military reconnaissance. Both real aperture radars (RAR) and synthetic aperture radars (SAR) were developed in the 1950s [2]. SAR with resolution smaller than 10 meters is normally used because a space-borne RAR can’t obtain the ground images with resolutions better than several kilometres [3]. Technically, SAR is a method of increasing cross-range resolution of targets imaged by radar and it is used for obtaining high azimuth and range resolution to construct all-weather earth images from both airborne and space-borne platforms [4]. A SAR system transmits and collects data pulses while flying along a track. It then processes the data as if it came from a physically long antenna [4], and in particular from an antenna that would be impossibly large [3]. Range resolution is improved by using compressed pulses. Fine azimuth resolution can be achieved by processing low resolution aperture data into an image [2]. SAR technology is used in a diverse range of applications such as Ground Penetrating Radar (GPR) [5], sea and ice monitoring [6], mining [7], oil pollution monitoring [8], oceanography [9], snow monitoring [6], classification of earth terrain [6] and others. This has led to the development of a number of airborne and spaceborne SAR systems [6]. SARs have been available since 1950, but due to the lack of computer power and advanced digital signal processing algorithms the SAR system could not be used in an efficient way [1].

2. Motivation and Objectives

The interpretation of images from SAR data is restricted by the system's ability to resolve closely spaced targets. In addition the intensity of the reflection from an artefact can also assist in identifying its features and state. In many cases the signal processing of SAR data involves taking Fast Fourier Transforms, where there is a trade-off between resolution and sidelobes. In a Fourier Transform, the band-limited property of the measured signals causes relatively high sidelobes, which tends to degrade the resolution of the final formed image [10]. The Fourier transform is a valuable theoretical technique, used widely in fields such as applied mathematics, statistics, physics, and engineering. The relationship between a function and its transform is given with certain amount of integration that is required to obtain the transform in a given application. In general, the user of this mathematical tool is interested in the functions and their transforms and not in the process of obtaining one from the other. If the transform function for a specific application could be obtained in a certain way that can remove – or at least minimize – undesirable side-effects of sidelobes in the case of Radar systems and enhance the resolution, then that will have a huge effect on the final result/outcome of the time-spectra transformation for that application.

The generation of the picture out of the SAR data is a computationally intensive task. Both range compression and azimuth compression utilize Fast Fourier Transform (FFT) algorithms and Inverse Fast Fourier Transform (IFFT) in order to perform convolution with their respective reference signals. Thus FFT and IFFT occupy about 70% of the total computation operation in SAR image formation [11]. Furthermore, this kind of processing does not take into account either any contextual information we have, or the final objectives of the SAR mission regarding the automated decisions or interpretations to be made [12]. What's more, conventional image formation method is basically only data driven and this limits the output quality. In addition, there is no explicit mechanism in the image formation process to deal with limited quantity or quality of the observations. Therefore, in order for SAR systems to meet the challenges of future tasks, new processing techniques which are geared towards the final objectives of the mission are required [12]. More to the issue, the presence of significant sidelobes in the response may cause interference with other near echo signals, have unwanted effects in the detection process and create ambiguities in the estimation of target range [2].

Hence, the major objective in this thesis is to develop a modified algorithm, which is the Superimposed-FFT, based on conventional FFT in order to enhance the computation performance in SAR image formation. It is shown that the proposed algorithm can essentially achieve better resolution and lower sidelobes while preserving the targets' main-lobes positions and amplitudes with minimum computational burden compared to standard-FFT. Furthermore, as another objective, the same algorithm is used to design a Superimposed-IFFT for Frequency-domain-based schemes where the IFFT is a major part of the signal analysis, such as Vector Network Analyzer microwave measurement [13] and Step Frequency Continuous Wave that can be utilized in other applications such as Ground Penetrating Radar [14], Medical Imaging [15][16] and Sonar [17].

3. Considerations for Spaceborne SAR Design

The SAR data processing is challenging due to the changing properties of targets (such as vehicles, ships, and buildings) and terrains for the electromagnetic waves with various bands, views, polarimetric modes, and configurations. The parameters of a SAR system depend on the primary goal of the project. Different system-level objective will lead to different radar configuration. The range of applications considered in this project is of environmental and civil purposes. Some of these SAR applications are [2]: Environmental Monitor, Utility Maintenance, Watershed studies and Management, Hydrologic studies and Modelling, Land Use/Land Classification, city planning, Extraction Industries (i.e. Forestry, Oil and Gas, Mineral), Insurance (i.e. Fire and Land-slide probabilities) and others. For this project, real-life data sets from the RADARSAT-2 mission are obtained from [4] and [18] (for specific parameters refer to Appendix A). The SAR system is discussed elaborately in the next chapter. It is worth mentioning that most of the SAR design considerations don't have a direct effect on the Superimposition algorithm proposed in this dissertation. However, some of the design considerations for the range of applications mentioned earlier are briefly listed below:

i. Operating Platform

Basically SAR systems can be separated into two groups: airborne system operating on variety of aircraft and spaceborne system operating on satellite or space shuttle platforms. Spaceborne SAR has smaller range of incidence angle and larger swath width, but high data

rate is a problem. Whereas airborne SAR illuminated smaller footprint on the earth and the data rate is much lower.

ii. Operating Frequency

For remote sensing applications, frequency range from 1 to 30 GHz is normally used [6]. In the 1–10 GHz range, the transmitivity through air approaches 100%. Thus, a SAR operating in this frequency range is always able to image the earth's surface independent of the cloud cover or precipitation. As the radar frequency increases, the transmission attenuation increases. At 22 GHz there is a water vapour absorption band that reduces transmission to about 85% [19]. The operating frequency has no effect on the performance of the proposed superimposed-FFT from a signal processing perspective.

iii. Modulation Schemes

In SAR system, there are basically three types of widely used modulation schemes [11]: pulse, Linear Frequency Modulation (LFM) or chirp and phase coded. Pulse system is used in older generation radar, while modern radar uses LFM waveform to increase range resolution when long pulses are required to get reasonable signal to noise ratio. The same average transmitting power as in a pulse system can be achieved with lower peak amplitude. The LFM configuration is employed in this thesis as t is a widely used scheme that gives better sensitivity without sacrificing range resolution and ease of implementation. The phase-coded waveforms differ from the frequency modulation waveforms in that the pulse is subdivided into a number of equal duration sub-pulses. Each sub-pulse has a particular phase which is selected in accordance with a given code sequence. Both of the waveforms are designed to cluster the received signal by the pulse compression processing. That is the amplitude of pulse is increased and the width is decreased. Phase coded modulation is not prefer due to its difficulty to generate and it's usually used for long duration waveforms and when jamming may be a problem.

iv. Mode of Operation

Available data acquisition mode includes strip-mapping, squint mode, spotlight mode, ScanSAR, interferometry and polarimetric SAR [20]. Spotlight mode SAR provides high-resolution image but involves complex hardware and processing algorithm. Squint mode SAR is used to image while manoeuvring. It usually employed in military aircraft. ScanSAR,

which is used in this project, is normally used in spaceborne SAR in order to increase the swath width even though it requires powerful computation hardware. Polarimetric system capable of measuring scattering matrix *S* of target whereas interferometry SAR is the latest technology developed with capability of measuring terrain high and constructing three dimensional image. Hardware design of interferometry and polarimetric SAR is more complicated.

v. Polarisation

Conventional SAR system employed single polarisation to acquire information from earth. For remote sensing of earth terrain such as oil palm plantation or tropical forest, single polarisation is sufficient. A device which measures the full polarisation response of the scattered wave is called a polarimeter. Polarimetric systems differ from conventional system in that they are capable of measuring the complete scattering matrix of the remotely sensed media. By having the knowledge of the complete scattering matrix, it is possible to calculate the backscattered signal for any given combination of the transmitting and receiving antennas. This process is called the polarisation synthesis, which is an important technique used in terrain classification.

vi. Dynamic Range of Backscattering Coefficient σ°

The required system sensitivity is determined based on the various categories of earth terrain to be mapped such as manmade target, ocean, sea-ice, forest, natural vegetation and agriculture, geological targets, mountain, land and sea boundary. From the open literatures, the typical value of σ° falls in the range of +20 dB to −40 dB [21]. For vegetation the typical value of σ° vary from +0 dB to −20 dB.

vii. Antenna

Yagi, slotted-waveguide, horn, dish, and microstrip antennas have found some applications in SAR one time or another [2]. Yagi is suited for lower frequency applications, while dish is suited for very high frequency application. Modern civilian SAR systems generally operate in L- C and X-band, where slotted-waveguide and microstrip antennas provide the best performance [22].

4. Quality Metrics Measurement

SAR image quality measurements play an important role in the development of SAR image digital processing methods. The main objective of SAR image quality measurements is to examine the performance of a SAR system. SAR image quality measurements are based on analysis of a point target. In this dissertation, the assessment of quality of performance for the various techniques of SAR image formation is performed using the following metrics:

i. Main-lobe Beamwidth (Spatial Resolution)

The spatial resolution is the distance between two objects on the ground at which the images of the objects appear distinct and separate. In SAR images, the spatial resolution is measured as the distance between the points with intensities 3dB below the maximum intensity of the main lobe peak in the azimuth and range directions [23], see Figure I-1. The difference of width of main-lobe for two or more signals generated using different techniques gives an indication to quality of resolution of each technique. The narrower the main-lobe is, the better resolution the technique is producing.

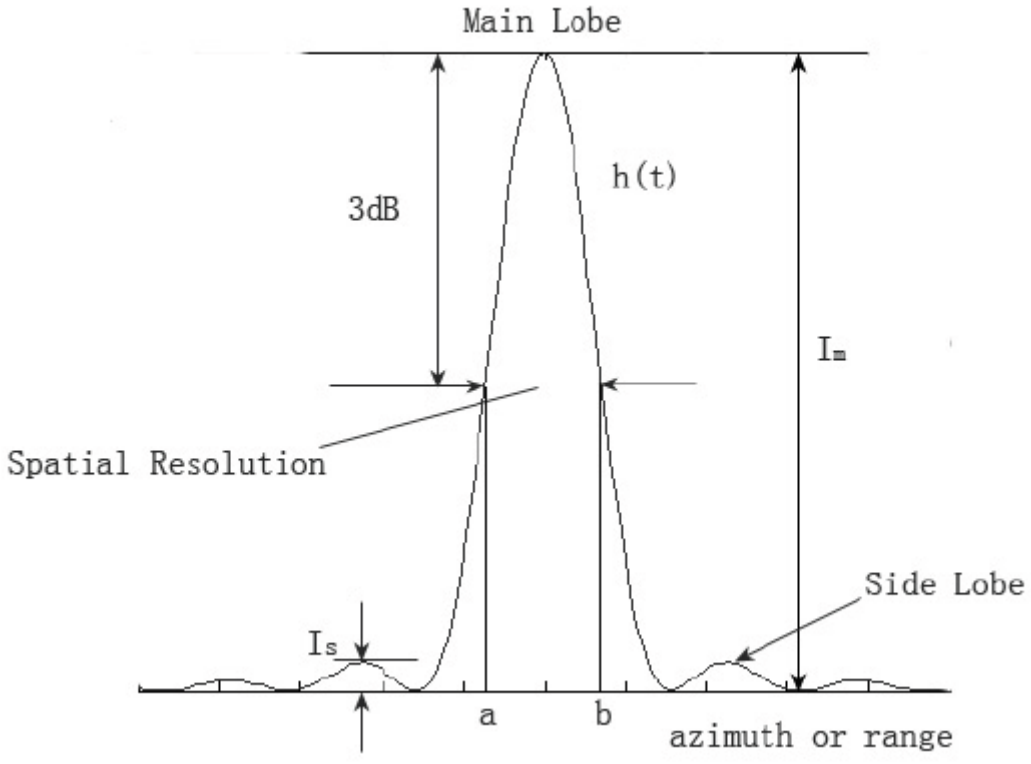

Figure I-1: Graphical representation of a SAR point target response showing several quality parameters.

ii. Peak sidelobe Ratio (PSLR)

The Peak Sidelobe Ratio (PSLR) is the ratio between the returned signal of the main-lobe and that of the first sidelobe of the point signal [24]. This parameter is normally expressed in decibels. In other words, PSLR measures the ability to image a weak reflective target affected by a strong reflective target nearby that is defined by the ratio of the extracted peak intensity within the sidelobe area to the peak intensity in the main-lobe area according to:

$$PSLR_{dB} = 10\log|I_S| - 10\log|I_M| \quad \textbf{(Eq. I-1)}$$

where I_S is the peak intensity of the sidelobe area and I_M is the peak intensity of the main-lobe area, see Figure I-1.

iii. Integrated Sidelobe Ratio (ISLR)

The Integrated Sidelobe Ratio (ISLR) is the ratio of the energy in the sidelobes to that contained in the main-lobe. This parameter is also normally expressed in decibels. In other words, ISLR measures energy spilling over to sidelobes from the main-lobe. It characterizes the ability to detect weak targets in the neighbourhood of bright targets [25]. Hence, ISLR describes properties of the signal for conditions when multiple objects are likely to be present in the range profile. There are several different ways for calculating the ISLR proposed by many authors in the literature [26][27][28], with differences in the adoption of the areas in which the energy is integrated. In this dissertation, two mathematical models are adopted:

The first one, which is used for 1-D signals, is evaluated as sum of squares of all corresponding discrete values. The mathematical formal definition given by [29] is:

$$ISLR_{dB} = 10log\frac{\int_{-\infty}^{a}|h(\tau)|^2 d\tau + \int_{b}^{\infty}|h(\tau)|^2 d\tau}{\int_{a}^{b}|h(\tau)|^2 d\tau} \quad \textbf{(Eq. I-2)}$$

Where $h(\tau)$ stands for the impulse response function in azimuth or range direction and $[a;b]$ stands for the range of main lobe at 3dB below the maximum intensity peak. These values are shown on Figure I-1. However, it must be noted that integration is done for the limited time period which cuts off part of the sidelobes energy. This simplification was used because in most practical applications ranges of observable targets with significant response amplitude are limited by physical factors [29].

The second mathematical model for ISLR is the European Space Agency's (ESA) for 2-D SAR images, which is used in chapter 6. With the factors to define main-lobe and sidelobe areas found in [23] indicates that both main-lobe and sidelobe areas can be considered as elliptic and concentric elliptic areas, respectively. In general case, the dimensions of these areas can be approximated by ($2\Delta x$, $2\Delta r$) for main-lobe and ($10\Delta x$, $10\Delta r$) for sidelobes where Δx is the spatial resolution in azimuth and Δr is the spatial resolution in range, both are defined by -3dB beamwidth of the main-lobe. Based on those analyses, ISLR is defined as [25]:

$$ISLR_{dB} = 10log\left|\oiint_{(10\Delta x,10\Delta r)}|I|dA - \oiint_{(2\Delta x,2\Delta r)}|I|dA\right| - 10log\left|\oiint_{(2\Delta x,2\Delta r)}|I|dA\right| \quad \textbf{(Eq. I-3)}$$

where I is the intensity and dA is the elemental of the area.

iv. Mean Square Difference (MSD)

This metric is used when no reference image is available, it is used to compare two images generated using two techniques and it gives a quantified value of the difference without specifying which one is the best in terms of quality. Mean Square Difference (MSD) measures the average absolute difference per pixel between two images [28], the first image is the SAR image generated using the conventional technique of standard-FFT and the second image is the image generated using the technique that is being assessed. Mean-Square difference between the two images is calculated using the following:

$$MSD = \frac{1}{MN}\sum_{i=1}^{M}\sum_{j=1}^{N}\left(x\_1_{i,j} - x\_2_{i,j}\right)^2 \quad \textbf{(Eq. I-4)}$$

where M and N are the number of rows and columns of the image, x_1 and x_2 are the pixel values of the first and second images.

v. Image Line Intensity Profile

Due to the lack of reference image to assess the enhancement, if any, to the quality of the new SAR image generated by the proposed superimposition technique, the Mean-Square difference is being used to give a quantitative value of change in SAR images generated by the various techniques. Even though, some existing techniques are published to provide qualitative assessment to reference-less images [30], such as the one developed by Laboratory for Image & Video Engineering at the University of Texas in Austin, which is

named "Blind/Referenceless Image Spatial Quality Evaluator" [31], it was found that these techniques are actually designed on a foundation of models of statistical regularities observed in natural scenes, where ‘natural scenes’ subsume any image taken using an optical camera with no artificial processing [28]. Intuitively, this kind of assumption, which doesn’t take the SAR image formation model into consideration, is not adequate for this project and, hence, the utilization of the intensity profile technique is considered [25].

The intensity profile of an image is the set of intensity values taken from regularly spaced points along a line segment or multiline path in an image [32]. The beauty of this technique lies in this simplicity of the method. However, in order to make a good understanding of the image sharpness and clarity, some considerations have to be kept in mind before placing the lines on the image [33]. One thing is that the line has to cross edges that separate high-intensity areas and low-intensity areas in order to examine the sharpness of change at the edge between these two areas. Also, a line, which could be the same line mentioned earlier, has to go through an area of high intensity to show resolution of peaks in comparison to other peaks of nearby targets. Finally, a line, which again can be the same line, has to go through an area of low intensity to show the effect on noise, especially speckle noise, on the smoothness of that area.

5. Contributions of this Dissertation

The first major contribution of this dissertation is the development of Repetitive Superimposition (RSI) that utilizes windowing functions. This technique showed excellent results in suppressing sidelobes and preserving main-lobe’s height and position. However, it had a very small impact on enhancing the resolution as the widths of the main-lobes were only slightly narrowed.

The second major contribution of this dissertation is the utilization of the normalization process to formulate the Normalized Superimposition (NSI) that also employs the conjugate on half of the used signals to mimic the matched filter performance in lowering the noise in the final signal. Results presented in the dissertation show that this technique did preserve main-lobes’ position and height and as well as enhancing the resolution of the final image noticeably and it also significantly reduced the influence of noise.

Overall, this dissertation proposes a new, effective and efficient FFT/IFFT techniques that can be utilized to enhance SAR image formation and also to enhance many other FFT/IFFT-based applications in which it is advantageous to maintain main-lobes' height and position while suppressing sidelobes, combating noise and enhancing resolution. These characteristics are proven by simulation and measurement in this dissertation.

6. Dissertation Outline

A brief description of each chapter is presented below: Chapter 2 provides a comprehensive literature review of the theory of SAR and the SAR image characteristics in conjunction with the different techniques of image formation. Chapter 3 reviews existing sidelobe suppression techniques and introduces the new proposed Superimposition methodology. Superimposition is extended in terms of number of inputs and the mathematical method of superimposing the inputs. The two new proposed techniques are Repetitive Superimposition and Normalized Superimposition. Chapter 4 presents data for a basic radar system that is designed, programmed and simulated in the presence of Additive White Gaussian Noise (AWGN) and speckle noise with promising results that showed superiority of the superimposition technique to combat noise and suppress sidelobes. Chapter 5 deals with the IFFT version of superimposition. First, a transmission line is simulated in ideal setup (i.e. no noise) using Ansoft in order to study the quality of performance of superimposition in terms of spatial resolution, PSLR, ISLR and processing time. Then, a Beatty Standard experiment is conducted in order to have a real-life data to confirm the simulation results and in order to examine the ability of weak peaks nearby stronger peaks and in the presence of noise. At the end of this chapter some Ground Penetrating Radar simulation and image formation using real-life GPR data is performed showing superiority of the new proposed techniques of superimposition. Chapter 6 analyses the performance of the new proposed techniques of superimposition in comparison with conventional techniques in SAR systems using point spread function simulation and real-life SAR data, which were obtained from [4], with amazing results showing clear superiority of the superimposition technique. Finally, chapter 7 summarizes the dissertation contents, highlights its contributions and findings and suggests new extensions for the research to be considered in future projects.

Chapter II: Literature Review of Synthetic Aperture Radar

1. Introduction

This chapter presents the fundamentals of synthetic aperture radar (SAR) system design and theory that are necessary for the development of the research central to this dissertation. SAR is used to produce high-resolution mapping of the earth's surface in both range and azimuth dimensions [19]. A synthetic aperture is produced by signal processing. The aperture has the effect of lengthening the antenna, as the line of sight direction changes along the radar platform trajectory. Even though, SAR has been in the market since 1950, due to the lack of computer power and advanced digital signal processing algorithms the SAR system could not be fully exploited until a few decades later [6]. SAR Antennas can be carried on a variety of platforms to view and image targets. Satellites provide a large fraction of the remote sensing imagery. Spaceborne SAR has several unique characteristics which make it very useful for observing the Earth's surface. Satellites are designed to follow an orbit which, in conjunction with the Earth's rotation, allows them to cover most of the Earth's surface over a certain period of time. The area imaged on the surface, is referred to as the swath. Imaging swaths for spaceborne SAR generally vary between tens and hundreds of kilometres wide [6]. Sensors on satellites generally can "see" a much larger area of the Earth's surface than would be possible from a sensor onboard an aircraft. Also, because they are continually orbiting the Earth, it is relatively easy to collect imagery on a systematic and repetitive basis in order to monitor changes over time [2].

The geometry of orbiting satellites can be calculated accurately and facilitates correction of remote sensing images to their correct geographic orientation and position. However, aircraft sensors can collect data at any time and over any portion of the Earth's surface while satellite sensors are restricted to collecting data over only those areas and during specific times dictated by their particular orbits. Satellite orbits are matched to the capability and objective of the sensor(s) they carry. Orbit selection can vary in terms of altitude, height above the Earth's surface, and orientation and rotation relative to the Earth [2].

SAR is an active microwave remote sensing technique that produces wide-area images of high resolution. While passing by a target, the SAR illuminates the area with a series of coherent pulses. The series of radar echoes from the target area are digitized and processed to form the image. SAR compliments optical imagery in a variety of applications and has a number of advantages. The radar is its own illumination source, thus it can operate equally well day or night. The choice of frequencies in the microwave band allows imaging through clouds, precipitation, dust, and smoke, and at the low-frequency end of the microwave spectrum, foliage and dry ground penetration are possible. Like all radar systems, narrow pulses yield fine range resolution. To get fine azimuth resolution, a physically large antenna is needed. This is an impossible task to implement in reality [6]. SAR can be seen as an alternative way to get high azimuth resolution. SAR collects the data while flying and then processes it as if it comes from a physically long antenna [7].

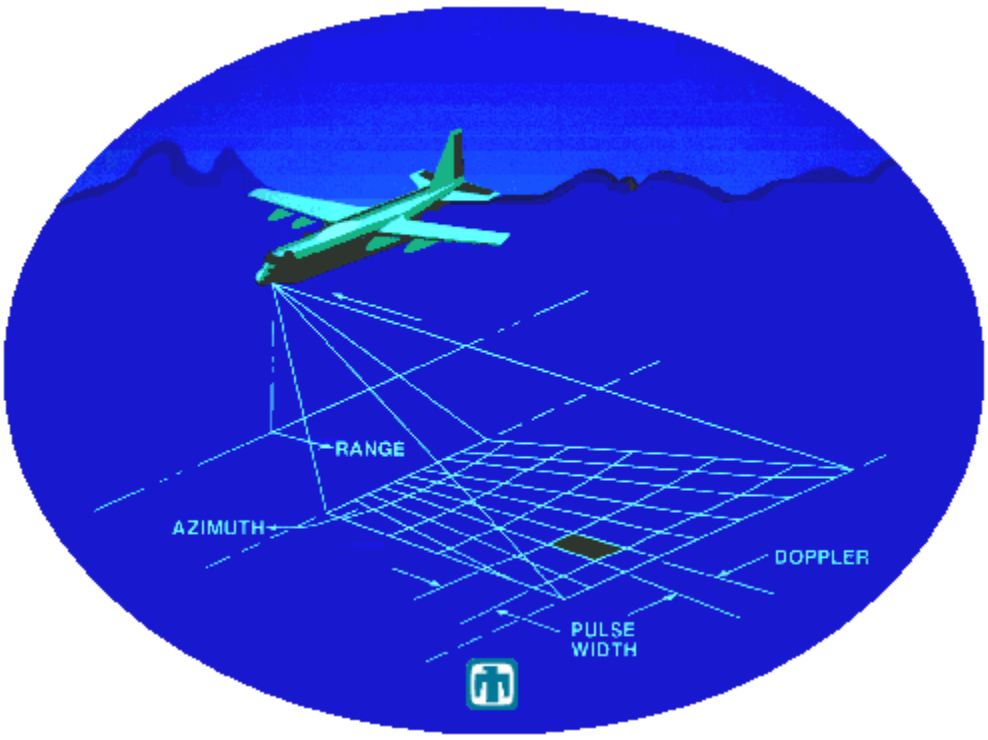

Figure II-1: Simple illustration of data collection by synthetic aperture radar. (Image obtained from the web site of Sandia National Laboratories.)

Typically, SAR produces a two-dimensional (2-D) image. One dimension in the image is called range (or cross track) and is a measure of the "line-of-sight" distance from the radar to the target. Range measurement and resolution are achieved in synthetic aperture radar in the same manner as most other radars: the range is determined by precisely measuring the time from transmission of a pulse to receiving the echo from a target. In the simplest SAR, range

resolution is determined by the transmitted pulse width, i.e. narrow pulses yield fine range resolution [9]. The other dimension is called azimuth (or along track) and is perpendicular to range. It is the ability of SAR to produce relatively fine azimuth resolution that differentiates it from other radars. To obtain fine azimuth resolution, a physically large antenna is needed to focus the transmitted and received energy into a sharp beam. The sharpness of the beam defines the azimuth resolution. Similarly, optical systems, such as telescopes, require large apertures (mirrors or lenses which are analogous to the radar antenna) to obtain fine imaging resolution [9].

2. Synthetic Aperture Radar System Model

The choices of SAR system parameters and hardware components are often driven by specific applications. The parameters used for a SAR data collection determine the processing methods that can be used. A basic SAR system can be subdivided into five processes in a high-level block diagram [34], as shown in Figure II-2: timing and control, signal generation and transmission, signal reception and data recording, motion measurement and estimation, and image formation. Each of these processes is briefly discussed below except for Image formation part, which is discussed in detail in section 11 of this Chapter.

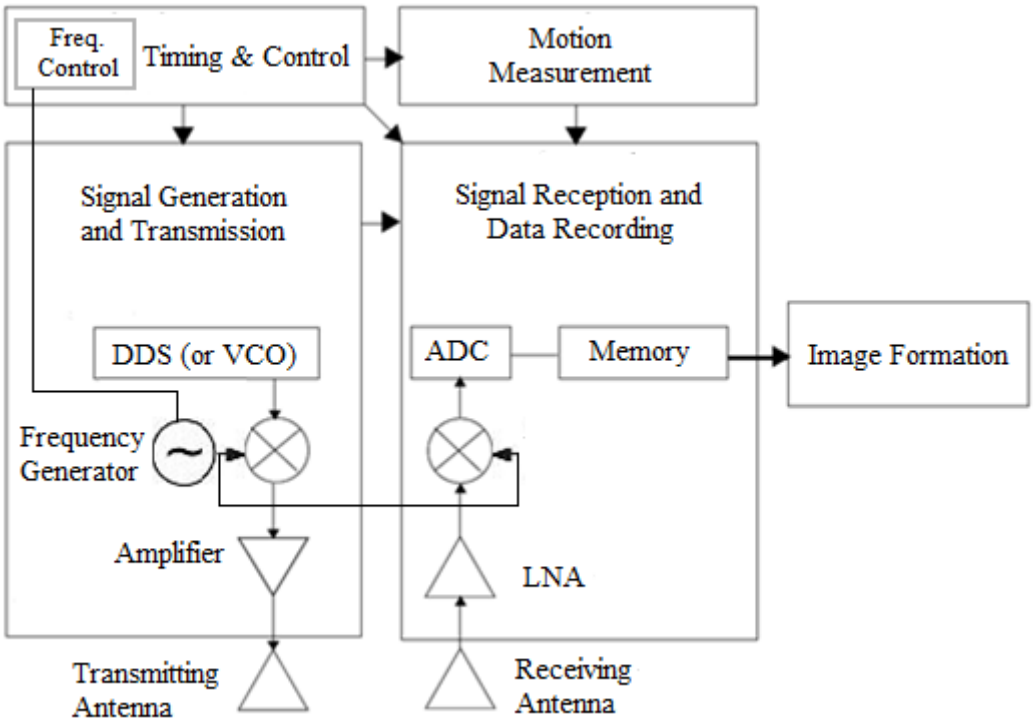

Figure II-2: Basic high-level SAR system block diagram

a) Timing and Control:

To form an image, the SAR signal must be coherent over the entire series of pulses that make up a data collection. An important part of that is maintaining coherence and consistent timing between the separate subsystems that make up the SAR. The timing and control system maintains coherence from pulse to pulse and between subsystems and determines the timing for turning the radar on and off and for switching between transmit and receive.

b) Signal Generation and Transmission:

Before the SAR signal is generated, a number of important system parameters are determined, including centre frequency, bandwidth, pulse length, and pulse repetition frequency (PRF). The signal can be generated using a direct digital synthesizer (DDS) or a voltage controlled oscillator (VCO). A DDS allows a specific waveform to be generated from programmed digital controls. However, the most common SAR signal is a Frequency Modulated Continuous Wave (FMCW) chirp, see Figure II-3, where the signal spans the bandwidth over the pulse length, changing in frequency at a linear rate.

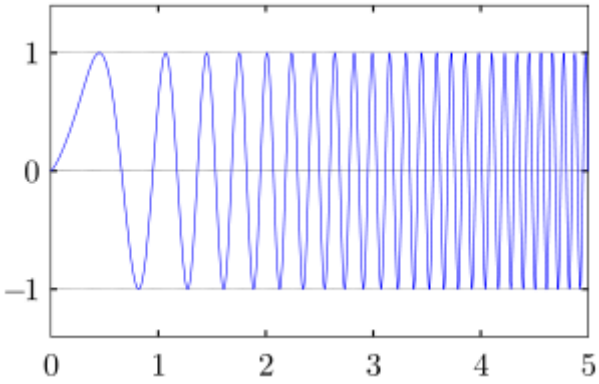

Figure II-3: A linear chirp waveform; a sinusoidal wave that increases in frequency linearly over time

The SAR signal is usually generated at or near baseband and then mixed up to the desired operating frequency before transmission. FMCW transmitted signal can be expressed as:

$$s_t(t) = a(t)e^{j(2\pi f_0 t + \pi k_r t^2 + \varphi)} \quad \textbf{(Eq. II-1)}$$

where $a(t)$ is the signal amplitude and, as a function of t, defines the pulse length with a rectangular function, f_0 is the frequency at the beginning of the chirp, k_r is the chirp rate, and φ is the starting phase. In the transmission chain, a power amplifier increases the transmit power to a specified level. The transmitted signal needs to have enough power so that the

signal-to-noise ratio (SNR) is large enough to generate a quality image. SNR also depends on the specific imaging parameters, especially range to target and antenna beamwidth. The antenna is designed with certain beam widths in azimuth and elevation and can be pointed in different directions for different SAR imaging modes. The beamwidth and antenna pointing determine the illuminated footprint on the ground. The platform motion, the antenna pointing, and the antenna beamwidth determine the Doppler frequencies of the return signals from the targets in the illuminated area, the Doppler bandwidth. The maximum Doppler frequency cannot be greater than the Doppler bandwidth of the system, defined by the PRF, or else Doppler aliasing occurs.

When frequency non-linearities are present in the transmitted signal, the signal modulation is not an ideal chirp anymore and that causes a range resolution and contrast degradation when the de-ramping technique is used [35]. For an ideal scatterer response, the beat frequency corresponding to the target is not constant, resulting in a more broadened response after a Fourier transform. The non-linearities in the beat signal are the difference between the transmitted and received non-linearities [36]. In the beat signal, their influence is therefore greater for larger distance. However, for short distance, the transmitted and received non-linearity phase difference is small and results in compensation in great part of the original non-linearities [35]. Some hardware and software approaches are reported in the literature to address chirp non-linearity: Hardware solutions include the use of a pre-distorted VCO steering signal to have a linear FM output and complex synthesizer concepts with phase locked loop [37]. Conversely, the former approach fails when the external conditions, i.e. the temperature, changes while the latter requires quite costly devices. The use of DDS offers a quite cost-effective solution [38], but the transmitted bandwidth can still be limited when compared to the one obtained directly sweeping the VCO. Different local oscillator could be used to transmit large bandwidth when using DDS solution, however, the system complexity is increased [37]. Software solutions, on the other hand, make use of some reference response to estimate the frequency non-linearity directly from the acquired de-ramped data, and try to compensate them using different methods: re-sampling of the data in order to have a linear behaviour [39], and matched filtering with a function estimated from the reference response [40].

c) Signal Reception and Data Recording:

The amplified signal transmitted through the antenna propagates to the target area. The propagation environment consists of the layers of atmosphere, usually approximated as free space, with the notable exception of ionospheric induced distortions such as Faraday rotation for orbital SAR, and the distributed scatterers that make up the target scene. A very small portion of the transmit signal is reflected back to the radar. The reflected signal from a point target can be expressed as [34]:

$$s_r(t) = \acute{a}(t-\tau)e^{j(2\pi f_0(t-\tau)+\pi k_r(t-\tau)^2+\varphi)} \quad \textbf{(Eq. II-2)}$$

where $\acute{a}(t)$ is an attenuated version of $a(t)$ and τ is the two-way time of flight to the target at range R, and C is the speed of light.

$$\tau = \frac{2R}{C} \quad \textbf{(Eq. II-3)}$$

For monostatic operation the radar echoes are received through the transmit antenna, isolated from the transmit path by a circulator. For bistatic operation, separate transmit and receive antennas are used, with the receive antenna separated from the transmit antenna by a known baseline. The receiver is very sensitive in order to detect the return echoes and is protected in many systems from the powerful transmit signal by being shut off during signal transmission. Additionally, a technique called range-gating is used to limit the collected data to a narrow set of ranges. This can reduce the data volume by only collecting data reflected from the area we are interested in imaging. This is often done by careful timing of when the receiver is turned on. The received signal is amplified with a low-noise amplifier (LNA) and mixed down to an appropriate band for sampling. One option for sampling is offset video with a single channel at a rate at least twice the bandwidth of the signal [34]. After the signal from (Eq. II-2) is mixed down by a frequency, f_{md}, which is the frequency that the chirp has reached by the time the transmitted signal has been to the target and reflected back the receiving antenna. Hence, the signal that is ready to be recorded is:

$$\begin{aligned} s_{rmd}(t) &= \acute{a}(t-\tau)e^{j\left(2\pi f_0(t-\tau)-2\pi f_{md}t+\pi k_r(t-\tau)^2+\varphi\right)} \\ &= \acute{a}(t-\tau)e^{j\left(2\pi(f_0-f_{md})t-2\pi f_0\tau+\pi k_r(t-\tau)^2+\varphi\right)} \end{aligned} \quad \textbf{(Eq. II-4)}$$

SAR systems used to record the data optically on film and used analog optical processing to produce the image. However, modern SAR systems digitize the data and either store it on board, transmit it to a ground station, or process it on-board.

d) Motion Measurement:

An important part of SAR data collection and processing that isn't directly part of the radar is the motion measurement system [41]. SAR processing requires knowledge of the position and path of SAR platform during data collection, or at least an estimation of the path. Motion measurement systems used with the SAR systems have employed a variety of methods including manually recording the velocity readings from the SAR platform instrumentation during data collection, utilizing a low rate GPS solution inserted into the SAR data, and employing a high rate inertial measurement unit (IMU) coupled with GPS and carefully time-tagged and aligned with the collected SAR data. The better the motion measurements, the more accurately the SAR data can be processed to form a well focused image.

3. Airborne/Spaceborne Synthetic Aperture Radar Geometry

This section focuses on the geometric properties of SAR images and introduces some commonly used terms. As an example, aircraft radar is used for illustration as shown in Figure II-3. The aircraft is assumed to fly along a mathematical straight line at an altitude, H. An antenna is mounted on the side or below the aircraft and ideally pointed perpendicularly to the aircraft trajectory. A SAR may look to the right, i.e. be right-looking, or look to the left, i.e. be left-looking. The height of the antenna is small, typically 10 cm to 30 cm, providing a fairly broad beam in the elevation plane at common radar frequencies L-band (1.25 GHz), C-band (5.3 GHz) and X-band (10 GHz). The length of the antenna is typically larger, e.g. 0.5 m to 2 m, providing a narrower beam in the along-track plane. SAR scans the terrain as it moves along its trajectory, and that an image can be generated by arranging the received echoes line by line. The image has two coordinates: range, r, and azimuth, x. It is noted that strictly speaking, a radar does not measure range, but time-delay, Δt. However, assuming free-space propagation and no internal delay in the radar, r and Δt are related through $r = (C/2)\Delta t$, where C denotes the speed of light. It is worth mentioning that the along-track coordinate is often denoted azimuth despite the fact that azimuth conventionally means angle in a rotating radar or more generally angle in an equator plane.

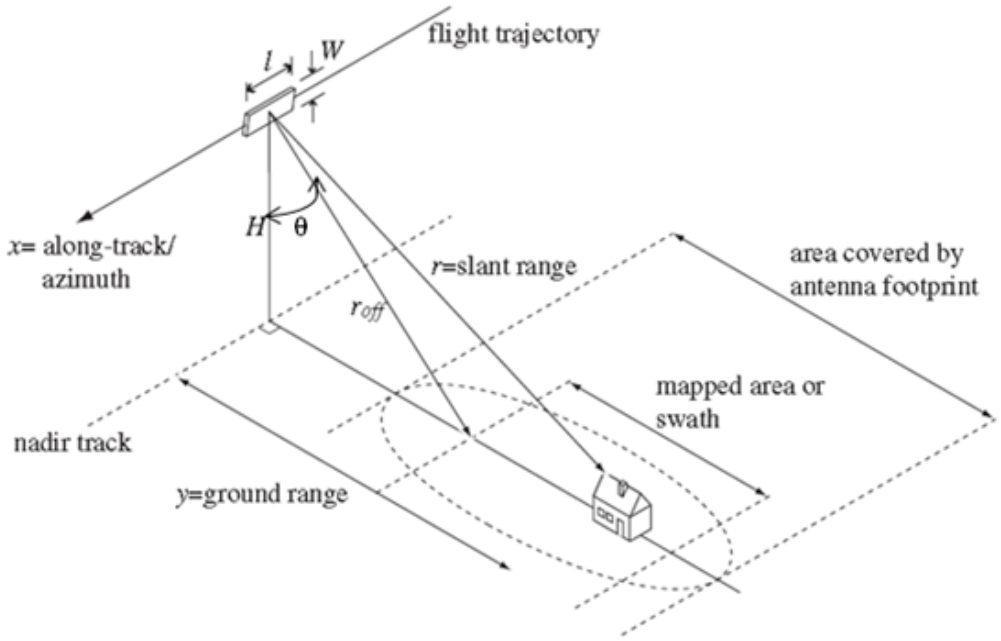

Figure II-4: airborne SAR geometry with commonly used terms

The formation of the synthetic aperture is illustrated by Figure II-5. During the flyby, the radar system constantly records the coherent signals reflected from the target area. A point target, A, within the area as is first detected at the radar system position 1. The observation period in which information about the target point A can be recorded, extends to the third position, and hence, Synthetic Aperture Radar gets a better angular resolution when compared to the Real Aperture Radar [42]. In SAR, the achieved angular aperture in azimuth direction, θ_{sa} is:

$$\theta_{sa} = \frac{\lambda \cdot H}{2 \cdot L_{sa}} \qquad \textbf{(Eq. II-5)}$$

where λ is the wavelength, H is the height of the SAR platform, and L_{sa} is the distance travelled by the SAR platform. The improvement in angular resolution by a factor of 2 results from the fact that the phase gradient or the path object-antenna in the case of synthetic aperture radar is twice as large [42].

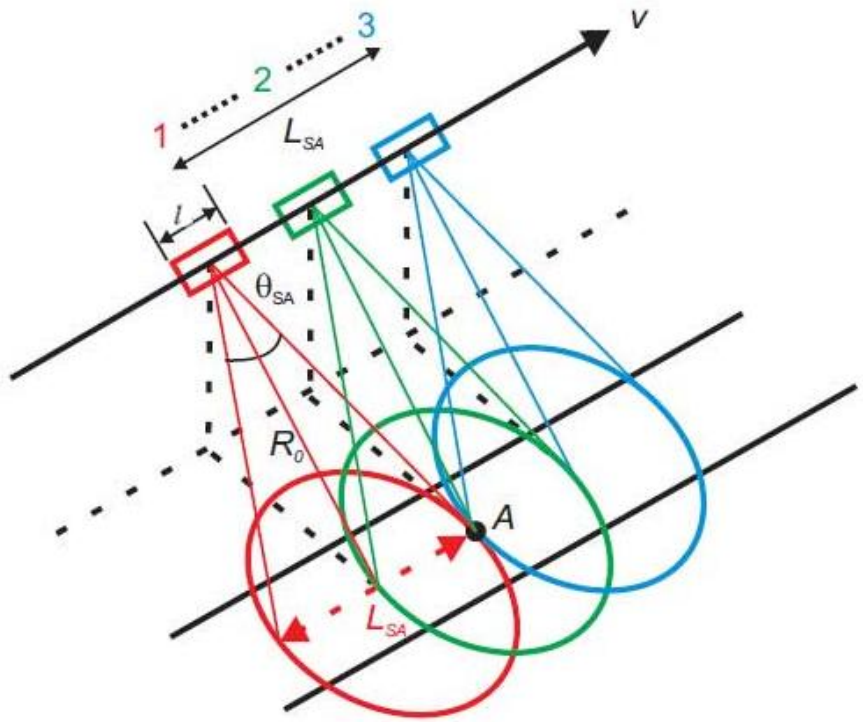

Figure II-5: Principle of the lateral resolution of synthetic aperture radar [42]

SAR radar pulses usually are of a long duration, T_p, corresponding to a length of CT_p in free space. Typical lengths are 2 km to 6 km. The antenna with a length, l, has an approximate angular beam width of $\beta_a \approx \lambda/l$, where λ is the wavelength. With an example λ = 5 cm (C-band), l = 1 m, and r_0 = 10 km, the coverage of the antenna beam in azimuth is $r_0\beta_a$ = 500 m. This means that all scatterers within a very large volume contributes to the received echo at one (r, x) image pixel, see Figure II-4.

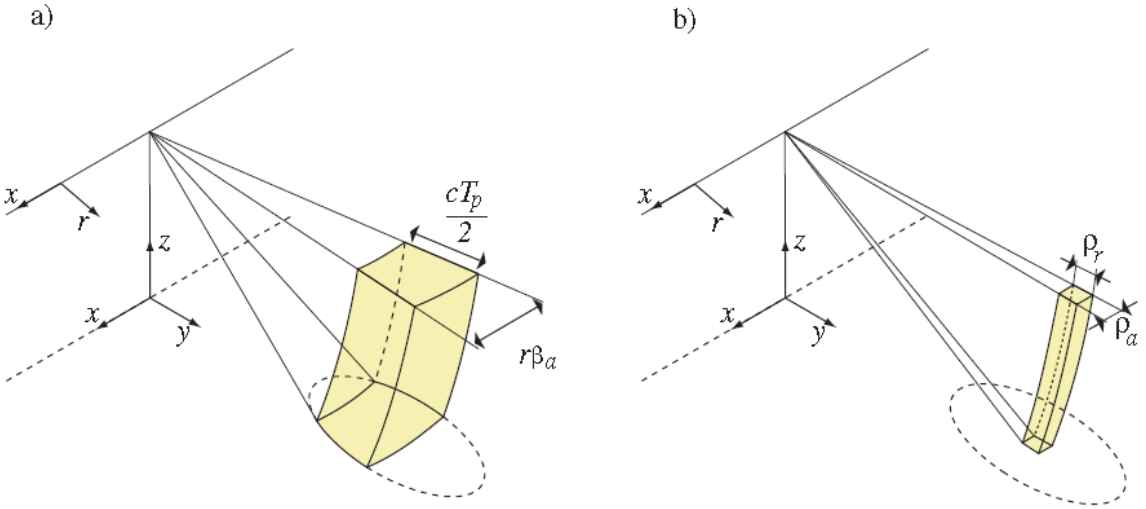

Figure II-6: a) All scatterers with the shaded volume contribute to the received echo at (*r*,x). b) After advanced signal processing the image echo at (*r*,x) can be perceived coming from the much smaller volume with the width, ρ_r, in the direction away from the radar and the width, ρ_a, in the azimuth direction.

Thus, without signal processing a SAR would have a very poor resolution. However, it is possible to apply advanced signal processing to the received echoes. This can improve the resolution of the SAR tremendously by a technique denoted pulse compression, the resolution in slant range, ρ_r, can be improved to $\rho_r = C/2B$, where B denotes the bandwidth of the transmitted pulse. This technique is used in many different kinds of radar systems. What makes a SAR unique, is the possibility to improve the azimuth resolution, to $\rho_\alpha = l/2$, where the antenna length, l, typically is less than a few meters. In contrary to other radars, the azimuth resolution is independent of range. The scatterers that contribute to a resolution cells can be perceived as confined within a long thin volume of dimensions ρ_r by ρ_α, see Figure II-4 (b). The synthetic aperture corresponds to a synthetic antenna length l which is equal to the distance travelled by the sensor, L_{sa}, in which a target is illuminated by the beam [8]:

$$L_{sa} = \frac{\lambda \cdot H}{l \cdot \cos(\theta)} \qquad \textbf{(Eq. II-6)}$$

where θ is the depression angle, the azimuth resolution ρ_a of SAR is given by:

$$\rho_a \approx r \cdot \theta_{sa} = \frac{\lambda \cdot H}{2 \cdot L_{sa} \cdot \cos(\theta)} = \frac{l}{2} \qquad \textbf{(Eq. II-7)}$$

this shows that resolution is only dependent on the length of the actual antenna, but not on the distance between sensor and target. However, airborne/spaceborne radar could collect data while flying this distance and then process the data as if it came from a physically long antenna. The distance the airplane/satellite flies in synthesizing the antenna is known as the synthetic aperture [43]. A narrow synthetic beam width results from the relatively long synthetic aperture, which yields finer resolution than is possible from a smaller physical antenna.

Achieving fine azimuth resolution may also be described from a doppler processing viewpoint. A target's position along the flight path determines the doppler frequency of its echoes: Targets ahead of the aircraft produce a positive doppler offset while targets behind the aircraft produce a negative offset. As the aircraft flies a distance (the synthetic aperture), echoes are resolved into a number of Doppler frequencies. The target's Doppler frequency determines its azimuth position [44]. The improvement in angular resolution by a factor of 2 results from the fact that the phase gradient or the path object-antenna in the case of synthetic aperture radar is twice as large [42]. This fact can be explained that real aperture radar transmits simultaneously with all antenna elements and the phase difference can only occur

on the way back from the object to the antenna. In contrast the antenna elements of radar with synthetic aperture transmit separately and at different times. Therefore the phase difference of both the transmit path (radar-target) as well as the return path (target-radar) must be taken into account [42].

While this section attempts to provide an intuitive understanding, SAR is not as simple as described above. Transmitting short pulses to provide range resolution is generally not practical. Typically, longer pulses with wide-bandwidth modulation are transmitted which complicates the range processing but decreases the peak power requirements on the transmitter. For even moderate azimuth resolutions, a target's range to each location on the synthetic aperture changes along the synthetic aperture. The energy reflected from the target must be "mathematically focused" to compensate for the range dependence across the aperture prior to image formation. Additionally, for fine-resolution systems, the range and azimuth processing are coupled (dependent on each other) which also greatly increases the computational processing [45].

4. Radar Polarimetry

The characteristics of a scatterer influence the polarimetric parameters of the scattered electromagnetic wave. Consequently, using radar polarimetry, the polarimetric characteristics of a scatterer can be derived. With this information it is possible to distinguish between different scattering mechanisms and to calculate physical parameters from the investigated scene [10].

i. Scattering matrix

To determine the scattering behaviour of a target, the relationship between the polarization characteristics of the incident and scattered waves is investigated. The polarization states of both waves can be described as a vector, so that the polarization behaviour of the target can be represented by:

$$\begin{bmatrix} \overrightarrow{E_H^s} \\ \overrightarrow{E_V^s} \end{bmatrix} = [S] \cdot \begin{bmatrix} \overrightarrow{E_H^i} \\ \overrightarrow{E_V^i} \end{bmatrix},$$

(Eq. II-8)

where:

$$[S] = \begin{bmatrix} S_{HH} & S_{HV} \\ S_{VH} & S_{VV} \end{bmatrix}$$

(Eq. II-9)

with $\overrightarrow{E_i}$ denoting the incident field and $\overrightarrow{E_s}$ the scattered field. The scattering matrix [*S*] is obtained from the magnitudes and phases measured by the four channels of a polarimetric radar. *H* and *V* denote the horizontal linear and vertical linear polarizations, respectively [10]. *HH* and *VV* are referred to as co-polarized channels, while *HV* and *VH* are called cross-polarized channels [10]. In the monostatic case, [*S*] is symmetric, as the reciprocity property holds for most targets and $S_{HV} = S_{VH}$. Note that also other polarizations with orthogonal states can be used, such as left and right circular [10].

ii. Polarimetric parameters

Total power

The total power *P* received by a polarimetric radar is the sum of the squared modulus of all the elements of the scattering matrix [46].

$$P = |S_{HH}|^2 + 2 \cdot |S_{HV}|^2 + |S_{VV}|^2$$

(Eq. II-10)

Co-polarized correlation coefficient

The Co-polarized Correlation Coefficient (*CCC*), permits separating even and odd bounce contributions by analyzing its phase information. It is given by [46]:

$$CCC = \frac{\langle S_{HH} \cdot S_{VV}^* \rangle}{\sqrt{\langle |S_{HH}|^2 \rangle \cdot \langle |S_{VV}|^2 \rangle}} \qquad \begin{matrix} 0 \leq |CCC| \leq 1 \\ 0^0 \leq \angle CCC \leq 180^0 \end{matrix}$$

(Eq. II-11)

where $*$ is the complex conjugate operator, and $\langle . \rangle$ is the average operator. If the magnitude of *CCC* is unity, the received signals from the two channels are linearly related. If it is less than one it may mean that the backscattering in the two channels is not directly related, that noise is present, or that the received waves are only partially polarized [46]. The *CCC* phase angle is the phase difference between the two co-polarized channels. This value can assist in classifying a pixel, as it depends on the number of bounces that the wave experiences. An ideal single bounce (or odd-bounce) scatterer has a *CCC* phase of 0°, while an ideal double

bounce (or even-bounce) scatterer has a *CCC* phase of 180° [46]. In practice, this parameter shows some variations, so that odd or even-bounce scattering mechanisms are characterized by a *CCC* phase range near the ideal values [46].

5. SAR operation modes

Several sensor operation modes for acquiring SAR data were developed in the past. The most common modes which are implemented in spaceborne SAR missions are StripMap (SM), SpotLight (SL), and ScanSAR (SC) [47]:

The **SM-mode** (see Figure II-7 (a)) is a standard mode in SAR. The radar antenna has a fixed viewing angle with respect to the platform flight path. The antenna records, while the platform is moving along the azimuth direction, the return from the footprint, which covers a theoretically unlimited strip on the ground [47].

The **SL-mode** (see Figure II-7 (b)) aims at improving the azimuth resolution. The radar antenna steers the beam direction to illuminate the required scene for a longer period compared to the standard SM mode. A larger synthetic aperture is created by dedicated processing, resulting in a better azimuth resolution [47]. Due to the antenna steering, the use of the SL mode decreases the ground coverage of the acquisition. The hybrid SM/SL mode offers a compromise between better azimuth resolution than SM mode, and increased ground coverage with respect to the SL mode [47].

The **SC-mode** (see Figure II-7 (c)) provides a larger swath. The larger coverage is obtained by scanning several adjacent sub-swaths with quasi-simultaneous beams, each with a different incidence angle. This will result in a worse azimuth resolution compared to the SM mode because the same azimuth bandwidth is used for the sub-swaths [47].

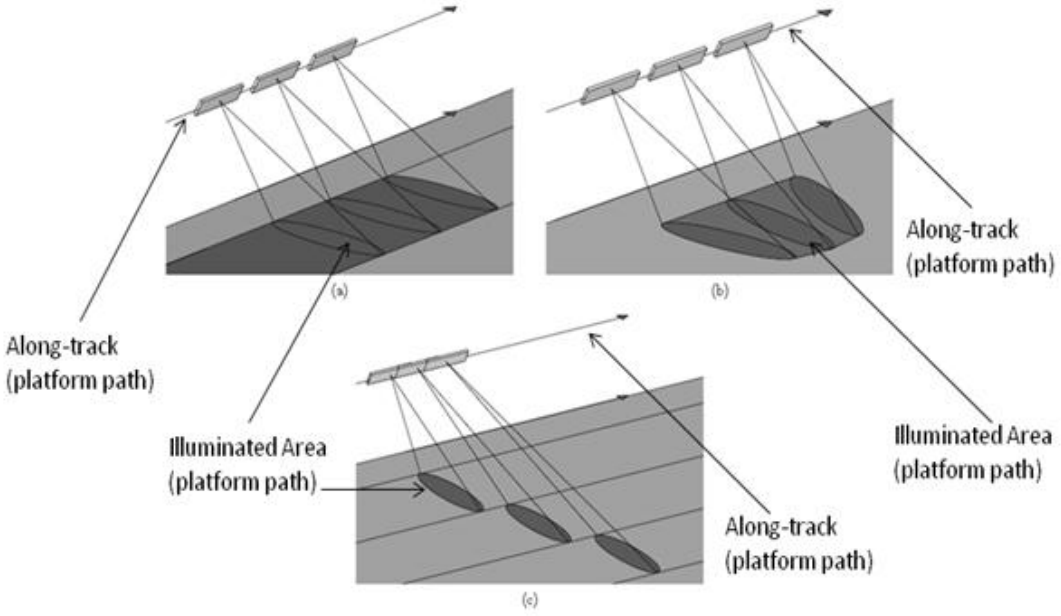

Figure II-7: SAR operation modes: (a) StripMap mode. (b) SpotLight mode. (c) ScanSAR mode.

6. Characteristics of SAR

i. Geometric distortions

The side looking geometry of SAR together with non-flat terrain causes geometric distortions, such as foreshortening. Furthermore, it can cause layover and shadow effects, which are visible as relatively bright and dark regions in SAR imagery, respectively [48].

Foreshortening: Figure II-8 shows the foreshortening phenomena, which is a dominant effect in mountainous areas. Inclined surfaces, which are oriented towards the sensor, appear shortened in SAR imagery. For instance distance $\overline{AB}$ is much longer then its projection $\overline{A'B'}$ on SAR slant range image space. The slant range compression results in a brighter area $\overline{A'B'}$, since it contains the entire energy scattered by the longer $\overline{AB}$ area [48].

Layover: SAR measures the distances between an object and the sensor. Hence, if the inclination of the surface is larger than the incidence angle, the top of the elevated structure is shifted in the image towards the sensor. Layover effect is related to this, it is only different in the sense that if a slope is steeper than the radar beam, parts of the ground surface, the slope facing the sensor, and parts of the slope turned away from the sensor are equidistant to the SAR antenna. Therefore, their backscattering returns to the sensor at the same time, causing the layover effect, where the different signals cannot be separated. For instance, in Figure II-8, the slope $\overline{BC}$ is steeper than the incidence angle of the radar beam so that $\overline{AB}$, $\overline{BC}$, and

$\overline{CD}$ are located within the same distance to the sensor. Hence, their backscattering overlays in the area $\overline{C'B'}$ + $\overline{A'B'}$ + $\overline{C'D'}$ [48].

Shadowing: Shadows are areas where no backscattering is recorded at the sensor, because they are occluded from the radar beam. This occurs when surfaces which are turned away from the sensor are steeper than the SAR illumination, as shown in Figure II-8. The slope $\overline{BC}$ is steeper than the incidence angle of the radar beam so that $\overline{AB}$, $\overline{BC}$, and $\overline{CD}$ are located within the same distance to the sensor. Hence, their backscattering overlays in the area $\overline{C'B'}$ + $\overline{A'B'}$ + $\overline{C'D'}$ [48].

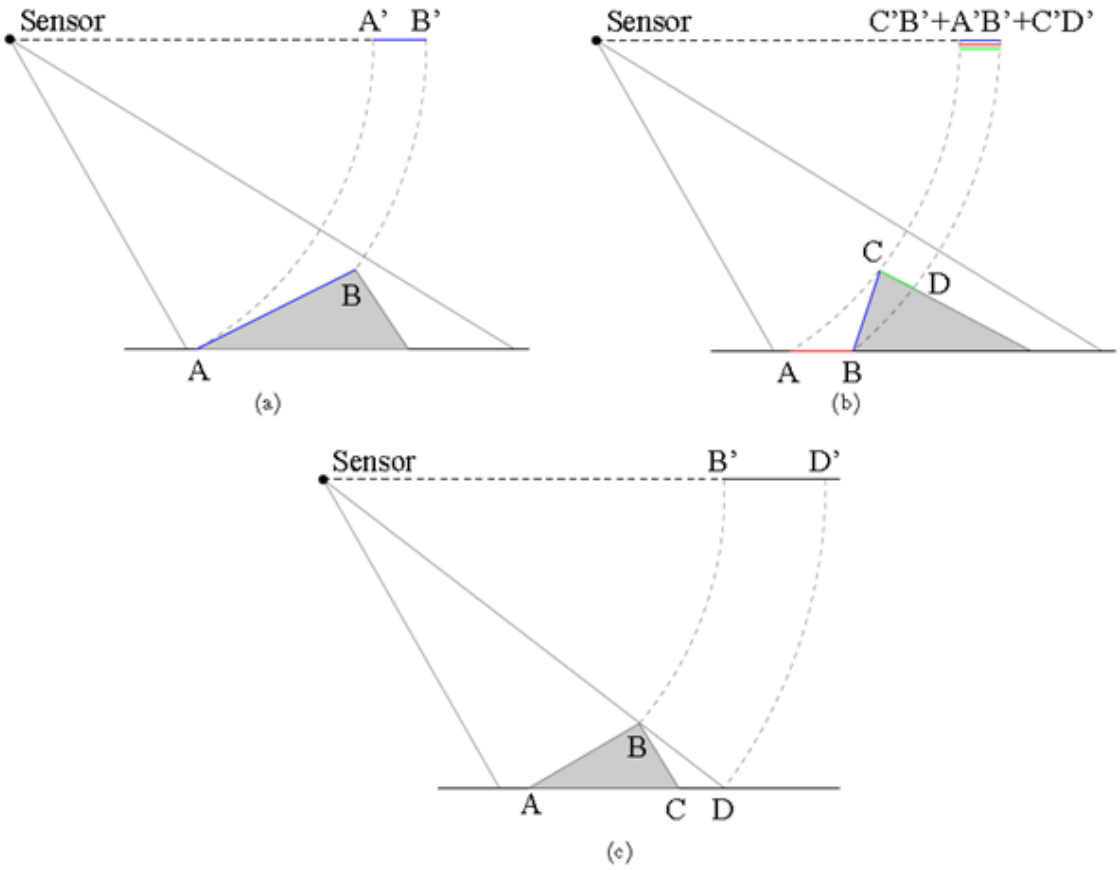

Figure II-8: Geometric effects of SAR [48]. (a) Foreshortening, (b) Layover and (c) Shadowing

ii. Surface scattering

The scattering of microwaves from a surface is composed of a mix of specular and Lambertian scattering, depending on the surface roughness σ_s with respect to the wavelength [8]. For a perfectly smooth ($\sigma_s \ll \lambda$) and infinitely large (size $\gg \lambda$) surface, the field is entirely scattered in the specular direction (see Figure II-9 (a)). Hence, no backscattering is

recorded by the sensor. A perfectly rough surface ($\sigma_s \gg \lambda$) instead scatters according to the Lambertian cosine law (see Figure II-9(c)). For a slightly rough surface ($\sigma_s < \lambda$) the scattering is characterized by a large specular component, and a Lambertian component with less power scattered in all directions (see Figure II-9(b)). The rougher the surface, the weaker are the specular and the stronger are the Lambertian components [8].

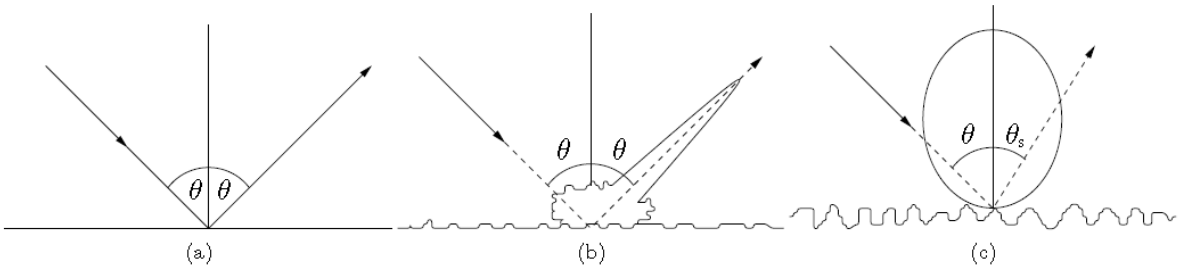

Figure II-9: Specular and Lambertian scattering from surfaces (adopted from [8]). (a) Scattering from smooth surface. (b) Scattering from slightly rough surface. (c) Scattering from rough surface.

Besides being dependent on the surface roughness, the scattering is also influenced by the relative dielectric constant ϵ_r and the relative permeability μ_r of the surface material. For SAR imaging the influence of μ_r is generally negligible [8] and therefore $\mu_r = 1$. ϵ_r depends on the dielectric properties of the material and varies with respect to the material moisture content and the SAR frequency. Materials with low ϵ_r have less reflectivity and hence a higher penetration into the medium [8].

7. Synthetic Aperture Radar Modulation Schemes

In SAR system, there are basically three types of widely used modulation schemes: pulse, Frequency Modulated Continuous Wave (FMCW) or chirp, Stepped-Frequency Continuous Wave (SFCW) and phase coded [22]. Modern spaceborne/airborne radars use FMCW to increase range resolution when long pulses are required to get reasonable signal to noise ratio. The same average transmitting power as in a pulse system can be achieved with lower peak amplitude. The lower peak power allows for the use of commercially available microwave components that have moderate peak power handling capability. In this section, phase coded modulation is not considered due to the fact that it is difficult to generate. Phase coded modulation is normally used for long duration waveforms and when jamming may be a problem [49]. It is worth mentioning that, as a basic SAR imaging system, it is useful to consider a simple model, which is widely considered in literature [49], where the transmitter gain, propagation attenuation, reflection gain (and phase), and receiver gain are ignored [49].

i. Pulse Modulation

One of the most popular transmitted signals in radar systems is the pulsed linear frequency modulated (LFM) waveform, sometimes referred to as a chirp signal [42][6]. There are many reasons for using the LFM waveform. One reason is that it has good pulse compression properties [6]. A basic model of pulsed SAR utilizes the matched filter to maximum the attainable signal to noise ratio [49]. In other words, a matched filter is designed to maximise the response of a linear system to a particular known signal, see Figure II-10.

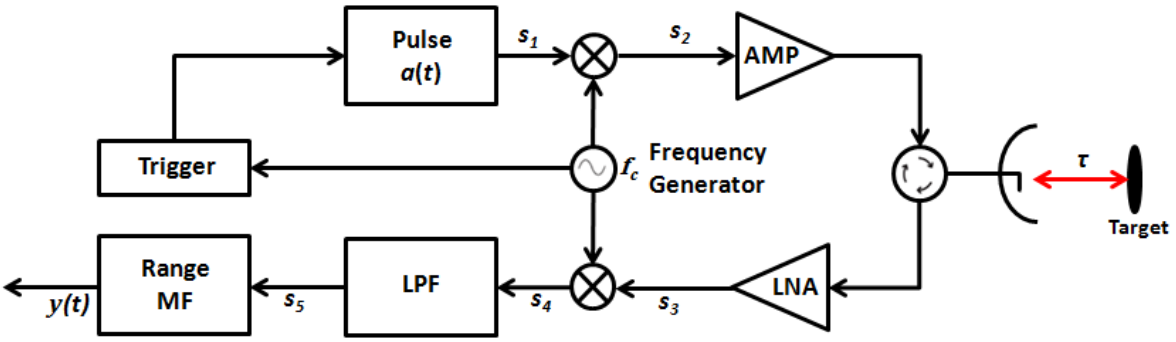

Figure II-10: Signal Model for pulsed SAR.

The transmitted waveform, s_2, is generated by modulating a pulse, a(t), using a chirp that sweeps from the carrier frequency, f_c, with linear frequency rate, α, that is amplified and then fed to the transmitting antenna, radiated, reflected from a target and return to receiver. The output of receiver, after demodulation and Low-Pass Filtering (LPF), is fed into the Range Matched Filter. The matched filter impulse response, $h(t)$, is simply a scaled, time reversed and delayed form of the input signal, as shown in (Eq. II-18). The one SAR pulse and its echo from one point target are, at each of the different points in the system, described by [49]:

$$s_1(t) = a(t) \quad \textbf{(Eq. II-12)}$$

$$s_2(t) = a(t)\cos\left(2\pi f_c t + \pi\alpha t^2\right) \quad \textbf{(Eq. II-13)}$$

$$s_3(t) = \acute{a}(t-\tau)\cos\left(2\pi f_c(t-\tau) + \pi\alpha(t-\tau)^2\right) \quad \textbf{(Eq. II-14)}$$

$$s_4(t) = \acute{a}(t-\tau)\cos(2\pi f_c(t-\tau) + \pi\alpha(t-\tau)^2)\cos(2\pi f_c t) \quad \textbf{(Eq. II-15)}$$

$$s_5(t) = \frac{1}{2}\acute{a}(t-\tau)\cos(-2\pi f_c\tau + \pi\alpha(t-\tau)^2) \quad \textbf{(Eq. II-16)}$$

$$y(t) = h(t)\otimes s_5(t) \quad \textbf{(Eq. II-17)}$$

The range compression is applied using convolution, ⊗, of the low-pass filtered signal with the impulse response of the matched filter (range MF) that is represented as:

$$h(t) = K\, s(\tau - t) \quad \textbf{(Eq. II-18)}$$

where K is a constant. The Fourier transform (FT) of the impulse response is known as the transfer function of the matched filter, $H(j\omega)$, and can be written as:

$$H(j\omega) = FT\{h(t)\} = \int_{-\infty}^{+\infty} h(t) e^{-j\omega t} dt \quad \textbf{(Eq. II-19)}$$

by substituting for $h(t)$, the transfer function becomes:

$$H(j\omega) = K \int_{-\infty}^{+\infty} s(\tau - t) e^{-j\omega t} dt \quad \textbf{(Eq. II-20)}$$

changing the time variable as $t_0 = \tau - t$, then $H(j\omega)$ is given as:

$$H(j\omega) = -K \int_{-\infty}^{+\infty} s(t_0) e^{-j\omega t_0} dt_0 \quad \textbf{(Eq. II-21)}$$

since the FT of s is written as:

$$S(j\omega) = \int_{-\infty}^{+\infty} s(t_0) e^{-j\omega t} dt \quad \textbf{(Eq. II-22)}$$

and the complex conjugate of $S(j\omega)$ is $S^*(j\omega)$, which is given by:

$$S^*(j\omega) = S(-j\omega) \quad \textbf{(Eq. II-23)}$$

hence, $H(j\omega)$ is [50]:

$$H(j\omega) = -K e^{-j\omega\tau}\, S^*(j\omega) \quad \textbf{(Eq. II-24)}$$

The transfer function of the matched filter obtained is the complex conjugate of the spectrum of the signal to which it is matched. Hence, the impulse response $h(t)$ of the matched filter is a scaled, time reversed and delayed version of the desired signal. The matched filter has the property of being able to detect the signal even in the presence of noise. It yields a higher output peak signal to mean noise power ratio for the input than for any other signal shape with the same energy content [41].

ii. Step Frequency Continuous Wave (SFCW)

Linear SFCW radar incorporates a source that is stepped between a start frequency, f_0, and a stop frequency, f_{N-1}, in equal linear increments. The output signal from the source is power divided with one side transmitted and the other side connected to the receiver mixer. At the receiver, a return signal from the target is mixed with a portion of the source signal and then digitized at each step and stored. Traditional demodulation schemes derive the in-phase and quadrature (I and Q) components by demodulating to baseband by two oscillator signals separated by π/2 rad (i.e. in quadrature) [51]. Each one of these signals is then filtered individually and sampled by a separate ADC. After each complete sweep of *N* steps, a Discrete Fourier Transform (DFT) is performed [14]. A block diagram of the linear-SFCW radar is presented in Figure II-11.

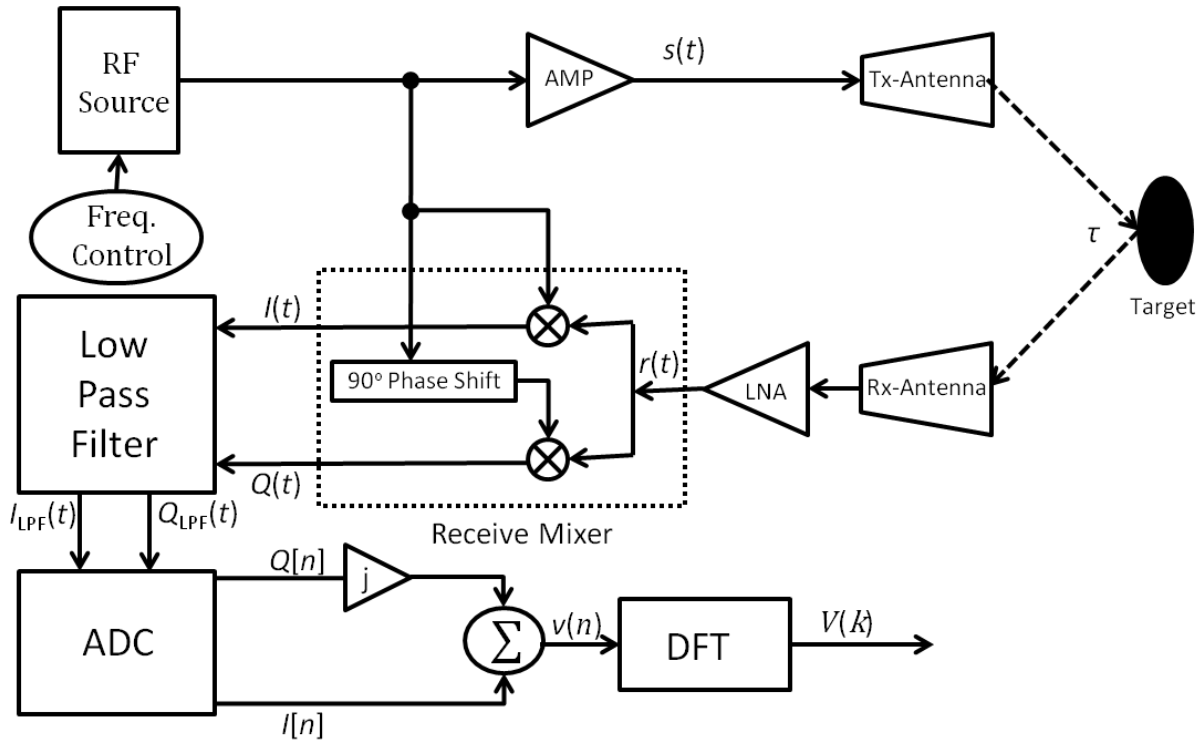

Figure II-11: Block diagram of the SFCW radar technique.

The frequency of the transmitted signal is increasing with time in a stepwise way [19], as depicted in Figure II-12. The CW pulse is represented as a sequence of *N* shorter sub-pulses, each having a constant frequency and duration *Ts*. The range resolution is the same as for linear FMCW and for the determination of the maximum unambiguous range [2], the stepped modulation can be thought as a linear FMCW sampled with a frequency equal to 1/*Ts*,[52] hence:

$$R_u = \frac{C}{2\alpha T_s} = \frac{C}{2\Delta f} = \frac{C\,N}{2B} \quad \textbf{(Eq. II-25)}$$

where Δf is the amount of frequency step, α is the rate of change of frequency and B is the total bandwidth. Range information is based on the time-of-flight principle, which is a phase path difference measurement [14].

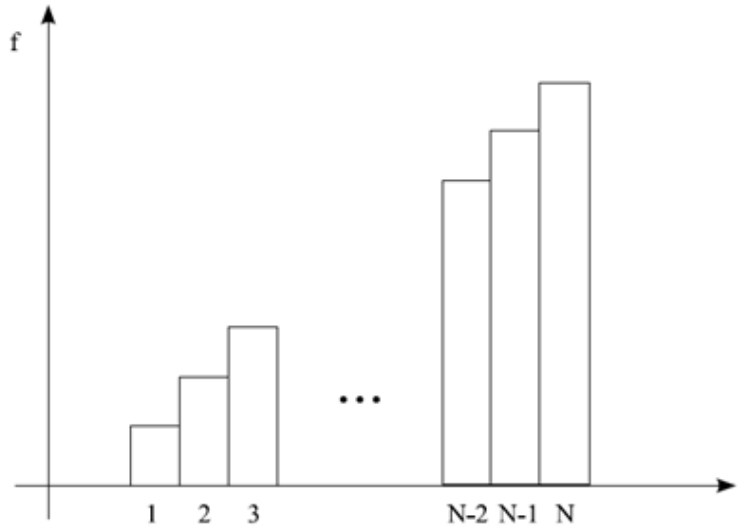

Figure II-12: Linear SFCW signal. The waveform is composed of *N* sub-pulses of duration *Ts* and constant frequency. The frequency is linearly increasing on a sub-pulse basis.

To put this model in a mathematical analysis, a source signal transmitting at frequency f_0, first sub-pulse, is considered as follow:

$$s(t) = A\cos(2\pi f_0 t) \quad \textbf{(Eq. II-26)}$$

where A is the amplitude of the transmitted signal, Then, the received signal is:

$$r(t) = \acute{A}\cos(2\pi f_0(t-\tau)) \quad \textbf{(Eq. II-27)}$$

where $\acute{A}$ is the amplitude of the return, τ is the two-way time flight to the target. Then, by substituting for the phase of the received signal, φ_r, where:

$$\varphi_r = -2\pi f_0 \tau \quad \textbf{(Eq. II-28)}$$

the received signal can be expressed as:

$$r(t) = \acute{A}\cos(2\pi f_0 t - 2\pi f_0 \tau) = \acute{A}\cos(2\pi f_0 t + \varphi_r) \quad \textbf{(Eq. II-29)}$$

Based on the following trigonometric formula:

$$\cos(a+b) = \cos(a)\cos(b) - \sin(a)\sin(b) \quad \textbf{(Eq. II-30)}$$

Eq. II-29 can be rewritten in terms of the I-and-Q components as:

$$r(t) = \acute{A}\cos(\varphi_r)\cos(2\pi f_0 t) - \acute{A}\sin(\varphi_r)\sin(2\pi f_0 t) \quad \textbf{(Eq. II-31)}$$

then, the signals at the output of the mixer are:

$$\begin{aligned} I(t) &= \acute{A}\cos(\varphi_r)(\cos(2\pi f_0 t)\cos(2\pi f_0 t)) \\ Q(t) &= \acute{A}\sin(\varphi_r)(\sin(2\pi f_0 t)\sin(2\pi f_0 t)) \end{aligned} \quad \textbf{(Eq. II-32)}$$

these signals are low-pass filtered with a cut-off frequency of f_0, as a result:

$$\begin{aligned} I_{LPF}(t) &= \frac{\acute{A}}{2}\cos(\varphi_r) \\ Q_{LPF}(t) &= \frac{\acute{A}}{2}\sin(\varphi_r) \end{aligned} \quad \textbf{(Eq. II-33)}$$

After that, the signals are digitized using ADC, which generates $I[n]$ and $Q[n]$. The digitized signals at the output of ADC are summed to form the DC voltage value for each sub-pulse. In the case of f_0, the DC voltage is:

$$v(0) = \frac{\acute{A}}{2}e^{-j2\pi f_0 \tau} \quad \textbf{(Eq. II-34)}$$

The value of $v(0)$ is stored and the same process is repeated for each step frequency of the sweep up to f_{N-1}. At each step, n, ADC is performed and a new value for $v(n)$ is generated. This sequence is the radar return signal [14]:

$$v(n) = \frac{1}{2}\sum_{i=0}^{N-1}\delta(n-i)\acute{A}e^{-j2\pi f_i \tau} \quad \textbf{(Eq. II-35)}$$

where $\delta(n)$ is the dirac-delta function or unit impulse. At each step n, the data from all N steps are then converted into the time-domain pulse response equivalent with a DFT:

$$V(k) = \begin{cases} \frac{1}{N}\sum_{n=0}^{N-1} v(n)\, e^{-j(2\pi/N)kn} & ,0 \le k \le N-1 \\ 0 & ,otherwise \end{cases} \quad \textbf{(Eq. II-36)}$$

iii. Frequency Modulated Continuous Wave Modulation

With pulse positioning the range information is obtained by measuring the time difference between a transmitted and a received signal while in FMCW the distance between the antenna and the target is proportional to the difference in frequency between the transmitted and the received signal [11]. The idea of the FMCW is almost as old as the pulse radar, though it has not been commercialized due to lack of relevant technology but that has changed in the last few decades.

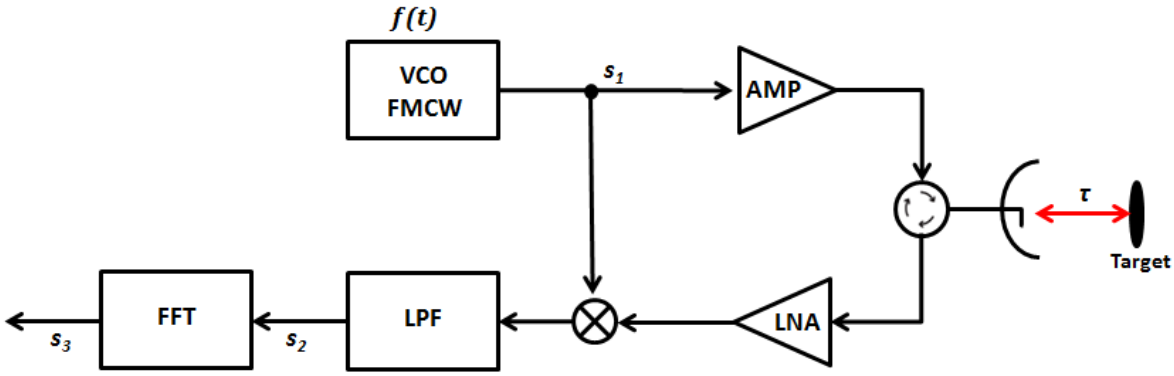

Figure II-13: Basic diagram of FMCW SAR.

FMCW transmits a frequency sweep, see Figure II-14 (a), often called a chirp. The signal is reflected from distant targets and detected by the receiver where the return signal is mixed with a copy of the transmitted signal to determine the range of the target [11]. The transmitted waveform has a time varying frequency, f (t), as seen in Figure II-14 (b), given by:

$$f(t) = f_0 + \alpha \cdot t \qquad \forall t < T \qquad \textbf{(Eq. II-37)}$$

where f_0 is the initial frequency, α is the Rate of Change of Frequency that is a linearly increasing frequency sweep where the starting frequency is f_0 and then it increases to f_1 at the end of the sweep after a time T called the sweep period. The bandwidth B is the difference between f_1 and f_0. The rate of change of frequency is then given by:

$$\alpha = \frac{B}{T} \qquad \textbf{(Eq. II-38)}$$

and the phase of the waveform is given by:

$$\phi(t) = 2\pi \int f(t)dt = 2\pi \cdot (f_0 t + \frac{1}{2}\alpha \cdot t^2) \quad \textbf{(Eq. II-39)}$$

By assuming an ideal point target, the received signal frequency f_R, as shown in Figure II-14 (b) is given by:

$$f_R(t) = f_0 + \alpha \cdot (t - \tau) \quad \textbf{(Eq. II-40)}$$

where τ is the two-way time of flight defined in (Eq. II-3).

In a homodyne FMCW receiver, the received signal is mixed with a replica of the transmitted waveform and low pass filtered (LPF). This process is usually called stretching or de-ramping. The resulting output is called the beat frequency, f_B, which is presented in Figure II-14 (c). Mixing of these two signals produces sum and difference frequencies, f_T + f_R and f_T - f_R. The resultant signal is then low pass filtered to remove the f_T + f_R term. The term that remains is the beat frequency f_B. The beat frequency is shown to be directly related to the range after substituting τ and α by values shown in (Eq. II-3) and (Eq. II-38), respectively:

$$f_B = f_T - f_R = \alpha \cdot \tau = \frac{B}{T} \cdot \frac{2R}{C} = \frac{2BR}{CT} \quad \textbf{(Eq. II-41)}$$

Thus by knowing the beat frequency and the positioning parameters of *B* and *T*, we can retrieve range information from the return signal. FMCW positioning often store the beat frequency signal to allow for off-line processing using Fourier transform techniques. The Fast Fourier Transform (FFT) is the mathematical tool used to interpret the spectrum of the beat frequency signal in terms of antenna range [53]. Thus, In order to compress the range response, FFT is performed on the beat signal, making the signal content available in the frequency domain. The response of a single target is qualitatively shown in Figure II-14 (d).

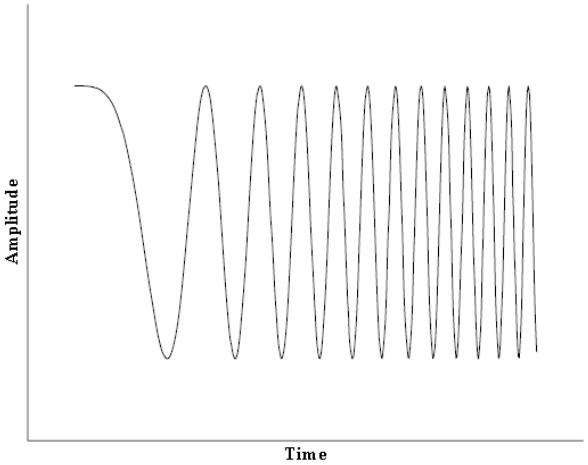

(a) Amplitude of a chirp signal (transmitted signal, S_1). The frequency is linearly increasing with time

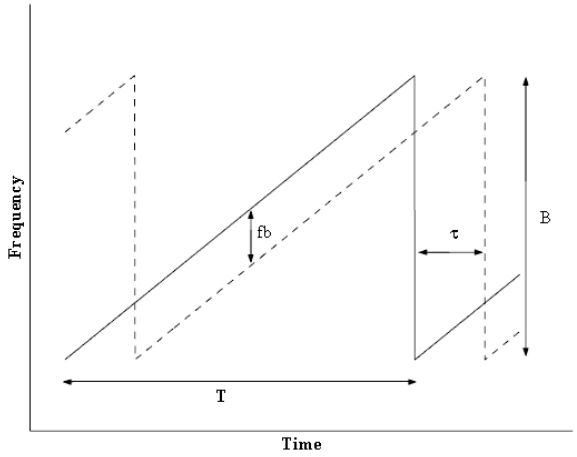

(b) Frequency plot of the chirp signal *f*(t). The received signal (dashed) is a delay version of the transmitted (solid)

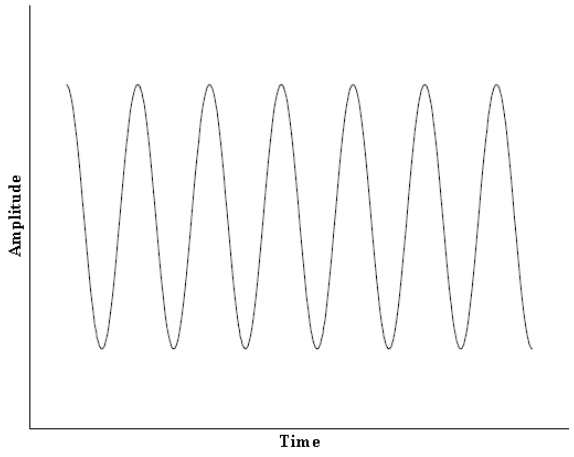

(c) Beat signal representation in the time-domain (output of LPF, S_2). The frequency is proportional to the scatterer distance.

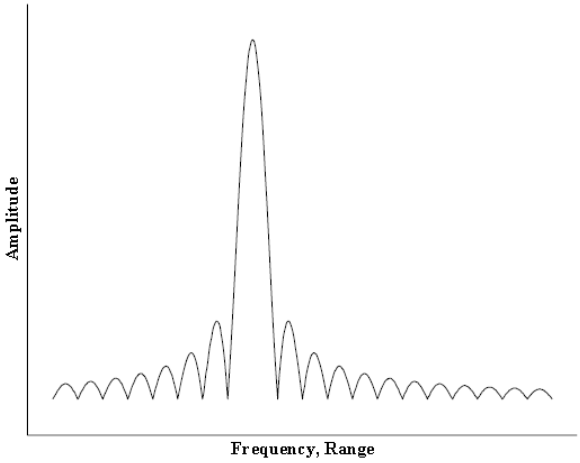

(d) Beat signal representation in the frequency-domain (S_3). The frequency axis can be directly associated with range.

Figure II-14: Overview of the Linear FMCW radar Principle

In practice, the resulting signal from an FMCW sensor is the superposition of different sinusoidal signals corresponding to the environment being illuminated by the radar waves [53]. In this case, the sidelobes of a strong target response could cover the signal of a weaker scatterer. In order to reduce sidelobes, a windowing function is applied to the signal before applying the Fourier transform, however, this is done at the expense of broadening the main lobe [12] and hence, resolution is deteriorated. This point target scenario can be extended to multiple targets also [54]. For each target, there is a return with a frequency corresponding to the distance. Each return also has amplitude corresponding to the round trip attenuation to its specific target. These can be seen as peaks in the frequency domain and this can be further extended to distributed targets. In this case, the return doesn't consist of only individual peaks

but actually have spread peaks corresponding to returns from other scatterers. The fact that the excursion of the linear FM ramp determines the range resolution of the system makes it easy for FMCW positioning to have very good range resolution. It also makes it very easy to change the range resolution as well, so that, for example, on navigation radar it is possible to use a different range cell width on each range scale, so as to optimize the resolution of the display on each range scale [3].

The target range is proportional to the beat frequencies, which means that the number of range cells which need to be processed by the FFT can be limited by simply filtering the signals to reduce the bandwidth into the FFT to cover only those ranges which are of interest. This can lead to a dramatic reduction in the complexity of the digital processor. Additionally, the fact that the FMCW waveform is highly deterministic is actually an advantage in rejecting interference because it allows definite predictions to be made about the form which any genuine signals should have [41]. This allows interference which is uncorrelated with the expected returns to be very effectively suppressed. This applies in particular to interference from pulse radars and to narrow-band interference.

a) FMCW SAR Transmitted Signal

The transmitted radar signal, $s_{tx}(t)$, shown in Figure II-14(a), is of the following mathematical form [2]:

$$s_{tx} = \text{rect}\left(\frac{t}{T_r}\right) e^{\left(j2\pi f_o t + \pi K_r t^2\right)} = a_t(t)\, e^{\left(j2\pi f_o t + \pi K_r t^2\right)} \quad \textbf{(Eq. II-42)}$$

where rect is a rectangular function that is generated at baseband, mixed to the carrier, and is denoted by $a(t)$. The signal is a function of range time or quick time t where the carrier frequency is f_o, the chirp pulse duration is T_r, and the range chirp, or FM rate, is K_r. Anther important parameter is the signal bandwidth B_o which can be denoted by the following equation:

$$B_o = |K_r| T_r \quad \textbf{(Eq. II-43)}$$

Figure II-15 depicts the transmitted radar signal as a cosine with a linearly ramping up frequency over a transmit duration followed by a null receive duration. The transmit window is called the pulse envelope, $a(t)$, and defines the duration of the transmission. During the receive duration, the antenna waits to receive reflected radar signals from the targets contained in a one-dimensional range slice echo as function of quick time [4].

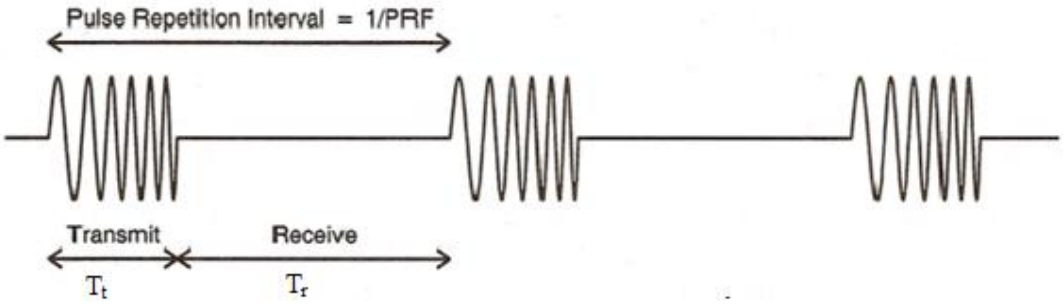

Figure II-15: Number of Transmitted Radar Pulses [4]

The magnitude of the radar signal at the antenna during transmit-duration and receive-duration are depicted in succession in Figure II-15. The pulse repetition frequency (PRF):

$$PRF = \frac{1}{(T_t + T_r)} \quad \textbf{(Eq. II-44)}$$

where T_t and T_r represent the duration of the transmitted and received signals respectively. PRF defines the number of pulses transmitted per second (pps) [4].

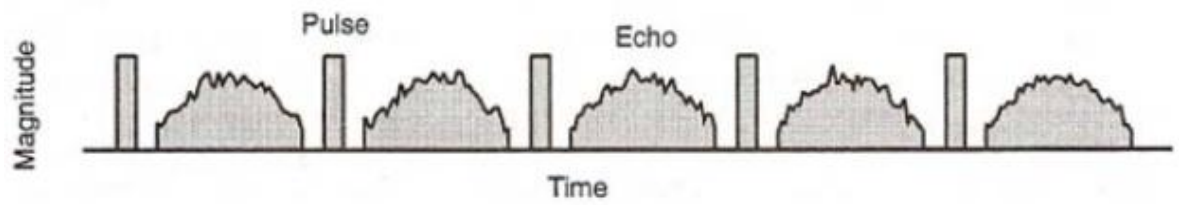

Figure II-16: SAR Antenna Activity [4]

b) FMCW Received SAR Signal

The SAR received radar signal, $s_{rx}(t,\eta)$, is simulated by the form shown in the equation below after demodulation which removes the high frequency carrier wave and brings the signal to baseband [6]:

$$s_{rx} = \sum_{m=0}^{M-1} \left[F_m a_t \left(t - \frac{2R_m(\eta)}{C} \right) w_a(\eta - \eta_c) e^{-j4\pi\left(\frac{f_o R_m(\eta)}{c}\right) + j\pi K_r\left(t - \frac{2R_m(\eta)}{c}\right)^2} \right] + n_m(t,\eta)$$

(Eq. II-45)

this signal has two time dimensions: range time/quick time, *t*, and azimuth time/slow time, η. Equation (Eq. II-45) is a summation of the reflections from *M* different point targets, which is presented by the summation operation. The received signal is the a time delayed, attenuated, phase shifted, amplitude modified – due to azimuth beam pattern affects – version of the transmitted signal with additive white Gaussian noise (AWGN) added [6]. The time delay is

$\frac{2R_{m(\eta)}}{C}$, the attenuation factor from reflection at the target is F_m, the phase shift from reflection at the target is φ, the azimuth beam pattern amplitude modification is $w_a(\eta - \eta_c)$, and the additive white Gaussian noise is $n_m(t,\eta)$. The time delay is calculated by the distance the radar beam travels, twice the instantaneous slant range divided by the speed of the radar beam, approximately the speed of light [4]. The centre lobe of the beam pattern produces the largest reflection strength, but the smaller sidelobes also produce reflections and the overall received signal strength from a point target over azimuth time, η, resembles a *sinc* squared function centred [2] at the beam centre crossing time η_c, which is the azimuth time at which the centre of the beam pattern crosses the centre of the target area [4].

8. Influence of Sidelobes on Temporal Resolution in SAR

In SAR, the pulse responses of range and azimuth are both sinc functions with high levels of sidelobes [53]. The band-limited property of the radar signal affects the size of the sidelobes in the targets' response [55]. Furthermore, in some cases the accumulated sidelobes can be mistaken for a false target and/or have a blurring effect on generated SAR images [56]. It is well known that a system impulse response with low sidelobes is of great importance in SAR images because sidelobes contribute to noise and may interfere with nearby scatterers. The theoretical values of PSLR and ISLR without using any sidelobe suppression techniques are -13.2 dB and -9.7 dB, respectively, which do not meet practical requirements [22]. Therefore, it is necessary to perform sidelobe suppression with the aim of achieving SAR images of high quality [34].

In order to demonstrate the effect of sidelobes in SAR processing, two responses of two targets in a basic FMCW radar system, as explained in section 7 of Chapter 2, of a saw-tooth chirp that is sweeping from 0.3 GHz to 0.5 GHz in 5msec is simulated. Four scenarios are considered. In the first scenario, the two targets are of equal magnitude and they are located far from each other. In this scenario the two targets are completely resolvable and sidelobes levels are not affected, see Figure II-17. In the second scenario, one of targets has a weaker response but they are still positioned to be of some distance apart and the response is shown in Figure II-18. The indication of the weak target response is a small fluctuation at 5.2 kHz. In this scenario, the second target is almost impossible to be detected using the standard-FFT technique. In the third scenario, the two-target responses are simulated to be of the same magnitude but they are positioned very close to each other. In Figure II-19, it can be noticed

that a third peak at 2.7 kHz, which can be mistaken for a false target, is generated due the accumulation of the sidelobes from the two targets. Finally, in the fourth scenario, the targets are simulated so that they are still positioned very close to each other but with one of them having a weak response. As shown in Figure II-20, the standard-FFT barely gives any indication of the presence of the second weak target.

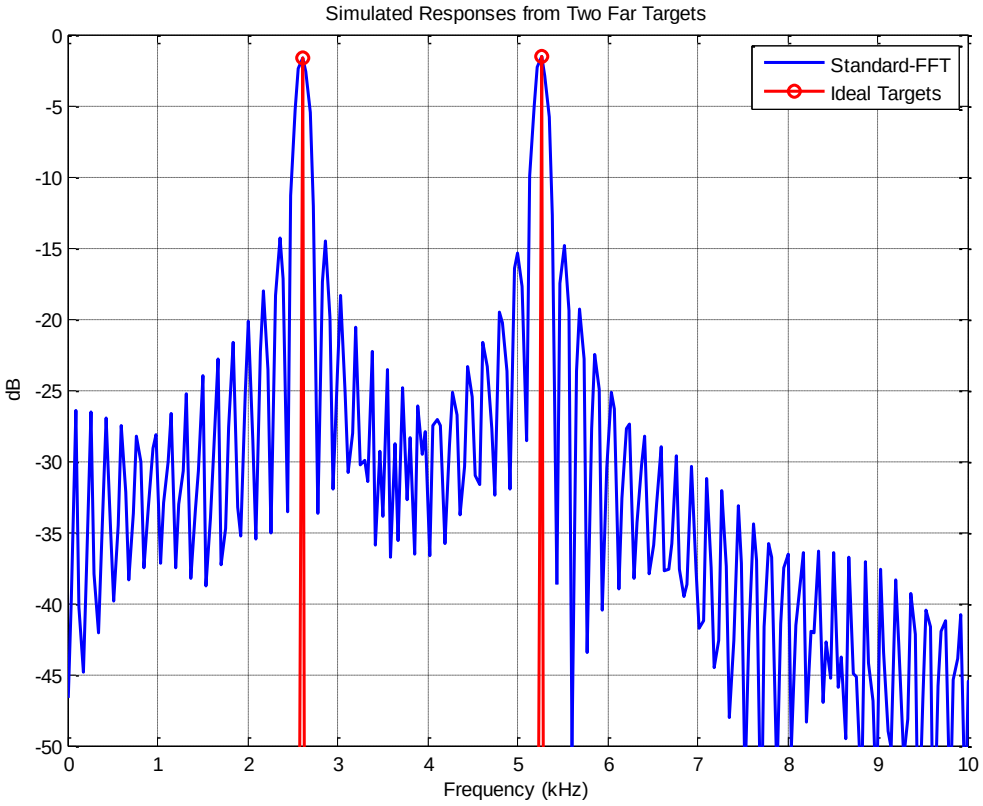

Figure II-17: Simulating Target responses that have equal magnitudes and with some distance apart.

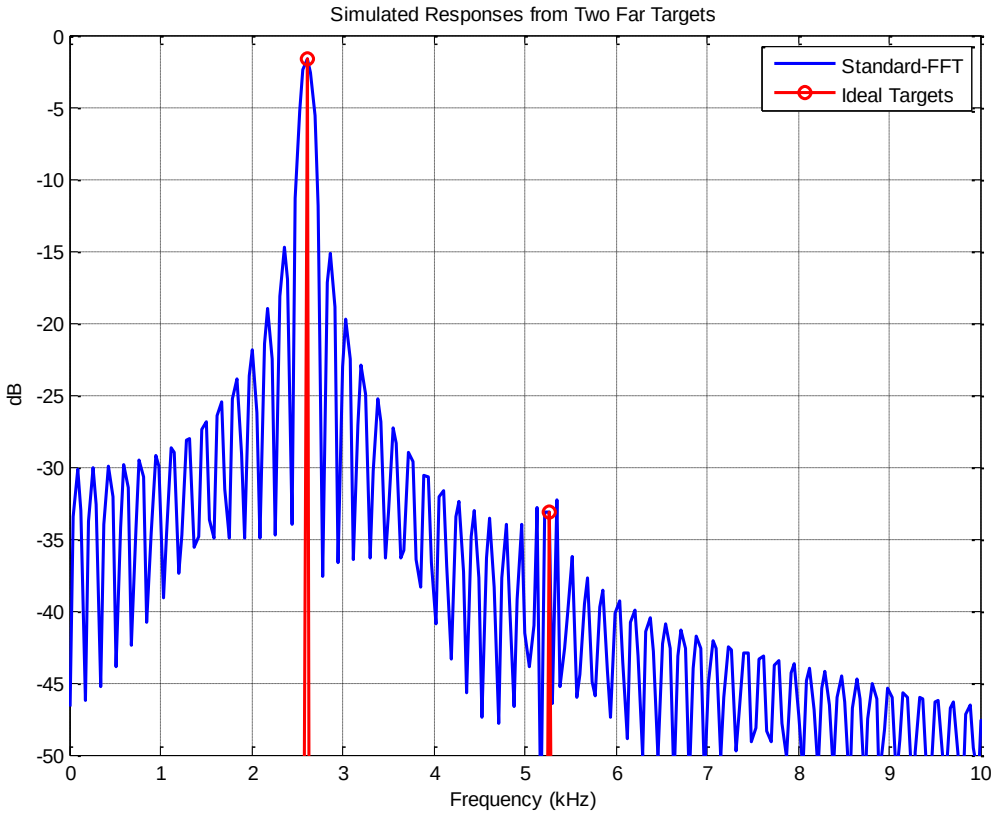

Figure II-18: Simulating Target responses that have different magnitudes and with some distance apart.

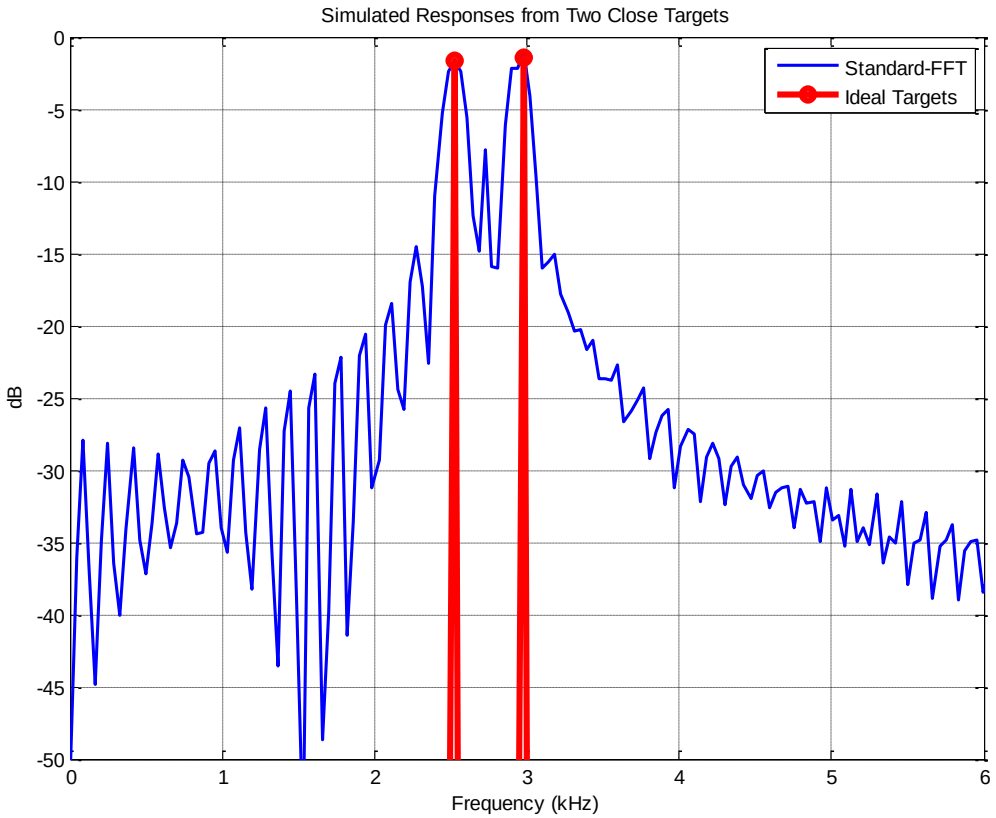

Figure II-19: Simulating Target responses that have equal magnitudes but are very close to each other.

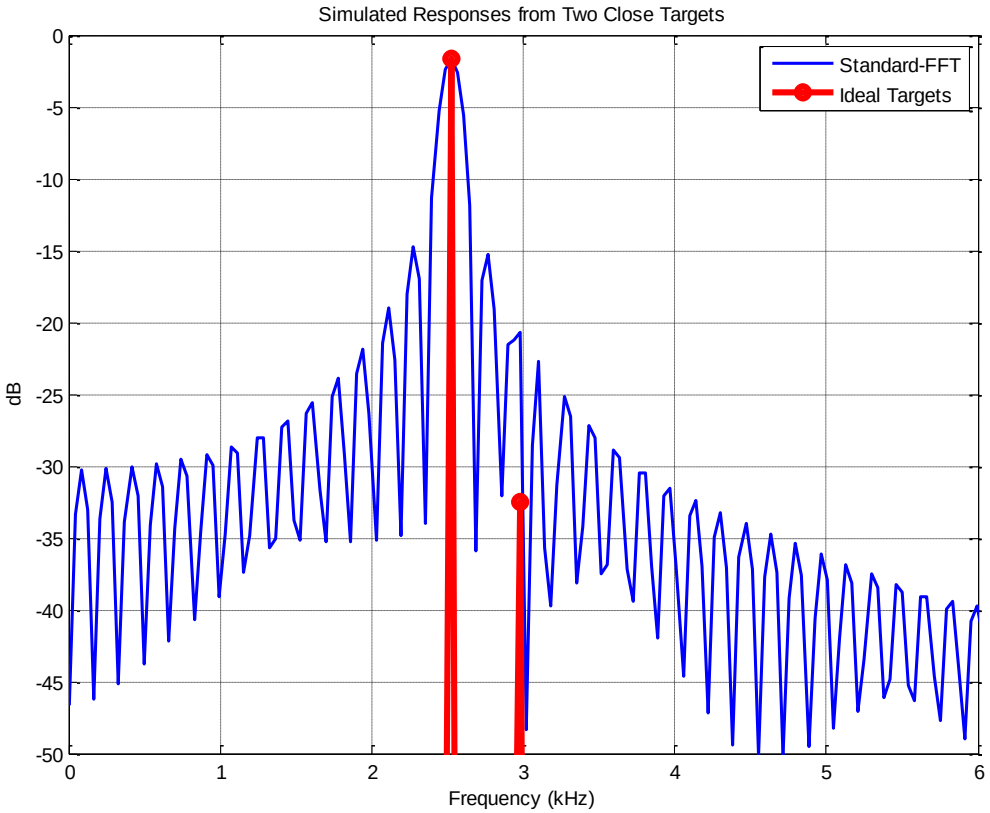

Figure II-20: Simulating Target responses that have different magnitudes but are very close to each other.

9. Pulse Compression

SAR processing is a two-dimensional problem. In the SAR data, the signal energy from a point target is spread in range and azimuth, and the purpose of SAR focussing is to collect this dispersed energy into a single pixel in the output image [34]. In range, the signal is spread by duration the linear FM transmitted pulse. In azimuth, the signal is spread by the duration it is illuminated by the antenna beam, or the synthetic aperture. As a point target passes through the azimuth antenna beam, the range to the target changes. On the scale of the wavelength, this range variation causes a phase variation in the received signal as a function of azimuth. This phase variation over the synthetic aperture corresponds to the Doppler bandwidth of the azimuth signal, and allows the signal to be compressed in the azimuth direction. The range variation to point target can result in a variation in the range delay to the target that is larger than the range sample spacing, resulting in what is called range migration. This range migration of the signal energy over several range bins must be corrected before azimuth compression can occur. The range-Doppler algorithm performs this correction very efficiently in the range-time, azimuth-frequency domain [57].

i. Range Compression

In principle, a SAR that uses a short pulse to achieve good range resolution would work perfectly. The present section solely concerns pulse compression by using linear FM signals although other methods like de-ramp exists. Most modern Spaceborne/Airborne SAR systems, though, use linear frequency modulation (LFM) pulse compression techniques to achieve better SNR [34]. In collecting the SAR data, a long-duration linear FM pulse is transmitted. This allows the pulse energy to be transmitted with a lower peak power. The linear FM pulse has the property that, when filtered with a matched filter, the result is a narrow pulse in which all the pulse energy has been collected to the peak value. Thus, when a matched filter is applied to the received echo, it is as if a narrow pulse were transmitted, with its corresponding range resolution and signal-to-noise ratio [57]. In that case, range compression is certainly a part of the data processing and therefore, pulse compression is usually an integrated part of SAR processors. The purpose of pulse compression is to be able to use a transmitted pulse, $a(t)$, of length, T, having an autocorrelation, $r(t)$, with a width much smaller than T. One way to achieve that is by transmitting a pulse that sweeps linearly over a bandwidth B, where B and T can be chosen independently, this result in:

$$\rho_r = \frac{C}{2}\rho_t \approx \frac{C}{2}\frac{1}{B} \qquad \textbf{(Eq. II-46)}$$

where ρ_t is the spatial resolution in time – the natural measurement scale of a radar.

The actual voltage on the antenna is the real part of $s_2(t)$ can be expressed as:

$$Re\{s_2(t)\} = \begin{cases} \cos(\varphi(t)) & if\ 0 \le t \le T \\ 0 & otherwise \end{cases} \qquad \textbf{(Eq. II-47)}$$

Hence, the instantaneous frequency, $f_i(t)$, and the phase, $\varphi(t)$, are as follow:

$$f_i(t) = \begin{cases} f_c + \frac{B}{T}\left(t - \frac{T}{2}\right) & if\ 0 \le t \le T \\ 0 & otherwise \end{cases} \qquad \textbf{(Eq. II-48)}$$

and:

$$\varphi(t) = \begin{cases} 2\pi\left(f_c t + \frac{B}{T}\left(t - \frac{T}{2}\right)^2\right) + \varphi_0 & if\ 0 \le t \le T \\ 0 & otherwise \end{cases} \qquad \textbf{(Eq. II-49)}$$

In most SAR systems both phase terms cause a large number of oscillations over the pulse, i.e. $f_cT \gg 1$ (large carrier frequency) and $TB \gg 1$ (large time-bandwidth product) [2].

For illustration purposes, though, an example with T = 0.25μs, B = 100 MHz, and f_c = 100 MHz with a few oscillations is shown in Figure II-21. It is possible to calculate the exact shape of the autocorrelation, but it is quite complicated. Alternatively, one could just note the fact that a linear FM signal only gives a large cross correlation for almost exact alignment of the two signals [41]. This is what is needed for efficient pulse compression. By looking at the wave-form, it may be understood intuitively, in order to estimate the width of the autocorrelation and to understand why weighting reduces sidelobes another approach is required. The key is to realize that the linear sweep of the instantaneous frequency corresponds to a linear sweep in the frequency domain, resulting in a rectangular spectrum. Figure II-22 indicates where the different parts of the signal in time-domain end up in frequency domain. Since the frequency is swept linearly in the time domain, the energy in the frequency domain is also distributed approximately linearly in time [12].

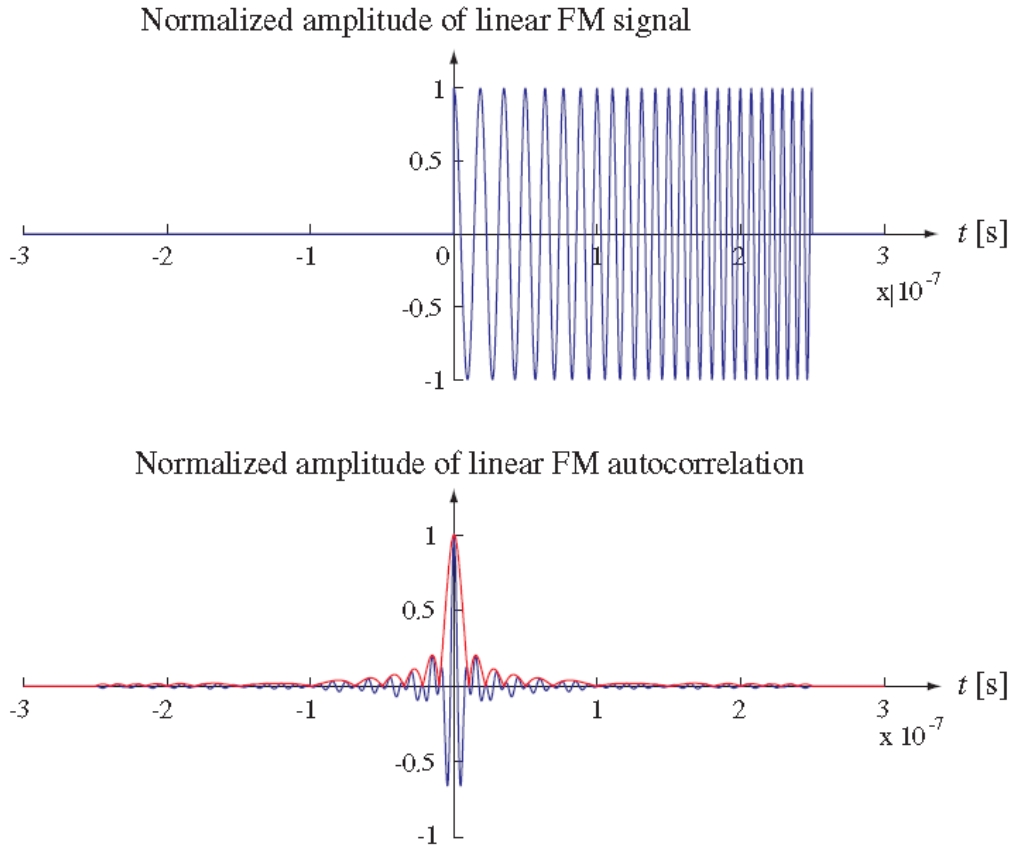

Figure II-21: LFM signal (top) and its autocorrelation (bottom) including its envelope in red.

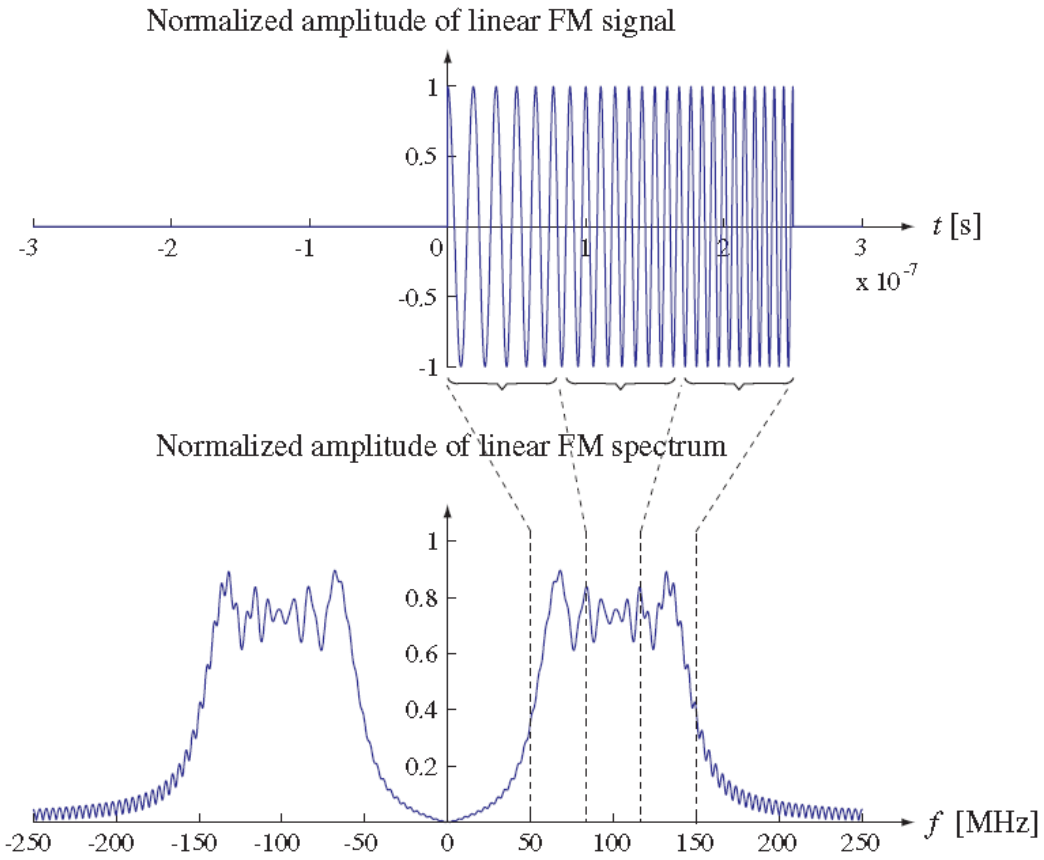

Figure II-22: LFM (top) and its spectrum (bottom). The corresponding parts of signal energy in the time and frequency domains are indicated by the dashed lines.

The matched filtering of the received echo at baseband, $s_4(t)$, corresponds to a convolution operation, ⊗, with the impulse response of the matched filter. This convolution corresponds to correlation with a copy of the transmitted pulse, $s_1(t)$. Thus, the matched filter output is:

$$s_5(t) = s_4(t) \otimes s_1(t_h - t) \qquad \textbf{(Eq. II-50)}$$

where t_h determines the origin of the time axis. This equation representation in Frequency domain is:

$$S_5(f) = S_4(f) S_1^*(f) e^{j2\pi f t_h} \qquad \textbf{(Eq. II-51)}$$

For a linear FM signal the spectrum, $S_1(f)$, is approximately rectangular, and thus the spectrum of the autocorrelation is also approximately rectangular with a width of B [53]. The autocorrelation would have approximately sinc shape, with a -3dB width of $1/B$. This correspondence between time and frequency domain is of great benefit for digital pulse compression, since it is much faster to compute the matched filter output by transforming $s_4(t)$ to the frequency domain, multiply by the matched filter transfer function, $S_1^*(f)$, and transform back to the time-domain, than carrying out a direct convolution calculation.

However, care should be taken when the discrete FFT method for convolution is applied, as it corresponds to a cyclic convolution [53].

ii. Range Migration

One consideration has to be made about the theoretical SAR resolution. In order to achieve the maximum resolution, the full Doppler bandwidth has to be processed. As the platform moves during data acquisition, the distance between the target and the radar changes producing the signal Doppler bandwidth. This range variation can be larger than the range resolution, causing the target response to migrate through different resolution cells. This phenomenon is called Range Cell Migration (RCM) [6]. Furthermore, the range migration depends on the distance and this is what makes the SAR reconstruction an inherent two-dimensional inversion problem [34]. Range migration is corrected using the relation between range and Doppler frequency [11]. This relation is derived with the assumption that the radar moves regularly and the target is stationary. Conversely, if the radar moves irregularly or the target is moving, this technique may not work well because the relation between the range and the Doppler frequency is distorted. The inertial navigation unit may provide information about the irregular motion of the radar, which can be used to derive the relation between the range and the Doppler frequency [4]. However, this information may be unavailable or inaccurate, or the target may be moving. In such cases, range migration needs to be corrected automatically [58] using Range migration correction (RMC) techniques, as shown in Figure II-23.

iii. Azimuth Compression

In its basic form, azimuth compression follows the same line as range compression [2]. First the point target response (PTR) is calculated. Then, the received image data are correlated with the PTR to obtain the compressed image. For two reasons, though, azimuth compression is more complicated than range compression [2]: The first is that the PTR is a 2-D function, due to range migration. The second is that the PTR is range dependent. This implies that one cannot just use a single 2-D filter to compress the entire image, but each azimuth line must be compressed individually. The range-Doppler algorithm, however, eliminates the need for a two 2-D reference function by removing the range migration before application of the compression filter. This cannot be done in the range-azimuth domain since targets at different azimuth positions needs to be corrected differently, see Figure II-23.

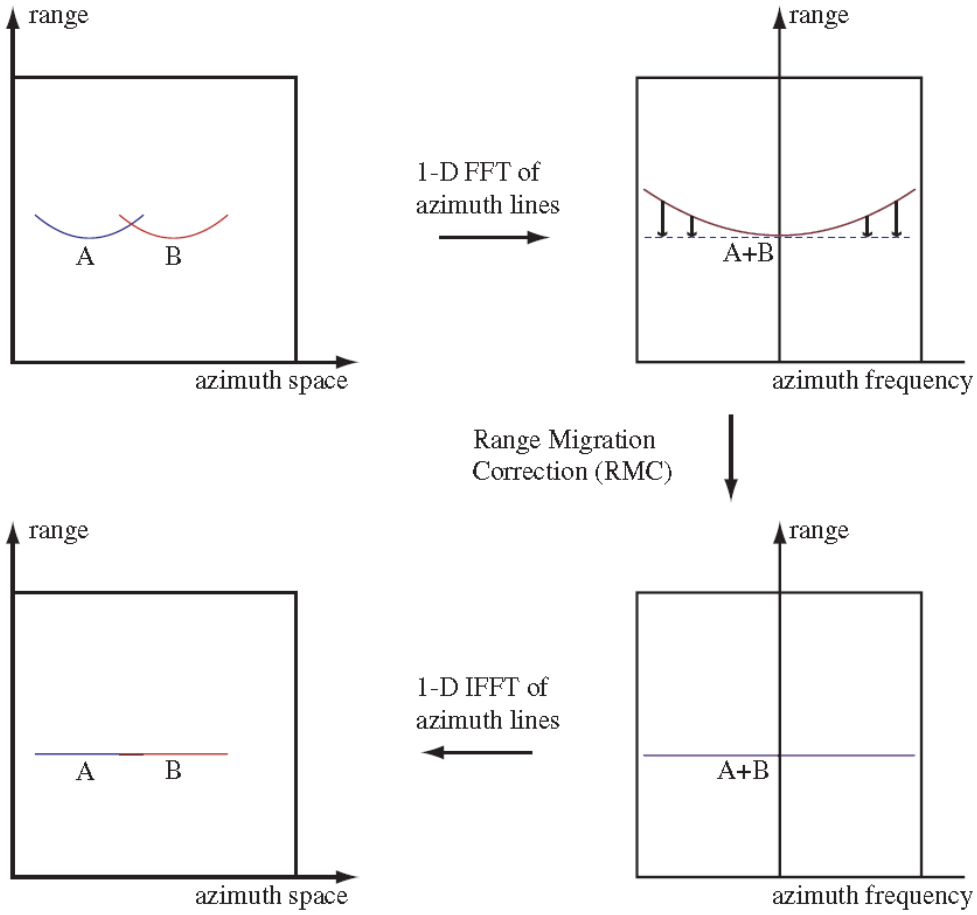

Figure II-23: Range Migration Correction (RMC) before Azimuth compression [41].

The moving target follows either an elliptical or a hyperbolic path depending on the sign of a parameter α [59], which is defined as:

$$\alpha = 1 - \frac{v_p^2}{v^2} \qquad \textbf{(Eq. II-52)}$$

where:

$$v_p = |v_p| \quad and \quad v = |v_t - v_p| \qquad \textbf{(Eq. II-53)}$$

where v is the relative target speed, v_p is the SAR-platform speed and v_t is the target speed. As shown in Figure II-24, for an in-bound target approaching the radar, the relative target speed v is larger than v_p, hence, α is positive. Consequently, the target migration path is a convex downward ellipse [59]. Conversely, for an out-bound target departing from the radar, v is less than v_p and α becomes negative. In this case the target migration curve is a concave upward hyperbola [59].

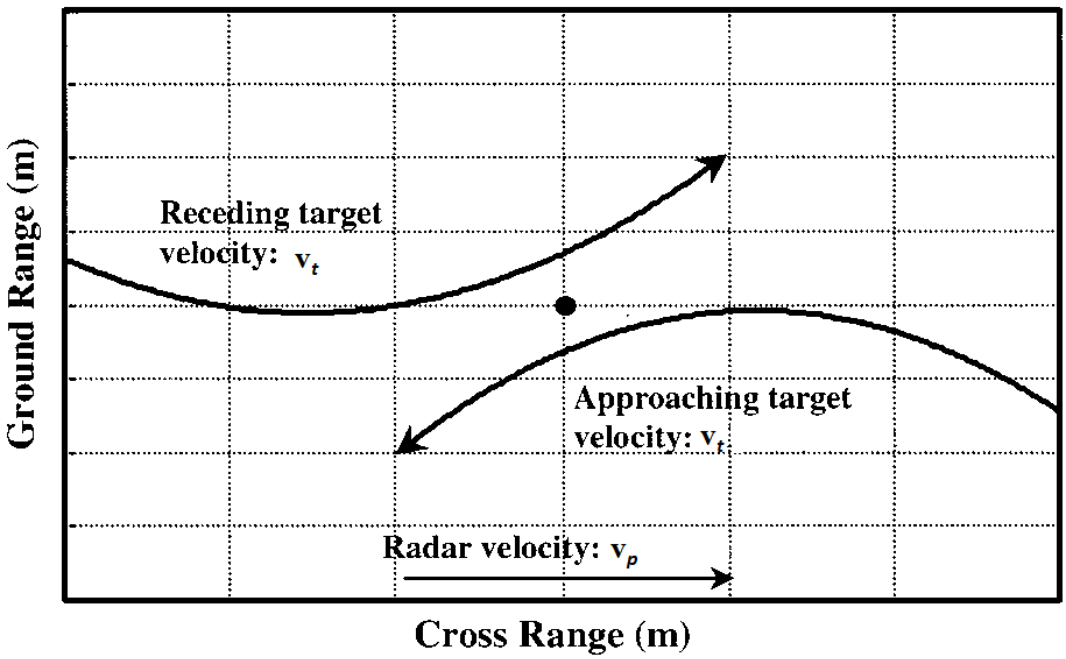

Figure II-24: An example of target migration paths in the SAR image [59].

For small range migrations, the energy of a point target will only shift slowly in the range direction as function of azimuth [41]. In other words a point target will have a long duration in azimuth. The phase of the PTR corresponds to a linear frequency modulation. Thus, there is a linear relation between the azimuth (space) and the azimuth (frequency) domain [41]. Therefore the curved PTR in the range-azimuth (space) domain maps to a curved PTR in the range-azimuth (frequency) domain. The key feature now is that all PTRs, from targets at a given closest approach range, will appear at the same location in the range-azimuth (frequency) domain. Thus, the curvature can be straightened so that all (most) energy appears in one azimuth line. Now, the energy of the PTR is located in one azimuth line, the phase is quadratic, and thus the azimuth compression can be carried out line by line. The compression filter, though, needs to be updated for each line, since the phase variation depends on closest approach range.

Since azimuth (frequency) is also denoted Doppler, the algorithm has been named the range-Doppler algorithm [12]. In the remaining part of the section a simple mathematical description of the range-Doppler algorithm is provided. The heart of the range-Doppler algorithm is the assumption that the azimuth dependence of the PTR is:

$$s(x) = a_x(x)e^{-j\frac{4\pi}{\lambda}\Delta r(x)} \quad \textbf{(Eq. II-54)}$$

where $a_x(x)$ is a slowly varying amplitude modulation and $\Delta r(x)$ is the range difference to closest approach. By using a least square quadratic approximation to $\Delta r(x)$ [41], the azimuth signal can be expressed as:

$$s(x) = a_x(x)e^{-j2\pi\frac{x^2}{\lambda r_0}} \quad \textbf{(Eq. II-55)}$$

Note that azimuth-space and not azimuth-time is used as independent variable. Most treatments of the range-Doppler algorithm used azimuth-time and assume a constant velocity, so that $x = vt$. However, $\Delta r(x)$ is a function of x and only indirectly of t, since it only matters where the individual pulses are transmitted and received – not at what instant. The only drawback of using x as independent variable is that it is necessary to work with spatial frequencies, which are not as familiar as "regular" frequencies. The relation between x and spatial frequency, f_x, is calculated similar to the instantaneous frequency of a linear FM modulated signal:

$$f_x = \frac{1}{2\pi}\frac{d\varphi(x)}{dx} = -\frac{2x}{\lambda r_0} \quad \textbf{(Eq. II-56)}$$

or

$$x = -\frac{\lambda r_0}{2} f(x) \quad \textbf{(Eq. II-57)}$$

thus the range migration in the spatial frequency domain is:

$$\Delta r(f_x) = \frac{\left(-\frac{\lambda r_0}{2} f_x\right)^2}{2r_0} = \frac{\lambda^2 r_0}{8} f_x^2 \quad \textbf{(Eq. II-58)}$$

When working with digital signals, the relations between sample number in the spatial domain, n, and space, x, and the relation between sample number in the spatial frequency domain, m, and spatial frequency, f_x, are:

$$time - domain: \qquad x(n) = n\Delta_x \quad \textbf{(Eq. II-59)}$$

$$freq - domain: \qquad f_x(m) = \frac{m}{N}\frac{1}{\Delta_x} \quad \textbf{(Eq. II-60)}$$

where N denotes FFT length and Δ_x is sample spacing.

iv. Range Walk

Azimuth compression assumes that each scatterer remains within the same range bin during the observation interval. However, since the range gates are defined with respect to a

radar that is moving, the range gate grid is also moving relative to the ground. As a result a scatterer appears to be moving within its range bin [11]. This phenomenon is known as range walk, which is the image distortion generated by relative motion within the surface footprint. Range walk could also be caused by irregular satellite motion, such as spacecraft yaw and tilt, or by orbit-changing manoeuvres [60]. A small amount of range walk does not bother Doppler processing as long as the scatterer remains within the same range bin [4]. However, range walk over several range bins can constitute serious problems that could be resolved using some standard techniques such as Linear Range Walk Correction (LRWC) [4][61].

v. Range Doppler Algorithm (RDA)

As shown in this section so far, SAR processing is achieved in two main steps: first, range compression and second, azimuth compression within each bin at the end of the observation interval. The block diagram of a SAR signal processing in the frequency domain is shown in Figure II-25. This block diagram of basic Range Doppler Algorithm (RDA) which is an algorithm designed to achieve block processing efficiency using frequency domain operations in both range and azimuth while maintaining the simplicity of one-dimensional operations [4]. First, range compression is performed by range FFT and then a range matched filter multiply followed by range IFFT to complete range compression. The second step is azimuth compression that starts by transforming the data into the range Doppler domain, where Doppler centroid estimation is performed. Then RMC, which is the step of correcting for the changing range delay to a point target as the target passes through the antenna beam (range migration), is utilized. After that, Azimuth matched filtering is applied as a frequency domain matched filter multiply at each range gate. Finally, azimuth IFFT is done to transform the data back to the time domain, resulting in a compressed complex image.

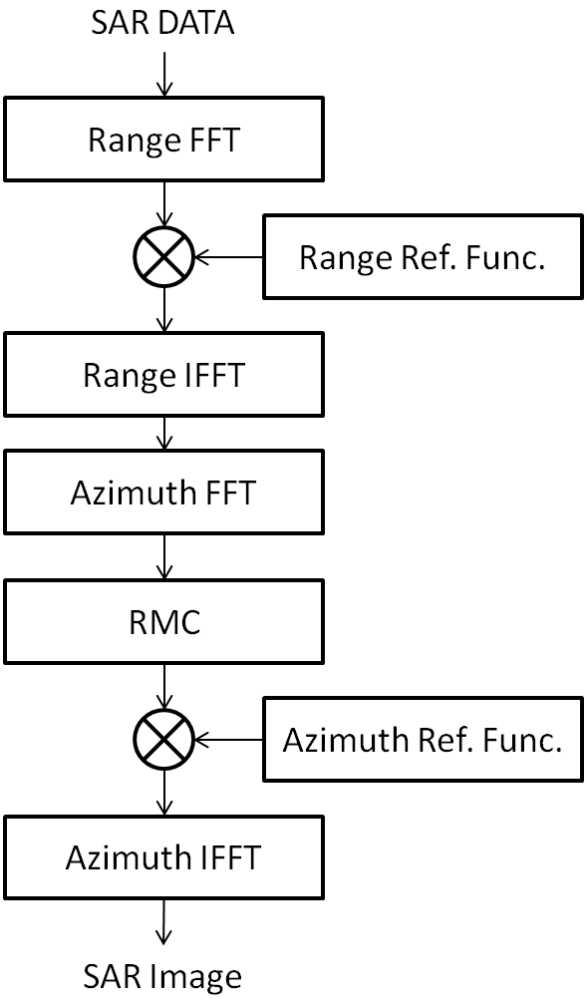

Figure II-25: RDA Signal Processing Block Diagram for SAR System

10. Speckle

SAR is a coherent system, which means that it transmits and receives signals of the same wavelengths. The microscopic scattering of these signals returning from distributed targets cause interference in the resolution cell (pixel) and this interference manifests itself as a sort of "salt and pepper" effect which is usually referred to as speckle [57]. It has been verified in several works that the standard deviation of the signal is proportional to its mean over homogeneous areas [62] which suggests the use of a multiplicative model for representing speckle. In reality it is not a noise effect but the result of constructive and destructive interferences between the complex returns from the scatterers in a resolution cell. Since the resolution cell is large compared to the wavelength, *N* targets are present in one cell. Their individual scattering contributions sum up coherently resulting in a single complex value measured at the sensor [63], see Figure II-26, which is expressed as:

$$A \cdot e^{i\varphi} = \sum_{n=0}^{N} A_n \cdot e^{i\varphi_n} \qquad \textbf{(Eq. II-61)}$$

where A is the modulus and φ is the phase.

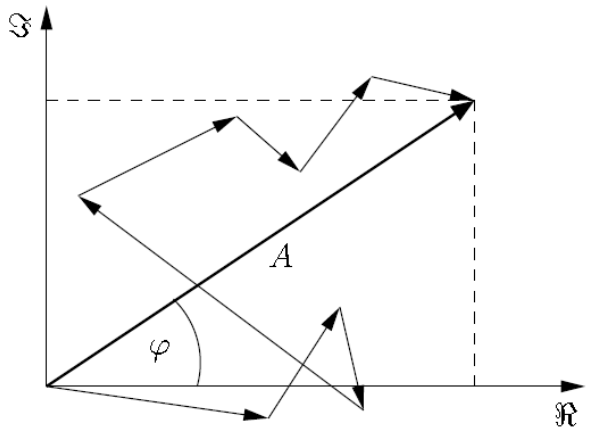

Figure II-26: Coherent sum of individual scatterers [62].

The speckle effect depends on the scatterers present in the scene and can be reduced by averaging different measurements of the same target implying a reduction of the spatial resolution [45]. An example of a single-look SAR image that is contaminated by speckle noise from [64] is presented in Figure II-27. The presence of speckle in a SAR image forms an obstacle to the extraction of topographic information and some form of pre-processing of the images to suppress or ensure its removal must be taken into account in the development of any stereo-matching strategy. The full removal of speckle noise without losing information in SAR images is still a long way off [30]. As yet, there is no speckle filter that is appropriate for all Radar images. A complete statistical description of speckle noise and reflectivity models used in speckle filtering can be found in [65]. However, some of the most common techniques for removing speckle in literature are: the multi-look processing, the use of non-adaptive speckle filters, and the commonly used technique of adaptive speckle filtering.

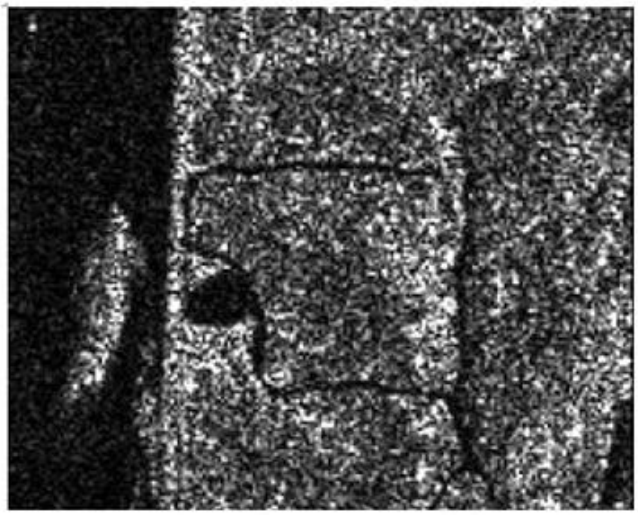

Figure II-27: An example of single-Look RADARSAT raw image contaminated by speckle noise [64].

i. Multi-Look Processing

The effect of speckle in a Radar image can be suppressed by averaging several images (looks), formed using smaller aperture lengths, to reduce the noise variance; a process usually referred to as multi-look processing [66]. It is essentially a signal processing procedure requiring sophisticated hardware and software and is therefore usually performed by the data provider. The number of 'looks' used in the averaging process determines the amount of speckle that will be reduced in the resulting image; the greater the number of looks the more reduction in the effects of speckle, however, this comes at a cost because it also leads to a degradation in the spatial resolution of the Radar image. The relationship between real aperture length L, spatial resolution ρ_r, and the number of looks N, is given by the following equation [8]:

$$N \approx \frac{\rho_r}{0.5L} \qquad \textbf{(Eq. II-62)}$$

So, for example, if real aperture length is 10m and the worst spatial resolution that would be acceptable is 25m, then the number of 'looks' required would be 5.

ii. Non-Adaptive Speckle Filters

Non-adaptive speckle filters are those that use the same set of rules for the entire image regardless of differences in image texture, contrast, etc. The most common filters make use of the statistical mean or median computed from a fixed size moving window [67]. Since these filters use basic statistical models, they have the advantages of being easy to implement, do

not require a lot of computer time and produce results quickly. The main disadvantage, however, is that they do not take into account the principles relating to the formation of the SAR imagery and therefore do not produce the best results. They may work well with additive Gaussian noise but are unsuitable for the multiplicative nature of SAR speckle noise [48]. With a statistical mean based filter, the image is convolved with a predetermined kernel by moving the fixed size window, say n x n, across the image pixel by pixel and substituting the digital number (DN) of the pixel in the centre of the window with the mean of all n^2 pixels in that window. Kernel sizes can range for 3x3, 5x5, 7x7, 9x9 or larger, but the larger the size the more smoothing is done to the image.

The median filter operates similar to the mean filter, but instead of substituting the centre pixel with an average, it replaces the centre pixel with the median value of the n^2 pixels in the window [67]. The advantage of this filter over the mean is that the pixel value is always replaced with a DN value from the dataset and not one that is computed. This filter is also more effective over the mean filter because it tends to preserve step edges and the output is not affected by spurious DN values in the window, thus making it effective in eliminating spike noises. For further information on non-adaptive filters the reader is directed to some of the most common remote sensing and image processing text, for example, [68].

iii. Adaptive Speckle Filters

In contrast to non-adaptive filters, adaptive filters tend to preserve the subtle image information. These adaptive filters should be able to smooth speckle in homogeneous areas while preserving texture and high frequency information in heterogeneous areas. It may not always be possible for filters to achieve these two requirements and at times there will have to be a trade-off between requirements [69]. Numerous adaptive filters have been proposed in the last few years that have achieved, to some degree, the suppression of speckle in SAR imagery. Most adaptive filters are formulated based on three main assumptions [62]: (a) SAR speckle is modelled as a multiplicative noise (see Equation Eq. II-61); (b) the noise and signal are statistically independent; and (c) the sample mean and variance of a pixel is equal to its local mean and local variance computed within a window centred on the pixel of interest. Some of the most common adaptive speckle filters [63] are: Lee Filter, Kuan Filter and Frost Filter.

The Lee Filter [62][70], which first approximates the multiplicative noise model as a linear model and then applies the minimum mean square error (*MMSE*) criterion to the linear model. The resulting DN value, R_{DN}, for the filtered pixel that is generated based on statistics derived from a fixed size moving window over the image is given by:

$$R_{DN} = (I_c \times W) + \left(I_m \times (1 - W)\right) \quad \textbf{(Eq. II-63)}$$

where I_c is centre pixel of the filter window, I_m is mean value of DNs within the filter window and W is a weighting factor given by:

$$W = 1 - \frac{Cu^2}{Ci^2} \quad \textbf{(Eq. II-64)}$$

where

$$Cu = \sqrt{\frac{1}{L}} \quad \textbf{(Eq. II-65)}$$

as L is number of looks, and

$$Ci = \frac{\sigma}{I_m} \quad \textbf{(Eq. II-66)}$$

where σ is the standard deviation of DNs within the filter window.

In Kuan filter [71][72], the multiplicative noise model is first transformed into a signal dependent additive noise model then the *MMSE* criterion applied to this additive model. The resulting speckle filter has a similar form to the Lee filter as in Equation Eq. II-63, but with a different weighting function given by:

$$W = \frac{1 - \frac{Cu^2}{Ci^2}}{1 + Cu^2} \quad \textbf{(Eq. II-67)}$$

And finally, the Frost filter [73] that is also based on the multiplicative noise assumption uses an exponentially damped convolution kernel which adapts itself to features based on local statistics. This filter differs from the Lee and Kuan filters in that the reflectivity of the scene is estimated by convolving the image with the impulse of the SAR system. The Frost

filter is outlined in the following equation, which shows the resulting DN value, R_{DN}, for the filtered image pixel using an *n x n* window:

$$R_{DN} = \frac{P_1 \times W_1 + P_2 \times W_w + \ldots + P_n \times W_n}{W_1 + W_2 + \ldots + W_n} \quad \textbf{(Eq. II-68)}$$

where P_i is DN for each pixel in the *n* x *n* window (i = 1...n) and *W* is weighting function given by: $W = \exp(-K \times Ci^2 \times |t|)$ where: *K* is the exponential damping factor and $|t|$ is absolute value of the pixel distance from the centre pixel to its neighbours in the filter window.

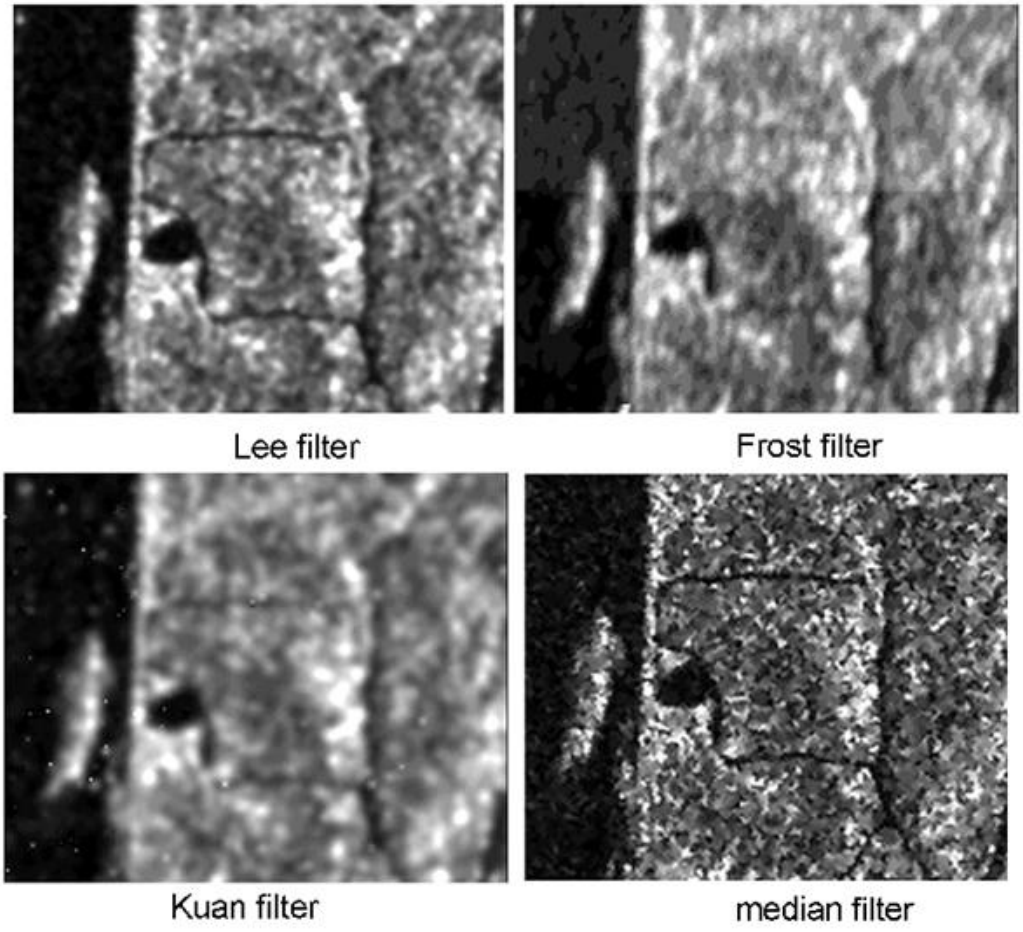

Figure II-28: comparing some different Speckle removing filters at the third iteration of the 3×3 moving window that is applied on SAR Image from Figure II-27 [64].

11. Brief Review of SAR Image Formation Techniques

The problem of SAR image reconstruction is to obtain an estimate of the reflectivity density based on the observed, pre-processed acquired SAR data, which is referred to as SAR raw data. In the following subsections, some of the main conventional SAR image formation

methods are briefly discussed where the importance of FFT and IFFT processes, which is about 70% of the total computation operation in SAR image formation [11], is very clear.

i. Polar Format Algorithm

Since the spotlight-mode SAR observation kernel consists of a band-pass Fourier transform of the reflectivity field to be imaged, the standard image formation algorithm has been the polar format algorithm [74] based on the two-dimensional fast Fourier transform (FFT). Nevertheless, there is no known fast FFT-type algorithm for computing approximate samples of the reflective density from polar samples of its Fourier transform. As a result, in the case of SAR, the known data samples are first interpolated to a Cartesian grid, assuming unknown samples. After interpolation, an inverse 2-D FFT is employed and the magnitude of the reconstructed complex image is displayed for viewing. Before FFT processing, the data can be windowed to reduce sidelobe levels. This is the algorithm that is frequently used in SAR systems today [74].

ii. Filtered Backprojection

Another image reconstruction method, suggested by the tomographic formulation of SAR, is the filtered backprojection (FBP) algorithm [75][34][76]. Backprojection is mostly associated with geometrically based methods. FBP can be derived by writing the 2-D inverse Fourier transform in polar coordinates. The radial slices in the frequency domain are then recognized as 1-D Fourier transforms of the projections of the field at the corresponding angle, by virtue of the projection slice theorem [34]. This reduces the double Fourier integral to two sequential operations: first the data at each observation angle are filtered by a ramp filter, and then the results are backprojected to obtain a reconstruction. FBP is the algorithm that is currently used in commercial Computerized Axial Tomography scanners, which are known as CT/CAT scanners [77]. A very interesting observation that worth mentioning here is about why FBP is the preferred technique for CT, whereas the 2-D FFT based polar format algorithm has been the choice for SAR [78]. Comparing CT and SAR reconstruction problems, there is a considerable difference between the shapes of the Fourier sampling grids. In CT, the sensor moves all around the object to be imaged. This produces Fourier samples in a disk shaped region [77] rather than an annular region as in SAR [78]. The nearly Cartesian nature of the grid in SAR makes interpolation more accurate than in the case of CT, so that the polar format algorithm is attractive in SAR. In CT, however, interpolation is much more

difficult, due to the circular distribution of the data. Hence, the FBP algorithm which does not require interpolation in the Fourier domain is preferred.

In [78], it has been argued that for the SAR problem the polar format algorithm, even with simple interpolation methods, produces high-quality reconstructions. Both the polar format and the FBP algorithms are based on the inverse operator for the case when perfect data are available throughout the spatial frequency domain [79]. These methods have no explicit mechanism to counter any imperfection in the data. Although there are algorithmic differences between the two methods, the reconstructions they produce are very similar.

iii. Backward Propagation Method

Recently there have been steps towards alternative algorithms for SAR image formation. The motivation for a class of these new approaches has been increasing the resolution of SAR images beyond the Fourier limit and the backward propagation method has been one of the important answers to that demand [80]. Backward-propagation is associated with wave equations based methods. This class of algorithms contains most migration algorithms, including the well known Kirchhoff migration, as well as the wave equation based, non-conventional SAR. The backward propagation method is capable of high resolution imaging and has been implemented for various important applications [80]. The first step is to measure the scattered wave-field over a linear aperture. Then the complex wave-field is Fourier transformed to obtain its spatial-frequency spectrum. Subsequently, the backward propagation filter (BPF) is used to backward propagate the received spectrum throughout the target region. An inverse Fourier transform in the z direction brings the result back to the spatial domain, which is the final step in forming the coherent image. This procedure is also known as computed holographic imaging.

Because of the coherence of the wave-field, the resulting image has limited resolution in the range direction. The resolving capability may be improved by moving from a holographic system to a multiple-frequency tomographic system, which means collecting data using multiple wavelengths and then incorporating the information into a single image. The backward propagation method can also be applied to multiple-frequency tomographic imaging. The multiple-frequency backward propagation procedure is a simple extension of the single-frequency procedure: a collection of coherent sub-images are superimposed to form a composite image. Because the formulation of the backward propagation filter depends

on the coherent operating wavelength, each coherent sub-image needs to be reconstructed independently. The weighting coefficients of the linear superposition depend on the characteristics of the source with respect to wavelength. If the source distribution is not a function of wavelength, the weighting is constant.

iv. Spectral Estimation-based Methods

In conventional methods, image resolution is limited by the system bandwidth. Let us consider the observed signal from a synthetic aperture, which is a collection of received returned signals. Since peaks in the spectrum of this signal correspond to strong point scatterers in the scene, one idea to overcome the resolution limit of conventional techniques is to use modern 2-D spectral estimation methods [81] rather than a Fourier transform for forming the SAR image [82][83], assuming that polar to rectangular re-sampling has already been done [81]. Algorithms based on this idea are usually termed "super-resolution" methods, and have become increasingly popular. For example, the Lincoln Laboratory baseline Automatic Target Recognition (ATR) system for SAR data currently uses a super-resolution technique known as high-definition vector imaging (HDVI) [84].

In addition to resolution improvement, other motivations suggested for the application of these methods are to remove sidelobe artefacts, and to reduce speckle [82]. When applied to SAR imaging, spectral estimation-based methods are quite successful in preserving gain on ideal point scatterers, reducing sidelobes and reducing main lobe widths, however most spectral estimation-based methods reduce gain on non-point-like scatterers such as trees, and they usually fail to improve the quality of images containing objects with distributed features [82]. Spectral estimation-based methods implicitly incorporate some prior information into their processing, and can produce better results by virtue of that. The problem with these approaches is that they are not very flexible in the form of the prior information provided to the algorithm. Hence, these methods provide no explicit means to accentuate one type of feature over another. A comprehensive comparison of various spectral estimation methods in SAR can be found in [82].

Spectral estimation-based SAR imaging methods require the estimation of a correlation matrix of the collected radar returns. This estimation is the most computationally intensive part of the methods. Since the amount of data from a typical SAR scene is quite big, this is done in the following manner. First a SAR image is formed using 2-D FFT processing, small

chips from that image are transformed back to the Fourier domain, and a correlation matrix is estimated for each of these down-sampled signal histories corresponding to each image chip. Finally the imaging algorithm is applied on these signal histories, and the formed images are mosaiced together to form the full scene. The method generally used for the correlation matrix estimate is the modified covariance method [85].

v. Data Extrapolation-based Methods

Another way of increasing the resolution beyond the Fourier limit is to expand the support of the data in the frequency domain, by estimating samples outside the annular data region by linear prediction filters [86][87]. There has also been some recent limited attempt to compare the performance of spectral estimation-based methods with data extrapolation-based methods. For example in [22] it has been reported that spectral estimation based techniques have a degraded performance with real world targets, as opposed to point targets, and may cause some loss of information about the target. In comparison, data extrapolation techniques offer increased resolution and better overall performance in these cases. On the other hand, according to [82], data extrapolation-based methods do not yield particularly good results, since they introduce significant amounts of noise.

vi. Estimation-Theoretic and Entropy-based Methods

There also exists some limited previous work taking an estimation-theoretic approach to the problem of image formation. These methods are closest in spirit to this perspective. In [88], a regularized inversion method has been proposed for stripmap-mode SAR, which involves de-convolution of the projections of the field by Tikhonov-type regularization, followed by backprojection. In [89], an estimation-theoretic ℓ_1-norm-based approach has been proposed for imaging closely-spaced multiple moving scatterers over a given spatial region. In [90] and [28], a stochastic inverse approach which seeks the best linear estimate of the reflectivity field in a stochastic least-squares sense has been proposed. This method starts from blurred image domain observations rather than projectional SAR data. A method similar in spirit to that in [91] and [92], which considers incorporating prior knowledge about the property of targets being limited in spatial extent has been introduced in [93]. Finally, a class of approaches for SAR imaging based on entropy methods has been developed in [94][95][96] and [97]. These methods appear to offer good noise suppression properties, however the experimental results in published work are too limited to show other possible

advantages over conventional methods. Rather than realistic SAR scenes, most results involve simple examples, such as two isolated point scatterers[94], a synthetic scene with reflectivity $1-j$ in the target region and zero in the background (hence not random phase [96] [97]), and a small scene consisting of straight lines and isolated point scatterers [95]. The method in [96] and [97] also requires post-processing (median filtering) to reduce some of the artefacts. The recent entropy-based work in [95] considers the problem of imaging distributed targets, however the method uses smoothness constraints which are built on the real and imaginary components of the field, rather than on the magnitudes directly.

12. The Radar Equation

The radar equation for a monostatic radar system can be written as [4]:

$$P_r = \frac{P_t G^2 \lambda^2 \sigma}{(4\pi)^3 R^4} \quad \textbf{(Eq. II-69)}$$

where P_r is the power received at the antenna, P_t is the power radiated by the antenna, G is antenna gain, R is distance from radar to the target, λ is operating wavelength, and σ is radar target cross section. Signals received by radar are usually contaminated by noise due to random modulations of the radar pulse during atmospheric propagation, or due to fluctuations in the receiving circuits. The effective noise power that the signal must compete with at the antenna is given by [4]:

$$N_r = kTF_N B_N \quad \textbf{(Eq. II-70)}$$

where N_r is the received noise power, k is Boltzmann's constant (1.38 x 10-23 J/K), T is nominal scene noise temperature, F_N is system noise factor for the receiver, and B_N is noise bandwidth at the antenna port. Consequently, the Signal-to-Noise ratio at the Receiver antenna port is effectively:

$$SNR = \frac{P_r}{N_r} = \frac{P_t G^2 \lambda^2 \sigma}{(4\pi)^3 R^4 kTF_N B_N} \quad \textbf{(Eq. II-71)}$$

The SNR after SAR processing, for a point target of cross section σ at range R is [4]:

$$SNR = \frac{P_t G^2 \lambda^2 \sigma\, n}{(4\pi)^3 R^4 k T F_N B_N} \quad \textbf{(Eq. II-72)}$$

where the number of elements, *n*, consists of the synthetic aperture and is expressed as [4]:

$$n = T_s f_r \quad \textbf{(Eq. II-73)}$$

where T_s is the time over which the aperture is formed and f_r is the pulse repetition frequency. T_s is related to synthetic aperture length, L via:

$$T_s = \frac{L}{v} = \frac{\lambda R}{2 v \rho_a \sin(\theta_0)} \quad \textbf{(Eq. II-74)}$$

where ρ_a represent azimuth resolution, θ_0 is the look angle of the antenna beam and v is the velocity of platform. The total number of pulse integrated over coherent integration time is:

$$n = \frac{\lambda R f_r}{2 v \rho_a \sin(\theta_0)} \quad \textbf{(Eq. II-75)}$$

Thus the final form of the SAR radar equation for a point target is:

$$SNR = \frac{P_t G^2 \lambda^3 \sigma\, f_r}{(4\pi)^3 R^3 k T F_N B_N 2 v \rho_a \sin(\theta_0)} \quad \textbf{(Eq. II-76)}$$

For a point target in a SAR image, the SNR improves with finer azimuth resolution.

13. Distributed Targets in SAR

In spite of the different purposes of radar systems, there exist two types of target received from radar echoes, the point target and the distributed target [98]. The former is where the point target echo occupies a space much smaller than the radar resolution cell. The latter is where a number of scatters combine over a space that is greater than the radar resolution cell. For most of the calculations done in the latter parts, the use of point targets was assumed. A point target is a relatively small element on the surface of the earth or imaging surface that reflects a transmitted pulse by a factor determined by its RCS. The range and azimuth resolutions make up a resolution cell. If two targets are positioned in the same resolution cell of a radar, as explained earlier, it is hard to individually identify them. Such targets are often referred to as unresolved targets. Another scenario for a distributed target

would be if a target is so large that it occupies multiple resolution cells of the radar then it is referred to as an extended target [98]. Examples of these can be seen in Figure II-29.

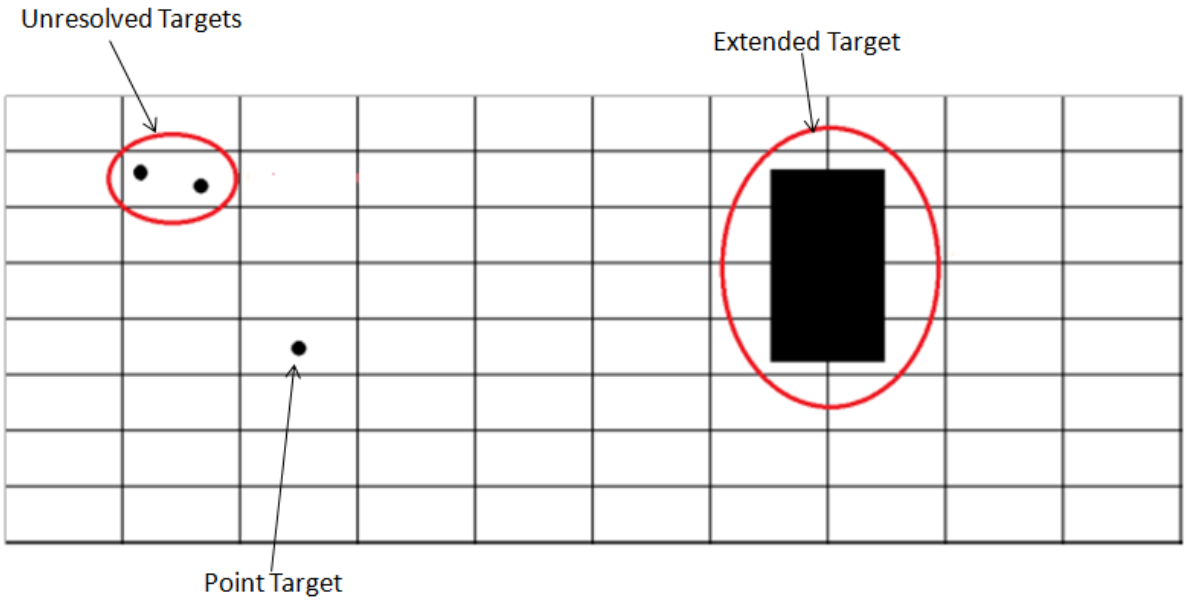

Figure II-29: Scene showing the two types of distributed targets (circled in red) where each box in the grid is a one resolution cell.

Only some targets in radar remote sensing are of the nature of discrete scatterers as treated in the preceding sections. More commonly, scattering takes place from regions on the earth's surface that are distributed in nature, such as an area of soil or snow, an agricultural field or even the surface of the ocean. Usually one type of radar target echo is regarded as the desired target in a radar system while the other is considered as clutter [49]. For example, a given point target echo such as an airplane is considered to be the desired target in an air traffic control (ATC) radar or a military radar, but it is regarded as clutter or interference for a weather radar. On the contrary, for the meteorological application of the weather radar, the distributed target echo such as cloud, precipitation, thunderstorm etc. is observed as the desired target, but the point target echo should be rejected to avoid an observation barrier. The use of the word clutter, which is sometimes used to describe the power from a distributed target, is an indication that small target detection is hampered by this component of the returned signal as well as by the system noise [30].

To have a better understanding of distributed targets, consider a region composed of an infinite collection of infinitesimal elements of effective area dA, many of which make up an individual pixel [30]. Furthermore, suppose the radar cross section of each of those infinitesimal areas is σ. The value of σ depends on a multitude of parameters of the target.

Only for the very simplest shapes – such as used in calibration measurements – can the value of σ be calculated analytically. However, in remote sensing applications, the targets usually extend in physical size beyond what one would regards as a point and each element dA of the distributed target can be assigned a local value of σ [21]. This inferred target area σ, relative to the geometrical area dA, is the specific backscatter coefficient at the particular point on the distributed target that, on average, has a radar cross section (RCS) per unit area of:

$$\sigma^0 = \sigma/\mathrm{dA} \qquad \text{where} \qquad \mathrm{dA} = \rho_a \rho_r \qquad \textbf{(Eq. II-77)}$$

σ^0 is referred to as the backscattering coefficient of the region, ρ_r is slant range resolution, and ρ_a is azimuth resolution. From its definition its units are m^2m^{-2}. Colloquially, it is often called sigma nought. The radar backscattering coefficient, σ^0, is sometimes termed normalized radar cross section. This coefficient is dependent on the sensor wavelength and polarization as well as scene geometry and terrain parameters. A good compilation of σ^0 of many scenes is given by Ulaby and Dobson [10]. Within each pixel area of dA there are numerous scatterers. Each scatterer will have a backscatter amplitude, phase and polarization. The complex returns from all scatterers in a resolution cell are coherently added. This results in a speckle effect that is quantified by the ratio of standard deviation of the fluctuations of the mean value σ_M, where M signifies the mean value of all pixels. Hence, the quantity of interest in the radar system is then not the deterministic power of a single echo pulse received in a response to a target with some deterministic cross section σ, but rather the ensemble average power for a single pulse with terrain in view having average specific cross section σ^0, In those terms, the radar equation for distributed target is:

$$\frac{S}{N} = \frac{P_t G^2 \lambda^3 \sigma^0 \rho_r f_r}{(4\pi)^3 R^3 k T F_N B_N 2v \sin(\theta_0)} \qquad \textbf{(Eq. II-78)}$$

σ^0 generally depends on several variables such as the nature of the target, i.e., in terms of material, its orientation and its shape [34]. Due to these variables, it is difficult to define a strict and standard model for the target as there could be different types of objects in a particular scene and their nature, orientations and sizes could differ. Given that the time spacing between samples is equal to the subpulse duration [98], consider that at sample-time index i, the sample of the time sequence received from the distributed target echoes can be represented as $x_i(m, n)$, where $m = 1, \ldots, n_{bins}$, and $n = 1, \ldots, n_p$, where n_{bins} is the number of range bins, and n_p is the number of subpulses. According to the echoes of the distributed target, at the output of each sample instant exists all the subpulse echoes so that at any

sample-time index i and at the first range-sampling instant, the first subpulse echo encounters the first range bin $x_i(1,1)$ contributing to the first sampled echo $y(i,1)$. Then, at the next range-sampling instant, the first subpulse echo now encounters the second range bin $x_i(2,1)$ and the second subpulse echo encounters the first range bin $x_i(1,2)$. Both range bins are combined to yield echo sample $y(i,2)$, and so forth. Thus, the output range cell can be mathematically described as [98]:

$$y(i,j) = \sum_{\forall m+n-1=j} x_i(m,n) \qquad \textbf{(Eq. II-79)}$$

14. Ground Penetrating Radar

Ground-penetrating radar (GPR) is a non-destructive electromagnetic technique used to locate metallic and non-metallic objects buried in the ground and layers within the ground. The ground is an electromagnetically opaque medium whose permittivity and conductivity can strongly affect the signals detected by the GPR. The amplitude, phase and time delay of the detected signals are interpreted to determine where the buried objects are located and perhaps identify the type of target that has been located [99]. A typical GPR investigation has antennas located at-or-near the surface of the ground. During the measurement sequence data is recorded at several different positions of the antennas, this motion of the actual antenna is used to 'synthesize' a very long antenna [14], see Figure II-30. This is similar, in concept, to what is done in SAR as explained in section 3, see Figure II-5. However, in GPR the aperture is synthesized from discrete points with no Doppler, rather than samples from a moving airborne/spaceborne radar [14].

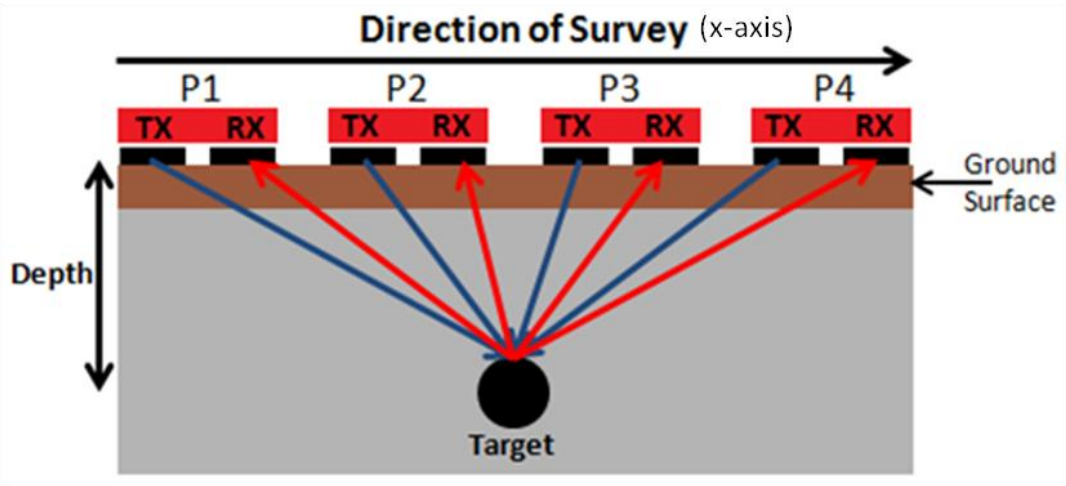

Figure II-30: Basic GPR measurement sequence.

The GPR data is often displayed as a collection of time-series returns, called A-scans as shown in Figure II-31 (a). These A-scans utilizes time and the propagation velocity of the electromagnetic (EM) waves in the medium to calculate the depth of the target. The reflection from air-to-ground surface, caused by the back-scattering of the EM waves due the difference in the reflectivity between air and ground, can be easily seen in the figure along the synthetic aperture direction. After that, the A-scans are then stacked side-by-side giving a depth profile of the subsurface resulting in the B-scan (’waterfall’ or ’wiggle’ plots) [14], as presented in the corresponding B-scan in Figure II-31 (b). The reflections on a point scatterer located below the surface exhibit defocused-hyperbolic characteristics in a B-scan that is mainly due to the data collection scheme and the finite beam width of the main lobe of the GPR antenna [100]. The exact shape of the reflections depends on the relative dielectric constant of the half-space, the height of the source, and the propagation time from source to wavefront multiplied by the wave velocity in the half-space [101]. This hyperbolic defocusing can be corrected using various migration or focusing algorithms [100] [101].

When the amplitude of the received signal is represented by a colour scale, or grey-scale, a 2D image that represents a vertical slice in the ground is formed, see Figure II-31 (c). The time axis or the related depth axis is usually pointed downwards. However, in real-life measurements, these plots or radargrams are much more complex and difficult to comprehend and require expert interpretation, particularly in typical situations where there are clutter objects such as voids, stones or debris in the ground accompanying the targets of interest. Much of the skill of the successful operator comes from combining observations drawn from the radar images with knowledge of the structure of the host materials and the characteristics of the targets [5]. Separating out clutter, and accounting for various environmental, system and subsurface effects require operator skill, experience and, significantly, time [99]. The analysis and interpretation of the large volumes of data generated by practical GPR surveys are extremely challenging and often presents an implementation bottleneck influencing the cost effectiveness and applicability of the technique [99].

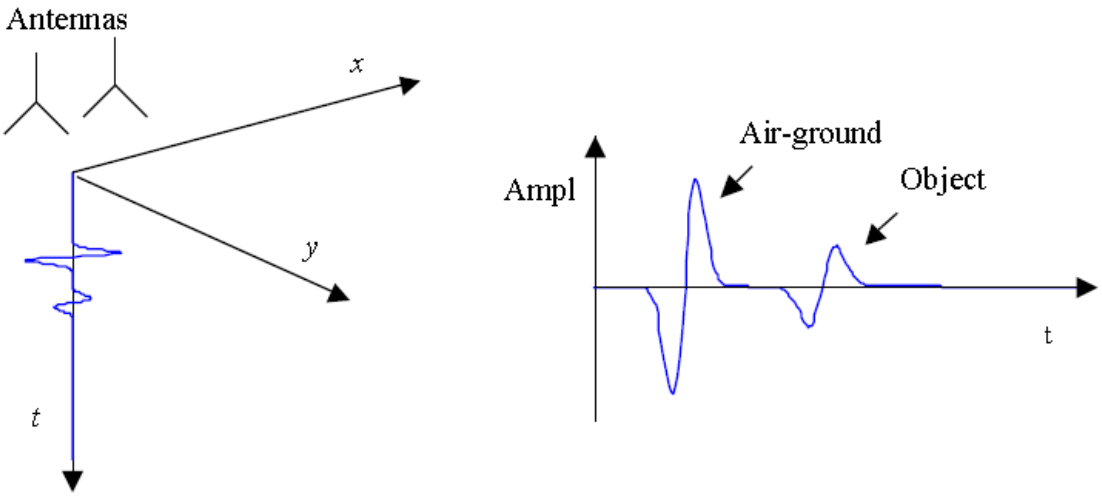

(a) Configuration and representation of an A-Scan.

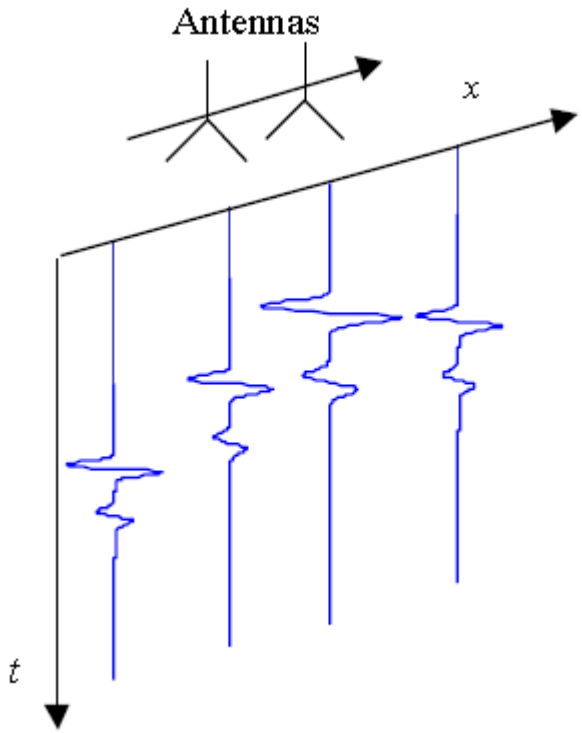

(b) Multiple A-Scans forming a B-Scan.

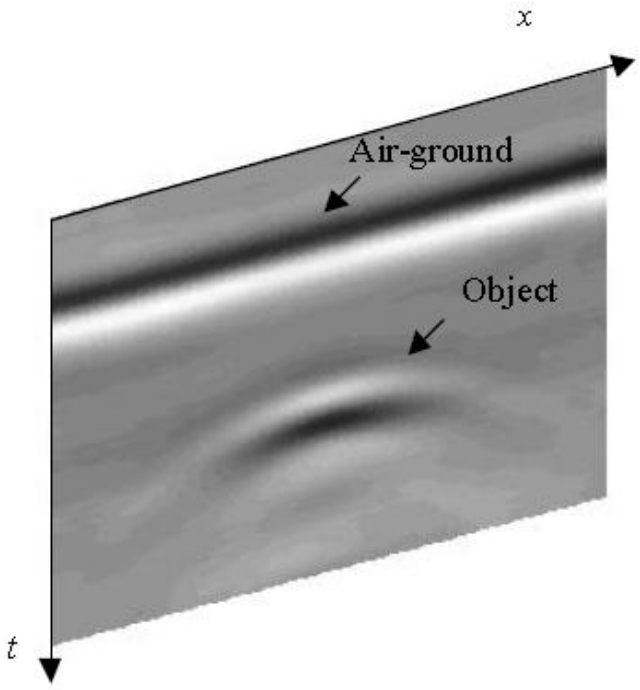

(c) Representation of the B-Scan on greyscale

Figure II-31: Representations of A-Scan and B-Scan of GPR measurement

Fourier and inverse Fourier transforms are often used in the analysis of the data [99] [102][103] and this introduces significant sidelobes in the response that may cause interference with other near echo signals creating ambiguities in the estimation of target range and be misinterpreted as false targets [104]. A variety of techniques have been used to focus GPR data, and these produce images of the sub-surface that require less operator interpretation. These techniques include backprojection, back-propagation, migration summations in time, phase or frequency and in frequency-wave number (f-k) domains [102][103]. The focussing process is largely the same as image formation in SAR. Focussing can be based on pulsed time domain data or on frequency domain data [103]. In this thesis, the technique that is considered is based on frequency domain data that is derived in Step Frequency Continuous Wave (SFCW) scheme [105][106][107]. Accordingly, the focussing scheme relies on IFFT evaluations, where the resulting side lobes can be misinterpreted as targets and broadening of main lobe responses by applying windowing reduces the schemes ability to resolve closely spaced targets. The targets don't need to be physically close to each other for their time responses to appear at very similar, or even equal, times. The focussing techniques generally require knowledge of the permittivity of the ground, either relying on measurements of permittivity or assumed values [14].

i. Image Formation from GPR Data

A basic scenario is shown in Figure II-32 where there are two buried targets and two separate paths between the transmitter, the two targets and the receiver. These two targets are some distance apart, but the path lengths that GPR measures from the transmitter to the targets and then to the receiver are quite similar. It is desirable for the signal processing to recognise these as two closely spaced responses, rather than have them merge into one due to the main lobe response broadening out in time. In Fourier analysis of time or frequency limited data, the relative level of the side lobes can be controlled by the use of window functions. These are designed specifically to ensure that the transition at the periodic extensions is not abrupt by trying to make the derivative of the boundary points equal to zero or near zero [53]. The windowing methods have a general characteristic of broadening the main lobe while reducing the side lobe level. As such side lobes are less likely to be interpreted as false targets, but the increased main lobe width reduces the ability to resolve closely spaced targets. The targets need not be physically close to each other for their time responses to appear at very similar, or even equal, times [14].

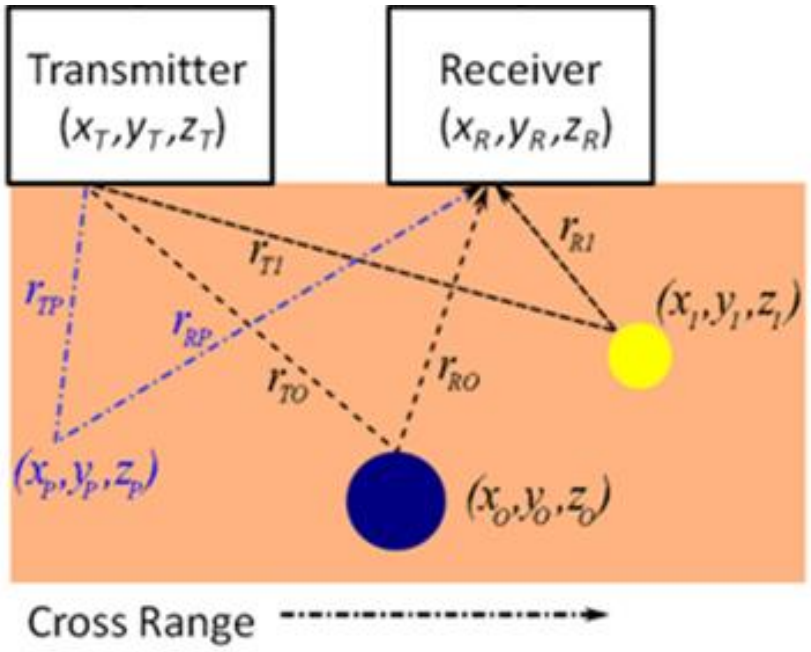

Figure II-32: Outline of SFCW GPR over two buried targets at coordinates (x_0, y_0, z_0) and (x_1, y_1, $z1$) and a reconstruction point (x_P, y_P, z_P).

The signal transmission between the transmitter and the receiver can be written as a function of time delay on the propagation path, τ, as:

$$\begin{aligned} T(\omega,\tau) &= G_T(\omega)G_R(\omega)\Gamma_O(\omega)e^{-j\frac{\omega}{c_m}(r_{TO}+r_{RO})} \\ &= G_T(\omega)G_R(\omega)\Gamma_O(\omega)e^{-j\omega\tau} \end{aligned} \quad \textbf{(Eq. II-80)}$$

where the gains of the transmitter and receiver antennas are $G_T(\omega)$ and $G_R(\omega)$ respectively, $\Gamma_O(\omega)$ is the reflection at the target, $c_m = c/n$ is the propagation velocity in the medium where n is the refractive index of the medium and ω is the circular frequency.

From a measure of the transmission in a GPR, and a knowledge of antenna gains, positions, refractive index and frequency, the reflection coefficient of the target is easily recovered [108]:

$$\Gamma_O(\omega) = \frac{T(\omega,t_P)}{G_T(\omega)G_R(\omega)}e^{j\omega\tau} \quad \textbf{(Eq. II-81)}$$

To form an image from GPR measurements, this equation has to be evaluated at all possible reconstruction points $(x_P,\ y_P,\ z_P)$ in the area being imaged. In the simple case where the ground is assumed to be uniform the propagation delay from the transmitter to the receiver via point P is $t_p = (n/c)\ (r_{TP} + r_{RP})$ and the reconstructed response at point P, due to a single measure, can be written in the time domain as:

$$s(t_P) = IFFT\left(\frac{T(\omega,t_P)}{G_T(\omega)G_R(\omega)}e^{j\omega t_p}\right) \quad \textbf{(Eq. II-82)}$$

This de-convolves the responses of the transmitter and receiver antennas and removed the propagation delay or phase introduced by the path between the transmitter, the point of reconstruction and the receiver. To obtain a time migration the values of $s(t_p)$ are usually combined or 'stacked-up' as an arithmetic mean to form a two dimensional image. The quality of the formed image is greatest when the reconstruction point coincides with the reflecting object.

15. Chapter Summary

In this chapter, a comprehensive discussion of Synthetic Aperture Radar fundamentals is introduced with a study of a basic SAR model and characteristics. After that, SAR modulation schemes are investigated with mathematical analysis showing that all of the techniques rely on FFT/IFFT and suffer from the same drawbacks of sidelobes and degraded

resolution due to main-lobe width broadening caused by standard Windowing-based sidelobe suppression techniques. Then SAR transmitted and received signals, using the FMCW modulation scheme is analysed followed by an overview of range compression and azimuth compression. A brief overview of standard and widely used image formation techniques for SAR is presented after that. Afterwards, distributed targets are introduced and analysed showing that most of real-life SAR measurements are of this type of targets rather than the discrete point scatterer type. Finally, Ground Penetrating Radar technique is presented with a brief overview on the basics of GPR image formation process.

Chapter III: Overview of Sidelobe Suppression Techniques & Introduction to Superimposition

1. Introduction

As can be seen from the previous chapter, the FFT and IFFT are at the core of the SAR and GPR image formation process [4] with many other microwave measurement applications. However, the band-limited property in the frequency domain affects the size of the sidelobes in the time domain [53]. Hence, in some cases the accumulated sidelobes can be mistaken for a false target and/or have a blurring effect on generated images [56]. A conventional solution to suppress sidelobes is by using windowing functions [55]. The relative level of the side lobes can be controlled by the use of window functions. These are designed specifically to ensure that the transition at the periodic extensions are not abrupt by trying to make the derivative of the boundary points equal to zero or near zero [109].

Window functions are generally categorized into: fixed windows and adjustable windows [109]. Many of the fixed windows are constructed as weighted sums, products or convolutions of simple functions or other window functions. For example, the Bartlett window is a time domain convolution of two rectangular windows, whereas both the Hann and Hamming windows are shifted sums of the frequency domain representation of the rectangular window [53]. In contrast, adjustable window functions are often derived based on optimality criteria. Dolph's criteria and Kaiser's criteria are two of the most popular optimality criteria used in adjustable window design [53]. The window functions resulting from Dolph's criteria are described by the Chebyshev polynomials. Dolph windows have the constant side lobe levels for all side lobes and, hence, have no side lobe roll off [110]. The Kaiser family of window functions are generated by solving Kaiser's optimization problem that is approximated by the modified Bessel function of order zero [111].

Nevertheless, windowing techniques cause a widening effect on the main-lobe of the target, which causes lower resolution [112]. As such sidelobes are less likely to be interpreted as false targets, but the increased main lobe width reduces the ability to resolve closely spaced targets. The targets need not be physically close to each other for their time responses to appear at very similar, or even equal, times. Hence, finding a balance between suppressing

sidelobes and maintaining a high resolution is an issue [113]. This is where the superimposition technique is advantageous [114]. However, interestingly, [115] showed that for SAR with a fixed bandwidth, the minimum mean-squared-error image rendering of a target scene is achieved with no windowing at all. The authors showed that windowing is unlikely to produce satisfactory peak to sidelobe ratios in this case. This begs the question "What are the alternatives to push down sidelobes?". This is what superimposition, presented in sections 4 and 5 of this chapter is answering.

First, similar to the example presented in section 8 of Chapter 2, two targets are simulated in a basic radar system of a saw-tooth chirp that is sweeping from 0.3 GHz to 0.5 GHz in 5 msec. Targets' responses are presented in Figure III-1, where one of them has a weaker response but they are of some distance apart, however, in the trace generated using standard-FFT the only indication of the weak response is a small fluctuation at 5.2kHz while the standard-FFT with Hamming window function has a much better detection of both targets but at the expense of resolution. More to the point, a second simulation of the two targets, see Figure III-2, where they are now very close to each other shows that standard-FFT doesn't give any indication of the presence of the second weak target while standard-FFT with Hamming window shows only one target while the other seems to have merged with the first one due to its very wide main-lobe. Hence there is a need for a new technique that can reduce sidelobes and enhance resolution while maintaining main-lobes' position and amplitude. A variety of techniques have been used to FFT/IFFT based applications such as SAR, GPR, medical imaging and VNA measurements for suppressing sidelobes and/or enhancing resolution. In this section, some of these widely used techniques are introduced and discussed. Then, superimposition methodology is presented with proposed two new improved techniques.

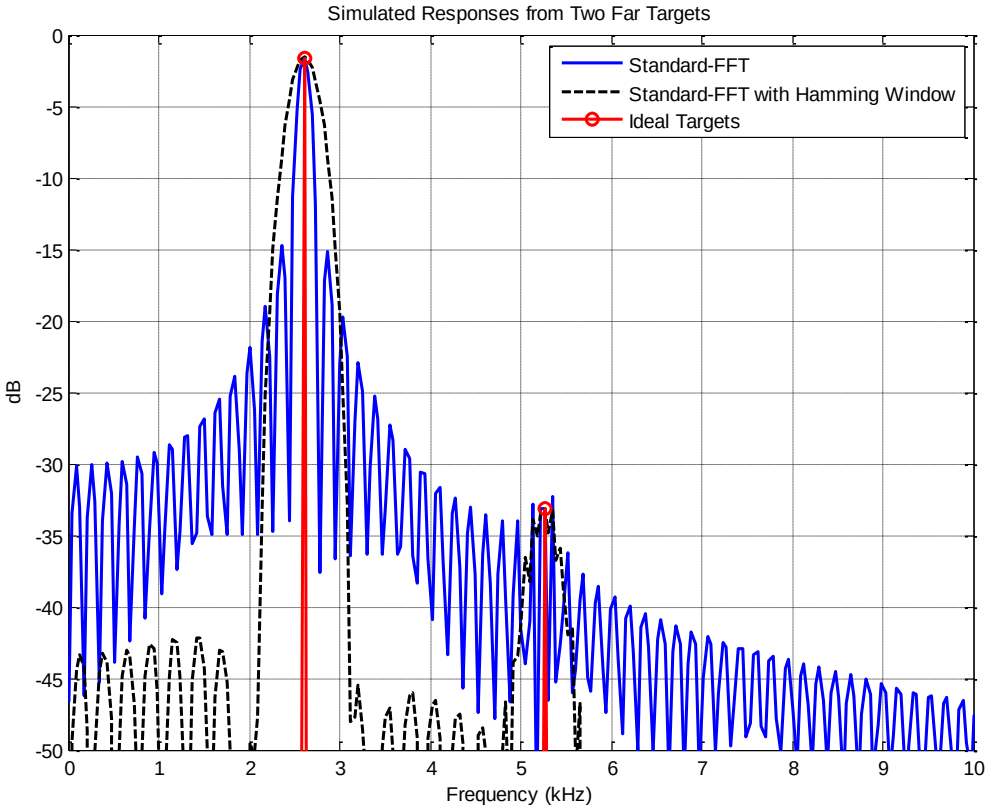

Figure III-1: Simulating Target responses that have different magnitudes but with some distance apart using standard-FFT and standard-FFT with Hamming Window.

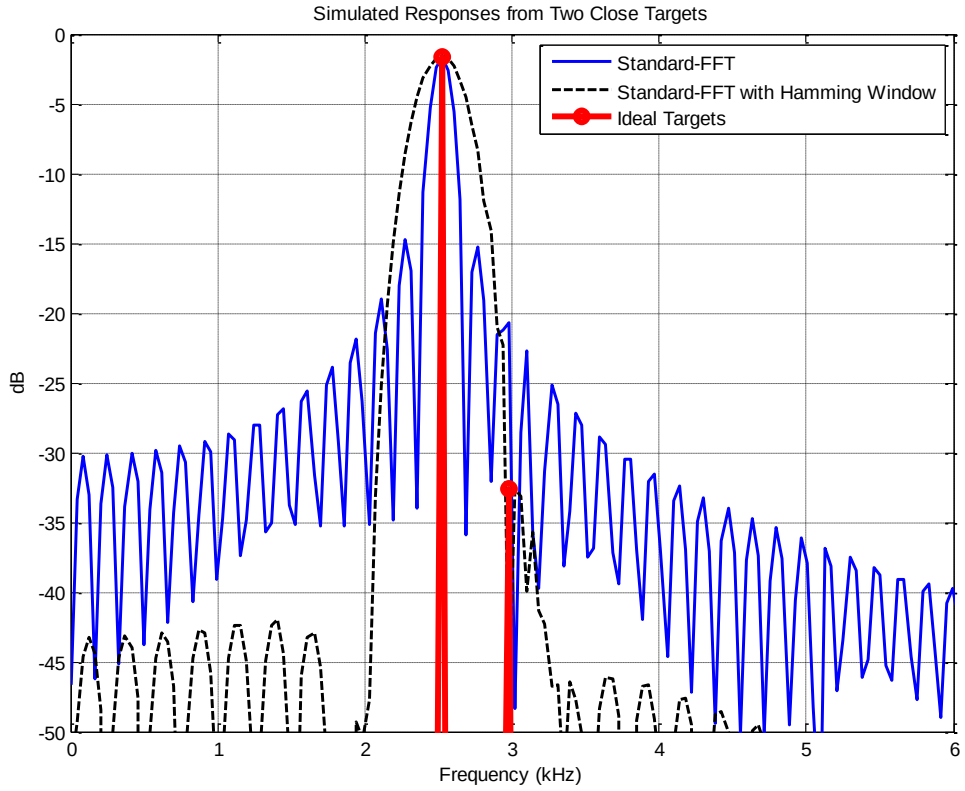

Figure III-2: Simulating Target responses that have different magnitudes and positioned very close to each other using standard-FFT and standard-FFT with Hamming Window

2. MUSIC Algorithm

MUSIC is an abbreviation for "MUltiple SIgnal Classification" [116]. MUSIC is essentially a method of characterizing the range of a self-adjoint operator, which is an operator that is its own adjoint, or, equivalently, one whose matrix is equal to its own conjugate transpose (Hermitian matrix). MUSIC algorithm has been widely applied to the problem of estimating the locations of a number of point-like targets in SAR [117][118][30]. To understand MUSIC algorithm, let's suppose *A* is a self-adjoint operator with eigenvalues of $\lambda_1 \geq \lambda_2 \geq ...$, and corresponding eigenvectors: v_1, v_2, ... Suppose the eigenvalues λ_{M+1} , λ_{M+2} , ... are all zero, so that the vectors v_{M+1}, v_{M+2}, ... span the null space of *A*. Alternatively, λ_{M+1} , λ_{M+2} , ... could merely be very small, below the noise level of the system represented by *A*. In this case, we say that the vectors v_{M+1}, v_{M+2}, ... span the noise subspace of *A*. Now, we can form the projection onto the noise subspace to be explicitly expressed by:

$$P_{noise} = \sum_{j>M} v_j {v_j}^{*T}$$

(Eq. III-1)

where the superscript *T* denotes transpose, the star denotes complex conjugate and ${v_j}^{*T}$ is the linear functional that maps a vector f to the inner product $\langle v_f, f \rangle$. The essential range of *A*, meanwhile, is spanned by the vectors: v_1, v_2, ..., v_M. The key idea of MUSIC is that because *A* is self-adjoint, we know that the noise subspace is orthogonal to the essential range. Therefore, a vector *f* is in the range if and only if its projection onto the noise subspace is zero [116], i.e., if $|| P_{noise} f || = 0$. And this, in turn, happens only if $\frac{1}{|| P_{noise} f ||} = \infty$

The previous equation can be expressed as the MUSIC characterization of the range of *A*. Nevertheless, it can be noted that for an operator that is NOT self-adjoint, MUSIC can be used with the singular value decomposition instead of the eigenvalue decomposition [116]. To put it briefly, MUSIC is a method for estimating the individual frequencies of multiple time-harmonic signals. Nevertheless, the application of this method in SAR imaging processing requires some adaptation and, for this reason, three main drawbacks appear: The first drawback is intrinsic to the nature of SAR: the MUSIC algorithm exploits the signal statistics (i.e. the data covariance matrix) in order to build up the noise subspace and to exploit its characteristics to retrieve the target location. To generate the statistics of interest, multiple acquisitions are required; therefore a single SAR survey is not an ideal working

condition for it. However, there are methods in the literature which transform the single acquisition into a multiple one [116]. The second drawback is that the complex reflectivity information cannot be easily recovered. The MUSIC response is not proportionally related to the target backscattering power. If a target is detected, the algorithm response consists of a high isolated power peak corresponding to its position, but this power is a measure of confidence rather than of target backscattering [116]. The third drawback is that it must be seeded with the number of targets to find. The MUSIC will indicate that number of targets regardless of the number of targets actually present. In the presence of relatively low levels of noise the MUSIC algorithm is prone to reporting the position of false targets in preference to weaker genuine target responses [119].

The same example of SAR used in previous section is considered again for the MUSIC algorithm, which is seeded with two targets. For the first case where the two targets are far from each others, the MUSIC algorithm produced the outcome in Figure III-3, it can be noticed that even though the algorithm found the targets' positions, it failed to preserve its original magnitude. Furthermore, in order to illustrate the third drawback of MUSIC algorithm mentioned earlier in this section, the SAR example presented in Figure III-3 is simulated again with MUSIC algorithm seeded for three targets for the case of two genuine targets. Results presented in Figure III-4 show two genuine targets at 2.6 kHz and 5.2 kHz with a third false-target at 4.13 kHz. Then, a second scenario where the two targets are located very close to each other is simulated using the MUSIC algorithm with outcome presented in Figure III-5. Here it can be seen that this time, even though the algorithm is correctly seeded with two targets, only one target is present due to the proximity of the two targets.

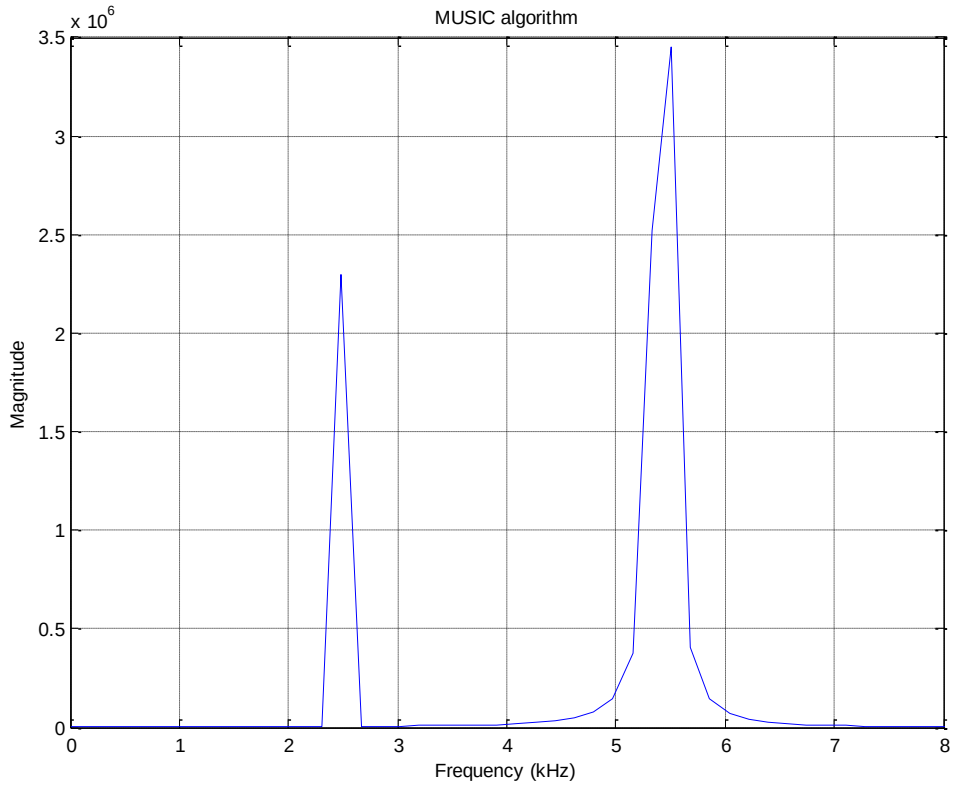

Figure III-3: Simulating Target responses that have different magnitudes but with some distance apart using MUSIC algorithm.

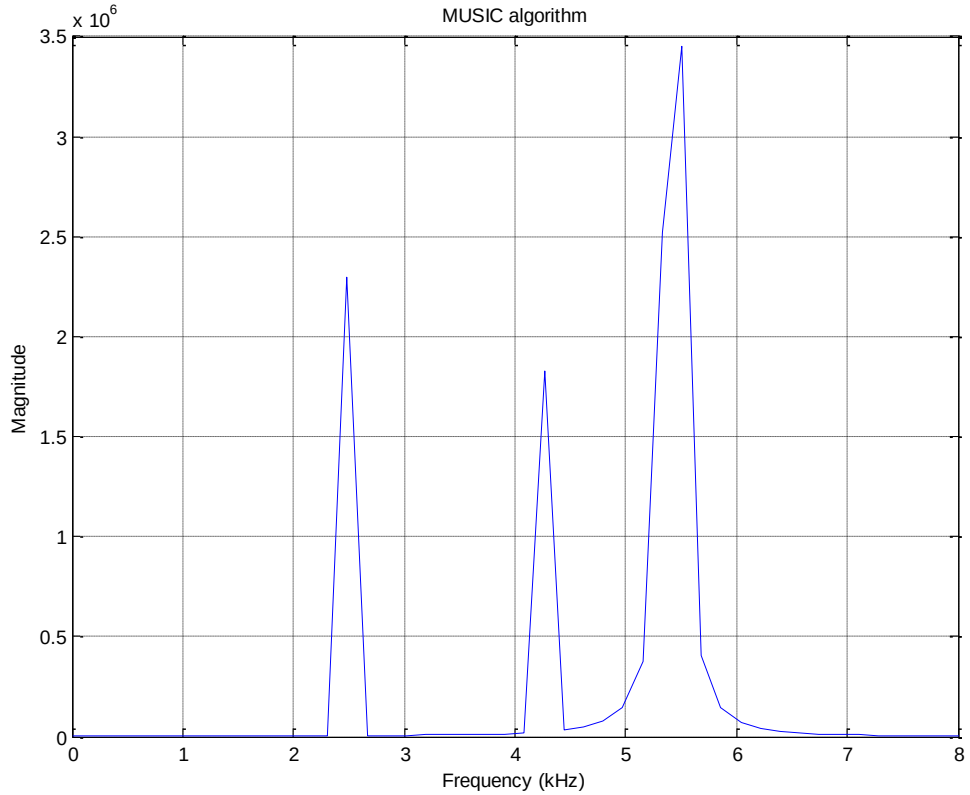

Figure III-4: Simulating Two Target responses that have different magnitudes using MUSIC algorithm that is seeded for three targets.

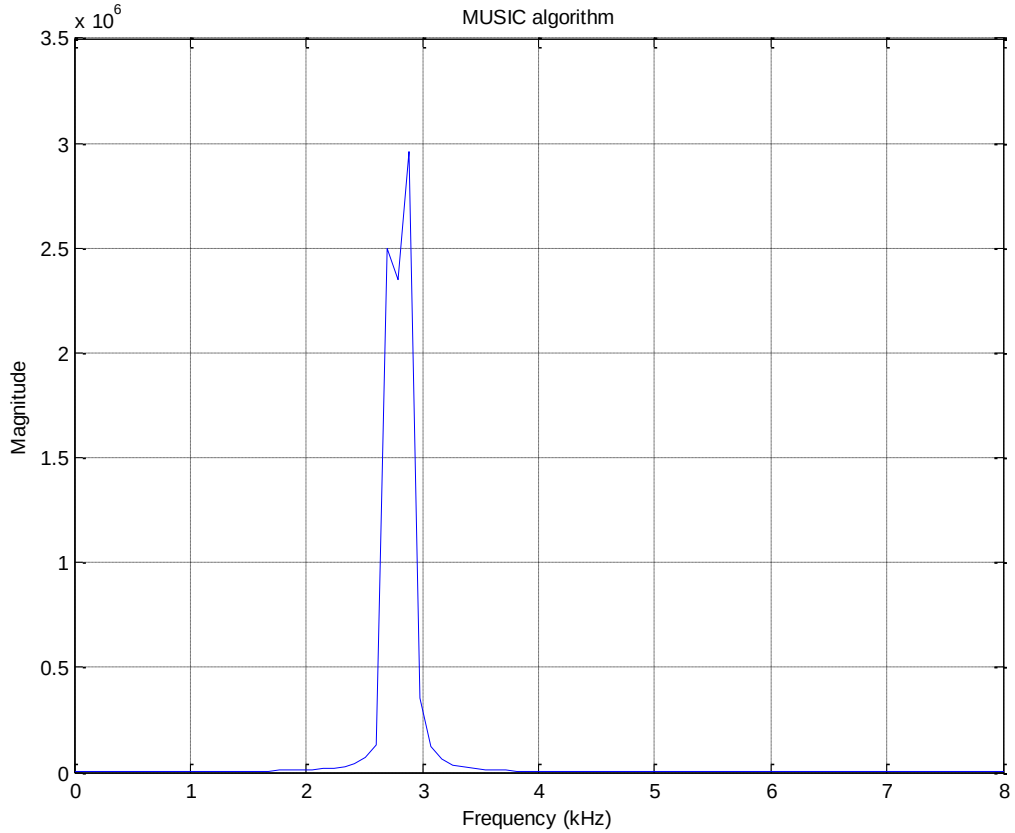

Figure III-5: Simulating Target responses that have different magnitudes and positioned very close to each other using MUSIC algorithm

3. Spatially Variant Apodization (SVA)

Apodization has traditionally used windowing functions that were applied across the data received by the radar. This technique was later developed into what is now known as Spatially Variant Apodization (SVA). SVA was first introduced in 1994 in a patent by R. J. Dallaire and H. C. Stankwiz [120]. The concept of spatially optimized windowing functions formulated around the spatially static cosine windowing function was established. In SVA, each position within the spatial domain corresponds to its own scaled cosine window. This cosine window is optimized over each spatial position to ideally reduce sidelobes while preserving the main-lobe. Hence, the window itself is adaptively defined at each image point. This technique was enhanced over the years by a number of research groups. However, they found that even though SVA can reduce sidelobes, it is not effective in increasing the resolution of SAR images. Furthermore, [121] reported that simulation and measurement results of this technique "suggest that it is best suited for situations involving isolated point targets, or for coherent imaging of extended targets" and not for generic SAR images.

More recently, another paper by P. Zhang, J. Shang and R. Yang in 2009 [122] proposed a procedure for utilizing Super-SVA to reduce sidelobes and enhance interferometric SAR resolution. SVA is overviewed in this section and it is simulated and compared to the improved techniques of Superimposition. SVA can be utilized using One-Dimension (1D) or Two-Dimension (2D) techniques. In 1D SVA, the sidelobes can be reduced through the application of SVA over the frequency domain. On the other hand, the 2D SVA utilizes the SVA method for each spatial coordinate. In other words, 2D SVA applies two independent spatially variant windowing: one over the data in the frequency domain, which is the same as 1D SVA, and one over the antenna elements by an array theory analogy. In this research work, the adopted technique is the 1D SVA since many of the simulations and measurements are performed in a one-dimensional setup that is designed to examine the superimposition technique and compare it to the other techniques – including SVA and Super-SVA – where the outcomes can be quantified.

i. One-Dimensional Spatially Variant Apodization (1D SVA)

A six stage procedure for applying 1D SVA is presented in Figure III-6. At the beginning, the frequency bandwidth is selected/specified for the simulation or measurement experiment. Once transmitted and then received, this signal is called the complex wave-number domain and it is represented by $S(l)$. This signal is then transformed using IFFT to obtain the complex down-range spatial values corresponding to this scattering range. The complex down-range profile is represented by $g(x)$, where x is the spatial displacement (m), and is obtained as follow:

$$g(x) = \frac{1}{L_{bw}} \int_{k_1}^{k_N} S(l) e^{jl2x} dk \qquad \textbf{(Eq. III-2)}$$

where $l_1 \leq l \leq l_N$, l_i is the i^{th} wave-number (rad/m) of N wave-numbers and L_{bw} is the initial wave-number bandwidth.

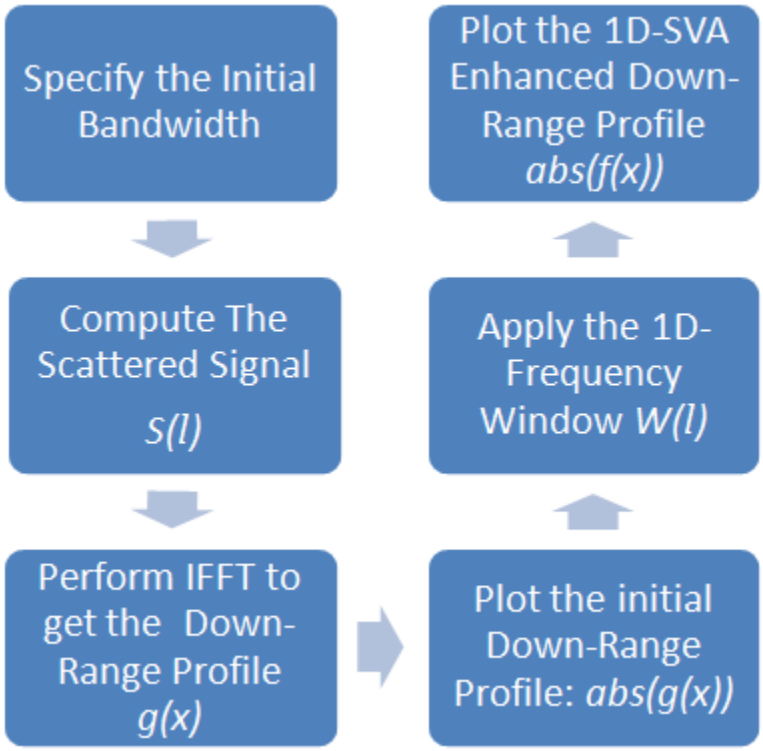

Figure III-6: Block diagram of the 1D SVA Technique

From the down-range spatial values, the down-range profile is (abs*(g(x)*). This profile is then enhanced through the reduction of sidelobes by applying 1D SVA. The complex SVA enhanced down-range profile is represented by *f(x)* and is obtained by:

$$f(x) = \frac{1}{L_{bw}} \int_{k_1}^{k_N} W(l) S(l) e^{jl2x} dk \qquad \textbf{(Eq. III-3)}$$

This function is the down-range profile for a typical radar system. $W(l)$ is a windowing function and is obtained by:

$$W(l) = 1 + 2\alpha(x)\cos\left(\frac{2\pi[l - l_c]}{L_{bw}}\right) \qquad \textbf{(Eq. III-4)}$$

The term *α(x)* is a spatially dependent value with the range [0,0.5] and l_c is the centre wave-number:

$$l_c = \frac{1}{2}(l_N + l) \qquad \textbf{(Eq. III-5)}$$

Ideally, the main-lobe width would be preserved and sidelobes reduced, but this can be achieved only if α is permitted to vary spatially over the entire down-range profile. To apply this, *α(x)* must be computed for each spatial location. Hence, the selection of *α* is presented in the next subsection.

ii. Computation of Alpha (α):

Figure III-7 illustrates the SVA windowing function $W(l)$ for various values of α. The first plot (upper left) presents the rectangular window, which is equivalent to a value of α = 0. The application of a rectangular window corresponds to the preservation of the original signal value *S(l)*. The second plot (upper right) shows the outcome of: $2\alpha(x)cos\left(\frac{2\pi[l-l_c]}{L_{bw}}\right)$, which is performed at each spatial position. This window has the form of a single cycle cosine function with amplitude that ranges from 0 to 1 for the restricted values of α between [0, 0.5]. The last plot (bottom) corresponds to the SVA windowing function $W(l)$. The SVA window is normalized such that $\int_{k_1}^{k_N} W(l)dk$ is 1 for all values of α. This is understood intuitively because the integration of a single cycled cosine function must be zero.

In order to have a better understanding of the behaviour and effect of α, windowed signals and down range profiles that correspond to a single point scatterer are simulated and presented in Figure III-8. The signal corresponding to a point scatterer is constant in magnitude. This is why the magnitude of the windowed signal appears to match the windowing function for α = 0, at which the windowing function is equivalent to a rectangular window that preserves the original signal. As the value of α increases, the main lobe width increases and the sidelobes' magnitudes decrease. Hence, by utilizing the information provided up to this point, a solution for the SVA enhanced down-range profile can be derived in terms of *α(x)*:

$$f(x) = g(x) + \alpha(x)h(x) \quad \textbf{(Eq. III-6)}$$

where *g(x)* is the complex down-range profile as explained earlier and *h (x)* is:

$$h(x) = \frac{2}{L_{bw}}\int_{k_1}^{k_N} S(l)\cos\left(\frac{2\pi(l-l_c)}{L_{bw}}\right)e^{j2xl}dk \quad \textbf{(Eq. III-7)}$$

Following this, an expression for the spatially variant scalar *α(x)* can be derived through a Least-Squares Minimization (LSM) of the power in the enhanced down-range profile *f(x)*. Starting with the LSM of $|f(x)|^2$:

$$\frac{d}{d\alpha}|f(x)|^2 = 0 \quad \textbf{(Eq. III-8)}$$

then as:

$$|f(x)|^2 = |g(x) + \alpha(x)h(x)|^2$$
$$= |g(x)|^2 + \alpha^2(x)|h(x)|^2 + 2\alpha(x)Re[g^*(x)h(x)] \quad \textbf{(Eq. III-9)}$$

Taking the derivative with respect to α:

$$\frac{d}{d\alpha}[f(x)]^2 = 2\alpha(x)|h(x)|^2 + 2Re[g^*(x)h(x)] = 0 \qquad \textbf{(Eq. III-10)}$$

so:

$$\alpha(x) = \frac{-Re[g^*(x)h(x)]}{|h(x)|^2} \qquad \textbf{(Eq. III-11)}$$

It is noted that α(*x*) could become singular if *h*(*x*) = 0. However, as explained earlier, α(*x*) is constrained to the range [0, 0.5]. This may be written as:

$$\alpha(x) = \begin{cases} 0 & \text{, for } \tilde{\alpha} < 0 \\ \tilde{\alpha} & \text{, for } 0 \le \tilde{\alpha} \le 0.5 \\ 0.5 & \text{, for } \tilde{\alpha} > 0.5 \end{cases} \qquad \text{where: } \tilde{\alpha}(x) = \frac{-Re[g^*(x)h(x)]}{|h(x)|^2} \qquad \textbf{(Eq. III-12)}$$

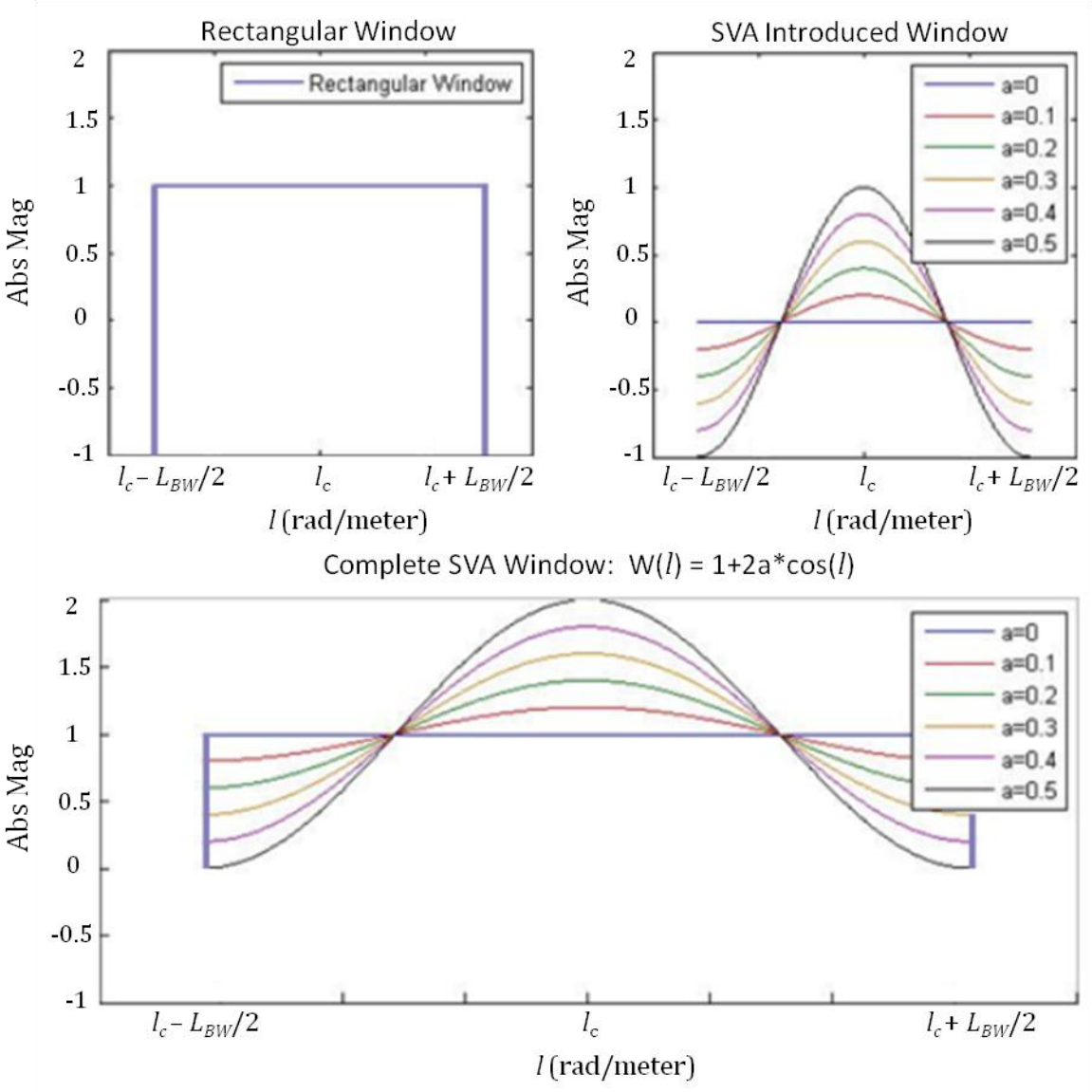

Figure III-7: 1D SVA Windowing Function

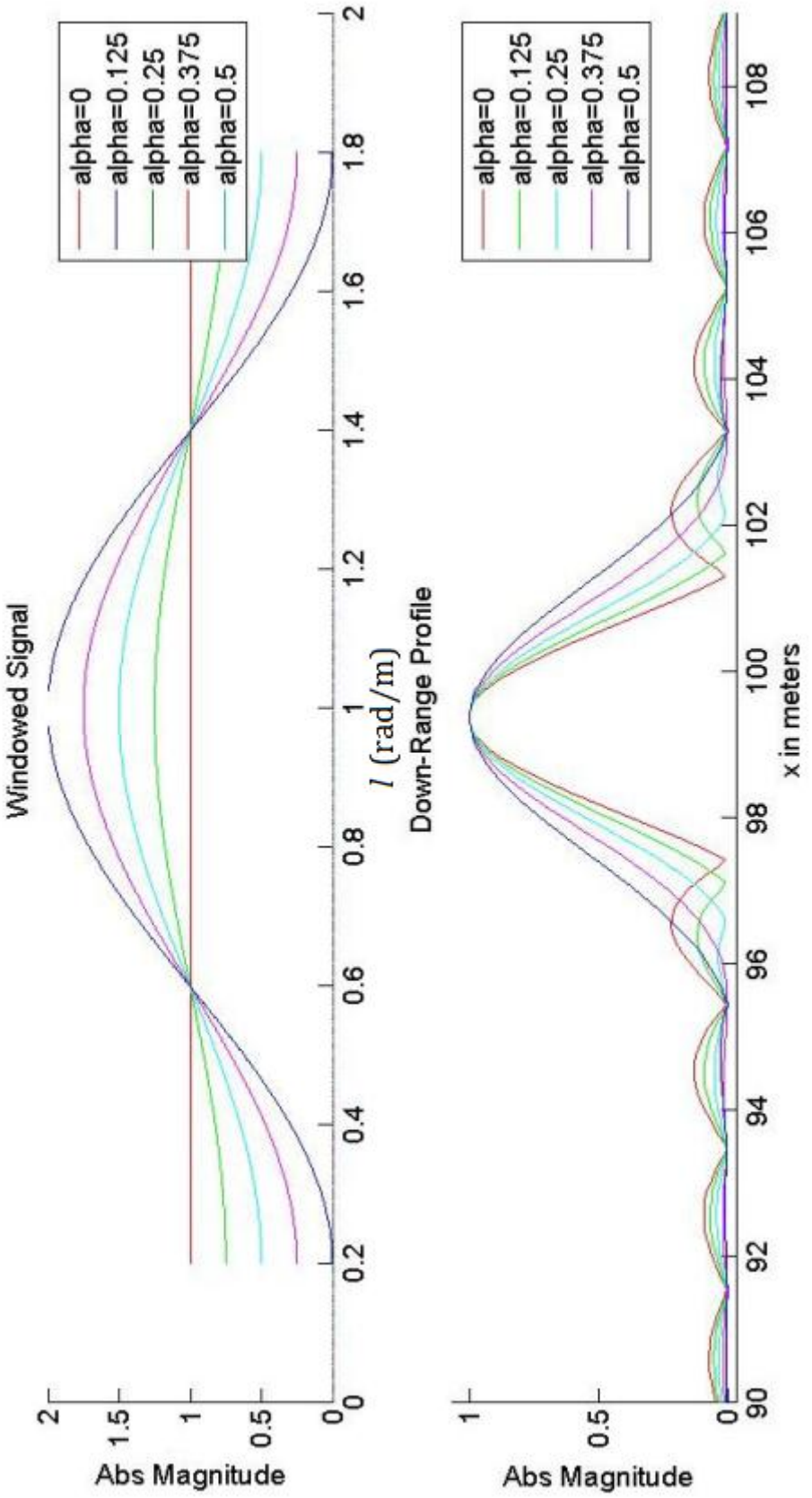

Figure III-8: 1D SVA Windowed Signal and Down-Range Profile

iii. One-Dimensional Super Spatially Variant Apodization (1D Super-SVA)

Super-SVA relies on the standard SVA for its non-linear transformation imposed upon the spatial domain data. This non-linear process results in a modified signal that is no longer band-limited permitting the Super-SVA technique for bandwidth expansion [122]. In order to avoid going through the lengthy derivation of the 1D Super-SVA, the final high-level mathematical representation are presented in this dissertation. The mathematical derivation is given in [122]. A high level block diagram of the 1D Super-SVA procedure is presented in Figure III-9. The first two blocks can be substituted by the 1D SVA explained in the previous subsection. The vertical stack of blocks represents the additional steps required by the 1D Super-SVA. With each loop of this stack, the initial bandwidth is artificially expanded. Even though any number of iterations may be performed, the processing time is significantly affected by this number.

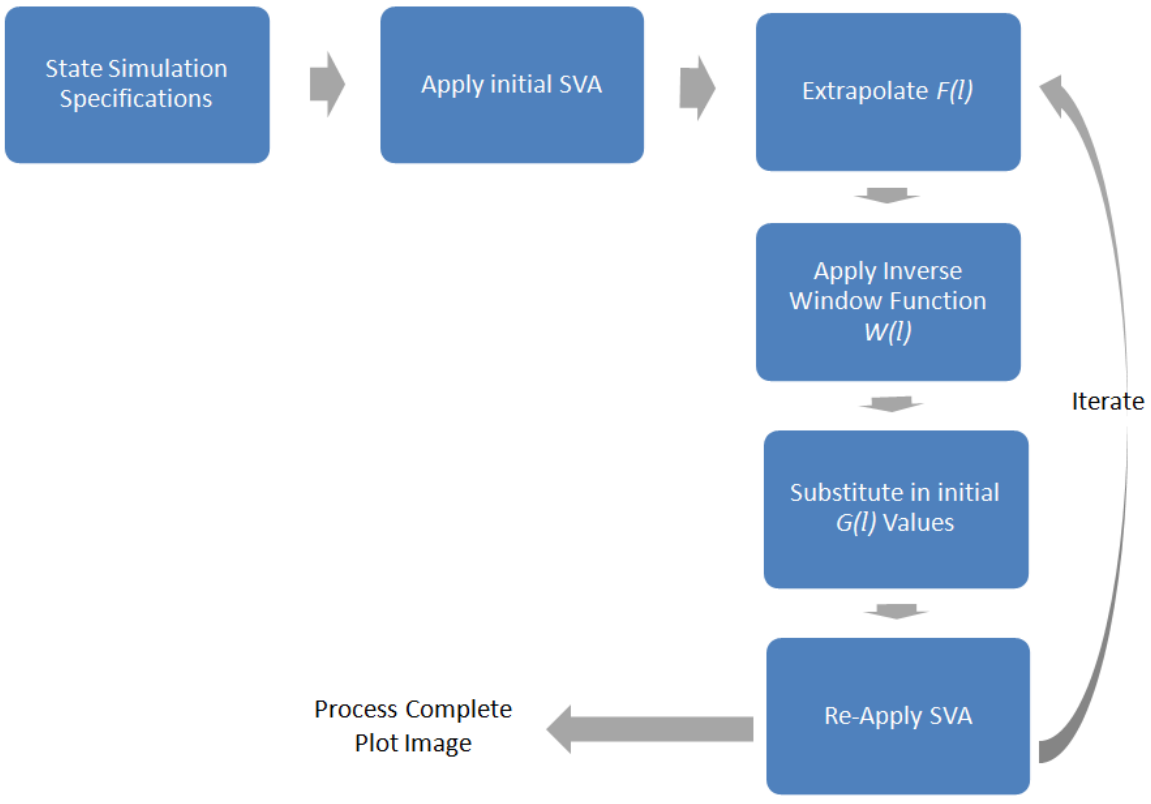

Figure III-9: Block Diagram of the 1D Super-SVA technique

Starting with the first block of the vertical stack, *F(l)* is the wave-number domain Fourier Transformation of *f(x)*, which is the complex spatial domain SVA windowed down-range profile. *F(l)* can be expressed as:

$$F(l) = L_{bw} \int_{x_1}^{x_P} f(x) e^{-j2xl} dx \quad \textbf{(Eq. III-13)}$$

where l is the wave-number (rad/m), x is the spatial displacement (m), P is the number of spatial positions and L_{bw} is the initial wave-number bandwidth. Then, the inverse window $W_{SSVA}(l)$ is approximated by the following solution:

$$W_{SSVA}(l) \approx \int_{-\pi/L_{bw}}^{\pi/L_{bw}} \text{sinc}(L_{bw} x) e^{-j2x(l-l)} dx \quad \textbf{(Eq. III-14)}$$

with the windowing function $W_{SSVA}(l)$ is derived, $S_{SSVA}(l)$, which is the approximation to $S(l)$ over the Super-SVA expanded bandwidth, can then be re-computed from $F(l)$ as shown below:

$$S_{SSVA}(l) = \frac{F(l)}{W_{SSVA}(l)} \quad \textbf{(Eq. III-15)}$$

where the bandwidth is expanded by no more than $\sqrt{2}\frac{L_{bw}}{2}$ per iteration of Super-SVA to prevent singularities. Hence:

$$l_c - \sqrt{2}\frac{L_{bw}}{2} < l < l_c + \sqrt{2}\frac{L_{bw}}{2} \quad \textbf{(Eq. III-16)}$$

Proceeding to the third block in the vertical stack, the initial signal over the initial bandwidth is re-inserted into the extrapolation, and an enhanced down-range profile can be computed. Finally, an inverse FFT is applied to the extrapolated initial signal, which is now substituted by $S_{SSVA}(l)$, and 1D SVA is applied once again. This new down-range profile corresponds to a wider bandwidth and hence it produces a relatively higher down-range resolution. The Super-SVA technique requires three spatial values in computing the SVA enhanced image, hence, if frequency data is collected from a wide range of angles with respect to the target, down-range and cross-range resolution is improved. However, problems started to arise [122] with limited angular-aspects scenarios such as in fixed aperture radar, slow moving radar and/or radar used for imaging very distant objects (i.e. spaceborne SAR). Furthermore, the processing time of Super-SVA technique is hundreds of times more than the standard Windowing-based techniques. Both SVA and Super-SVA are considered for the SAR simulation of the two targets presented in section 1, however, only the case of the closely positioned targets is considered. Simulation outcome using both SVA and Super-SVA techniques is presented in Figure III-10. The outcome shows that SVA has slightly changed amplitude and position of the weaker target while Super-SVA only changed the amplitude of the weaker target but preserved its position.

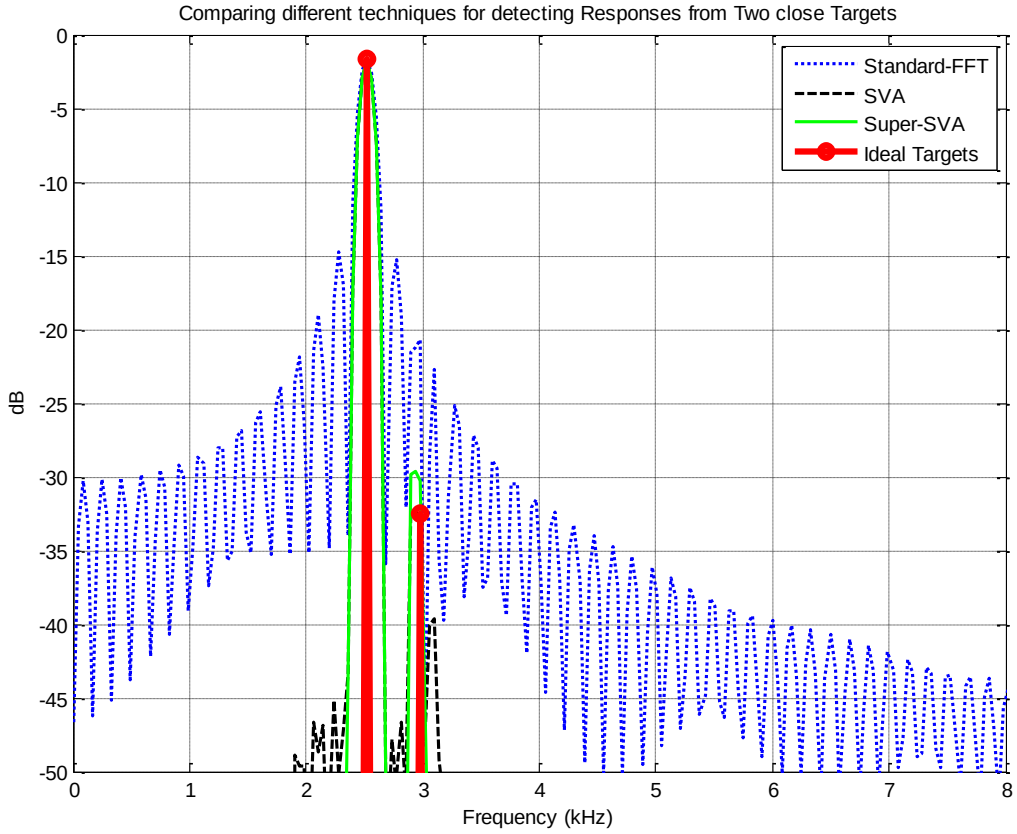

Figure III-10: Simulating Target responses that have different magnitudes and positioned very close to each other using SVA and Super-SVA techniques

4. Superimposition Technique

The proposed technique of superimposition offers sidelobe reduction with an improved resolution, particularly for closely located signals. The idea of the superimposition technique is to generate a second function from a subset of the original data so that the null adjacent to its main-lobe is aligned with the maximum point of the first sidelobe of the original sinc signal. After that, by superimposing both the sinc functions in the frequency domain, the final sinc-like signal will have very similar peak-width and amplitude to the original signal while having reduced sidelobes [123]. Accordingly, the new technique is based on superimposing multiple FFT/IFFT analyses of the same data followed by an averaging process. Starting with the truncating part, depending on the sidelobe being targeted and the truncation technique, the truncation ratio is chosen, and a new signal s_1 is generated from the original signal s_0 using the following equation:

$$s_1(t) = s_0(t) \cdot Windowing\left(\frac{t}{\tau_1} - \frac{\tau_1}{2}\right) \qquad \textbf{(Eq. III-17)}$$

where the new signal duration $\tau_1 = k_1\tau_0$, such that k_1 is the truncation ratio, which its calculated depends on the windowing technique as explained in the following subsections, and τ_0 is the original signal duration. Then, the spectra of both the original signal $s_0(t)$ and the truncated signal $s_1(t)$ are calculated using FFT, yielding $S_0(\omega)$ and $S_1(\omega)$ respectively. These signals are superimposed, which is a product of the spectra [53] as oppose to superposition, which is defined as sum of vectors/waves [54]. The new signal, S', which is the outcome of the superimposition process, is generated by multiplying the spectrums of the original signal, $S_0(\omega)$, and the truncated signal, $S_1(\omega)$, see Figure III-11.

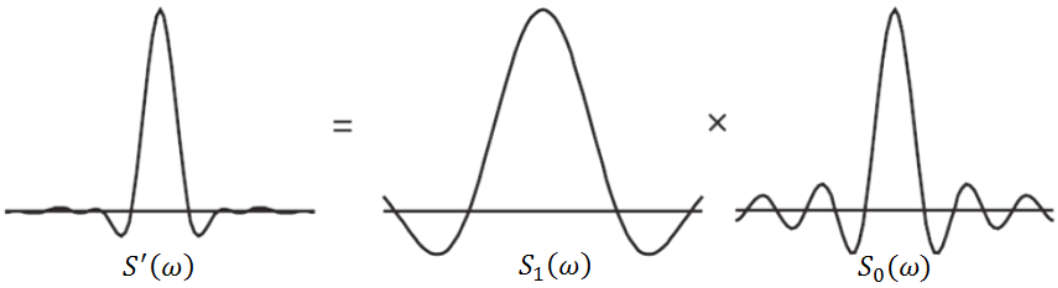

Figure III-11: Superimposition Process as product of signal in Frequency Domain [53].

Truncation of the original signal causes the truncated signal to lose its original height due to loss of power [12], see Figure III-12. Furthermore, the multiplication process between the original and truncates signals in frequency domain causes the superimposed signal to be squared. Hence, for these two issues, a normalization step is required to maintain relative strengths between the frequency components. This is done using a correction factor as described in equation (Eq. III–26)

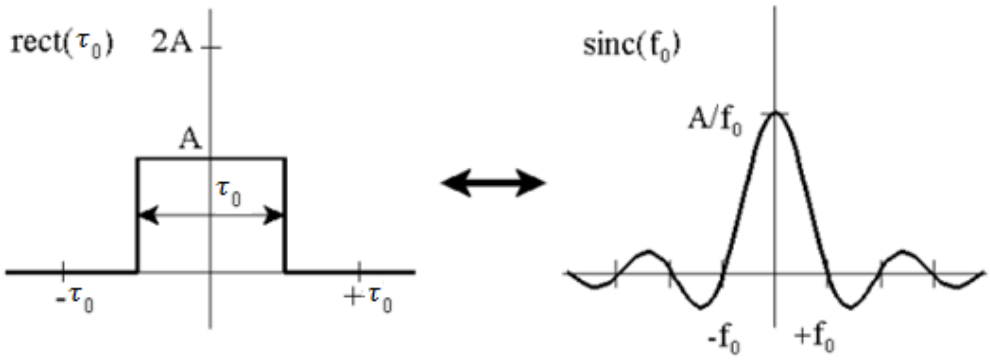

Figure III-12: Pulse width in time domain effect the main-lobe width in frequency domain [12].

Finally, an average-windowing function is used to further suppress sidelobes. The resulting sidelobes after superimposition are averaged over the width of two successive lobes due to the finite and causal nature of the signal that is alternating between sets of negative

and positive values in successive lobes, which yields the phase of the lobes to alternate between 0 and π [123], this have a cancellation effect, see Figure III-13. The averaging is performed using a uniform moving average filter [54]. The moving average filter is a convolution of the superimposed signal with: $M(\omega) = (2/\tau_0)\ \mathrm{rect}\{\omega\tau_0/2\}$, where $2/\tau_0$ is the width of the main-lobe in the original signal, and the averaged superimposed signal is [54]:

$$S'''(\omega) = S''(\omega) * M(\omega) \cong \int_0^{\omega} S''(\varphi) * M(\omega - \varphi) d\varphi \qquad \textbf{(Eq. III-18)}$$

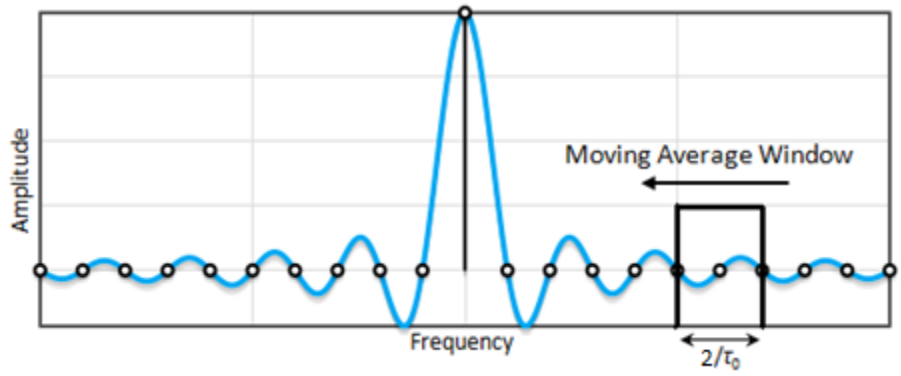

Figure III-13: Moving Average Window on sinc function representing target response.

In order to have a better understanding of superimposition, let's consider the original signal to be sinusoidal:

$$s_0(t) = A\cos(\omega_0 t) \qquad \textbf{(Eq. III-19)}$$

where A is the amplitude and $\omega_0 = 2\pi f_0$, f_0 is the frequency. Conversely, due to the time-limited property of real-life measurement, the original signal is, mathematically, subjected to rectangular windowing function [53] with duration τ_0. Hence, $s_0(t)$ is expressed as:

$$s_0(t) = A\cos(\omega_0 t) \times rect\left(\frac{t}{\tau_0} - \frac{\tau_0}{2}\right) \qquad \textbf{(Eq. III-20)}$$

and its corresponding Fourier Transform is [12]:

$$S_0(\omega) = \tau_0 e^{\left(\frac{-j\omega\tau_0}{2}\right)} \frac{A}{2}\left(sinc\left(\frac{\omega + \omega_0}{2\pi}\tau_0\right) + sinc\left(\frac{\omega - \omega_0}{2\pi}\tau_0\right)\right) \qquad \textbf{(Eq. III-21)}$$

Furthermore, even though further investigation on different windowing/truncation techniques is presented in the following subsections, let's consider the windowing function used in this discussion here to be a rectangular windowing function with width τ_1. Hence, Eq. III-17 can be rewritten as:

$$s_1(t) = A\cos(\omega_0 t) \times rect\left(\frac{t}{\tau_0} - \frac{\tau_0}{2}\right) \times rect\left(\frac{t}{\tau_1} - \frac{\tau_1}{2}\right) \quad \textbf{(Eq. III-22)}$$

since τ_1 is always less than τ_0 by design, $s_1(t)$ can be written as [53]:

$$s_1(t) = A\cos(\omega_0 t) \times rect\left(\frac{t}{\tau_1} - \frac{\tau_1}{2}\right) \quad \textbf{(Eq. III-23)}$$

and its Fourier Transform is:

$$S_1(\omega) = \tau_1 e^{\left(\frac{-j\omega\tau_1}{2}\right)} \frac{A}{2}\left(sinc\left(\frac{\omega+\omega_0}{2\pi}\tau_1\right) + sinc\left(\frac{\omega-\omega_0}{2\pi}\tau_1\right)\right) \quad \textbf{(Eq. III-24)}$$

Then, the spectrums of both signals are superimposed, see Figure III-11:

$$\acute{S}(\omega) = S_0(\omega) \times S_1(\omega) \quad \textbf{(Eq. III-25)}$$

Before continuing with this analysis, it is important to note that two components are affecting the accuracy of $S_0(\omega)$ and $S_1(\omega)$ as shown in Eq. III-21 and Eq. III-24 respectively. The first one is the loss of power that causes the signal peak to drop. In other words, the normalization process introduces an amplitude scaling factor of $1/\tau_i$ to deal with the power loss caused by the truncation ratio, k_i. The second factor is the complex component $\exp(-j\omega\tau_i/2)$ that is caused by the time shift of the rectangular function in the time domain which in turn caused this phase shift in the frequency domain, which is important as the phase relationship between the truncated signals is what the final step of averaging-windowing depends on. Hence, the Correction Factor (CF) used to maintain relative strengths between the frequency components in the signal is:

$$CF = \frac{1}{\tau_0\tau_1} e^{\frac{j\omega\tau_0}{2}} e^{\frac{j\omega\tau_1}{2}} \quad \textbf{(Eq. III-26)}$$

In addition, the magnitude of the superimposed signal is squared due to the product of the spectra of the original and the truncated signals. Thus, the normalization process in superimposition technique, besides scaling the superimposed signal with CF, takes the square-root of the superimposed signal. Consequently, the superimposed signal, $S'(\omega)$, is normalized as follow:

$$S''(\omega) = \sqrt[2]{S'(\omega)\,\frac{1}{\tau_0\tau_1} e^{\frac{j\omega\tau_0}{2}} e^{\frac{j\omega\tau_1}{2}}} \quad \textbf{(Eq. III-27)}$$

Finally, the moving average window filter is applied, see Figure III-13. However, the actual implementation of the moving average filter is done via a series of Fourier transforms using the convolution theorem [54] as described in the following equation:

$$S'''(\omega) = FT^{-1}[FT\{S''(\omega)\} \times FT\{M(\omega)\}] \quad \textbf{(Eq. III-28)}$$

It is worth mentioning that for simplicity, the previous analysis is for a signal with a single frequency, however, the processing technique described is linear, and therefore, the superimposition technique can – and is – applied to multi-frequency signals. Figure III-14 shows the IFFT-Superimposition algorithm. The algorithm is broken into four parts that were described above: Truncation, Superimposition, Normalization and Averaging.

i. Superimposition with Truncation

The truncation ratio is chosen so that the nulls of the spectrum of the truncated signal coincide with the max point of the sidelobes of the spectrum of the original signal. When both signals are superimposed, the original sidelobe is reduced and broken into two sidelobes. The zero crossings in the spectrum occurs at $\omega_0 + 2\pi\ /\ \tau_0$, $\omega_0 + 4\pi\ /\ \tau_0$, $\omega_0 + 6\pi\ /\ \tau_0$, … and so forth, where ω_0 is the signal frequency and τ_0 is the duration of the original signal. So, in general, the ith zero crossing occurs at:

$$\omega_{zero\_i} = \omega_0 + \frac{2\pi i}{\tau_0} \quad \textbf{(Eq. III-29)}$$

It can also be noted that the ith side lobe is bounded by the ith zero crossing and the (i+1)th zero crossings. Hence, the exact max point of the ith sidelobe can be expressed as:

$$\begin{aligned}\omega_{\max point} &= \omega_{zero\_i} + \frac{1}{2}\left[\omega_{zero\_i+1} - \omega_{zero\_i}\right] = \frac{1}{2}\left[\omega_{zero\_i+1} + \omega_{zero\_i}\right] \\ &= \frac{1}{2}\left[\left(\omega_0 + \frac{2\pi(i+1)}{\tau_0}\right) + \left(\omega_0 + \frac{2\pi i}{\tau_0}\right)\right] = \omega_0 + \frac{\pi(2i+1)}{\tau_0}\end{aligned} \quad \textbf{(Eq. III-30)}$$

therefore, to have the 1st zero crossing of the truncated signal coinciding with the max point of the ith sidelobe of the original signal:

$$\omega_0 + \frac{2\pi}{\tau_i} = \omega_{\max point} = \omega_0 + \frac{\pi(2i+1)}{\tau_0} \quad \textbf{(Eq. III-31)}$$

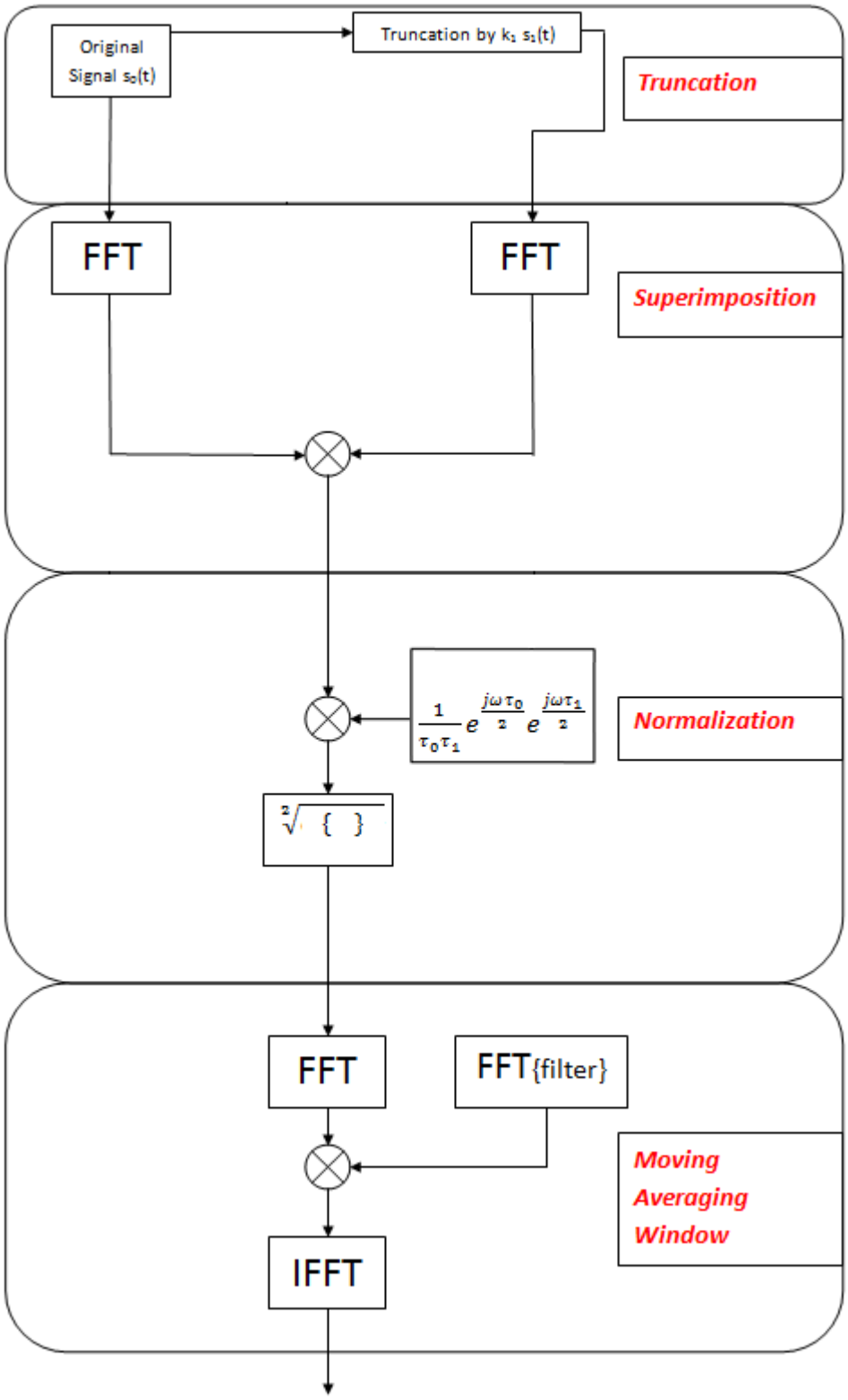

Figure III-14: Block Diagram for the algorithm of Standard-Superimposition technique

as a result, its duration must be such that:

$$\tau_i = \frac{2\tau_0}{2i+1} \quad \textbf{(Eq. III-32)}$$

hence, to target the ith sidelobe the truncation ratio, *k*, must be determined by:

$$k_i = \frac{\tau_i}{\tau_0} = \frac{2}{2i+1} \quad \textbf{(Eq. III-33)}$$

However, due to the periodic nature of the sidelobes in a sinc function, targeting a certain sidelobe using the superimposition technique results in other sidelobes being targeted whenever a midpoint of a sidelobe in the original signal coincides with a zero crossing point in the truncated signal. For example, in the case of targeting the 1st sidelobe in the original signal, zero crossings, as shown in (Eq. III-29), take place at 3π/2, 6π/2, 9π/2 ... and so on. Bearing in mind that, according to (Eq. III-30), the max-points of the first four sidelobes of the original signal are at 3π/2, 5π/2, 7π/2 and 9π/2, one can notice that, other than the 1st sidelobe, the 4th sidelobe of the original signal is also aligned with the 3rd zero crossing point of the truncated signal. In order to show the effect of the truncated signal when superimposed on the received signal, a sinc function is simulated with four different truncations in order to suppress the 1st, 2nd and 3rd sidelobes. The results for each case are shown in a three pairs of figures that are presented in Figure III-15, Figure III-16 and Figure III-17.

Starting with Figure III-15 (a), the two traces presented are of the original signal and the new version of the signal that is truncated to suppress the 1st sidelobe and hence, according to (Eq. III-33), it has a truncation ratio of k_1=2/3. Here, it can be noticed that the max-point of the 1st sidelobe in the original signal is aligned with the first min-point of the truncated signal, when these two signals are superimposed, the outcome, presented in Figure III-15 (b), shows how the 1st, 4th and 7th sidelobes are being suppressed. Similarly, Figure III-16 show how a truncation ration of k_2=2/5 is suppressing the 2nd and 7th sidelobe while, finally, in Figure III-17 the superimposition outcome is suppressing the 3rd sidelobe by using a truncation ration of k_3=2/7.

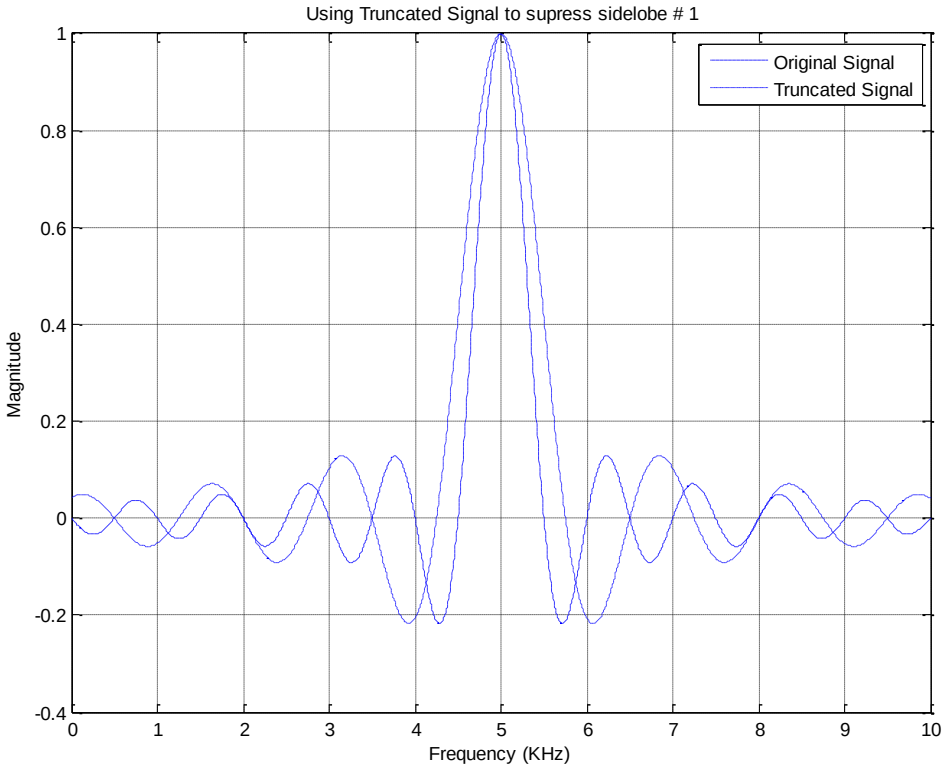

(a)

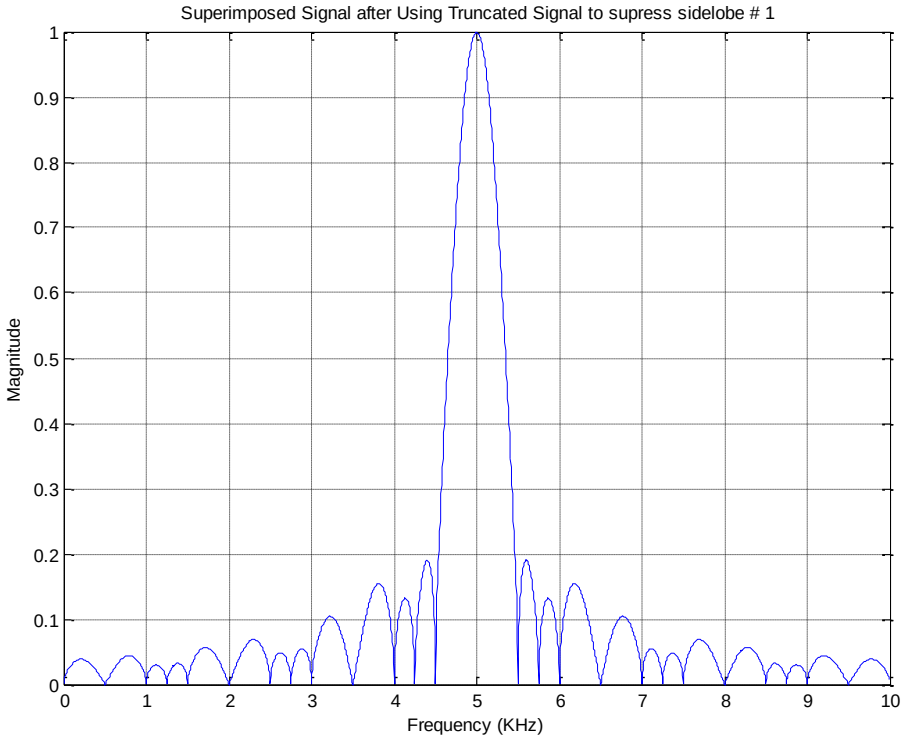

(b)

Figure III-15: (a) Original and Truncated Signals aligned (b) Superimposed signal suppressing 1st sidelobe

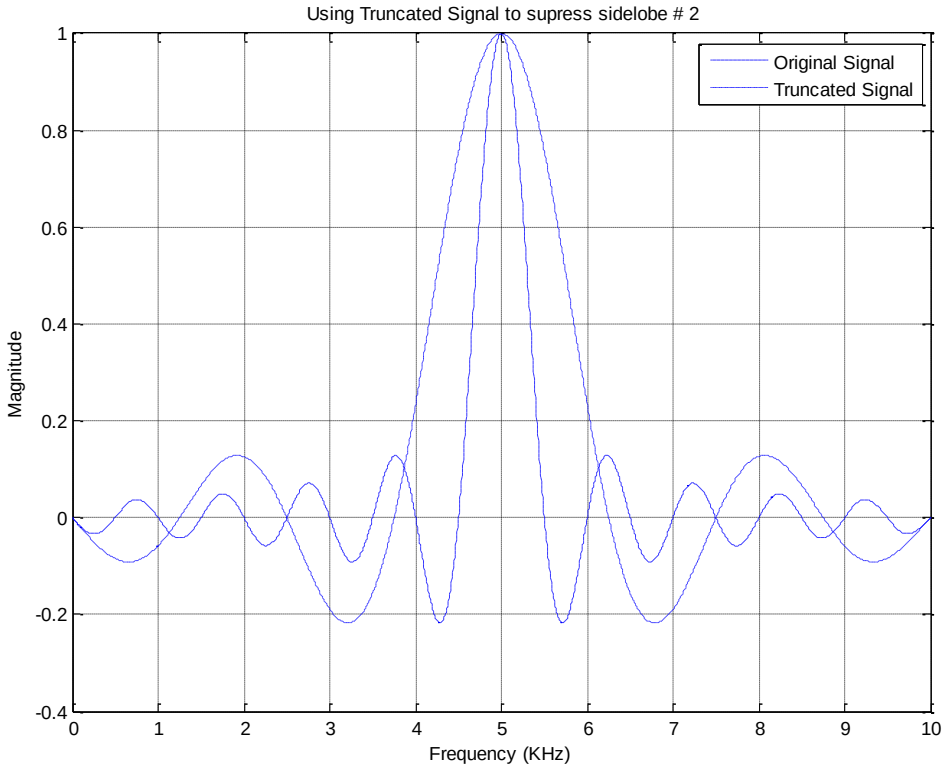

(a)

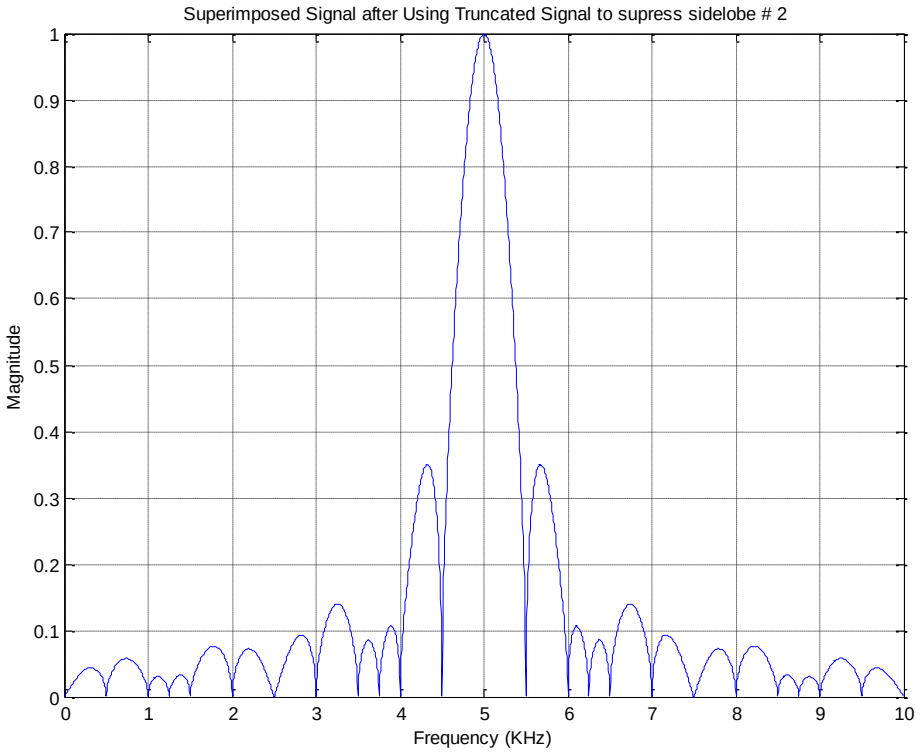

(b)

Figure III-16: (a) Original and Truncated Signals aligned (b) Superimposed signal suppressing 2nd sidelobe

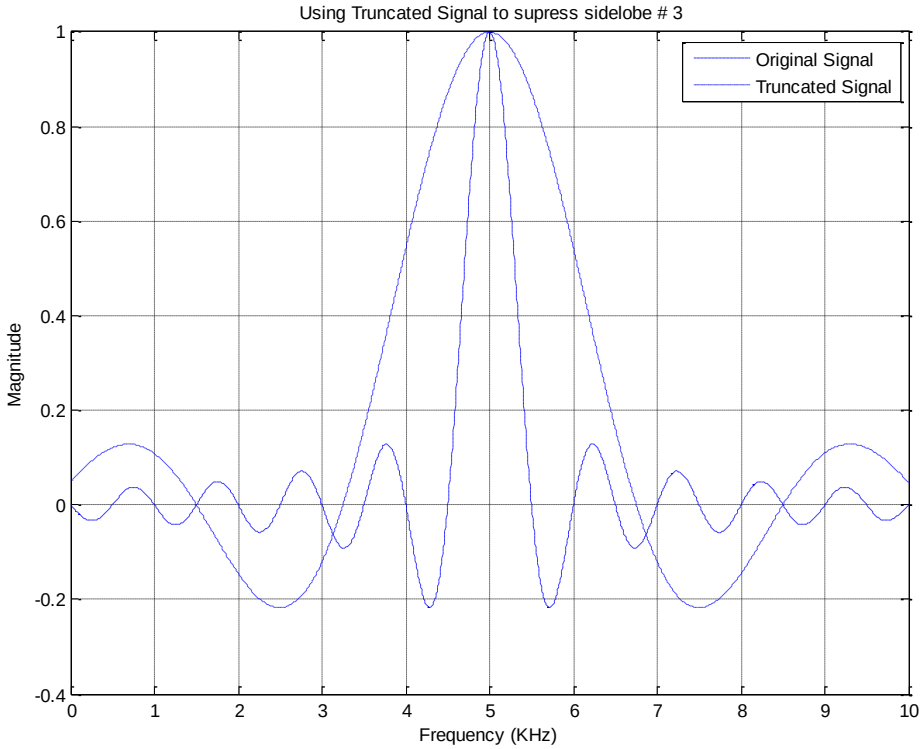

(a)

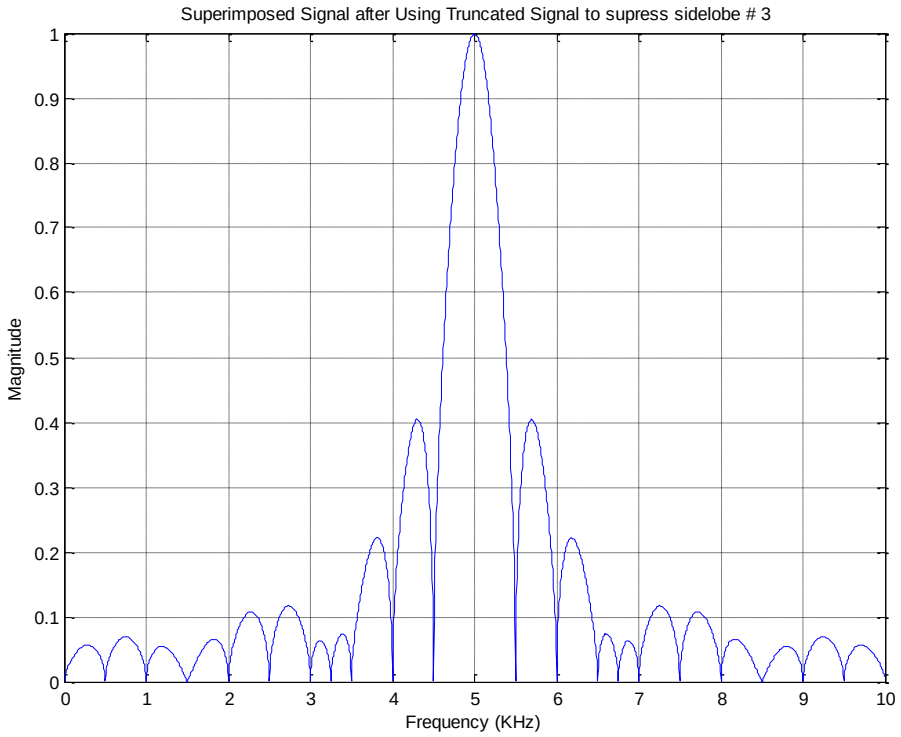

(b)

Figure III-17: (a) Original and Truncated Signals aligned (b) Superimposed signal suppressing 3rd sidelobe

ii. Superimposition with Windowing Functions

In Fourier analysis of time limited data, it is assumed that the signal is periodic with the duration of the signal. If the duration of the signal is not an integer multiple of the period of the signal, the periodic extension assumption leads to discontinuities, which in turn leads to leakage effect in the signal spectrum. Window functions are designed specifically to ensure that the transition at the periodic extensions are not abrupt by trying to make the derivative of the boundary points equal to zero or near zero. Window functions are generally categorized into: fixed windows and adjustable windows [53]. The fixed windows have one parameter, which is the window length that controls the main-lobe width. On the other hand, the adjustable windows have the window length – as in fixed windows – and one or more additional parameters that can control other window characteristics.

The vast majority of fixed windows are constructed as weighted sums, products or convolutions of simple functions or other window functions [53]. For example, the Bartlett window is a time domain convolution of two rectangular windows, whereas both the Hann and Hamming windows are shifted sums of the frequency domain representation of the rectangular window. In contrast, adjustable window functions are often derived based on optimality criteria [53]. Dolph's criteria and Kaiser's criteria are two of the most popular optimality criteria used in adjustable window design. The window functions resulting from Dolph's criteria are described by the Chebyshev polynomials. Dolph windows have the constant sidelobe levels for all sidelobes and, hence, have no sidelobe roll off. The Kaiser family of window functions are generated by solving Kaiser's optimization problem that is approximated by the modified Bessel function of order zero.

One major effect of a window function is an increase in the main lobe width of the signal spectrum, which in turn degrades resolution. However, as the superimposition technique is based on altering the width of the main lobe in signal spectra, this disadvantage is used to the benefit of the technique. By applying a window function to the data, initially, it means that the sidelobe can be targeted using a smaller truncation ratio with the additional benefit of sidelobe suppression. The Hann, Hamming, Chebyshev and Bartlet window-functions have zero crossing main lobe widths that are double that of the rectangular window function. This means that the amount of the data from the original signal that is discarded can be reduced by a half. For the Hamming Window, to target the i^{th} sidelobe using a combination of

windowing and truncating, where truncation is performed before applying the windowing function, the truncations ration to suppress the ith sidelobe, k_i, of the original signal is:

$$k_i = 4/(2i+1) \qquad \textbf{(Eq. III-34)}$$

Referring to the different traces of the signal in Figure III-18, where a Hamming window is used to generate a superimposed signal, it can be seen that the width of the main-lobes of the windowed signal has widened. However, the alignment of the centre of the first sidelobe of the original signal with the low point (i.e. zero-crossing) of the windowed signal gives a motivation for superimposition. However, it must be taken into consideration that the magnitudes of the windowed and superimposed signals are lessening due to the effect of truncation on the power of the signal. Hence, the magnitude of the signals must be increased to be equal to that of the original signal. In the case of superimposition, the magnitude is adjusted by multiplying it with the reciprocal of the truncation ratio, k, and then taking the nth root of the outcome, where n is the number of signals used in the superimposition process.

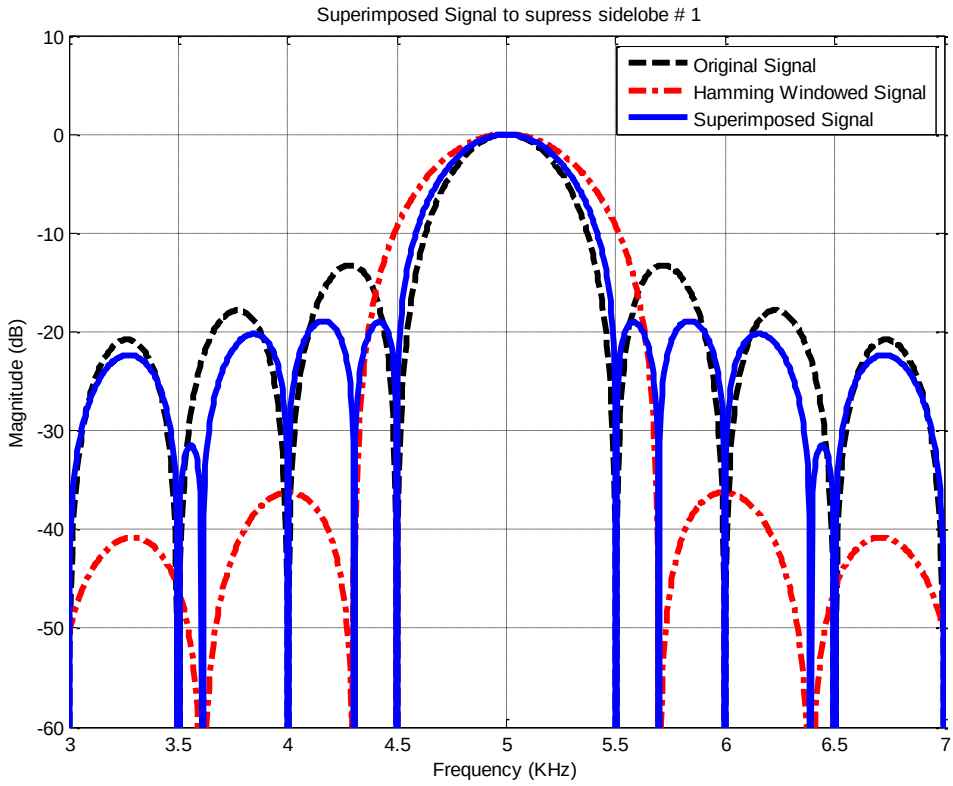

Figure III-18: Superimposed Signal using Hamming Window to suppress 1st sidelobe

In order to put the importance of superimposition in context, the simulation of the closely spaced two targets at the beginning of this chapter, Figure III-2, is simulated using superimposition with Hamming Window. In the standard-FFT with Hamming window output the sidelobes got greatly reduced, but the two targets merge into one main-lobe that is slightly wider than that for a single target. The superimposition with Hamming Window technique, see Figure III-19, reduces the sidelobes and still presents two separate main lobes showing that the two targets are clearly resolved into two identifiable responses even though the second target is more -30dB less than the first target.

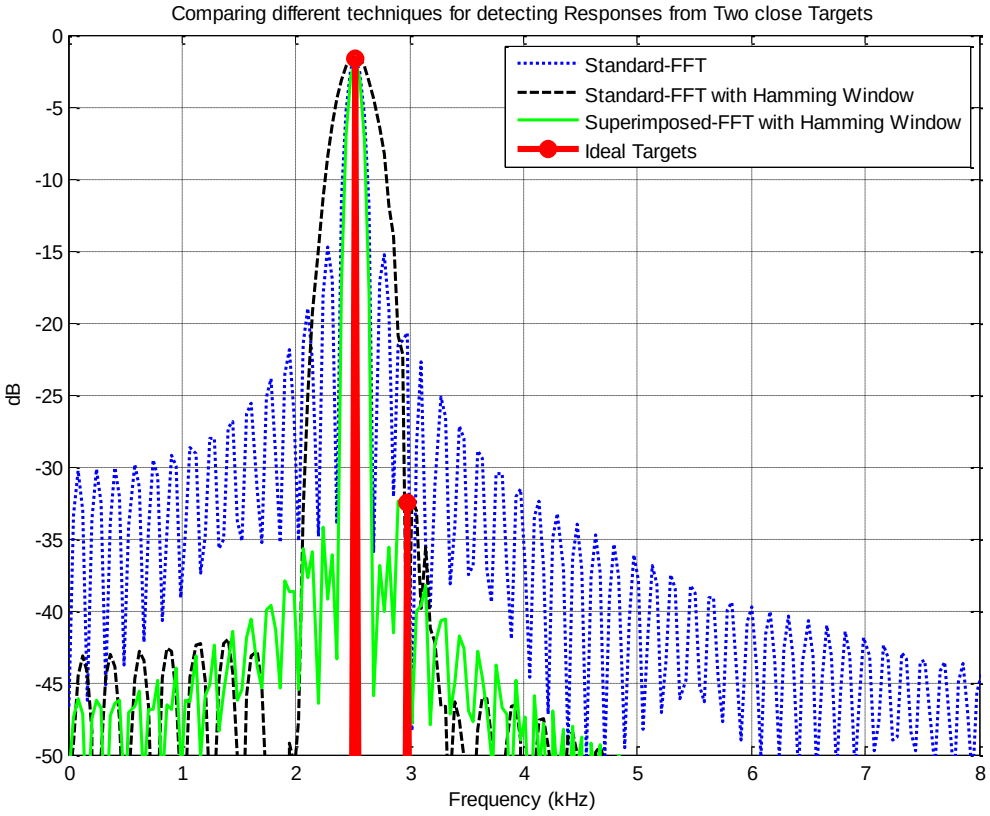

Figure III-19: Simulating Target responses of two targets that are of different power and placed very close to each other using superimposed-FFT with Hamming Window.

5. Improving Superimposition

In the previous section, the standard superimposition technique is presented in its basic format. By applying superimposition, an improved outcome is achieved as sidelobes are reduced with minor broadening of the target's main-lobe. Results have shown minimal resolution loss, noticeable sidelobe reduction and negligible distortion of peak position and amplitude of the signal spectrum. In this section, superimposition is improved using two new

techniques. The first simply, and yet effectively, repeats the process of superimposition: this one is referred to as the Repetitive Superimposition (RSI). Windowed versions of the truncated original signal are utilized in order to suppress all sidelobes. The second technique enhances the mathematical process of superimposition by normalizing the original signal and widened versions (using windowing and/or truncation), this one is referred to as Normalized Superimposition (NSI). Both of these techniques is presented and discussed in the following two subsections. In addition, more highly structured simulations and measurements are considered throughout the next three chapters in order to give a more accurate examination of the improved superimposition and SVA techniques.

Before continuing with this technique, an important observation that was deduced from the different simulation setups must be stressed. It was noticed in the case of only one main-lobe, a better overall result has been achieved by increasing the number of sidelobes that are subjected to direct suppression by aligning the zero-crossing points of the new widened signals over their peaks. On the other hand, in case of multiple main-lobes, and especially in the case of closely positioned ones, increasing the number of sidelobes that are subjected to direct suppression by the different superimposed signals was seen to have a destructive effect on the main-lobes. Hence, the number of directly affected sidelobes in this research work has been limited to a maximum of three only. The choice of three sidelobes was based on the observations of the results of many simulations and experimentations that are comprehensively discussed in following chapters.

i. Repetitive Superimposition (RSI)

In the standard superimposition, the original signal is used with only one other signal, which was generated from the original signal with a widened main-lobe using direct truncation and/or windowing, and showed to have suppressed sidelobes. Nevertheless, it has been found that by repeating the superimposition process, the sidelobes are reduced even further. This technique is named Repetitive Superimposition (RSI), see Figure III-20. RSI works by superimposing several different versions of the original signal which have different truncations. The different truncation values are calculated to have zero-crossings distributed along the sidelobes of the original signal width. However, even though the RSI technique depends on repeating the FFT process, it is important to bear in mind that with today's computational capabilities this processing takes only a few milliseconds for the 10-times RSI on a standard Personal Computer.

The output signal of final Repetitive Superimposed signal of order *N* is calculated using the following equation:

$$S_{RSI} = \sqrt[N]{\left(\prod_{i=0}^{N-1} S_i \left(\frac{1}{\tau_i} e^{\frac{j\omega\tau_i}{2}}\right)\right)} \quad \textbf{(Eq. III-35)}$$

RSI apply N^{th} root to the outcome of the multiplication of all the used signals and also apply scaling of CF, as shown in Eq. III-26, on the superimposed signal. The different truncation values are calculated to have zero-crossings distributed along the sidelobes of the original signal width. The number of repeats of the process (*N*) represents the number of the different versions of the signal that are superimposed on the original one and is denoted by RSI-*N*. For instance, if *N* is two, then the Two-times Repetitive Superimposition is denoted by RSI-2, which means that two different versions of the original signal are superimposed on it. The most favourable order of repetitions is discussed and determined using empirical methods to find the best compromise between performance and processing time and is presented in the next two chapters.

Using the conjugates of signals in Matched Filters has been shown to combat noise [62]. Hence, this approach is considered in superimposition where the conjugates of alternate signals used in the RSI process are taken. For example, in the case of RSI-4, the final signal is:

$$S_{RSI-4} = \sqrt[4]{(S_0 \times S_1^* \times S_2 \times S_3^*)\left(\prod_{i=0}^{3} \frac{1}{\tau_i} e^{\frac{j\omega\tau_i}{2}}\right)} \quad \textbf{(Eq. III-36)}$$

where S_0 is the original signal, S_1, S_2 and S_3 are three versions of the original signal that are truncated with different ratios. The effect of using the conjugate signals in superimposition is shown and discussed in section 6 of chapter 4.

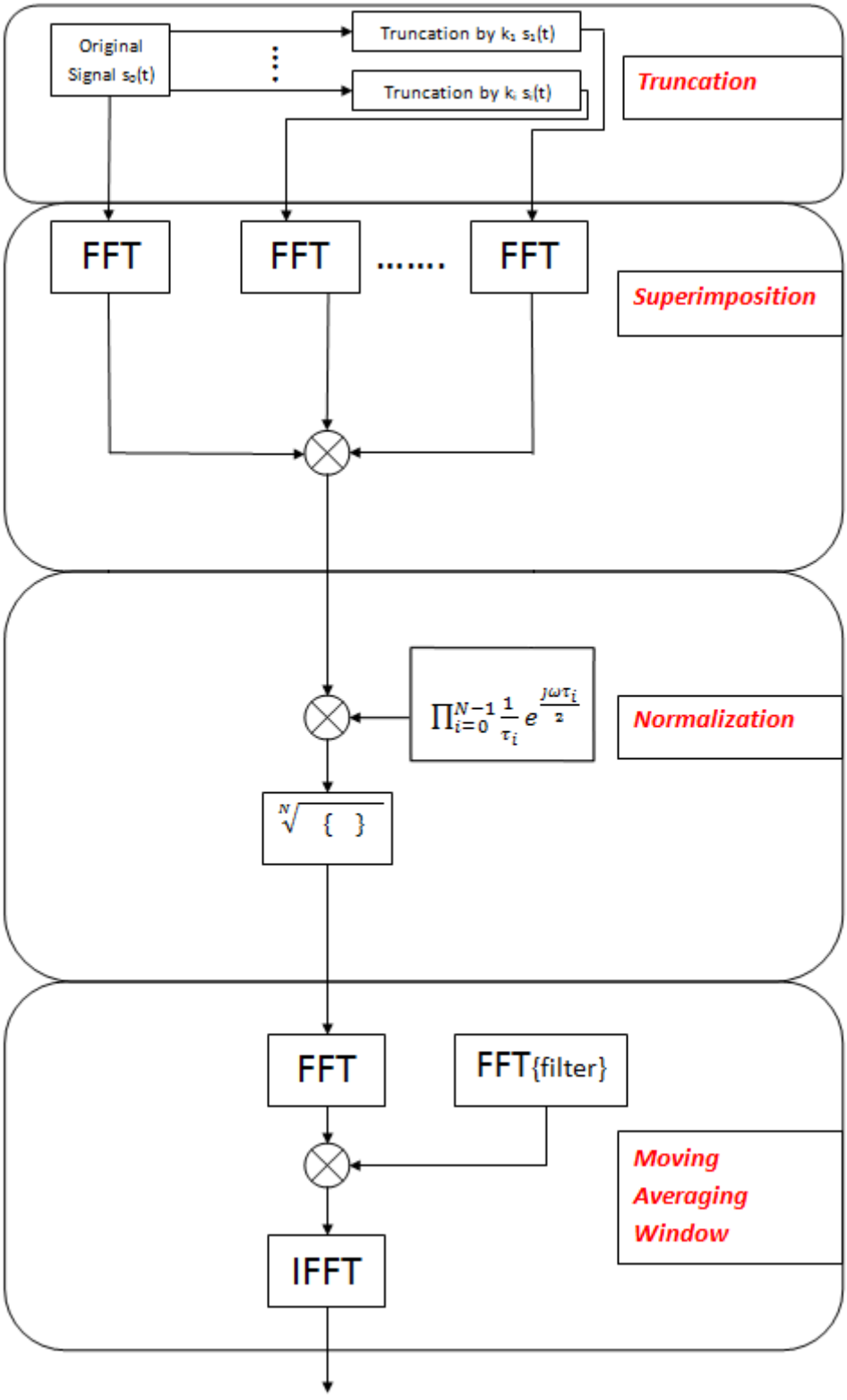

Figure III-20: Block Diagram for the algorithm of Repetitive Superimposition (RSI-N) technique

ii. Normalized Superimposition (NSI)

In both the standard-Superimposition and the Repetitive-Superimposition techniques, the original signal is directly superimposed with new truncated/windowed version(s) of the original signal. However, a new method of Normalized Superimposition (NSI), which works by normalizing a number of different versions of the original signal that have been truncated and/or windowed, has been considered, since the normalization process emphasizes the coincided max points of the main-lobe peaks and suppress the other unwanted peaks (i.e. sidelobes). All the signals S_1, S_2, … S_{N-1}, which have different truncation values of the original signal S_0 in the normalization process of N^{th} order, are calculated to have zero-crossing on the centre and distributed along the width of the original signal's sidelobes. The N^{th} order of the Normalized-Superimposition technique is denoted by NSI-*N*. The influence of the value of the order (*N*) is investigated in the next two chapters in order to decide on the most favourable order. The final Normalized Superimposed signal is calculated using the following equation:

$$S_{NSI} = \frac{\sqrt[N]{\left(\prod_{i=0}^{N-1}(S_i)\left(\frac{1}{\tau_i}e^{\frac{j\omega\tau_i}{2}}\right)\right)}\ N(N-1)}{\sum_{n=0}^{N-2}\sum_{m=1+n}^{N-1}\left(\left|\frac{S_n}{S_m}\right| + \left|\frac{S_m}{S_n}\right|\right)} \qquad \textbf{(Eq. III-37)}$$

$$= \frac{S_{RSI}\ N(N-1)}{\sum_{n=0}^{N-2}\sum_{m=1+n}^{N-1}\left(\left|\frac{S_n}{S_m}\right| + \left|\frac{S_m}{S_n}\right|\right)}$$

where the denominator incorporate all the different combinations of all the paired signals. The final NSI signal is corrected, similar to the RSI technique, by applying the N^{th} root to the multiplied signals, also apply scaling of CF, as shown in Eq. III-26, and in order to correct the geometric effect of the normalization process in the denominator, the numerator is multiplied by $N(N-1)$.

Finally, NSI also can utilize conjugates of half of the signals used in superimposition. So, based on the example of RSI-4 shown in Eq. III–36, NSI-4 that utilizes conjugates can be expressed as:

$$S_{NSI-4} = \frac{\sqrt[4]{(S_0 \times S_1^* \times S_2 \times S_3^*)\left(\prod_{i=0}^{3}\frac{1}{\tau_i}e^{\frac{j\omega\tau_i}{2}}\right)} \times (12)}{\sum_{n=0}^{2}\sum_{m=1+n}^{3}\left(\left|\frac{S_n}{S_m}\right| + \left|\frac{S_m}{S_n}\right|\right)} \quad \textbf{(Eq. III-38)}$$

$$= \frac{S_{RSI-4} \times (12)}{\sum_{n=0}^{2}\sum_{m=1+n}^{3}\left(\left|\frac{S_n}{S_m}\right| + \left|\frac{S_m}{S_n}\right|\right)}$$

iii. IFFT-based Superimposition

Even though only FFT-based schemes are considered so far in this chapter, the IFFT-based scheme can be applied as well. This subsection briefly introduces the mathematical representation of the IFFT-based superimposition scheme. Writing the original frequency domain signal as $S(\omega)$ and the truncation function as $T_n(\omega)$ the result of 2nd order, N, standard-superimposed-IFFT calculation is:

$$s_n(t) = IFFT\big(S(\omega)T_n(\omega)\big) \quad \textbf{(Eq. III-39)}$$

The algorithm used is almost the same to that used in FFT-based schemes presented earlier , as shown in Figure III-21. So, based on the description provided in subsection 5.i of this chapter, the N^{th} order of the IFFT-based RSI is represented as:

$$s_{RSI-N}(t) = \sqrt[N]{\left(\prod_{i=0}^{N-1} s_i(t)\frac{1}{\omega_i}e^{\frac{j\omega_i t}{2}}\right)} \quad \textbf{(Eq. III-40)}$$

where ω_i is the width of the i^{th} signal the spectra domain and based on the explanation of NSI in subsection 5.ii, the N^{th} order of IFFT-based NSI is calculated as follow:

$$s_{NSI-N}(t) = \frac{N(N-1)\ \sqrt[N]{\left(\prod_{i=0}^{N-1}\frac{1}{\omega_i}s_i(t)\,e^{\frac{j\omega_i t}{2}}\right)}}{\sum_{n=0}^{N-2}\sum_{m=n+1}^{N-1}\left(\left|\frac{S_n}{S_m}\right| + \left|\frac{S_m}{S_n}\right|\right)} \quad \textbf{(Eq. III-41)}$$

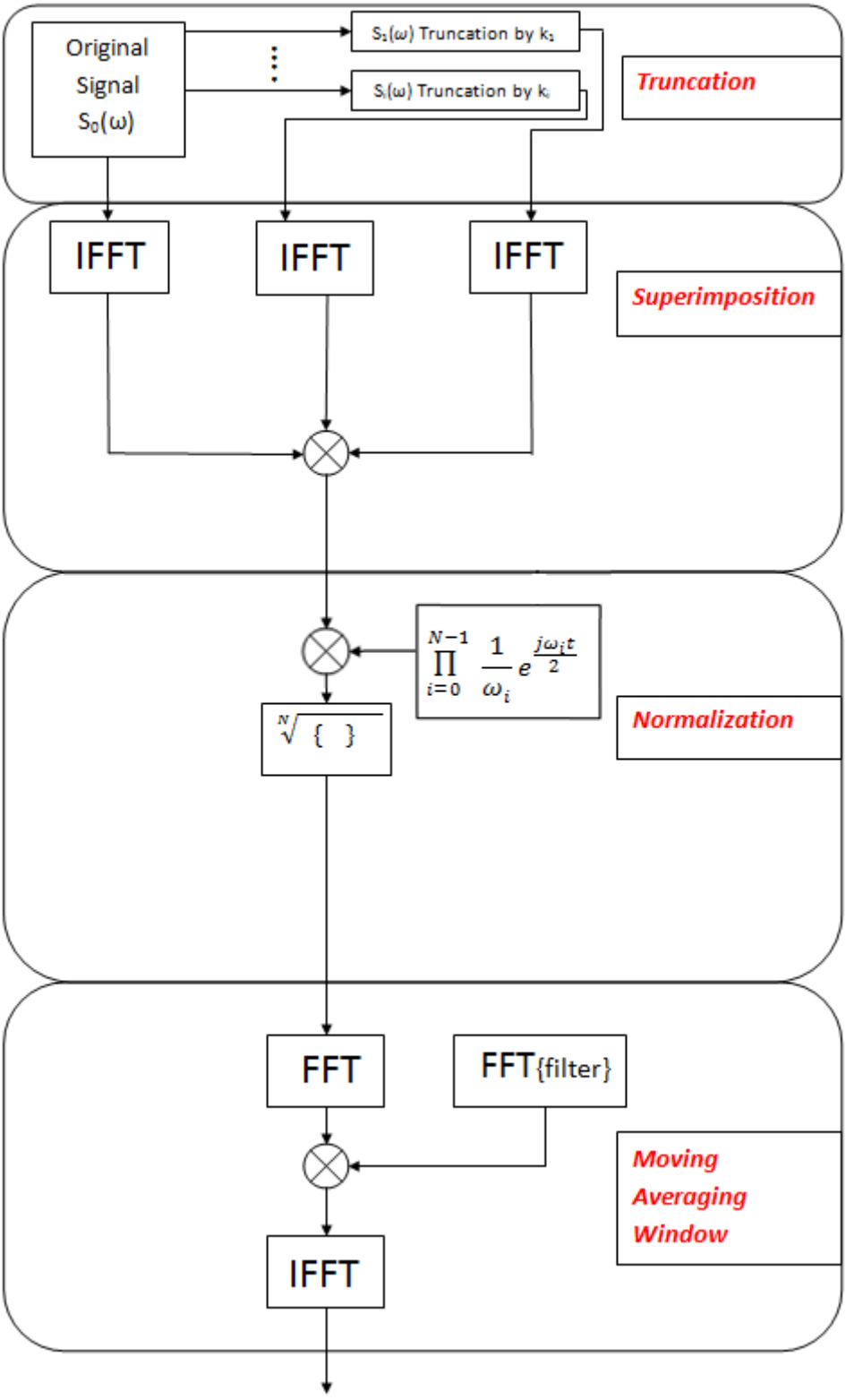

Figure III-21: Block Diagram for the algorithm of IFFT-based Repetitive Superimposition (RSI-N) technique

Finally, The moving average filter, which is mathematically defined as a convolution of the superimposed signal with: $m(t) = (2/\omega_0)\ \mathrm{rect}\{\omega_0 t/2\}$, where $2/\omega_0$ is the width of the main-lobe in the original signal, and the averaged superimposed signal is [54]. In the IFFT-based superimposition process, the moving average filter, just like in the FFT-based superimposition algorithm, is applied as a series of Fourier transforms using the convolution theorem [54] as described in the following equation:

$$s_{averaged}(t) = FT^{-1}\left[FT\left\{s_{superimposed}(t)\right\} \times FT\{m(t)\}\right] \quad \textbf{(Eq. III-42)}$$

6. Chapter Summary

This chapter started by illustrating the major issue of sidelobes in FFT calculations, which is a consequence of the band limitation of the SAR signal, and how even though conventional windowing functions do reduce unwanted sidelobes, they actually widen the main lobe of the targets and hence lower the resolution. After that, a critical review of some of the widely used techniques and solutions has been presented, starting with the MUSIC algorithm that loses the main lobe's original height and requires prior knowledge of the number of targets. Then, SVA and Super-SVA were reviewed. Finally, an introduction to Superimposed-FFT is presented with mathematical analysis and simulation of the methodology using both truncation and windowing techniques followed by newly proposed improved superimposition techniques of RSI and NSI.

Chapter IV: SAR Signal Model & Simulation

1. Introduction

The cost of building a new system is usually quite high and without a proper design, a mismatch might occur between the proposed system and the real-life system delivered. One aspect that is important to be investigated prior to the system implementation is its performance. Thus, simulation programmes are designed in order to examine the performance and characteristics of the proposed method of Superimposition in all its different techniques. The considered model is a basic simulation of a simple SAR using Matlab Software with and without the addition of noise in order to investigate the effect on the Superimposition technique.

2. SAR Matlab Simulation of One Target

A basic FMCW-SAR model is simulated at low frequencies so that the behaviour of the signals is more observable. Starting with the chirp, the model is simulated to run a saw-tooth from 3 kHz to 5 kHz in 5 msec, see Figure IV-1. Both the transmitted and received signals are simulated in a noise-free channel, noise is considered in a later stage of the simulation, and they are presented in Figure IV-2. The received signal is process as described in the previous section and the processed signal is then used to generate two new versions of it, the first one is the truncated signal, which is two-thirds of the original signal, and the second one is the truncated-and-windowed signal, which is the truncated signal being windowed using a Hamming window function, see Figure IV-3. Finally, the signals are transformed into the frequency domain using standard-FFT, standard-Superimposition and Superimposition with Hamming window. The three signals are presented in Figure IV-4, the graph shows noticeable suppression of sidelobes when using the Superimposition technique.

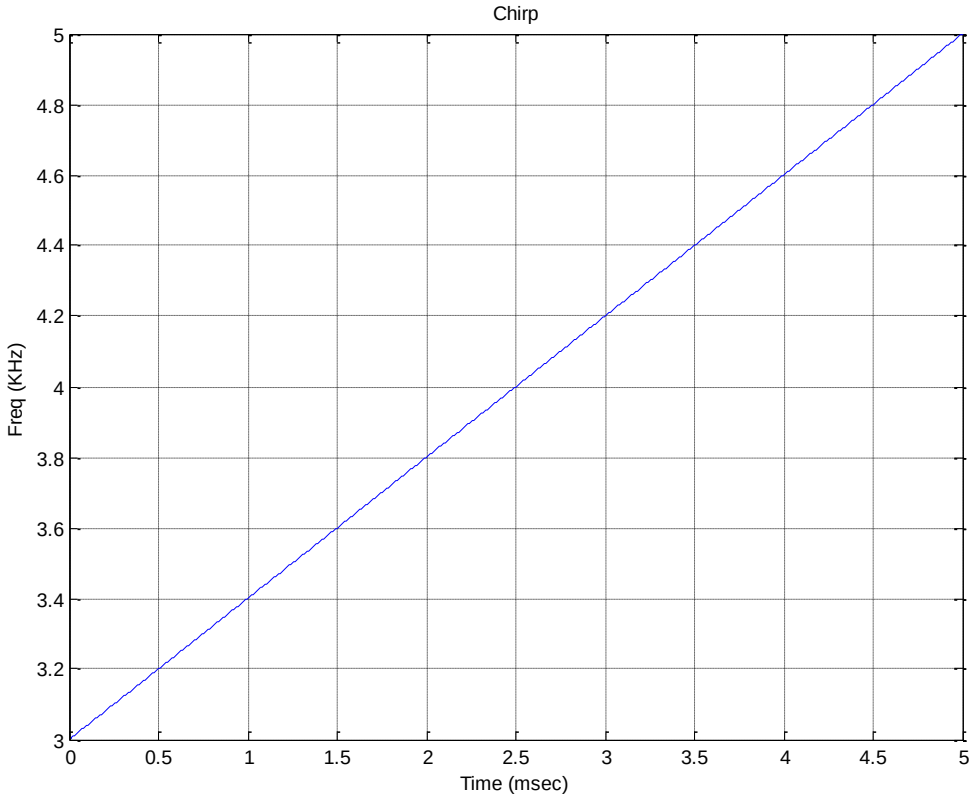

Figure IV-1: Low Frequency Chirp.

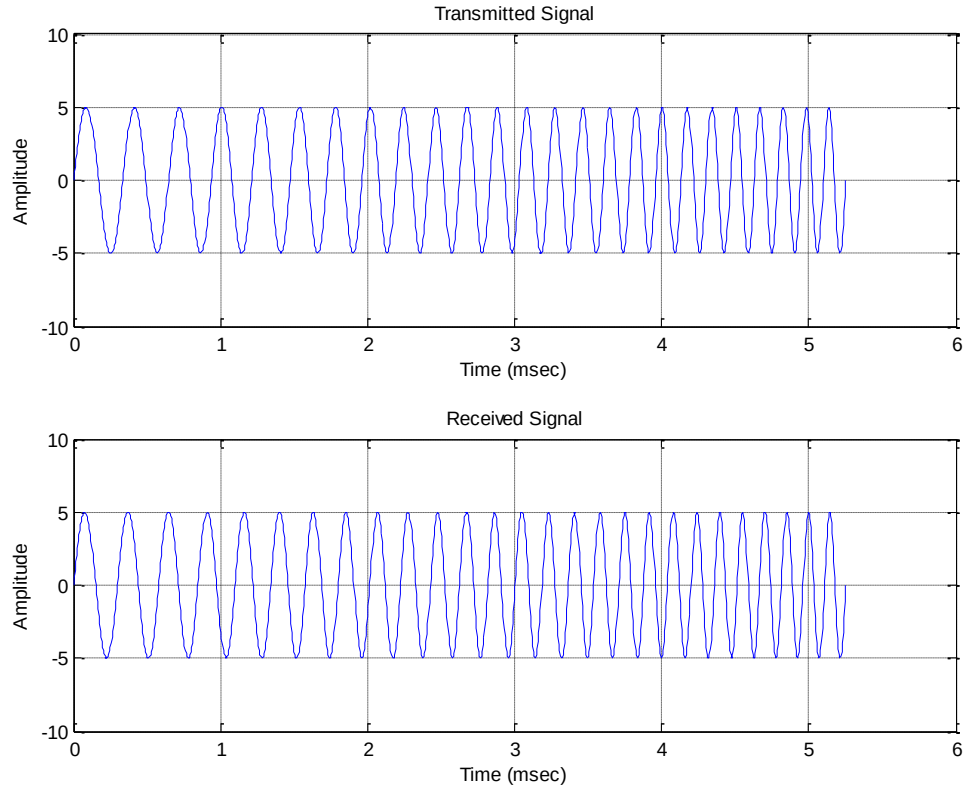

Figure IV-2: Transmitted and received signals in SAR model.

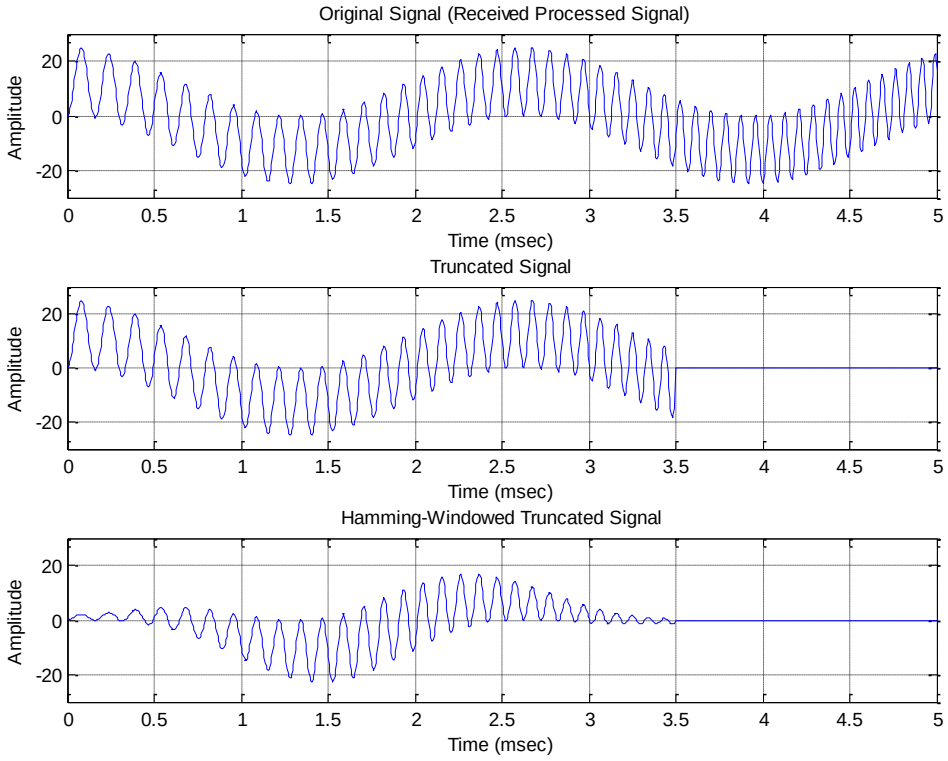

Figure IV-3: Processed received signal (before LPF) and the different versions of it (truncated, truncated & windowed) that is used in the superimposition process.

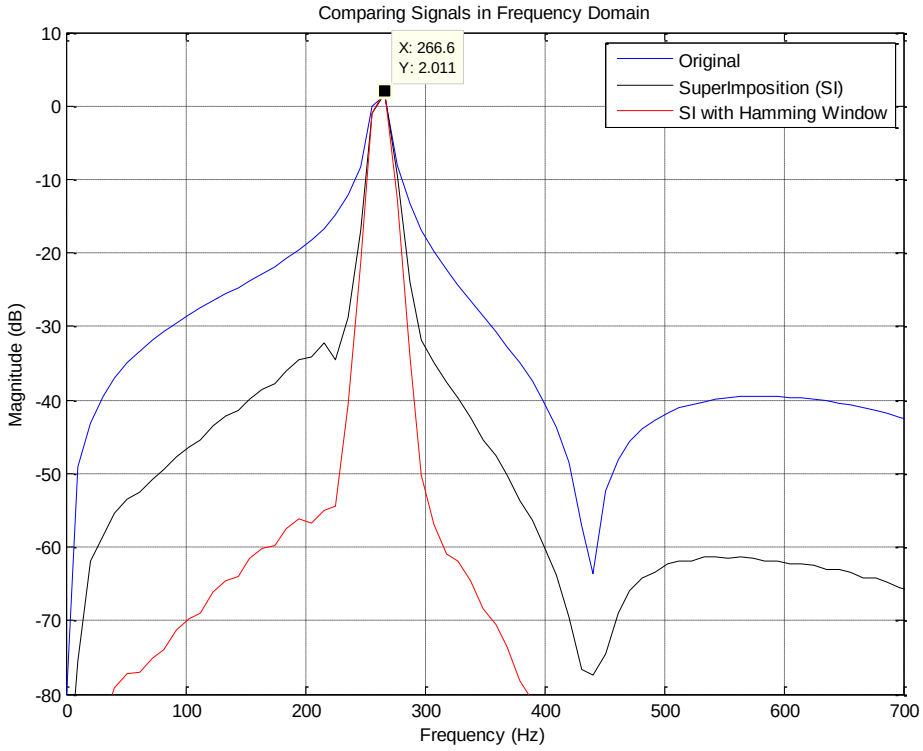

Figure IV-4: Comparing performance of the different techniques: standard-FFT (original), Standard-Superimposition (SI) & Superimposition with Hamming Window.

3. Matlab Simulation of One Target with Noise at Low SNR

The SAR model is then modified to work with high frequencies in order to mimic the performance of real-life SAR. Starting with the saw-tooth chirp, again, that goes from 0.3GHz to 0.5GHz in 5msec. In this simulation, the received signal, which is simulated for one target, is corrupted with multiplicative noise that simulates the effect of constructive and destructive interferences between the returned signal and the different complex returns from the scatterers in a resolution cell where the number of speckles follows a Poisson distribution that has a parameter $\lambda = 1$ that represents the average rate of occurrence, which is the total number of events (k) divided by the number of units (n) in the data ($\lambda = k/n$) [63]. Each speckle is given a random variable for magnitude that follows a Rayleigh distribution with a parameter of one and a uniform variable between $-\pi$ and π for the phase. Furthermore, an Additive White Gaussian Noise (AWGN), which is to incorporate the background radiation and thermal noise of the platform's electronics, is added in time domain, using Matlab built-in function 'AWGN', to have a Signal-to-Noise: SNR=10dB. The simulated signal is truncated by a third as the first sidelobe is the one being targeted for suppression. Then both of the original and truncated signals are transformed to the frequency domain using the FFT and then they were superimposed by multiplying operation in the Frequency Domain. Finally, a moving averaging window of 400Hz width has been applied to smooth the sidelobes.

A comparison between the original signal and the superimposed signal is shown in Figure IV-5. The new sinc signal is about 10dB lower at the first sidelobe, which means that it is not mistaken for a false target and the main-lobe is more clearly recognized. The same process is repeated starting with the simulated radar received signal reflected from a target after going through a channel with multiplicative and additive noise, however, this time the truncated signal is windowed using a Hamming window function. The three signals have been fed to the simulation code in order to generate the sinc function of the target in the frequency domain. It can be noticed that even though the superimposed (without windowing) signal has a well suppressed first sidelobe, the new signal from superimposition with windowing has better suppression in terms of a few dBs.

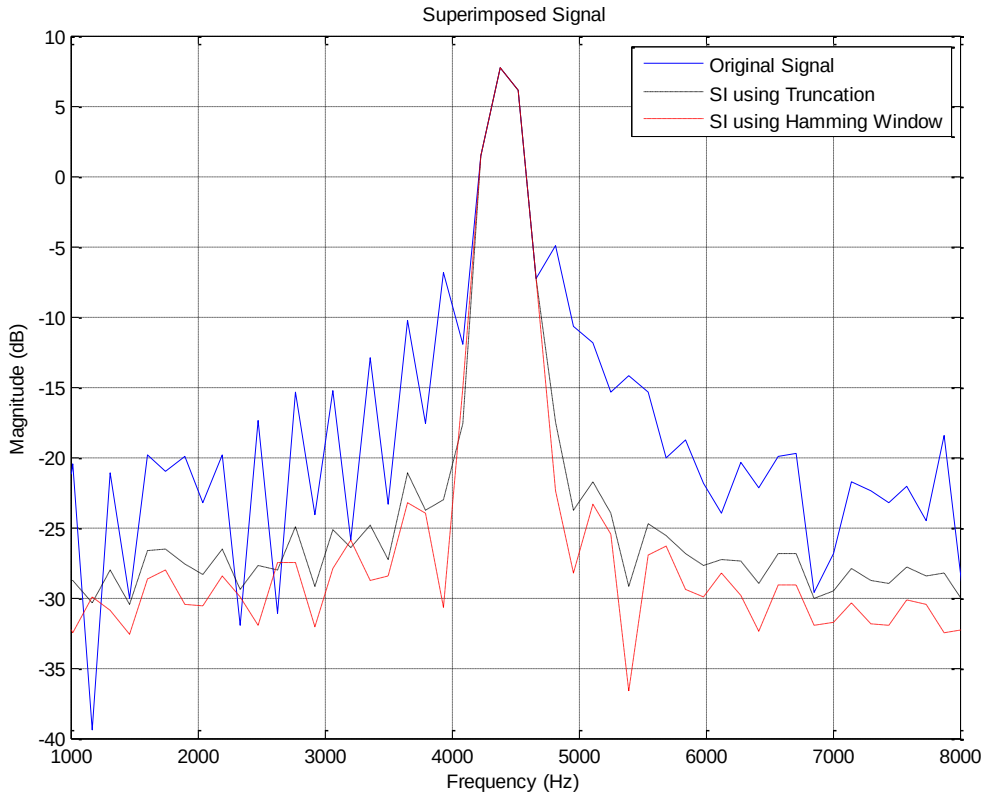

Figure IV-5: Comparing Original Signal, Superimposed signal (using Truncation) and Superimposed signal (using Hamming Window)

In general, the Signal-to-Noise (SNR) of the received signal must be high enough to obtain a quality signal at the receiver that can be used to identify clear and resolvable targets. SNR can be increased by raising the average transmitted power by raising the peak power. However, the physical limitations in implementations usually constrain the increase of peak power. Hence, despite the fact that increasing the length of transmit-event is usually in conflict with resolution [4], in real-life designs it is common to increase the length of the transmitted signal. Nevertheless, a pulse compression, using signal processor, is used to compress it back to the desired resolution [4].

A simulation has been conducted in order to see the effect of low SNR on the quality of the Superimposition technique. The same simulation in the previous section has been conducted again but with low SNR value of 0 dB, as oppose to the 10 dB that was used in the previous simulation, by adding AWGN to the original signal:

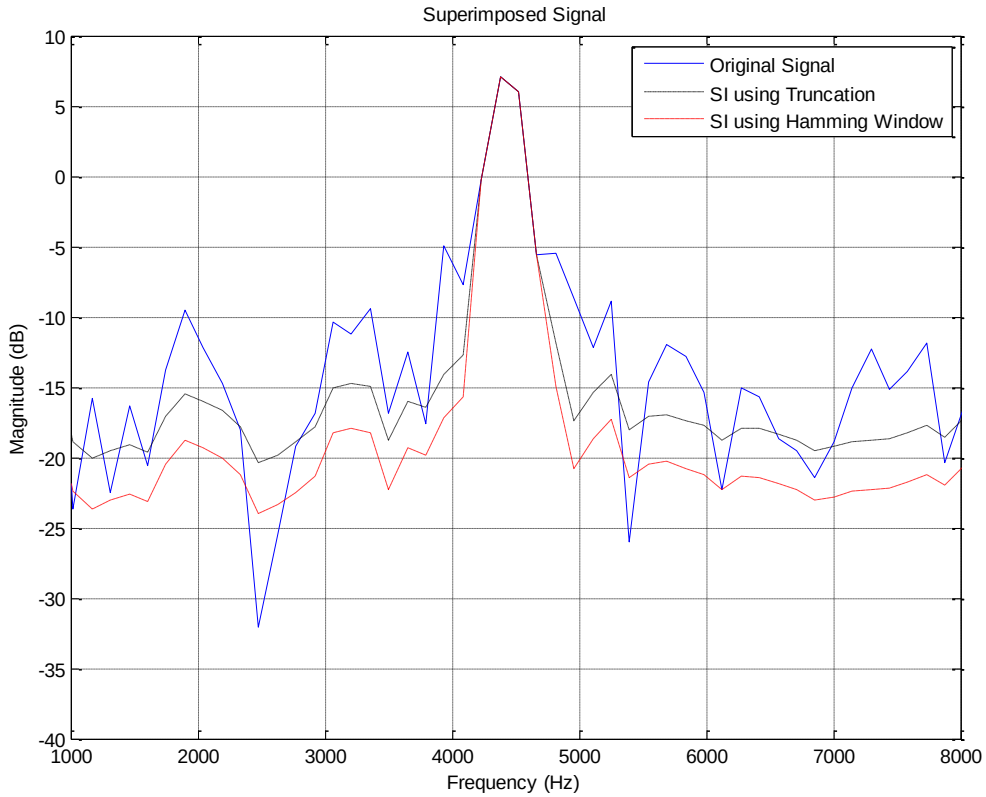

Figure IV-6: Comparing Original, Superimposed and Superimposed (with Hamming Window) at SNR=0dB

When comparing Figure IV-5 with Figure IV-6, it can be noticed that the sidelobes have been raised about 10dB. Hence, the sidelobes might be mistakenly identified as a false target. The performance of the Superimposed-FFT technique is still relatively better than the traditional-FFT. However, it is noticed that the performance of the superimposition technique degraded in a higher ratio than the degradation that happened to the original technique. The more robust techniques of improved Superimposition (i.e. RSI and NSI) combat this effect as discussed in section 6 of this chapter.

4. Matlab Simulation of Two Targets without Noise

The same system that is used in the previous section is developed to include two targets instead of only one. However, no noise is used in this simulation. The same procedure in f-space is followed to simulate the signal from two targets that are relatively far apart as shown in Figure IV-7. Expanded figures that compare the different techniques for both targets separately are presented in Figure IV-8 and Figure IV-9. It can be clearly noticed that the superimposition with window function is significantly superior to the other techniques especially in the last scenario when the two targets are closely positioned, see Figure IV-10.

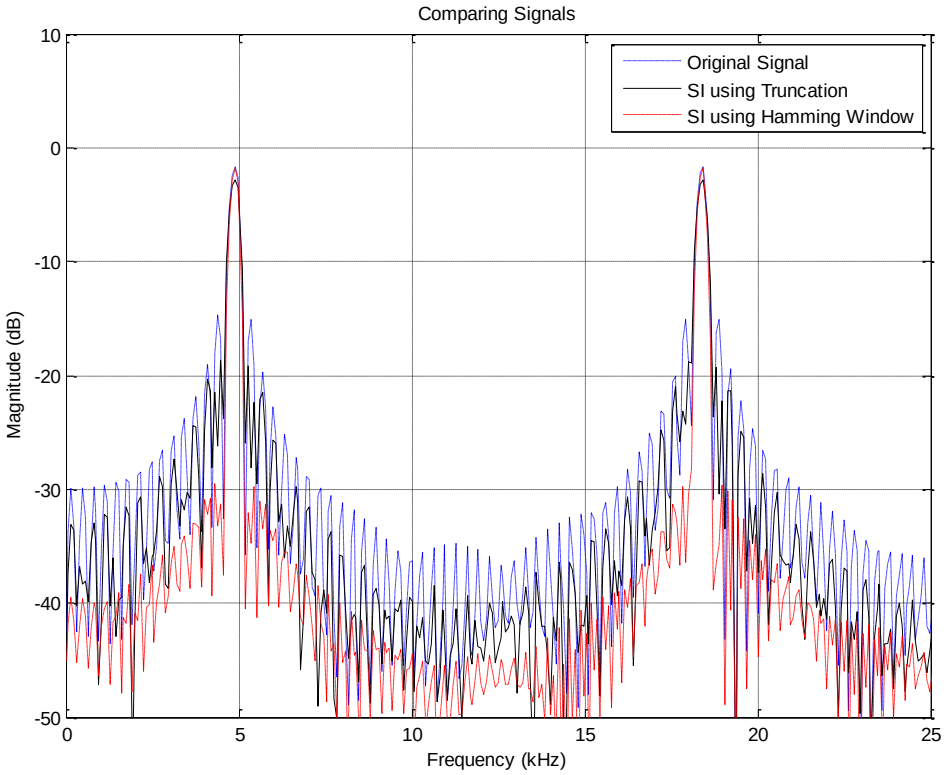

Figure IV-7: Comparing Original Signal, Superimposed and Superimposed (with Window) for 2 Targets

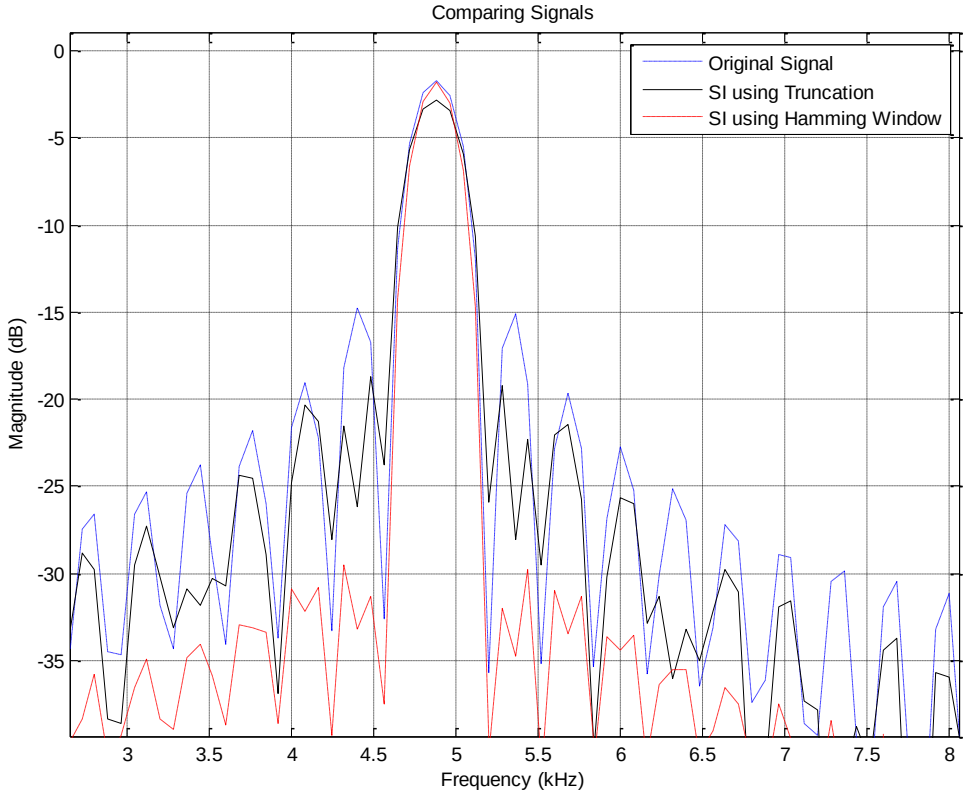

Figure IV-8: Comparing Original Signal and Superimposed Signal using Truncation at 1st main-lobe

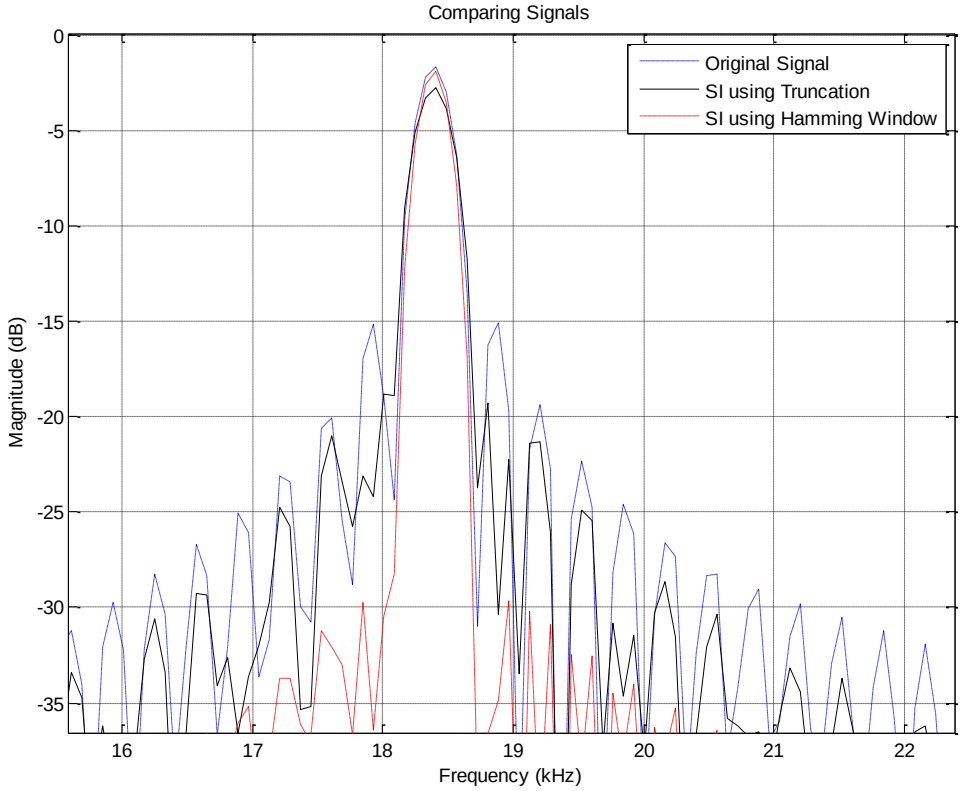

Figure IV-9: Comparing Original Signal and Superimposed Signal using Truncation at 2nd main-lobe

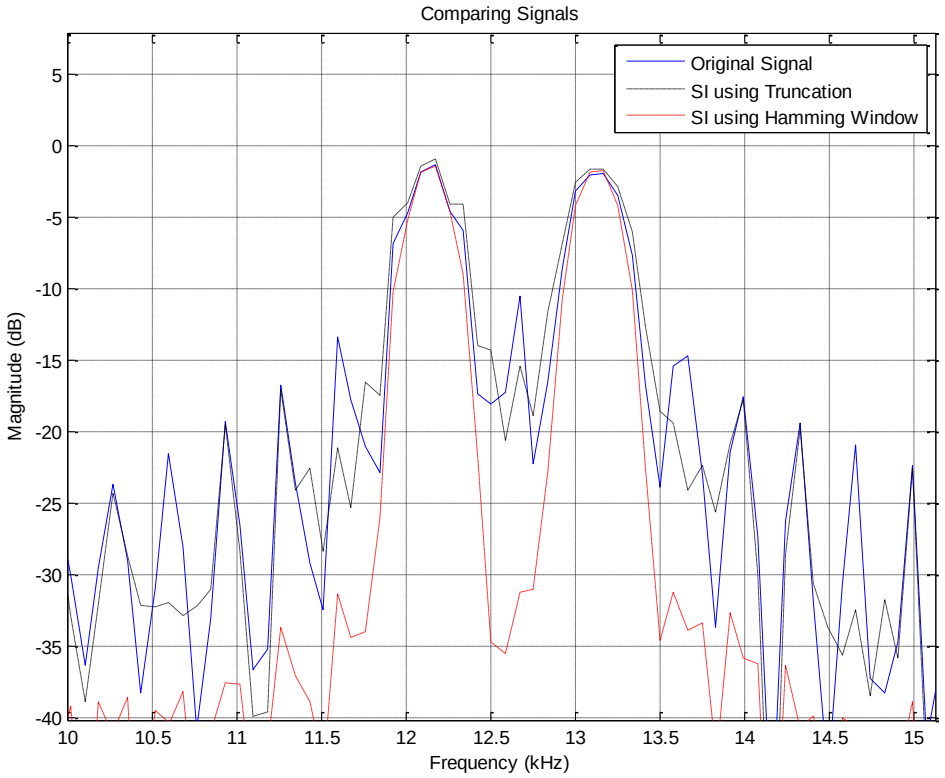

Figure IV-10: Comparing Original Signal, Superimposed and Superimposed (with Window) for 2 Targets

5. Matlab Simulation of MUSIC Algorithm

The MUSIC algorithm has also been simulated in order to test it against the proposed technique of superimposition. The same basic radar signal of one target, explained in section 3, is fed to a MUSIC built-in function in Matlab. The outcome is shown in Figure IV-11. It can be noticed that even though the MUSIC algorithm provides higher resolution, it requires pre-knowledge of the number of targets. Furthermore, it loses all information related to the amplitude of the original signal.

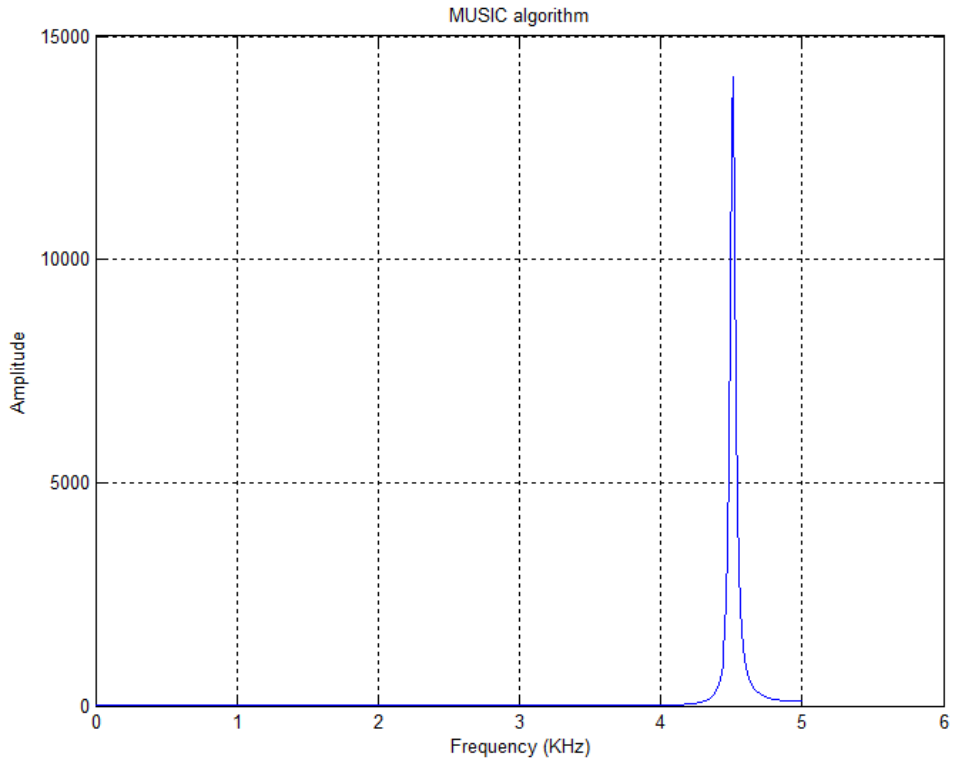

Figure IV-11: MUSIC algorithm, seeded with one target, outcome of original signal

After that, the radar signal of two targets is simulated using the MUSIC algorithm where it also produced a good result as shown in Figure IV-12. However, bearing in mind that the MUSIC algorithm needs to be seeded with the number of targets prior to implementation, this causes it to find the indicated number of targets regardless of the number of real targets that are actually present. So, if the number of target was set to four, then four targets, regardless if they exist or not, are generated [119]. In order to demonstrate this inaccuracy, two independent simulations using different noise sequences as shown in Figure IV-13 and Figure IV-14, is used. It can be noticed that the correct targets are fixed (in position) while the false targets are moving around with different noise sequences [119].

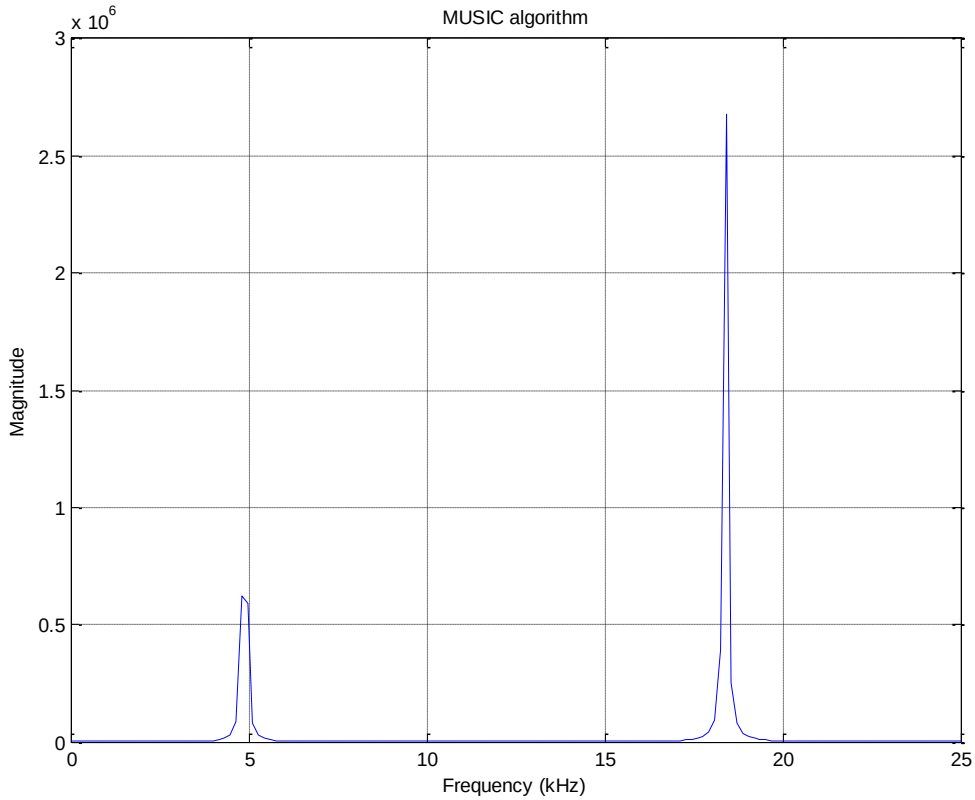

Figure IV-12: Outcome of MUSIC algorithm, seeded with number of targets to be 2, for Signal of 2 Targets

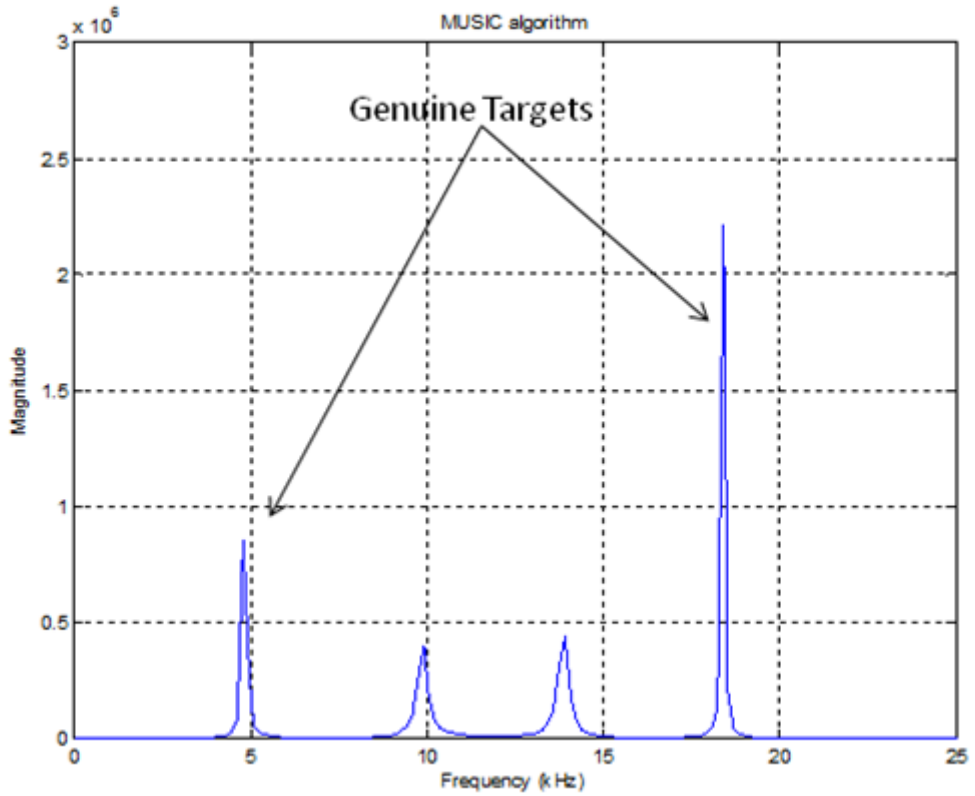

Figure IV-13: Outcome of the MUSIC algorithm simulation that is seeded with 4 targets for received signal of 2 genuine Targets with noise sequence added.

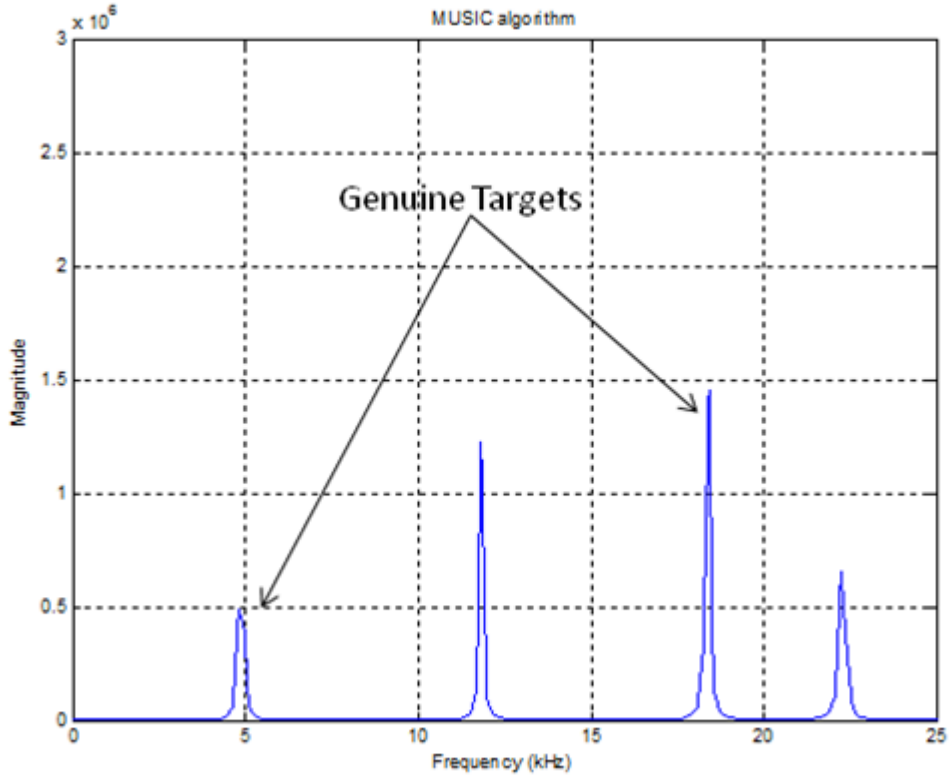

Figure IV-14: Outcome of the MUSIC algorithm seeded with 4 targets for a received signal of 2 genuine Targets with a different noise sequence to that used in Figure IV-13.

Finally, in the scenario when both targets are relatively close to each other, the superiority of the superimposition technique with a Hamming window function becomes clearer when compared to the MUSIC algorithm as shown in Figure IV-10 and Figure IV-15. Here it can be noticed that with the presence of these three peaks, i.e. the two main-lobes and the elevated sidelobe between them, the MUSIC algorithm produced a single wide target and the second target is not resolvable.

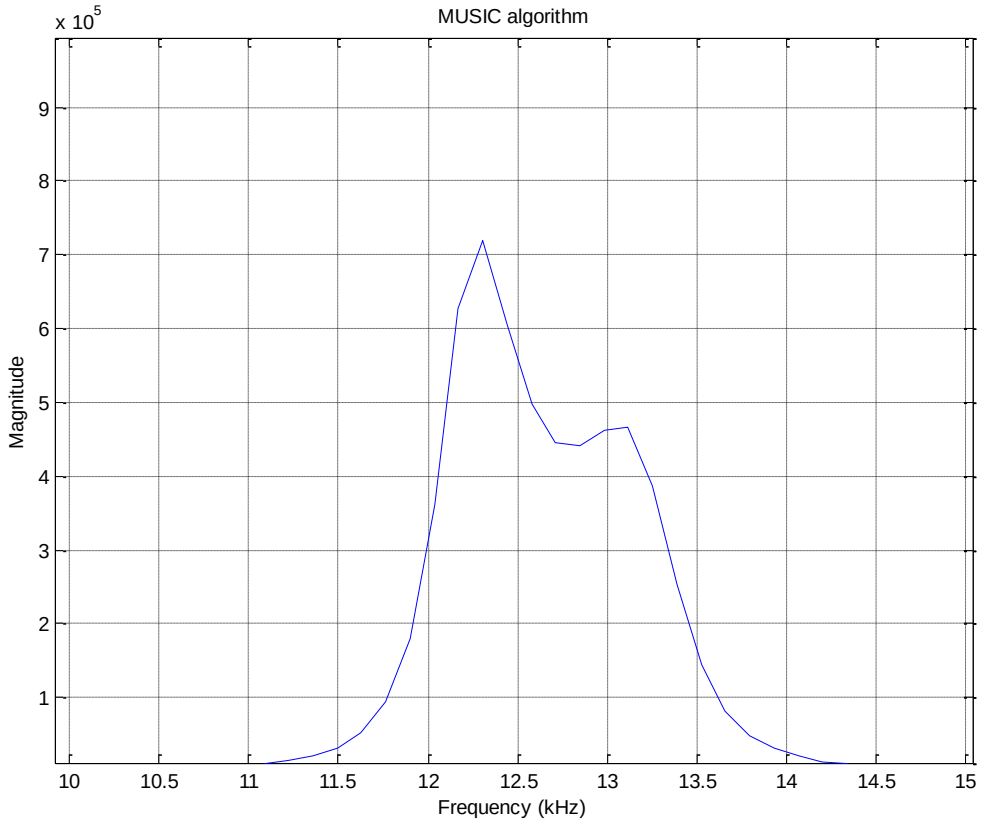

Figure IV-15: Outcome of MUSIC algorithm, seeded with number of targets to be 2, for Signal of 2 closely-positioned Targets at 12.2 kHz and 13.2 kHz

6. Matlab Simulation of Two Targets with Noise

This section presents an investigation of the ability of the Repetitive Superimposition technique (RSI) and the Normalized Superimposition technique (NSI) in particular to combat noise. It is worth recalling that the main difference between the RSI and the NSI is the use of multiplication-and-rooting process in RSI as opposed to the mathematical normalization process, which emphasizes the similarity of the integrated signals, in NSI. The same scenario described in section 4 is re-simulated but with the presence of both multiplicative and additive noise. The multiplicative noise is simulated to have a Rayleigh distributed magnitude and a phase that is uniformly distributed between $-\pi$ and π. The additive noise, on the other hand, is simulated using the Matlab built-in function of 'awgn' that can tune the signal, after incorporating the multiplicative noise, to have a specific SNR. The simulation has been conducted at 0dB SNR.

Concerning the RSI and the NSI techniques, four signals are used in the superimposition process. The number of signals is selected for the purpose of comparing the different procedures used in each technique in a unified setup; more simulation and discussion about the selection of the order of RSI and NSI is discussed in the next chapter. The first of these four signals is the complete original signal and the other three are truncated-and-windowed versions that are designed to have a zero crossing at the centre of the first three sidelobes. Hence, the techniques are denoted as RSI-4 and NSI-4. The system starts by simulating the signals that are generated using standard-FFT, RSI-4 and NSI-4 before the noise is applied, which are presented in Figure IV-16. The same signals are presented again with the use of a moving average window function of width 2 kHz, see Eq. III-18, and the result is shown in Figure IV-17. After that, both multiplicative noise and additive noise are inflicted on the signals as shown in Figure IV-18. And again, a moving average window function is applied and its effect on the signals is presented in Figure IV-19.

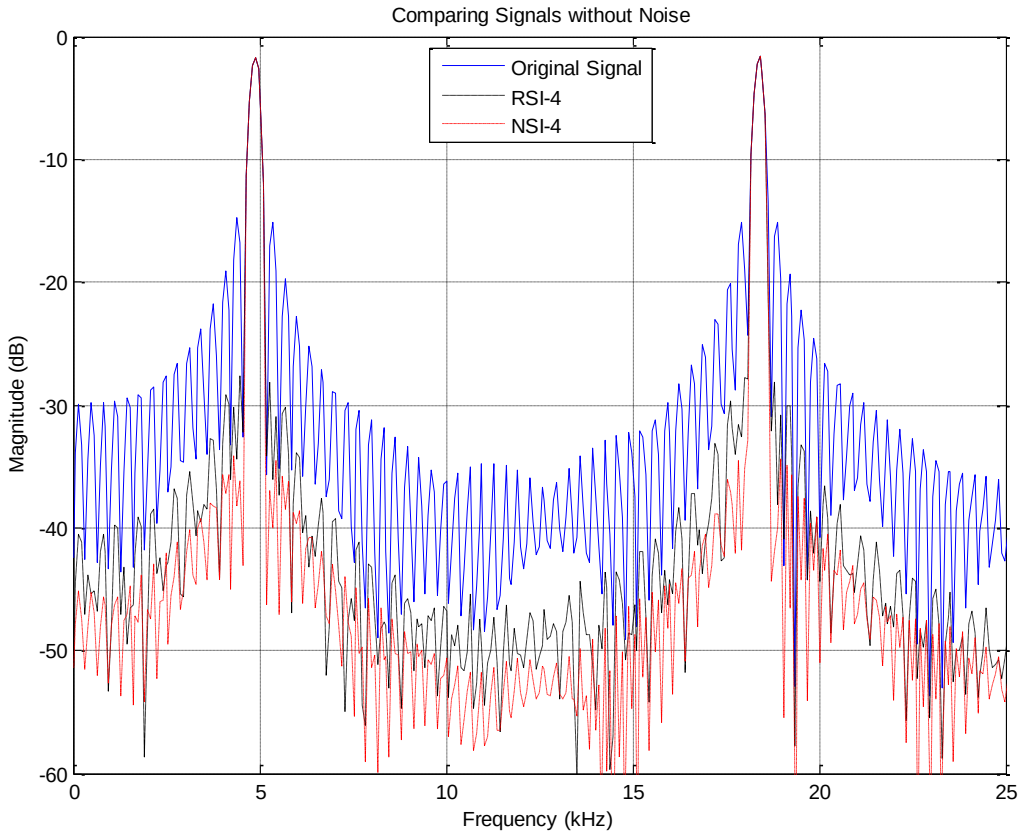

Figure IV-16: Comparing standard-FFT, RSI-4 and NSI-4 before applying the noise

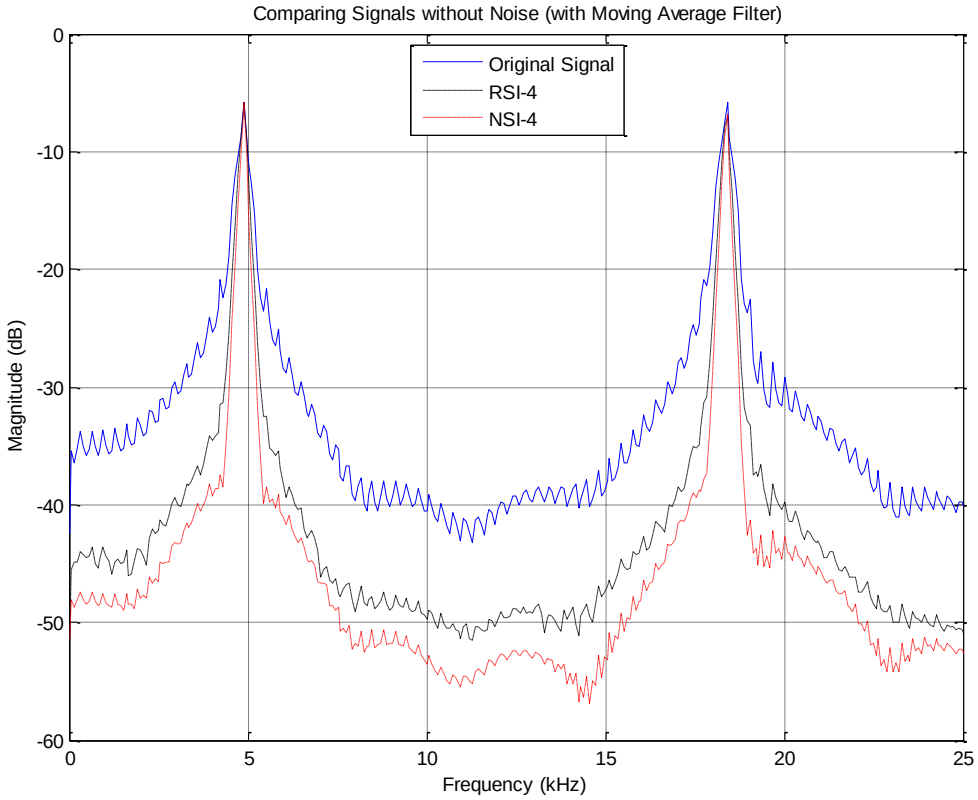

Figure IV-17: Applying moving average function – of 2 kHz width – to the different techniques of standard-FFT, RSI-4 and NSI-4

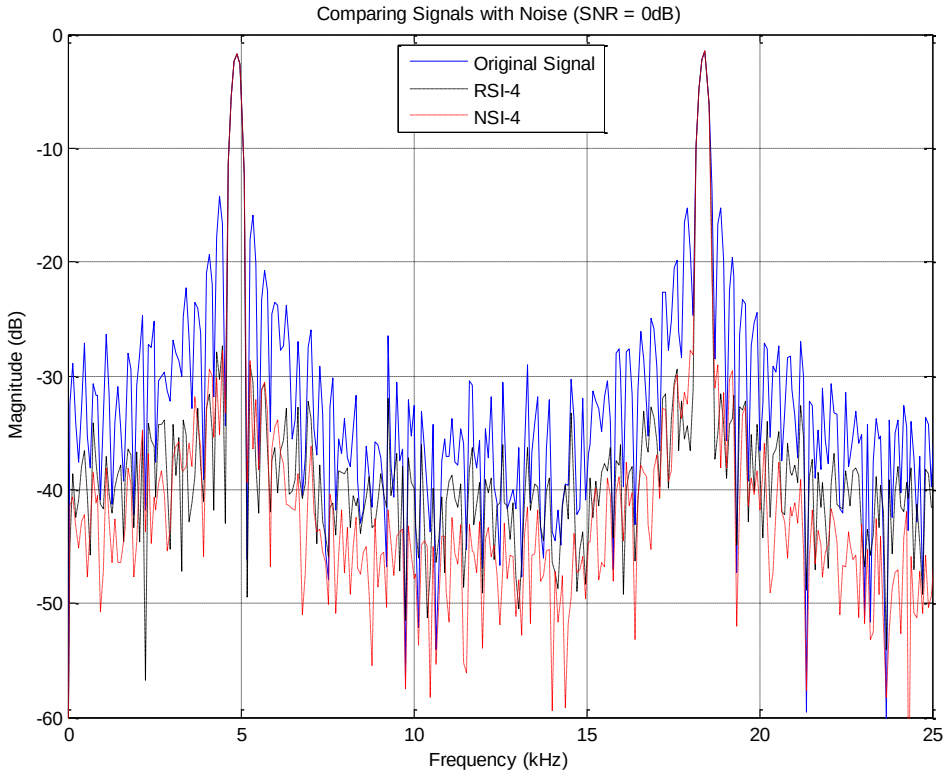

Figure IV-18: Comparing standard-FFT, RSI-4 and NSI-4 in the presence of noise at SNR = 0dB

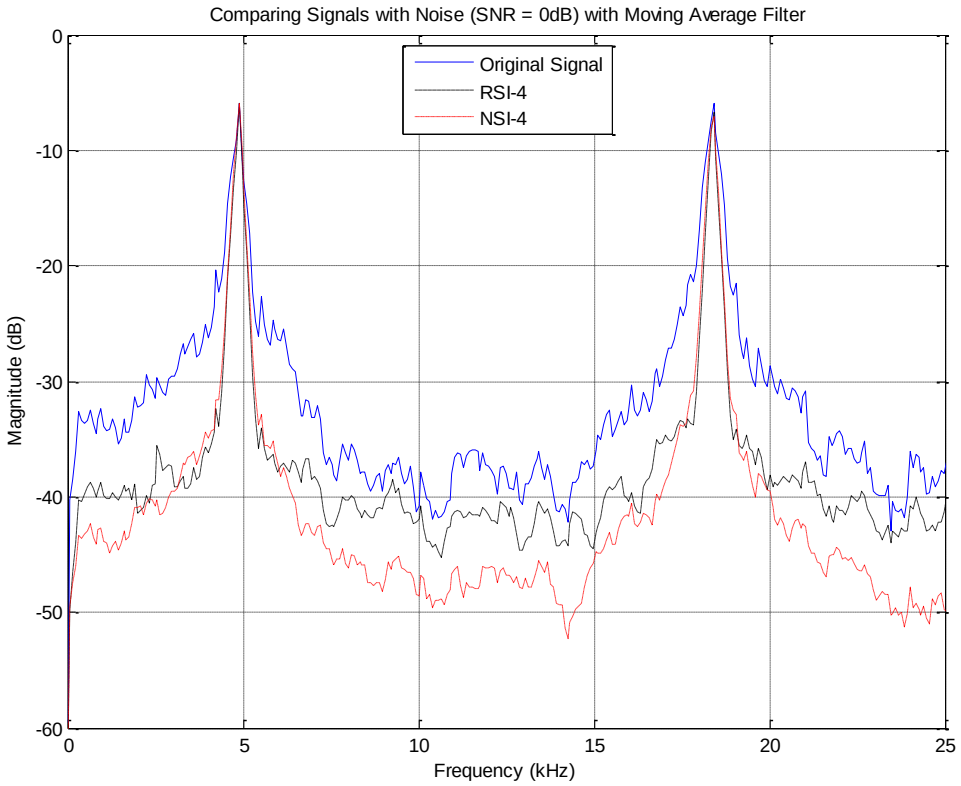

Figure IV-19: Applying a moving average – of 2 kHz width – to the outcomes of the different techniques of standard-FFT, RSI-4 and NSI-4 in the presence of noise at SNR = 0dB

In this simulation, four different scenarios have been considered:

+ Scenario 1: Using signals with the same noise sample.

In this scenario, the original signal with its original noise sample is truncated with different calculated ratios to align sidelobes' maximum points of the original signal with minimum points of the truncated versions and each of the truncated signals is superimposed on the original one.

+ Scenario 2: Using signals with different noise samples.

In this scenario, the original signal is simulated with different noise samples. Each version of the original signal with its unique noise sample is truncated with different calculated ratios to align sidelobes' maximum points of the original signal with minimum points of the truncated versions and each of the truncated signals is superimposed on the original one.

In the following two scenarios, half of the truncated signals used in RSI-4 and NSI-4 are conjugated and then superimposed on the original signal, as discussed in Eq. III-36 and Eq. III-38.

+ Scenario 3: Using conjugate signals with the same noise sample.

In this scenario, the original signal with its original noise sample is truncated with different calculated ratios to align sidelobes' maximum points of the original signal with minimum points of the truncated versions. Each version of the truncated signals is conjugated and then superimposed on the original signal.

+ Scenario 4: Using conjugate signals with different noise samples.

In this scenario, the original signal is simulated with different noise samples. Each version of the original signal with its unique noise sample is truncated with different calculated ratios to align sidelobes' maximum points of the original signal with minimum points of the truncated versions. Each version of the truncated signals is conjugated and then superimposed on the original signal.

In each of these scenarios, one original signal in the time domain is simulated without noise and another two signals are simulated with noise, which can be either the same noise sample or different noise samples for the two signals depending on the scenario being adopted. Then, all of the simulated signals are transformed to the frequency domain using each of the three techniques mentioned earlier.

Finally, the residual noise for each scenario is calculated by subtracting the noise-free signal from the NSI-4 output signal, the RSI-4 output signal and the standard-FFT output signal, which is referred to as Original Signal. Intuitively, the standard-FFT technique uses only one signal and is considered as a reference for the other technique since it remains almost the same in all the different scenarios, as a slight change is observed due to the different noise samples used in each of simulations. The average residual noise of the original signal is found to be -28dB. The residual noise outcome traces from each of the four scenarios listed previously are presented in Figure IV-20, Figure IV-21, Figure IV-22 and Figure IV-23 respectively.

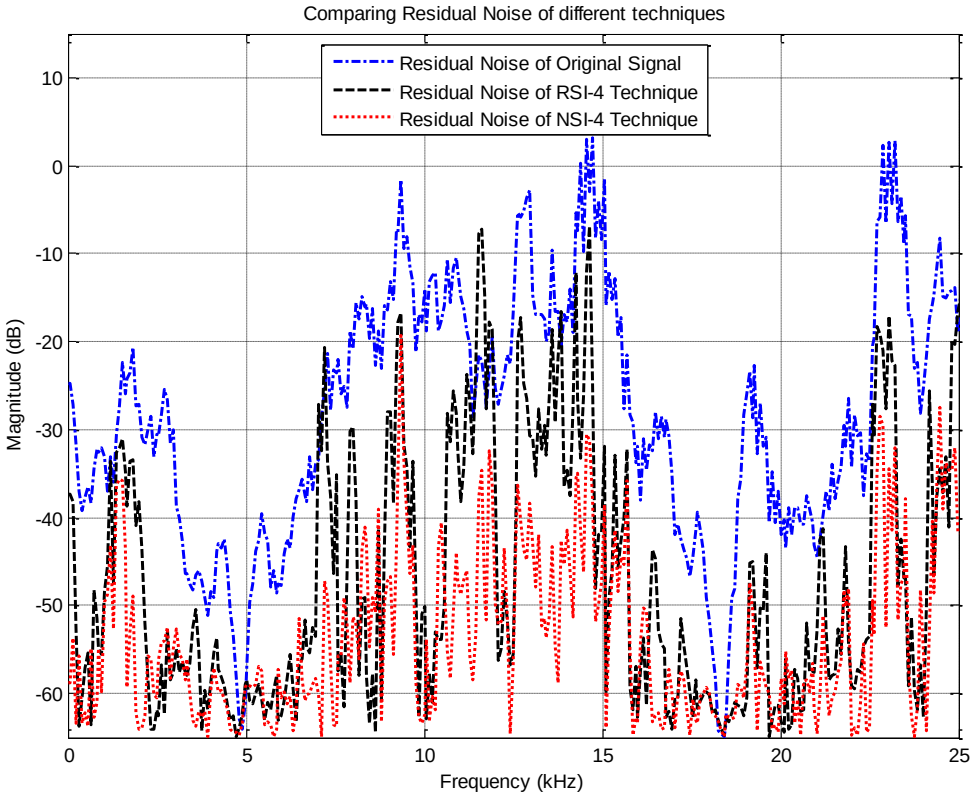

Figure IV-20: Residual Noise in scenario 1: using signals with same noise sample

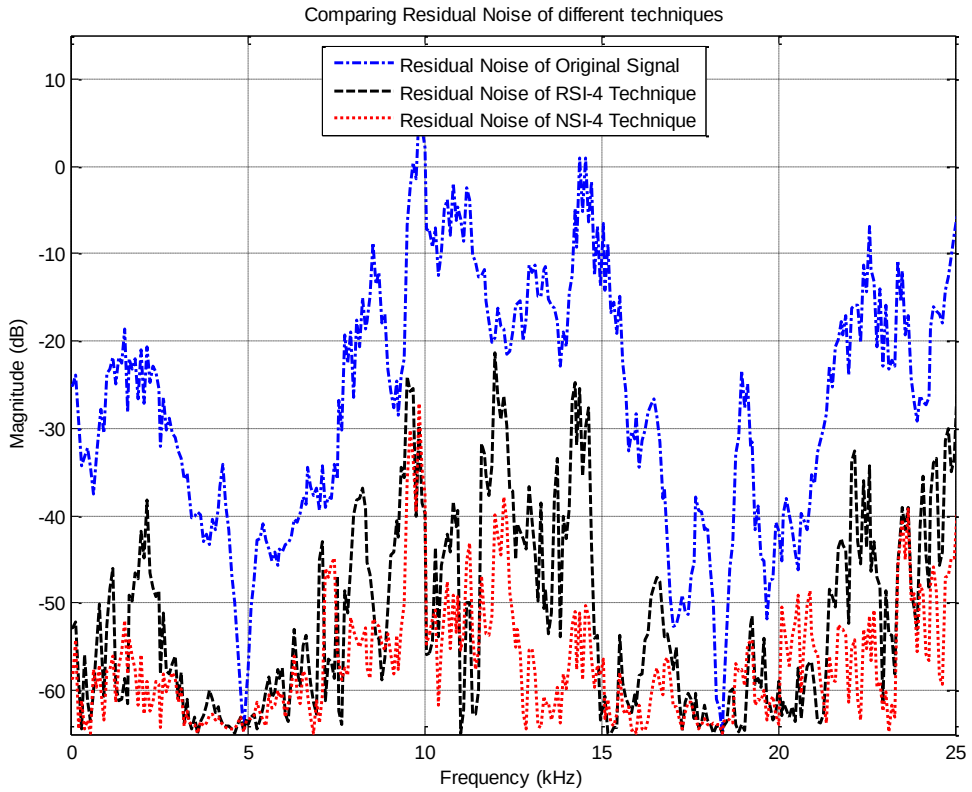

Figure IV-21: Residual Noise in scenario 2: using signals with different noise samples

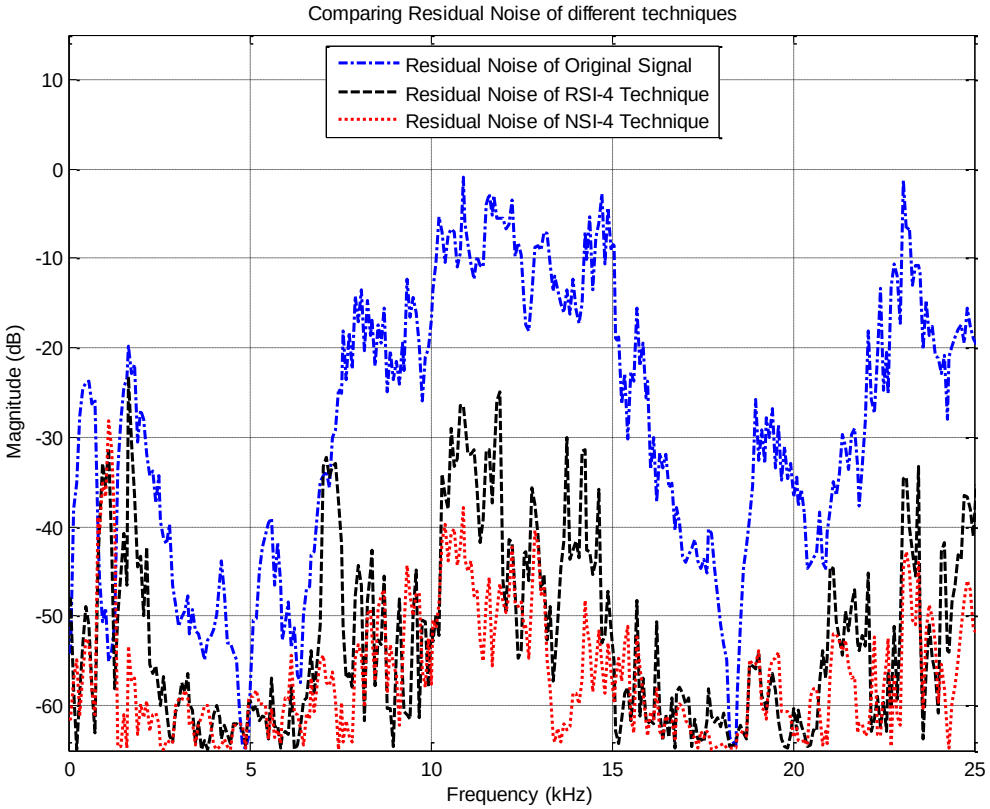

Figure IV-22: Residual Noise in scenario 3: using conjugate of signals with same noise sample

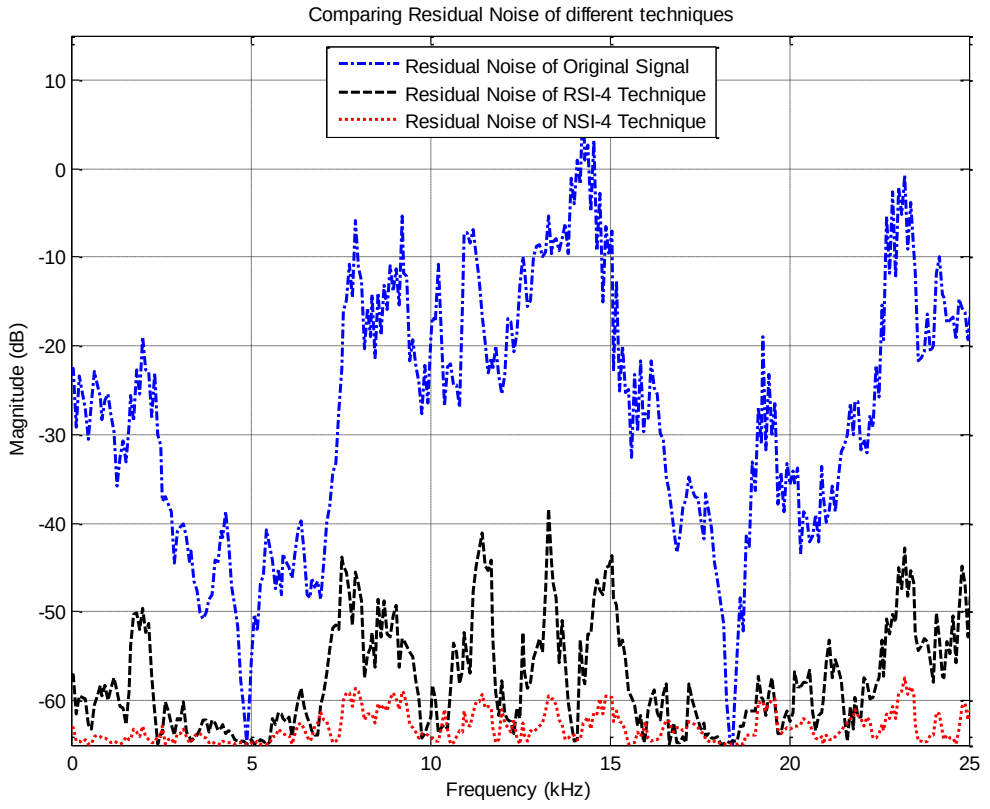

Figure IV-23: Residual Noise in scenario 4: using conjugate signals with different noise samples

Table IV-1: Average residual noise values for RSI-4 and NSI4 techniques in all scenarios

Scenario/ Technique	Residual Noise of: RSI-4 Technique	Residual Noise of: NSI-4 Technique
Scenario 1: Using Signals with same noise sample	-37.3dB	-46.1dB
Scenario 2: Using Signals with different noise samples	-50.4dB	-57.8dB
Scenario 3: Using conjugate Signals with same noise sample	-47.6dB	-56.9dB
Scenario 4: Using conjugate Signals with different noise samples	-54.8dB	-62.7dB

The average residual noise values are shown in Table IV-1. A number of observations have been noticed from the simulation outcome of the different scenarios:

1) There is a noticeable reduction of noise when using input signals that have independent noise samples to the superimposition model. So, in the case of superimposing, using the different noise samples (scenario 2) is resulting in more than 10dB less of residual noise, for both RSI and NSI techniques, than using the same noise sample (scenario 1). On the other hand, in the case of applying conjugate process, the difference between using the same noise sample (scenario 3) and a different noise sample (scenario 4) is about 7dB for both RSI and NSI techniques.
2) The impact of using the conjugate of the signals, which is similar to the process used in matched filters to combat noise [62], on suppressing the noise by about 10dB in the case of using same noise sample (scenarios 1 & 3) while it is only about 6dB in the case of different noise samples (scenarios 2 & 4).
3) By using the conjugate of the signals that have independent noise samples in the superimposition process (scenario 4), the noise is reduced by more than 16dB in both NSI and RSI techniques.
4) By using the conjugate, a narrowing effect on main-lobe has been noticed in the RSI technique and the effect is even more visible in the NSI technique.
5) In all the scenarios, the NSI technique outperforms the RSI technique by more than 7dB. This might be due to the fact that the RSI technique depends on applying direct superimposition while the NSI technique does the normalization process that emphasizes on the similarities between the considered signals, bearing in mind that when applying truncation and windowing, the only similarity – at least in theory – is the peaks of the main lobes.

6) Finally, It noticed, in all the scenarios, that the residual noise at 5 kHz and 18 kHz drops sharply, which is intuitive as this behaviour is due to the high signal power at these frequencies and hence the noise signal is ineffectual on the original signal.

i. Pure Noise Simulation

Interestingly, this noise suppression effect of superimposition techniques vanishes when applied to a pure noise signal. This might be due to not having sinc-like main-lobes that is used by the superimposition techniques to align zero-crossing points with maximum points of the sidelobes and hence suppresses sidelobes with the embedded noise signal in them. A simulation of a pure noise signal, which is generated with a power of 0 dBV with respect to 1Ω, is presented in Figure IV-24. This signal is averaged using both conventional averaging technique of four noise signals with independent noise samples, RSI-4 and NSI-4 techniques using scenario 4 described earlier in this section. Each one of the traces is a median of 1000 simulation of different traces with different noise samples in order to have a smooth trace that gives a clear indication to the level of noise. It is worth mentioning that the median, which gives a clear indication to the noise's central tendency [124] for each technique, is used in order to have a clean trace without the fluctuations of the trace generated using a single simulation. While the average and median can be the same or nearly the same, they are different if more of the data values are clustered toward one end of their range and/or if there are a few extreme values [124]. In statistical terminology, this is called skewness. The results show that noise is reduced by 6.1 dB when averaged using 4 noise signals. When the same process is re-simulated using 100 different noise signals with independent noise samples, the superimposition techniques of RSI-100 and NSI-100 are still producing the same outcome as simple averaging of 100 noise signals as the noise level is reduced by 19.8 dB.

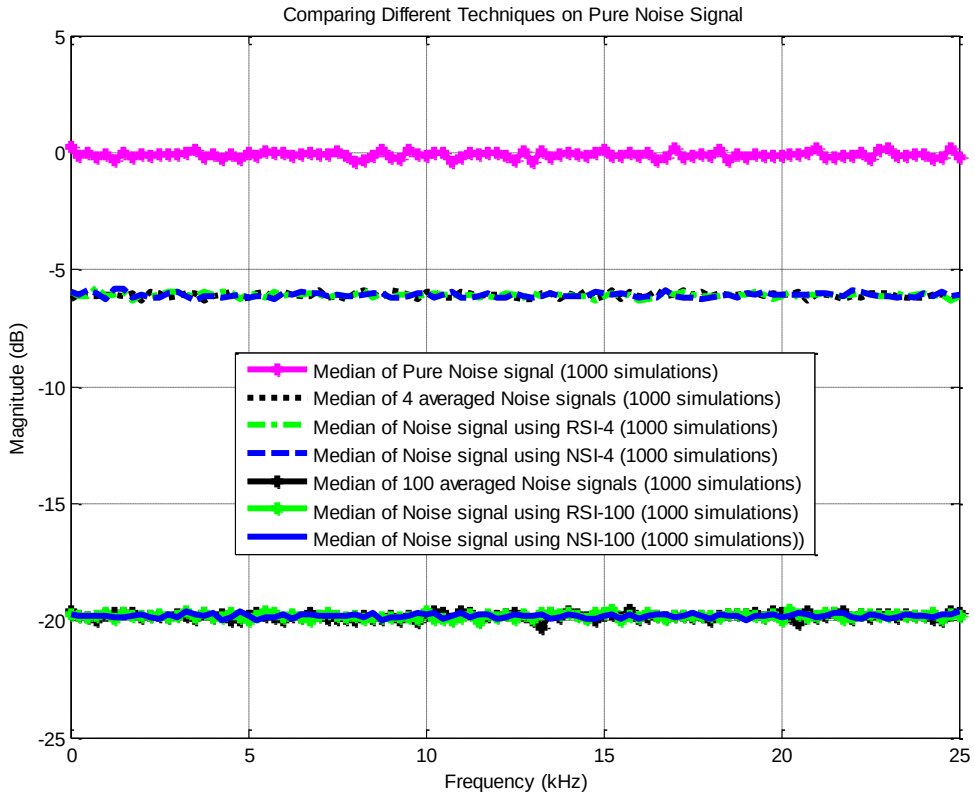

Figure IV-24: Comparing the effect of Averaging and Superimposition (NSI and RSI) on pure Noise signal

7. Simulating Distributed Targets in SAR

Distributed targets are often modelled as a finite number of discrete scatterers contained in each resolution cell, as explained in section 13 of Chapter 2. As the wave interacts with the target, each scatterer contributes a backscattered wave with a phase and amplitude change [125]. However, the individual scatterers are on much smaller scales than the resolution of the SAR. This simple discrete scatterer model is capable of much elaboration, forming the basis of the Neumann series expansion and approaches springing from it, such as the Born and distorted Born approximations [126]. These distributions apply to each speckled pixel in the scene, which is usually assumed to have constant backscattering coefficient. The implications of this speckle model are important as phase is of no importance for a single image of distributed target and instead only amplitude, log or intensity data are used [4].

The distributed target is simulated as a series of subpulses where each subpulse is a single response from a point reflector that is part of the distributed target. It is worth mentioning that in reality, the SAR data is usually oversampled and the pixels of the SAR image are correlated. Hence, based on the dispersed behaviour of a distributed target, the

subpulses are simulated to be reflected one by one so that each subpulse in the transmit-pulse defines a range bin [98]. So, when the first subpulse disperses a range cell to arrive at the second range cell in a distributed target, the second subpulse arrives at the first range cell. Both echoes of the subpulse are reflected at the same time. For the next subpulse duration, when the first subpulse disperses from the second range cell to the third, the second subpulse moves from the first range cell to the second and the third subpulse arrives at the first range cell. Besides, the echoes of these subpulses are reflected simultaneously, and so forth. The dispersing behaviour does not terminate until all subpulses pass through the distributed target area. However, with the approach taken in simulating this problem, the scene (a distributed target) is represented by as many point targets as cells, each with a defined position and RCS. It is important to keep in mind that since the RCS of a particular target depends on the orientation, material used and size of the target, each of these point targets – in real-life measurement – would be replaced with different reflectivity values, depending on the area of a cell occupied by the target. Although according to the assumption of uniform target reflectivity, the cells are simulated to have the same RCS values.

i. Simulation of a Distributed Target

A simulation of a distributed target is conducted where a number of scatterers with constant magnitude, which are named "rectangular distributed echo" in the literature, are equally spaced from each others [98]. SAR signals are then simulated using both standard-FFT and superimposed-FFT utilizing the NSI-4 algorithm. The simulation of 10 scatterers that are relative widely spaced for both standard-FFT and NSI-4 signals are presented in Figure IV-25. It can be noticed that the standard-FFT technique produces some kind of distinction for each of the scatterers as the Peak-to-Trough Ratio is around -3dB while the NSI-4 technique output signal produces a much more resolvable peaks with a Peak-to-Trough Ratio that is less than -9dB. Furthermore, the sides of the rectangular distributed echo for the output signal of the NSI-4 technique are sharper and closer to the edges of the ideal targets than the output signal of the standard-FFT technique.

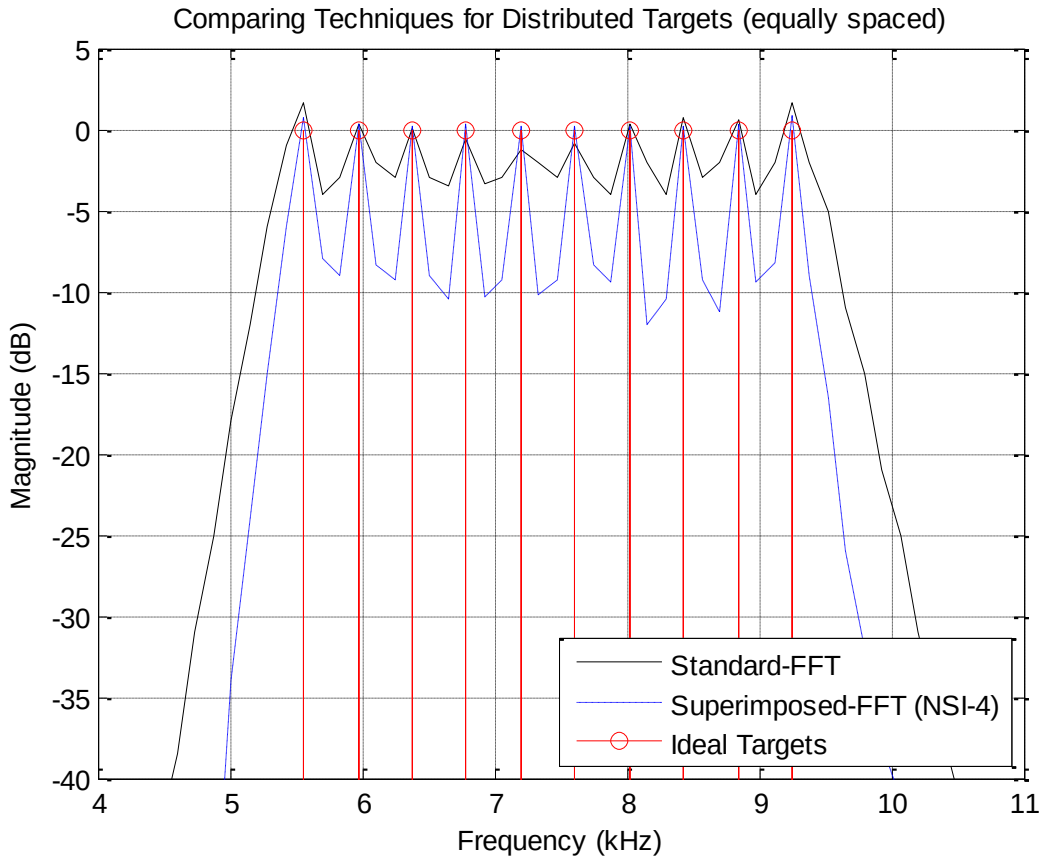

Figure IV-25: Simulation of Equally Spaced, with relatively large distant, scatterers for a rectangular distributed target.

Then, the simulation is repeated with 16 scatterers that are more closely spaced across the same frequency range as in the last example and the results are presented in Figure IV-26. The output signal of the standard-FFT technique is completely flat while the peaks of the ideal targets in the output signal of the NSI-4 are relatively distinguishable with a Peak-to-Trough Ratio of around -3dB. The sides of the rectangular distributed echo are still sharper and closer to the edges of the ideal targets when NSI-4 is used.

Finally, the simulation is repeated with 31 scatterers that are very closely spaced across the range to the extent that both NSI-4 and standard-FFT techniques are completely flat, see Figure IV-27. Nevertheless, the sides of the rectangular distributed echo from the NSI-4 output signal are, again, sharper and closer to the edges of the ideal targets that the edges of the output signal of the standard-FFT.

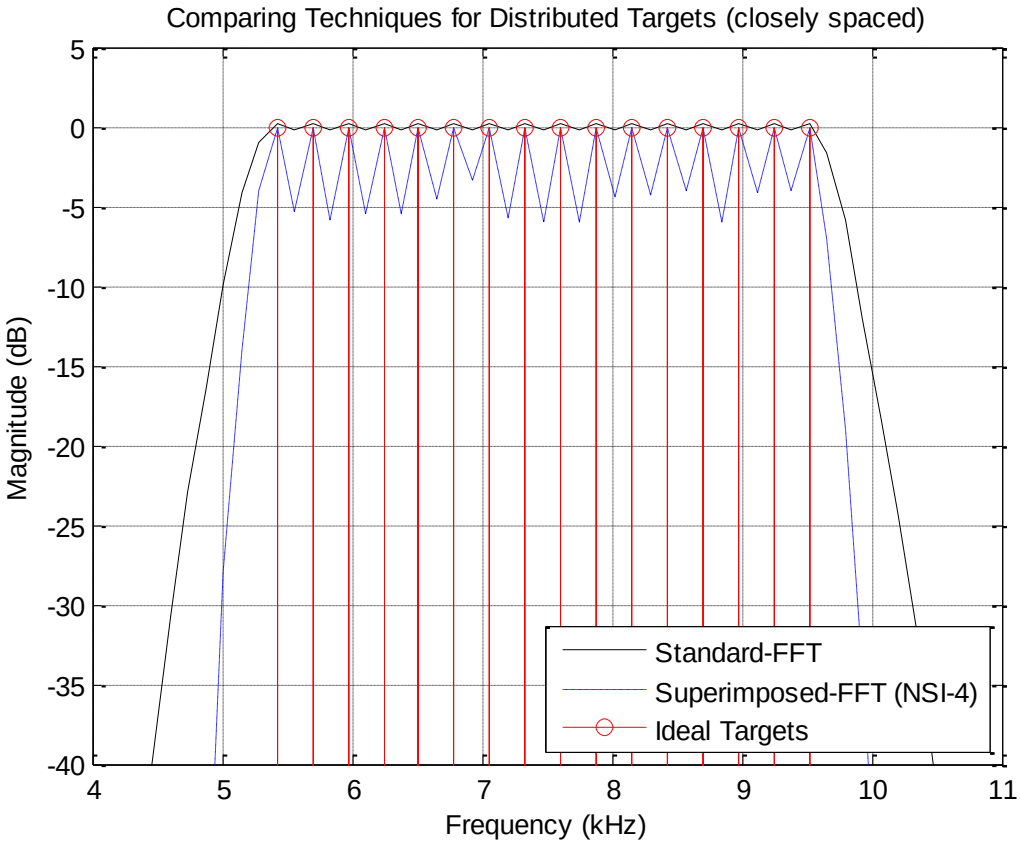

Figure IV-26: Simulation of Closely and Equally Spaced scatterers for a rectangular distributed target

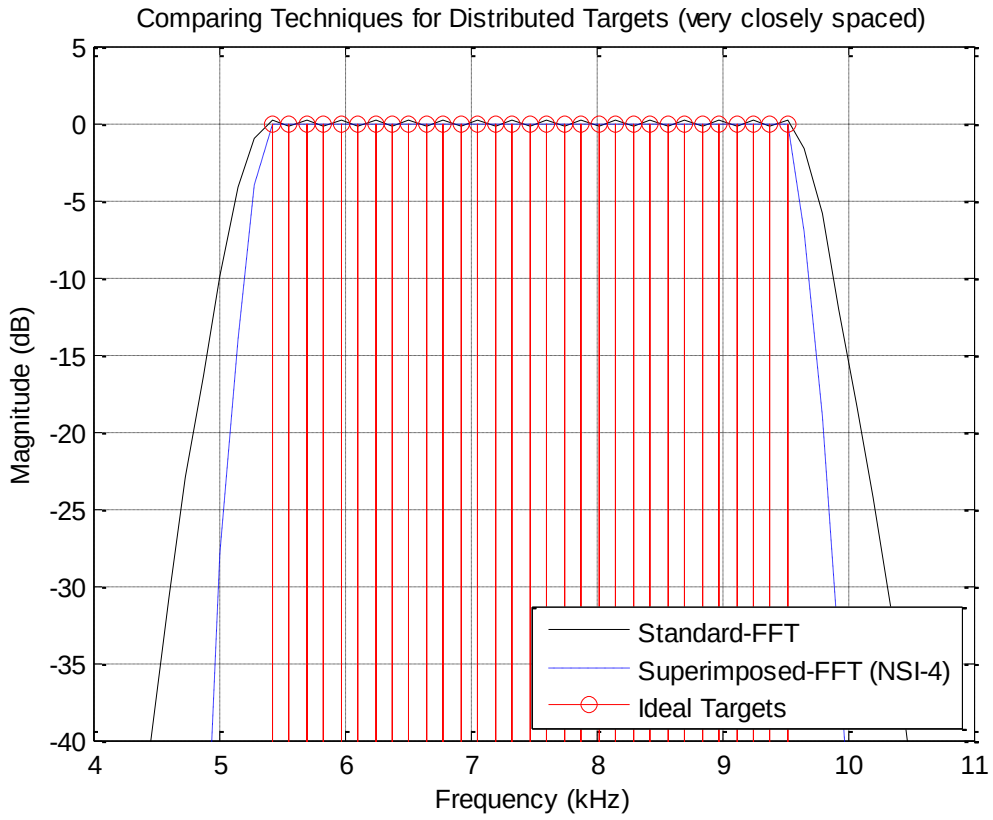

Figure IV-27: Simulation of a Very closely and Equally spaced scatterers for a rectangular distributed target

ii. Simulation of a Point Target against a Distributed Background

In this simulation, a scene is considered to contain both point and distributed targets with the assumption that the distributed targets have uniform reflectivity. A point target with a rectangular distributed echo in the background, which has a lower magnitude than the point target, is considered for different scenarios. These scenarios consider the point target at different positions in relation with the distributed echo to examine their interaction and effect on resolution of the targets. Starting with a point target that is positioned far from a background distributed echo consisting of 16 closely spaced scatterers, simulation results in Figure IV-28 show that in comparison to the standard-FFT analysis the NSI-4 output signal has a narrower main-lobe for the point target and a sharper edges for the rectangular distributed echo and therefore better identification of the point target and the distributed target as separate targets. The NSI-4 analysis also reveals some structure within the distributed target.

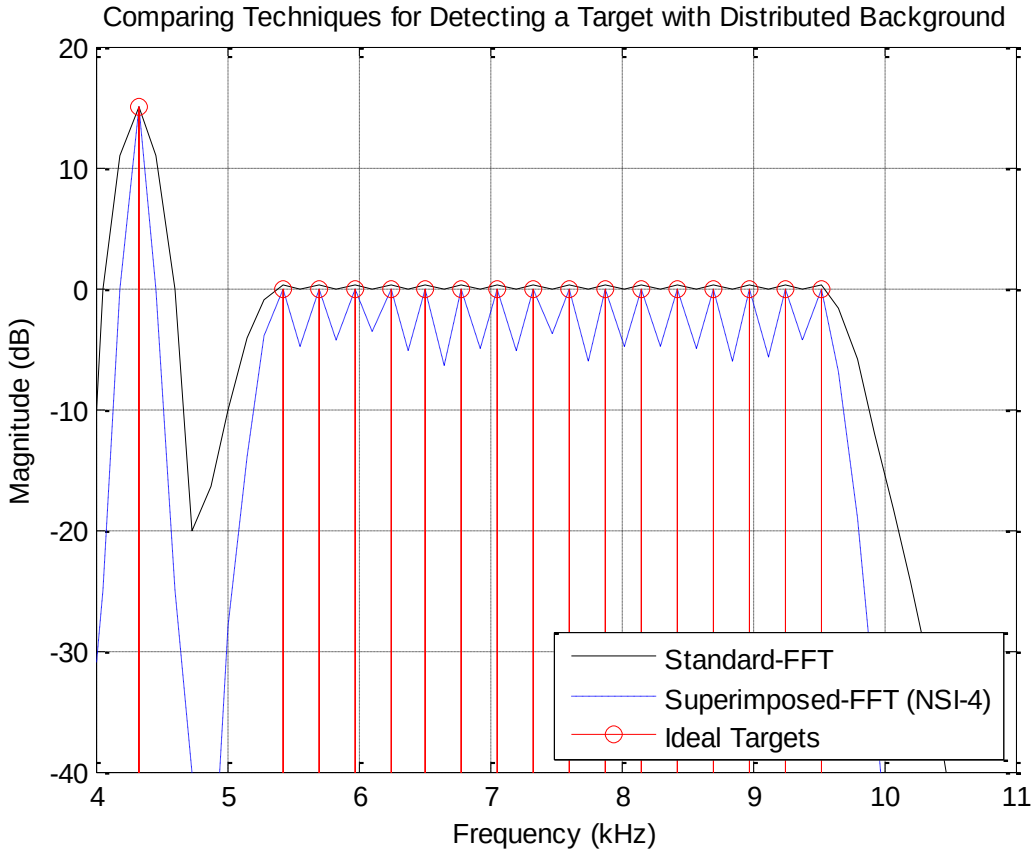

Figure IV-28: Simulation of a Point Target that is positioned far from a background of closely and equally spaced scatterers for a rectangular distributed echo

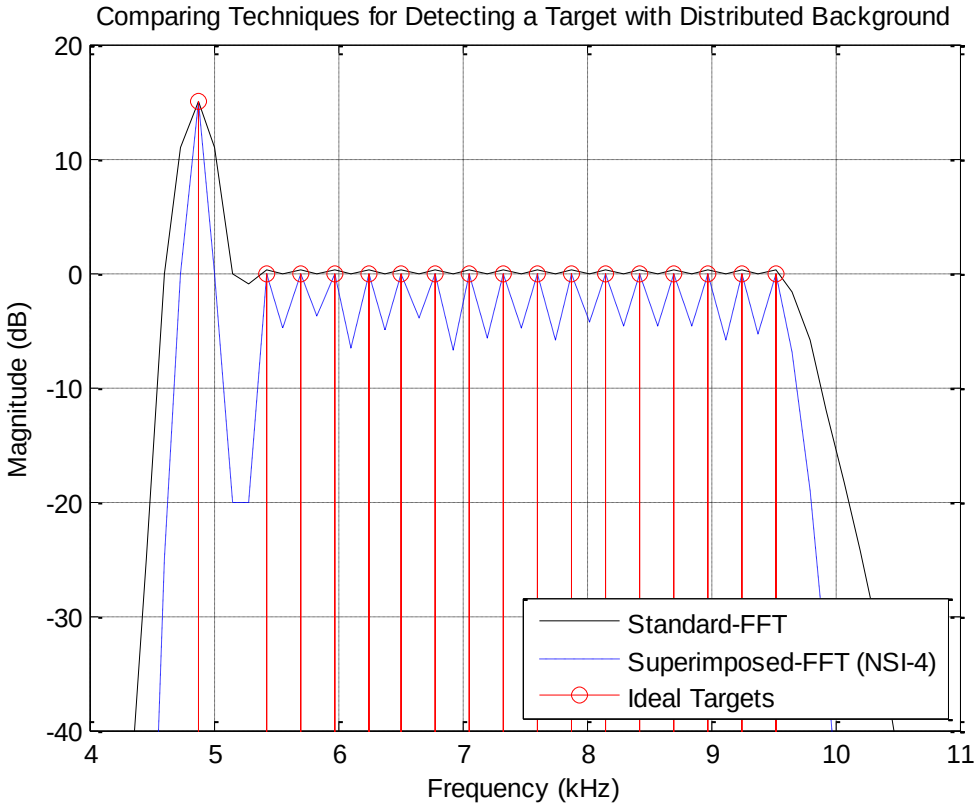

Figure IV-29: Simulation of a Point Target that is positioned close to a background of closely and equally spaced scatterers for a rectangular distributed echo

In Figure IV-29, the point target is positioned closer to the low-frequency end of the background distributed echo. The output signal of the standard-FFT is connecting the point target with the distributed echo without any distinction, which means that the point target might be mistaken to be part of the distributed target. The output signal of the NSI-4 technique produces a -20dB drop between the two target responses. Furthermore, the NSI-4 technique is still distinguishing the peaks of the scatterers within the distributed echo with sharper edges and narrower main-lobe width for the point target.

Figure IV-30 shows the comparison for the case where the point target is moved to be in the middle of the rectangular distributed echo. In this case, even though the peaks of the distributed echo's scatterers are not flat in the output signal of the NSI-4 technique with the Peak-to-Trough Ratio of around -3dB. Furthermore, the NSI-4 technique produces a narrower main-lobe width in comparison to the standard-FFT outcome and the edges of the NSI-4 trace of the rectangular distributed echo are sharper than the standard-FFT trace.

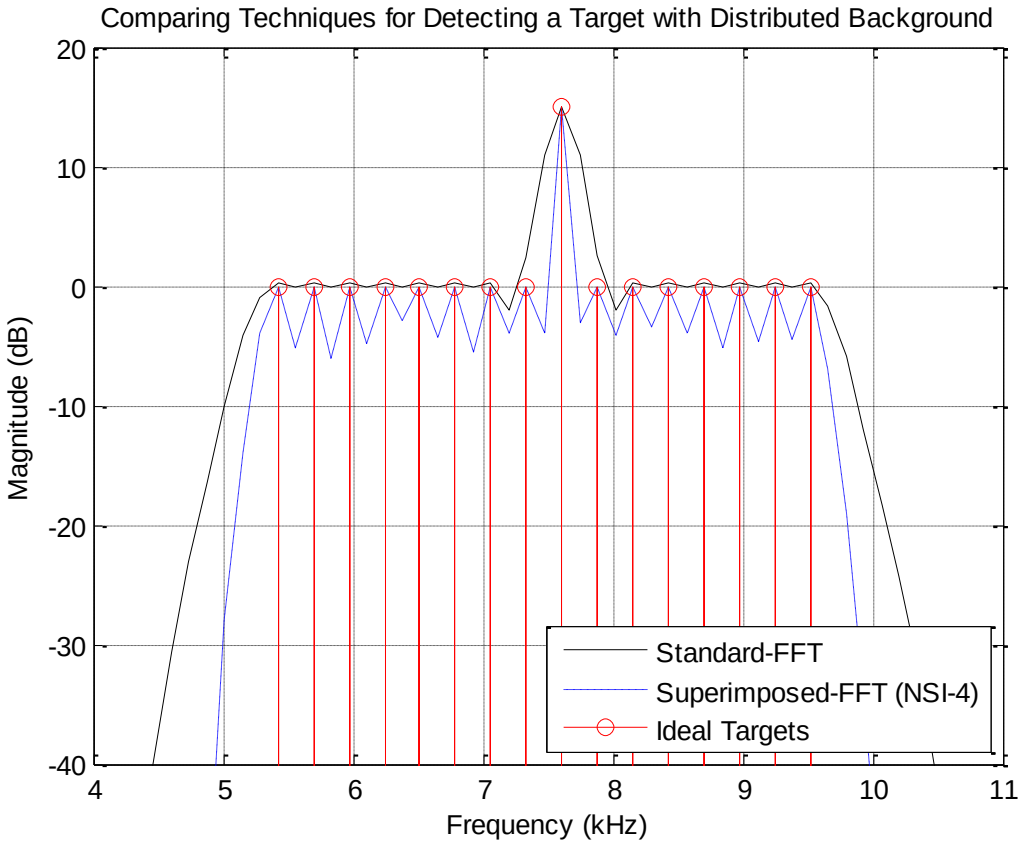

Figure IV-30: Simulation of a Point Target that is positioned in the middle of a background of closely and equally spaced scatterers for a rectangular distributed echo

Figure IV-31 shows the simulation of a point target positioned very close to the high-frequency end of a distributed background is conducted but with a rectangular echo consisting of 31 scatterers. While the output signals for the point target of both standard-FFT and NSI-4 techniques are not resolved from the background distributed echo. The NSI-4 output signal has a much narrower main-lobe width for the point target and sharper edges for the rectangular distributed echo.

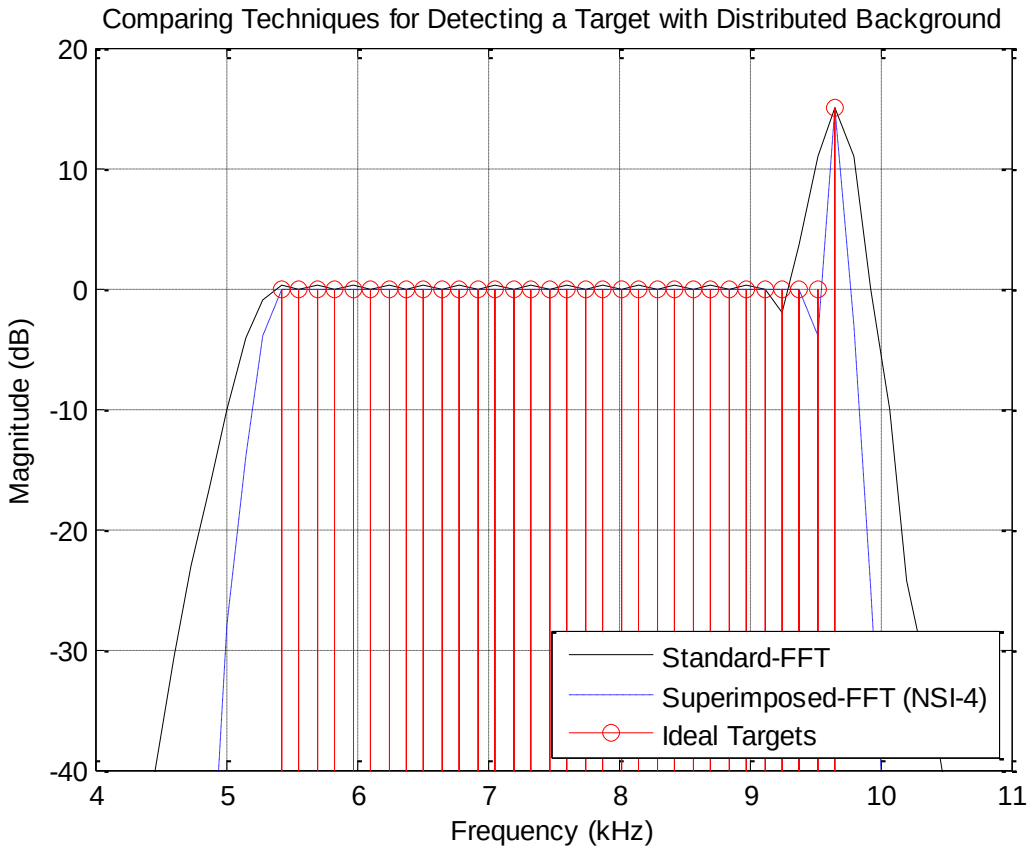

Figure IV-31: Simulation of a Point Target that is positioned at the high-frequency end of a background of a very closely and equally spaced scatterers for a rectangular distributed echo

8. Chapter Summary

This Chapter starts by presenting a basic SAR simulation using standard-FFT and Superimposition technique for one and two targets with, and without, the presence of additive and multiplicative noise. After that, the technique of MUSIC is considered and it was noticed that when compared with the superimposition technique for one target and for two targets, which are relatively far from each other, it is hard to weigh which one has a better performance. Nevertheless, as the number of targets is specified differently, the MUSIC technique showed a significant drawback as explain in section 5. Furthermore, when the system is simulated for two targets that are relatively close to each other, the superimposition technique showed significant superiority over the MUSIC technique that fused the two targets in one wide spike. Then, the Superimposed-FFT in its standard-setup, the RSI and the NSI techniques were simulated and compared in different scenarios. This examined the effect of applying different noise samples for each used signal, which is a simulation of multiple measurements. The effect of utilizing conjugate on the used signals was seen to suppress the

influence of noise even further. Results showed that using different noise sample and utilizing the conjugate can suppress the noise signal by up to -20dB more than using the same noise sample and without utilizing the conjugate. Finally, distributed targets are studied and then simulated as a background for a point target in order to examine the performance of the proposed superimposition technique, results showed superiority of the superimposition technique of NSI-4 in terms of resolvability and resolution.

Chapter V: IFFT-based Analysis Schemes

1. Introduction

Vector Network Analyzers (VNAs) are very powerful and flexible measuring instruments. Their basic capability is to measure the scattering parameters, which are usually referred to as S-parameters, of an RF or microwave device and display the result in the frequency domain. In addition to displaying performance in the frequency domain, many VNAs also offer a Time Domain option to enhance the analysis capability by presenting data in the time (or distance) domain. VNAs are able to measure magnitude and phase of complex S-parameters of a device under test (DUT) in the frequency domain. Then, by means of the Inverse Fourier Transformation (IFT), the measurement results can be transformed to the time domain. Thus, the impulse and/or step responses of the DUT can be obtained, which give a form of representation of its characteristics. Furthermore, the measured data in time domain can be processed to suppress unwanted signal components such as multi-reflections and sidelobes. After that, it can be transformed back to the frequency domain where the S-parameter representation can be reconstructed without the unwanted signal components, which is the same process used in SFCW-based GPR as discussed in section 14 of chapter 2.

One main problem is the unwanted sidelobes that are caused when applying FT or inverse FT to measured signals that have a band-limited property [12]. Two of the fundamental limitations associated with the IFFT: resolution and alias free range. Resolution is limited by the bandwidth of the measurement while aliasing is determined by the frequency step size. The principal property of interest in time domain processing for most microwave applications is resolution; or the ability to resolve one location from another. In practice, the data collection bandwidth in the frequency domain has a direct effect on information presented during the time domain analysis. Another important factor is the relative amplitude of the signals being processed. A large signal can swamp a smaller signal–where the greater the time (distance) separation between the two discontinuities the better the points of interest can be resolved. The presence of significant sidelobes in the response may cause interference with other near echo signals, have unwanted effects in the detection process and create ambiguities in the estimation of target range. Sidelobe reduction often made through suitable windowing techniques such as Hamming window. This and other windowing techniques reduce sidelobe levels but have a broadening effect on the main-lobe [109].

This chapter starts by VNA analysis of an impedance step discontinuity is designed and simulated by Ansoft simulation package to provide a comparative assessment to the quality of performance of the different standard techniques against the newly proposed technique of superimposition with its various methods of RSI and NSI. After that, real-life measurements are performed using the Beatty Standard 3.5Kit (HP 85053-60004) in order to examine the susceptibility of all used techniques to noise. Additionally, more noise is added to the measured data in order to study the ability of the different techniques to combat noise at very low SNR values. Finally, a simulation of GPR using standard-IFFT and Superimposed-IFFT techniques that is also applied to real-life data measured with an experimental SFCW GPR over an area of ground suspected to contain one buried pipe. It is important to emphasize that this chapter is included in the dissertation to show the importance of Superimposed-IFFT, as oppose to the Superimposed-FFT that is utilized in SAR, and to analyze its performance and importance to other IFFT-based microwave measurement applications such as VNA, GPR and medical imaging.

2. Ansoft Simulation

i. Simulation Setup and Parameters

This simulation of VNA was conducted in a noiseless ideal case in order to identify the performances of the different techniques. The Ansoft software was used to simulate an impedance step discontinuity where 50 Ω characteristic impedance-line is terminated by a 25 Ω load, see Figure V-1. The S_{11} reflection parameter is simulated over the range 40MHz to 20.04GHz using 501 data points. The magnitude and phase responses (shown in Figure V-2) are used to produce the complex signal in the frequency domain that is going to be converted to time domain using IFFT. The s_{11} signal is presented in (Figure V-3). The graph also shows a Hamming Window function and the generated signal using the standard-Superimposition.

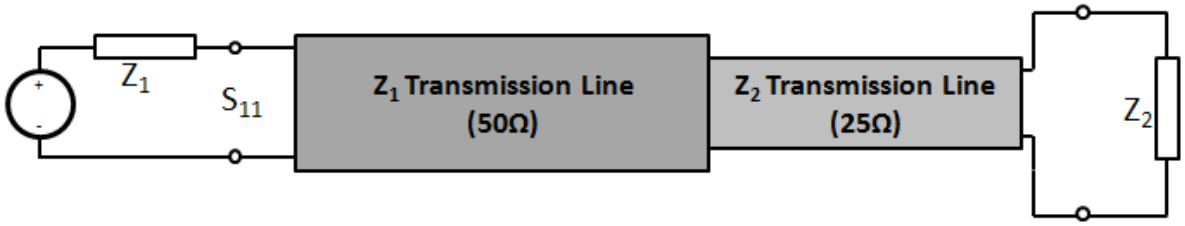

Figure V-1: Mismatch of transmission line characteristic impedances causes a discontinuity in the line parameters and results in a reflected wave

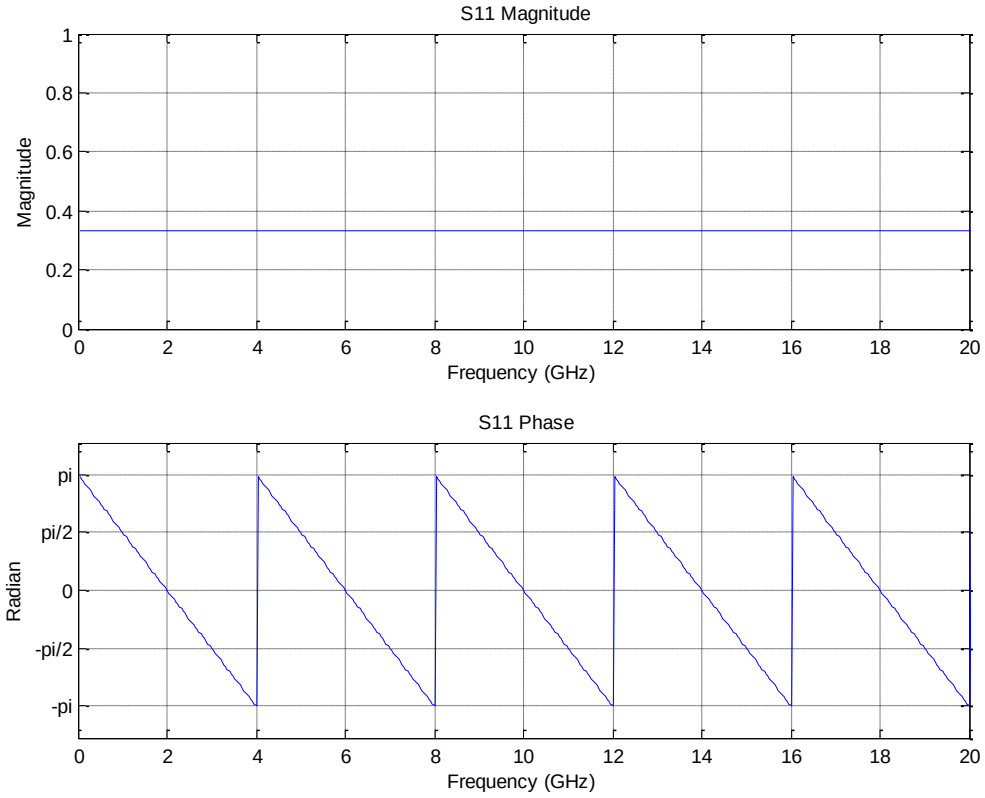

Figure V-2: Magnitude and Phase Responses of the Ansoft Simulation

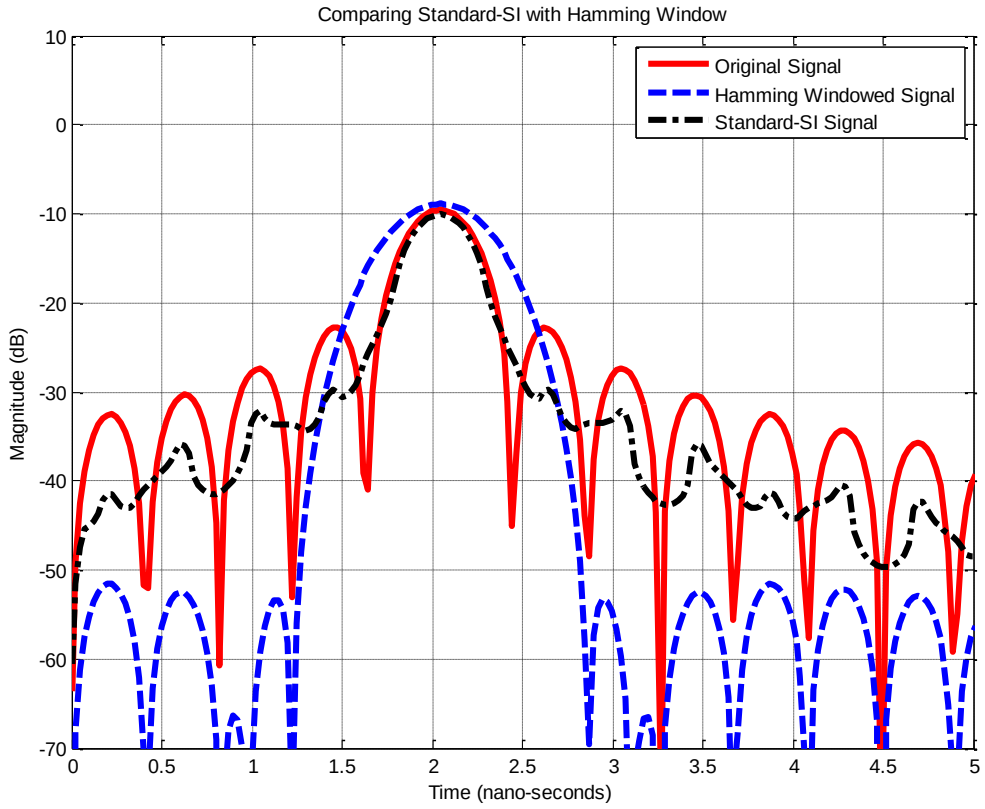

Figure V-3: Comparing Standard-SI with Original and Hamming Windowed Signals

ii. Standard Superimposition with Hamming Window

The superimposed signal is generated by truncating the original signal and then applying a Hamming Window to the truncated signal before superimposing it on the original one. Then, a moving average filter is also applied to further suppress the sidelobes by setting its width to be that of two sidelobes (i.e. a negative lobe and a positive lobe). The outcome of the standard-IFFT, standard-IFFT with Hamming Window and standard-superimposition with Hamming Window are presented in Figure V-3. The standard-superimposition analysis shows a noticeable decrease in the sidelobes, but not to the same level as that of the standard Hamming Window technique. However, it can be noticed that in the case of Hamming windowed signal, the width of the main-lobe has widened to the extent that the resolution is significantly worsened. On the other hand, the standard-Superimposition does preserve the main-lobe in the top 16 dB and further improved Superimposition techniques are presented and examined in the following subsections.

iii. Repetitive Superimposition (RSI)

The technique of RSI is presented in subsection 5.i in Chapter 3. In this subsection, many different designs are investigated with different numbers of signals used in the superimposition process and with different distributions along the first three sidelobes. A moving average filter is also applied to further suppress the sidelobes by setting its width to be that of two sidelobes (i.e. a negative lobe and a positive lobe). However, only four different values of the order (N) are presented to show the best compromise between performance and processing time for the RSI technique. These four techniques utilize two, six, ten and hundred input-signals to the superimposition process. First, for the RSI-2 case, the zero-crossing points are of the truncated signal are aligned, using equation (Eq. III-29), with the peaks of the first two sidelobes in the original signal. The RSI-6 case has three zero-crossings that are placed at one-third and two-thirds and centre of each of the first two sidelobes. RSI-10, which has been found to be the best choice, has four zero-crossings at one-, two-, three- and four-fifths through the first sidelobe; and three zero-crossings placed at one-third, two-thirds and centre of the second and third sidelobes. Finally, RSI-100, is designed to have 100 zero-crossing – from the 100 utilized input signals – distributed equally over the first three sidelobes. All RSI schemes are presented in Figure V-4.

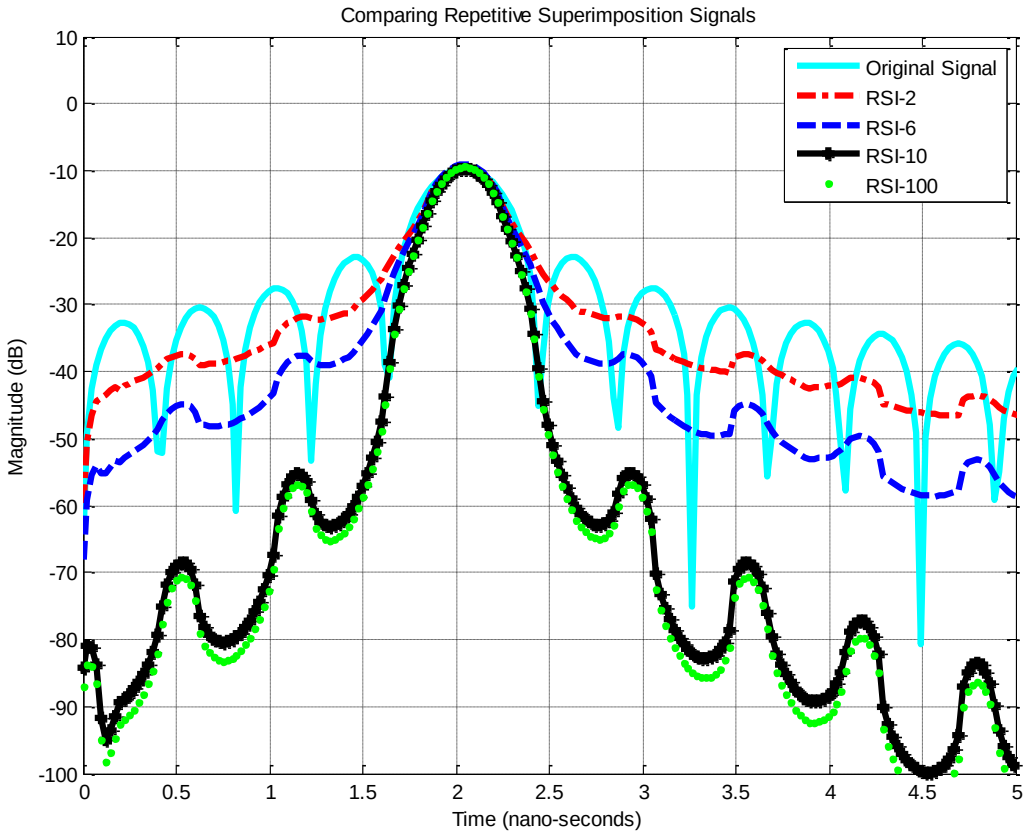

Figure V-4: Comparing Repetitive Superimposed Signals

Clearly RSI-2 gives a better result to the original signal in terms of sidelobe suppression. Furthermore, as the number of repetitions increased, the reduction in the sidelobes is more pronounced. However, as the number of repetition exceeded ten, the performance of the RSI is almost constant and the suppression of the sidelobe has stabilized. Hence further results are shown for RSI with ten repetitions. As the number of input-signals (N) is increased to a hundred, the performance of RSI enhances noticeably but with an expensive increase in the computational load as well. Having determining the better value of the order, N, for RSI technique to be ten based on the outcome presented in Figure V-4, a comparison with the widely used Hamming Windowing technique is presented for comparison in Figure V-5. It can be noticed that, other than the second sidelobe of the original signal, RSI-10 give superior suppression of sidelobes while quite accurately preserving the main-lobe. Indeed, it can also be noticed that the width of the main lobe is slightly narrowed, which means a slightly better resolution is achieved.

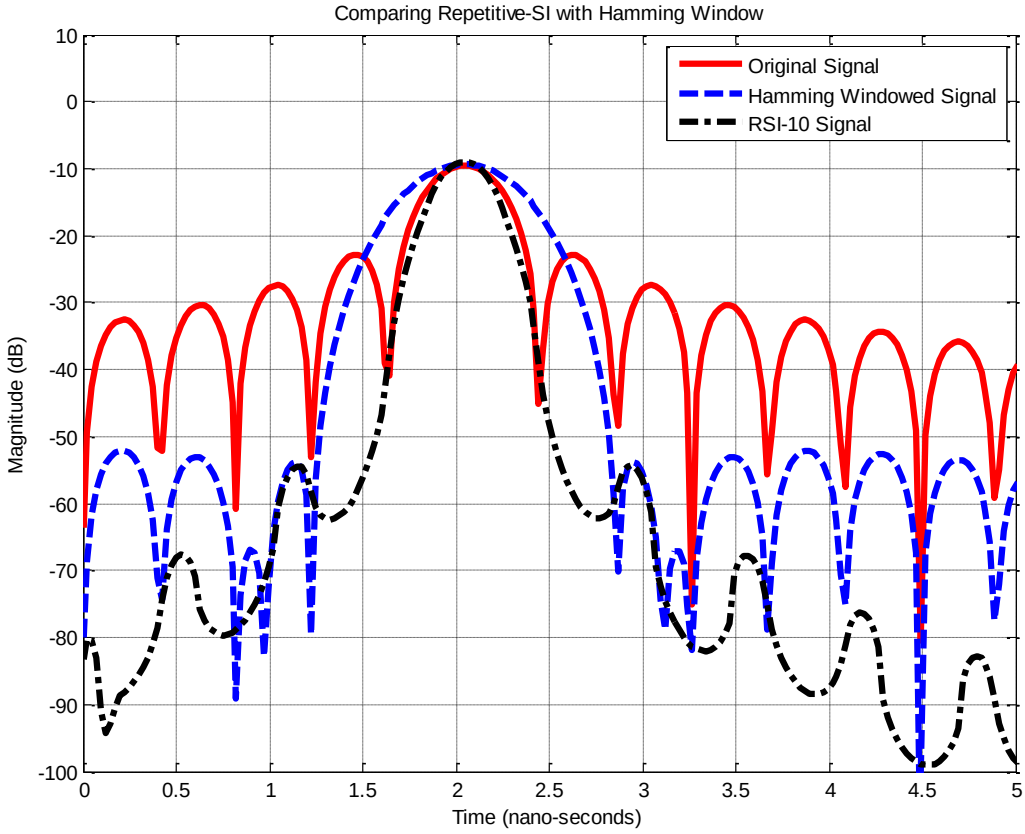

Figure V-5: Comparing RSI with Hamming Window

iv. Normalized Superimposition (NSI)

To determine the best choice for the order N in the NSI case, a number of different cases that have a different number of input signals and different distribution of zero-crossing points over the first two or three sidelobes have been examined. Only four different scenarios have been presented in this dissertation, which are: 2^{nd}, 3^{rd}, 6^{th} and 100^{th} orders of NSI. NSI-2 has zero-crossings aligned with the two peaks of the first two sidelobes; NSI-3 has three zero-crossings distributed at the centre of the first three sidelobes; NSI-6 has zero-crossings distributed at the centre, one-third and two-thirds of the first two sidelobes; Finally, NSI-100 is examined to show that as the order, N, of the NSI increases beyond the sixth order, the impact on the performance is trivial. Finally, NSI-100, is designed to have 100 zero-crossing – from the 100 utilized input signals – distributed equally over the first three sidelobes.

A moving average filter is also applied to all the designs to further suppress the sidelobes by setting its width to be that of two sidelobes. These four cases are presented and compared in Figure V-6. The results show a significant enhancement in the performance between the

first three orders (i.e. N = 2, 3 and 6) in terms of significant suppressing sidelobes, which means better detection of main lobes and less probability of false targets. More importantly, the results also show a sizeable narrowing of the main lobe, which means better resolution. A quantitative study of this narrowing effect and a comparison with the other techniques is presented in section 3 of this chapter. However, as the order of N increases (N =100), the enhancement is insignificant and doesn't justify the substantial increase in processing time. The normalization technique gives a superior performance in suppressing sidelobes with a relatively low cost of processing time due to the low order of normalization. In Figure V-7, NSI-6 is presented in comparison with RSI-10. As mentioned in the previous subsection, RSI-10 is generating a very significant improvement when compared with the standard-IFFT or the widely used technique of Hamming window. However, NSI-6 is far superior in terms of both sidelobe suppression and main-lobe narrowing.

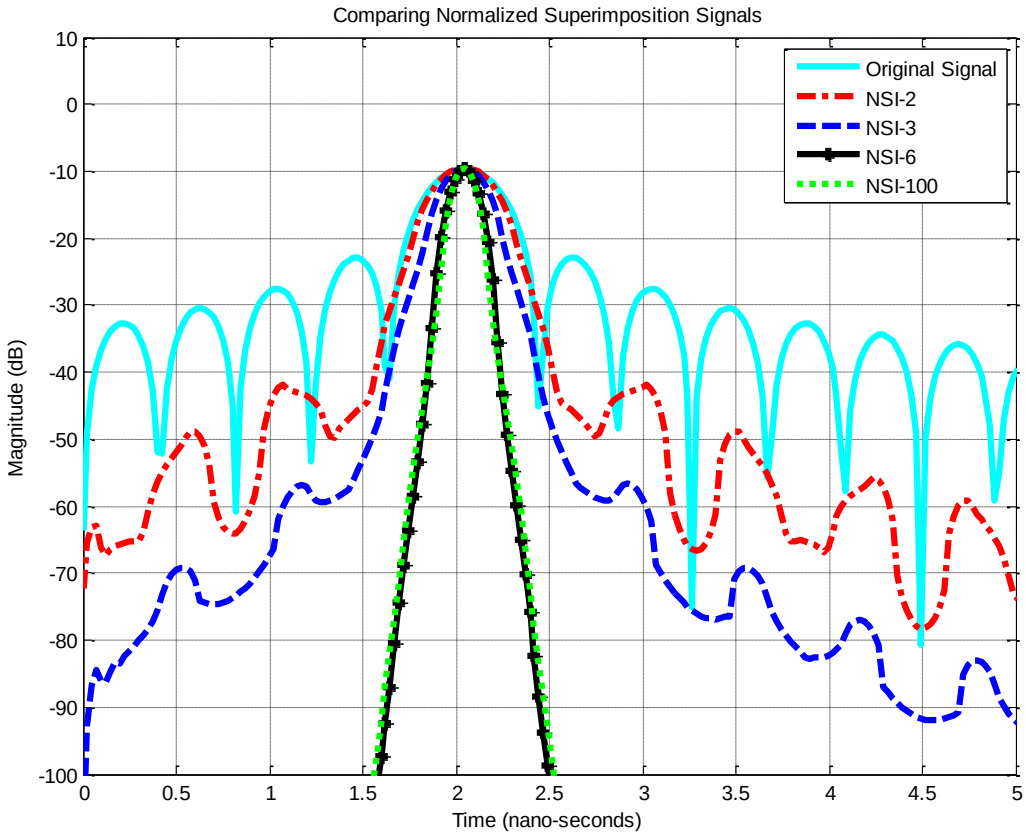

Figure V-6: Comparing Normalized Superimposition designs

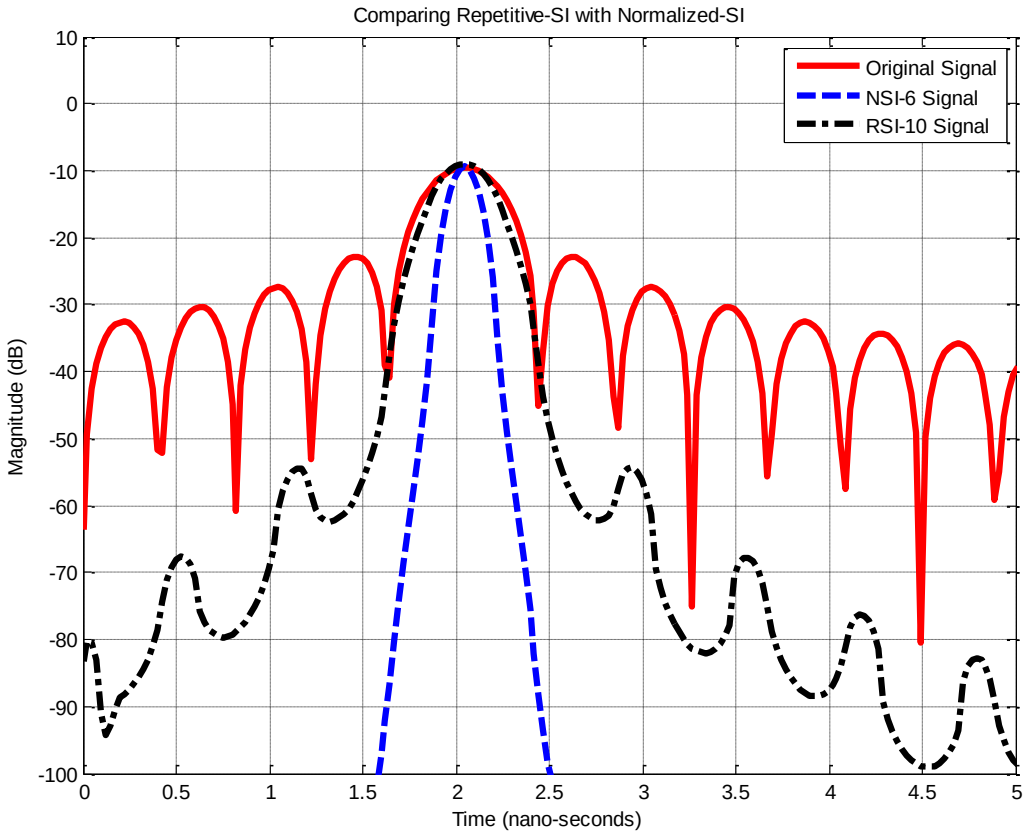

Figure V-7: Comparing NSI -6 technique with RSI-10 technique

v. Spatially Variant Apodization (SVA)

SVA was designed and used on the Ansoft derived simulation data described in the previous section. A comparison between the SVA and the widely used technique of Hamming window for suppressing the sidelobes is presented in Figure V-8. The results show that SVA performed slightly better than the Hamming Window in suppressing sidelobes. However, even though SVA did, just like the Hamming window technique, preserve the main-lobe's position and height, when it came to the width of the main lobe, unlike the Hamming Window technique, SVA preserved it as well.

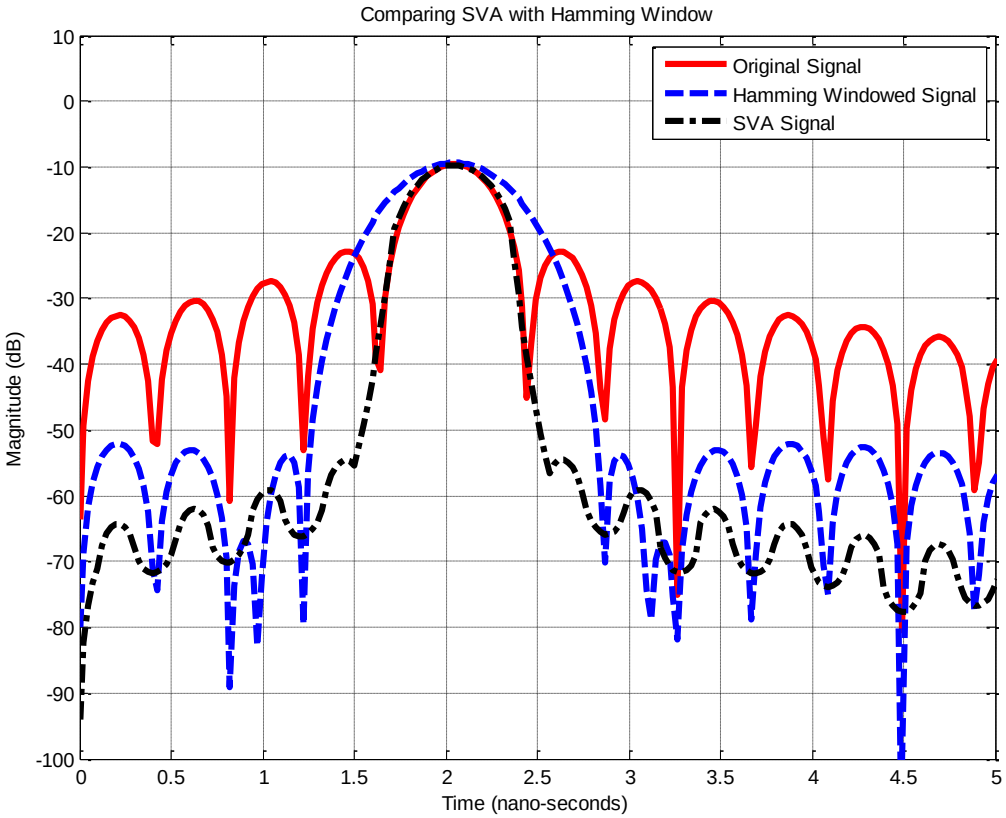

Figure V-8: Comparing SVA with Hamming Window

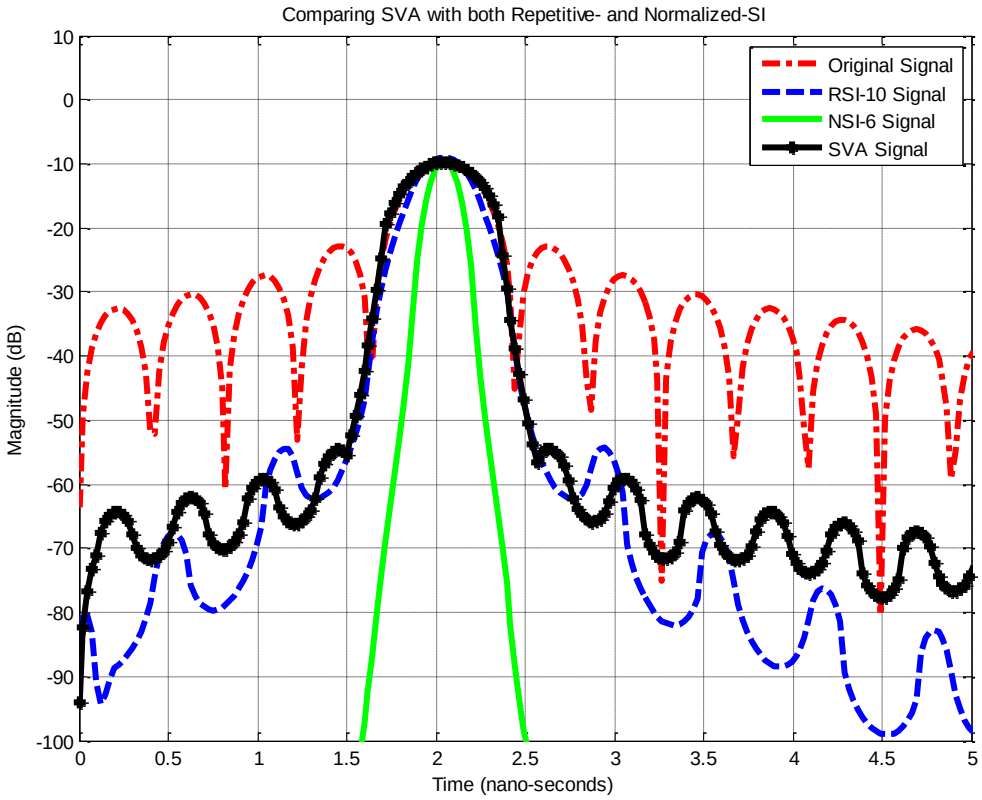

Figure V-9: Comparing SVA with RSI-10 and NSI-6 techniques

In Figure V-9, SVA is compared with the improved superimposition techniques of RSI-10 and NSI-6. SVA gave a similar performance to the RSI-10 technique, but it was outperformed by the NSI-6 technique. Additionally, it can be noticed that, even though the SVA technique preserved the main-lobe's position and height, it didn't have any effect on its width, and hence the resolution is not affected. On the other hand, RSI-10 has a minor narrowing effect, which means a small enhancement to the resolution, while NSI-6 has a major narrowing effect, which means a significant enhancement to the resolution.

vi. Super-Spatially Variant Apodization

Super-SVA was designed and examined in the Ansoft simulation experiment. At the beginning, just like the other techniques, it was compared with the widely used technique of Hamming window as shown in Figure V-10. The figure shows that Super-SVA suppresses sidelobes better than the Hamming Window technique. While the Hamming Window widens the main-lobe, Super-SVA narrows the main-lobe and hence enhances the resolution.

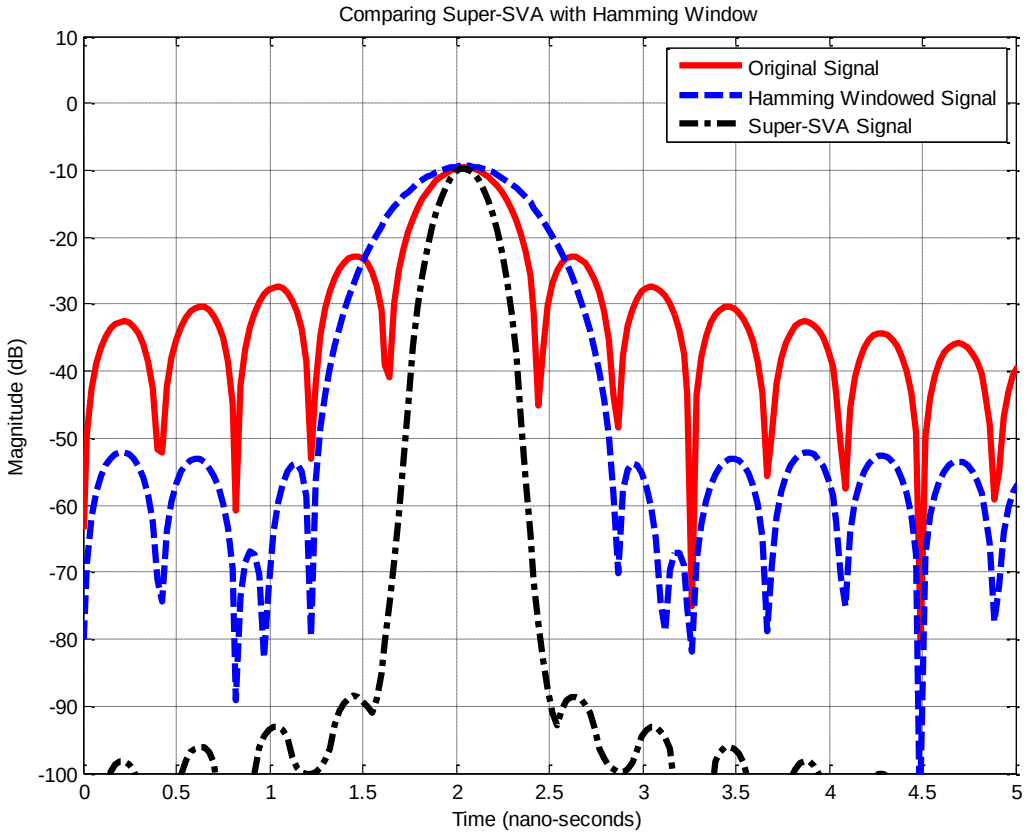

Figure V-10: Comparing Super-SVA with Hamming Window

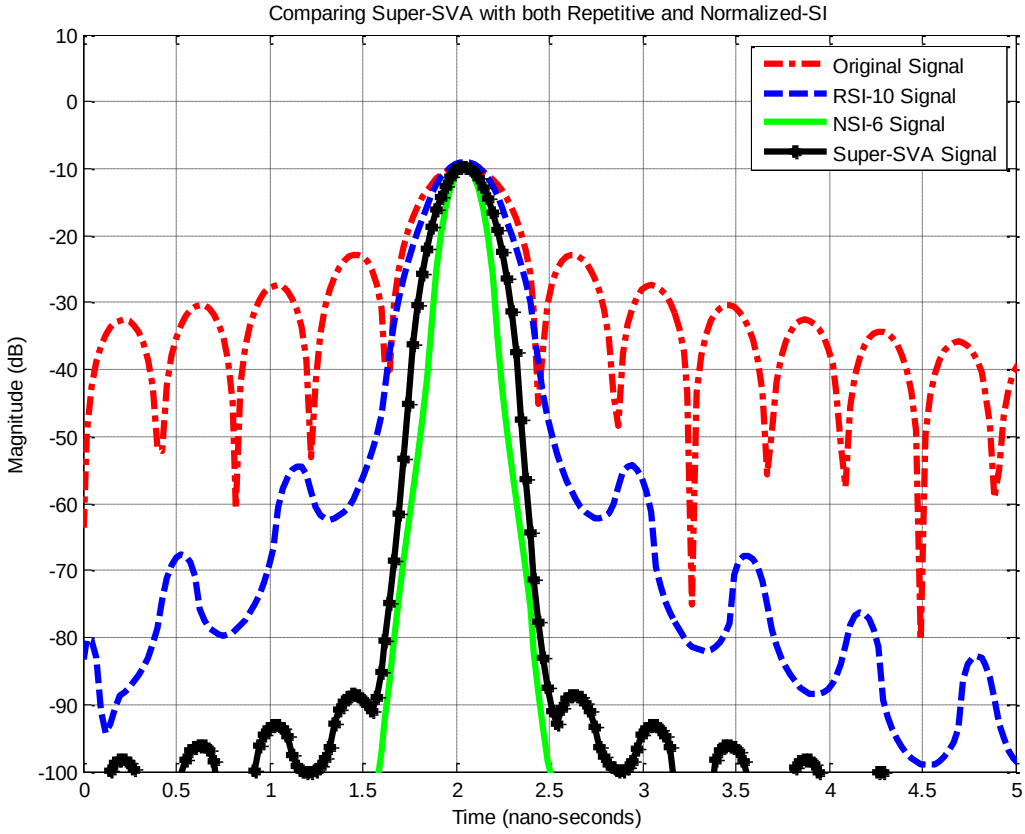

Figure V-11: Comparing Super-SVA with RSI and NSI techniques

In Figure V-11, Super-SVA is compared with the improved superimposition techniques of RSI-10 and NSI-6. On one hand, Super-SVA outperforms the RSI-10 technique in both suppressing sidelobes and enhancing resolution. On the other hand, NSI-6 is still superior to the Super-SVA technique in both sidelobe suppression and resolution enhancement. In terms of processing time, Super-SVA has a relatively high processing time when compared with the other techniques presented in this chapter due to its iterative loop. The processing time for the Ansoft simulation data on a standard laptop was 726msec in comparison with the 46msec that the NSI-6 takes.

3. Performance Assessment of the Different Techniques

Figure V-12 shows the comparison between the different techniques in terms of main-lobe width that is considered, as engineers usually do, at -3dB: First, the width of the original signal, which is the standard-IFFT technique that is used as reference for comparison, is 0.38nsec. Second, SVA technique insignificantly widens the original signal by 0.41nsec. Third, RSI-10 narrows the width of the lobe to 0.28nsec. Fourth, Super-SVA has an even

better resolution as the width of the main-lobe at -3dB has reduced to 0.20nsec. Finally, NSI-6 has the best resolution as the width has shrink to 0.16nsec, which is less than half of that of the original signal.

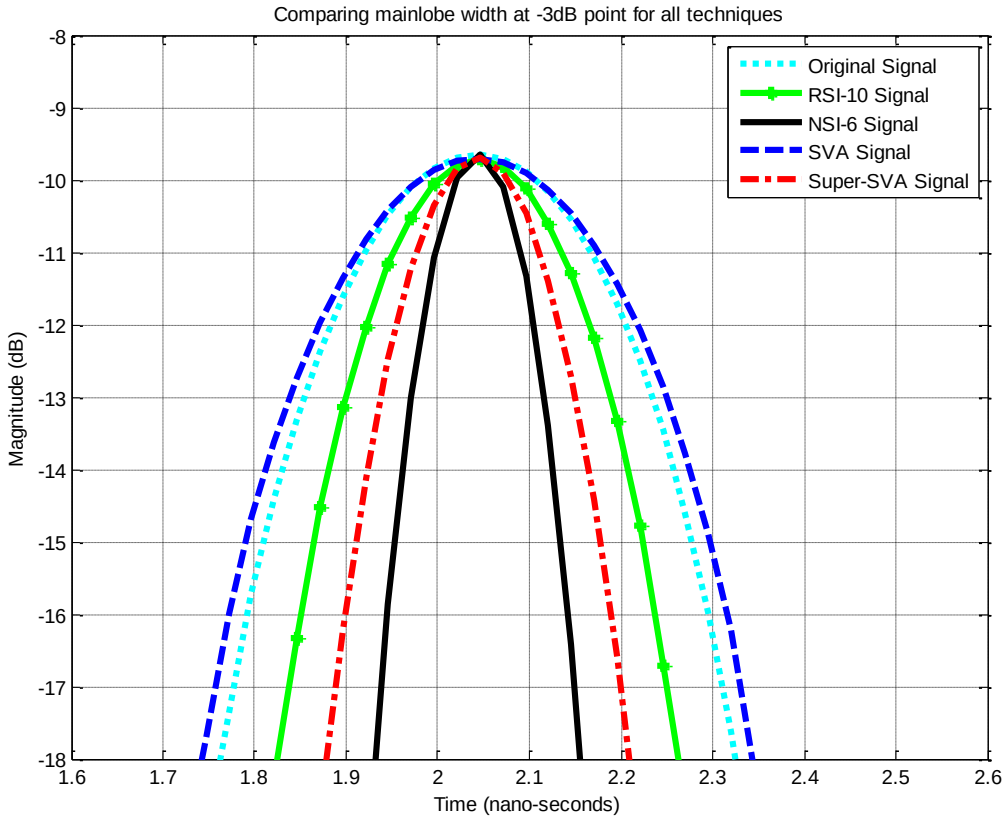

Figure V-12: Comparing width of main-lobe for all techniques at -3dB

After that, PSLR and ISLR values are compared for the different techniques. PSLR is straightforward calculated as it is the difference between the main-lobe and the 1st sidelobe, ISLR, on the other hand, depends on the integration period. In this simulation ISLR has a fixed integration period of 10nsec since simulation results showed that the value of ISLR doesn't get lower after this, which is caused by high level of sidelobes inherent to the radiated signal shape so that noise residuals doesn't make strong impact on ISLR when integration time exceeds this period [29]. All the different techniques that are used in the previous section are compared in terms of spatial resolution, which is define as main-lobe width at -3dB, PSLR, ISLR, processing time and memory space, in kilobytes (kB), allocated by Matlab to hold and process the required data for each technique. The processing time is measured using Matlab built-in function "cputime" while the memory required for each technique is measured using Matlab built-in function "memory". A summary of the performance assessment outcomes are presented in Table V-1.

Table V-1: Summary of Performance Assessment of the Different Techniques in Ansoft simulation

Technique	Spatial Resolution	PSLR	ISLR	Processing Time	Allocated Memory
Standard-IFFT	0.38nsec	-22.7dB	-9.7dB	7msec	3.6 kB
SVA	0.41nsec	-43.4dB	-30.9dB	81msec	51 kB
RSI-10	0.28nsec	-44.2dB	-32.2dB	62msec	32 kB
Super-SVA	0.20nsec	-78.1dB	-53.4dB	726msec	62.2 kB
NSI-6	0.16nsec	-112.3dB	-78.7dB	46msec	17.3 kB

4. Beatty Standard Measurement Setup and Procedure

In this Beatty Standard measurement, two impedance step discontinuities between 50Ω and 25Ω impedances, which are referred to as Z_1 and Z_2 respectively, transmission lines that are spaced by a known distance, and output S_{11} is terminated with 50Ω that is going to be excited by an impulse. Figure V-13 shows a diagram of the Beatty Standard experiment. The S_{11} received signal is measured using a Network Analyzer (Anritsu 37397C VNA) calibrated over the range 40MHz to 20.04GHz using 401 data points. The measured magnitude and phase responses of S_{11}, see Figure V-14, show the complex signal in the frequency domain.

i. Calculating Ideal Reflected Impulses

Figure V-13 shows the Beatty Standard experiment diagram and microwave signals behaviour in it. Starting with the first reflected impulse, X_1, it can be noticed that the reflected impulse is the microwave signal reflected from the 50Ω to 25Ω discontinuity. The reflection coefficient, Γ_1, of this impedance step can be calculated as follow:

$$\Gamma_1 = \frac{Z_1 - Z_2}{Z_1 + Z_2} = \frac{50 - 25}{50 + 25} = 0.333 \qquad \textbf{(Eq. V-1)}$$

where Z_1 and Z_2 are the 50Ω and 25Ω impedances, respectively.

And thus: $$X_1 = 20\log|\Gamma_1| = -9.54dB \qquad \textbf{(Eq. V-2)}$$

While in the case of the second reflected impulse, the microwave signal first goes through the 50Ω to 25Ω transmission line, with a transmission coefficient T_{12}, then it is reflected by

the 25Ω and 50Ω discontinuity, Γ_2, and finally goes back through the first impedance step with a transmission coefficient T_{21}. This can be expressed by the following equation:

$$X_2 = 20\log|T_{12}\Gamma_2 T_{21}| = -10.5\text{dB} \qquad \textbf{(Eq. V-3)}$$

where:

$$T_{12} = \frac{2Z_1}{Z_1 + Z_2} \quad \text{and} \quad \Gamma_2 = \frac{Z_2 - Z_1}{Z_1 + Z_2} \quad \text{and} \quad T_{21} = \frac{2Z_2}{Z_1 + Z_2} \qquad \textbf{(Eq. V-4)}$$

Finally, for the third reflected impulse, the microwave signal goes through the 50Ω to 25Ω transmission line (T_{12}), reflects off the 25Ω and 50Ω discontinuity (Γ_2) three times, on both sides of the 25Ω impedance, and finally goes through the 25Ω to 50Ω transmission line (T_{21}) and thus:

$$X_3 = 20\log\left|T_{12}\Gamma_2^3 T_{21}\right| = -30\text{dB} \qquad \textbf{(Eq. V-5)}$$

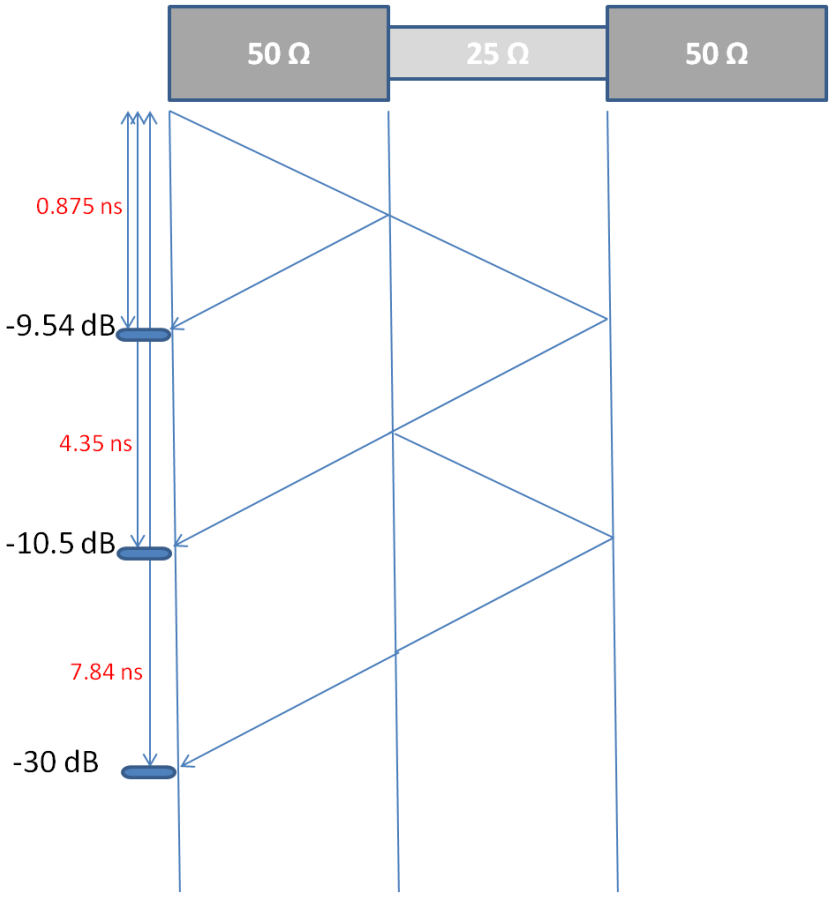

Figure V-13: Diagram of Beatty Standard Experiment

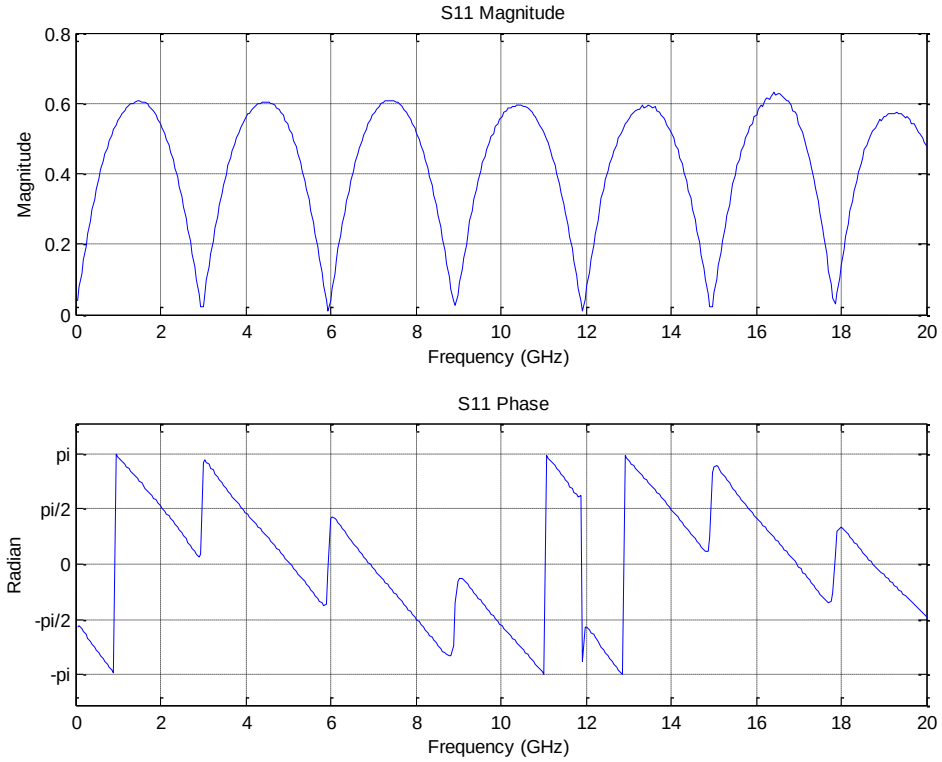

Figure V-14: S11 Magnitude and Phase responses in Frequency Domain for the measured Beatty Standard

ii. Results for the Standard-IFFT technique and Ideal Reflectors

The arrival of the first three ideal reflected impulses starts after 0.875nsec and they have magnitude return losses of -9.54dB, -10.5dB and -30dB. The three ideal reflected impulses are separated by 3.48nsec. Initially only the noise from the measurement is included in the experiment. Furthermore, different versions of the original complex signal are truncated and/or windowed in different ways in order to produce the different signals that are used in both of the improved Superimposition techniques: RSI-10 and NSI-6 in this experiment. All signals are zero padded to have a total of 8192 data points each in order to have more points in the Time-domain. All the complex signals are converted to the time domain using IFFT.

5. Results for Standard-Superimposition and Windowing Functions

The standard-Superimposed (SI) signal is created by multiplying the original signal by the windowed version of the truncated signal. So, the original signal is multiplied with the 1/3 truncated-and-windowed signal. The standard-SI signal is compared with standard-IFFT and a Windowing of the original signal (i.e. standard-IFFT) using both Hamming and Chebyshev windowing functions as shown in Figure V-15.

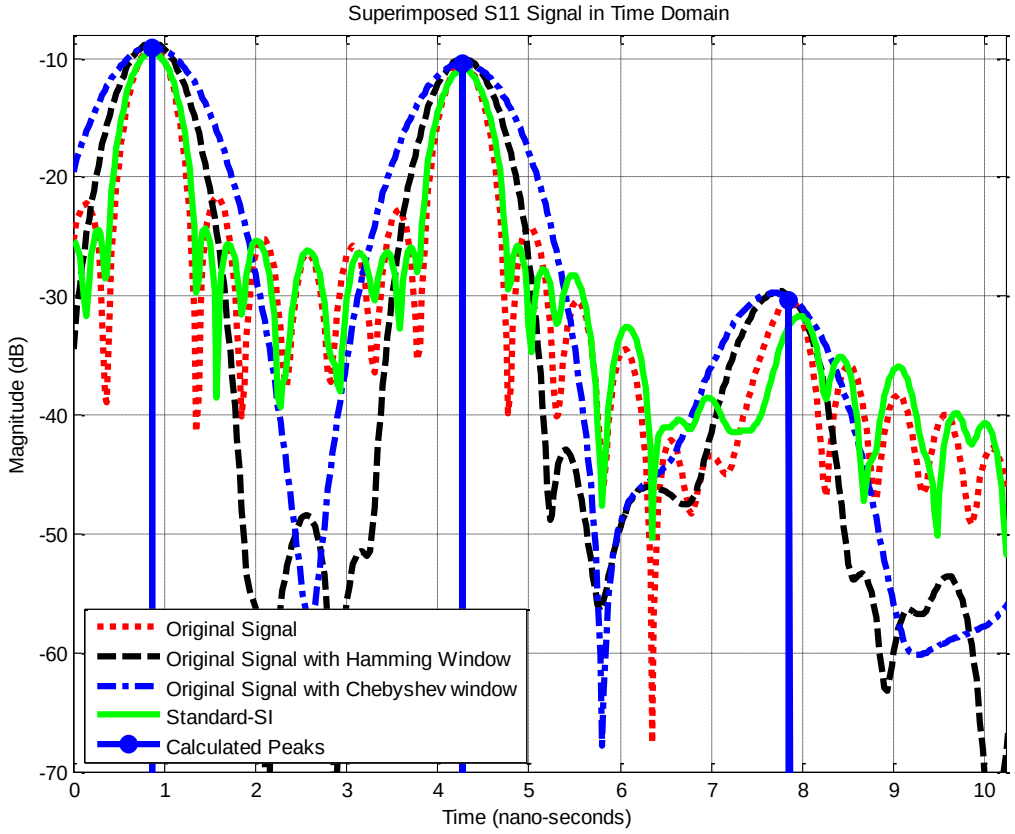

Figure V-15: Comparing Standard-SI with Windowing Functions (Hamming and Chebyshev)

The calculated peaks indicate the return loss of the ideal impulse response of the Beatty Standard. It can be noticed that only the first sidelobes are affected by the standard-SI technique. However, standard-SI does preserve the width of the main-lobe, which means that it preserves the resolution of the original signal. On the other hand, using the Hamming window function doubles the width of the main-lobe. Furthermore, the figure also shows that even though some other windowing functions (i.e. Chebyshev) have greater sidelobe reduction (about 7dB) than the Hamming window, but it also has a greater widening effect on the main lobe. The Chebyshev window function triples the width of the main-lobe. Hence, windowing functions, unlike Superimposition, have a severe degradation effect on the resolution.

6. Results for Improved Superimposition Techniques (RSI and NSI)

Improved Superimposition techniques of Repetitive and Normalized Superimposition are implemented in their most favourable design that was discussed in section 5 of Chapter 3: RSI-10 and NSI-6. It is worth mentioning that for the signals used in the RSI or NSI, half of

the input signals are conjugated before being superimposed on each other and the original signal. Hence, for NSI-6, six signals that are truncated and/or windowed with independent noise samples have been utilized. Similarly, for RSI-10, ten signals that are truncated and/or windowed with independent noise samples have been used with each other after being conjugated in the superimposition process. A moving average filter is also applied to further suppress the sidelobes by setting its width to be that of two sidelobes. Figure V-16, shows a comparison of these improved Superimposition techniques. The results show a superior performance of NSI-6 over the RSI-10 in terms of suppressing sidelobes. Furthermore, a noticeable narrowing effect, which produces better resolution, is generated by the NSI-6 technique. The RSI-10 technique preserves the main lobe width and hence preserves the resolution of the conventional IFFT analysis. Due to the superiority of NSI-6 technique, it is used for comparison with Spatially Variant Apodization (SVA) and Super-SVA in the following sections.

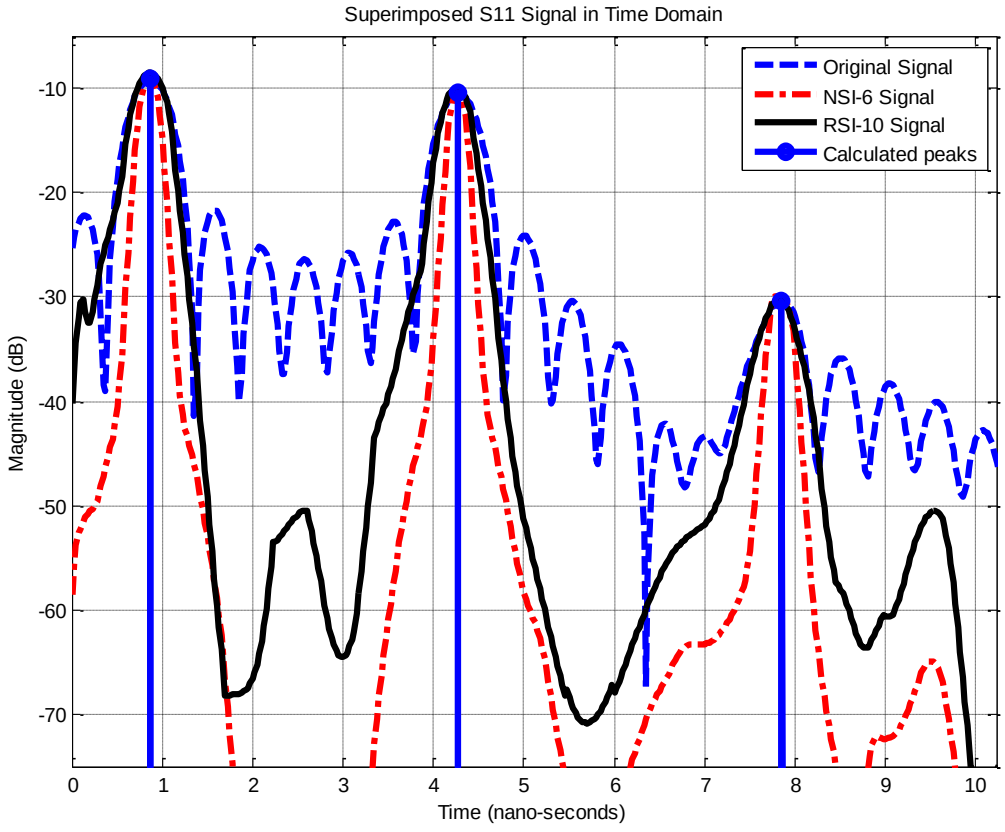

Figure V-16: Comparing Improved Superimposition techniques: NSI-6 and RSI-10

7. Results for Spatially Variant Apodization (SVA) and Super-SVA

Starting with SVA technique, the results are presented in Figure V-17 where it is noticed that SVA is outperformed by NSI-6 in terms of suppressing sidelobes with a difference of up to more than 30dB at some points. Furthermore, even though SVA is preserving the width of the first two main lobes, it is having a small widening effect on the third one. At that point NSI-6 is actually, as mentioned in the previous section, enhancing the resolution by narrowing the main lobes' width without changing their positions or heights.

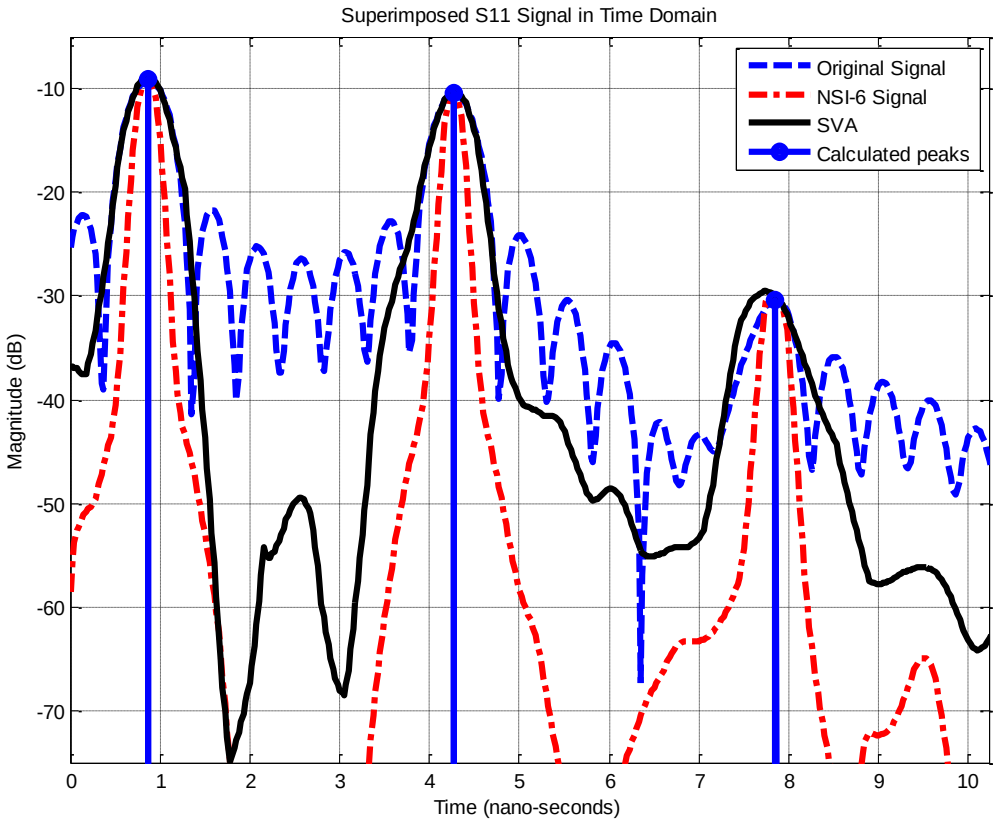

Figure V-17: Comparing SVA with NSI-6 technique

The Super-SVA data, presented in Figure V-18, shows that the NSI-6 technique is superior to the Super-SVA technique in suppressing the sidelobes by up to 10dB. Both techniques enhance the resolution by having a narrowing effect on the main lobes, even though the NSI-6 is narrows the main lobes by slightly more than the Super-SVA (about 0.04nsec in deference). However, as shown in the next section, the effect of high levels of noise stresses on the superiority of the new technique of NSI-6. A summary of the processing times and allocated memory, in Kilobytes (kB) using Matlab, for all the techniques in the Beatty Standard measurement is presented in the following table:

Table V-2: Summary of processing times and allocated memory for the different techniques in Beatty Standard measurement

Technique	Processing Time	Allocated Memory
Standard-IFFT	15msec	7.9 kB
SVA	164msec	74.1 kB
RSI-10	127msec	44.3 kB
Super-SVA	1512msec	131.7 kB
NSI-6	91msec	30.6 kB

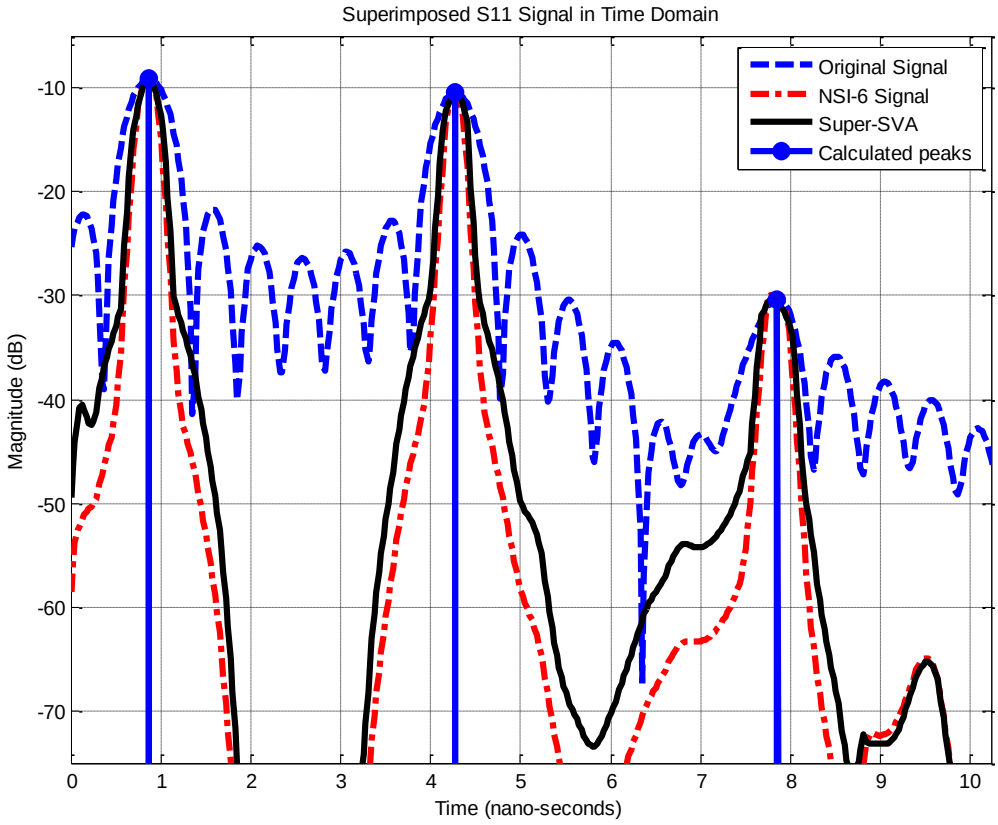

Figure V-18: Comparing Super-SVA with NSI-6 technique

8. Simulating Added Noise to the Beatty Standard Experiment

In all the previous results in this chapter, only noise caused by the measurement that is already embedded in the signals was considered. However, in order to examine the performance of the different techniques in the presence of noise, different cases are used to illustrate the performance at low, medium and high levels of SNR. An Additive White Gaussian Noise is incorporated in the original signal with a specific SNR in the frequency domain using the 'awgn' Matlab built-in function.

i. Simulating Added Noise to Beatty Standard with 0dB SNR

Starting with SNR = 0dB, the original signal, with and without noise, is presented in Figure V-19 along with the noise signal used in order to see the effect of the added noise on the measured signal. Then, in Figure V-20, the standard-SI technique is compared with the conventional Windowing using Hamming and Chebyshev functions. The results show that by adding noise to the original signal, the performances of both of Standard-SI and Windowing functions are noticeably affected. It can be noticed that the first two reflections are completely preserved, these signals being above the levels of added noise. On the other hand, the third reflection is significantly distorted since it has a relatively low signal-power. Actually it can be considered to be undetectable due to the presence of false targets that are generated by due to the noise.

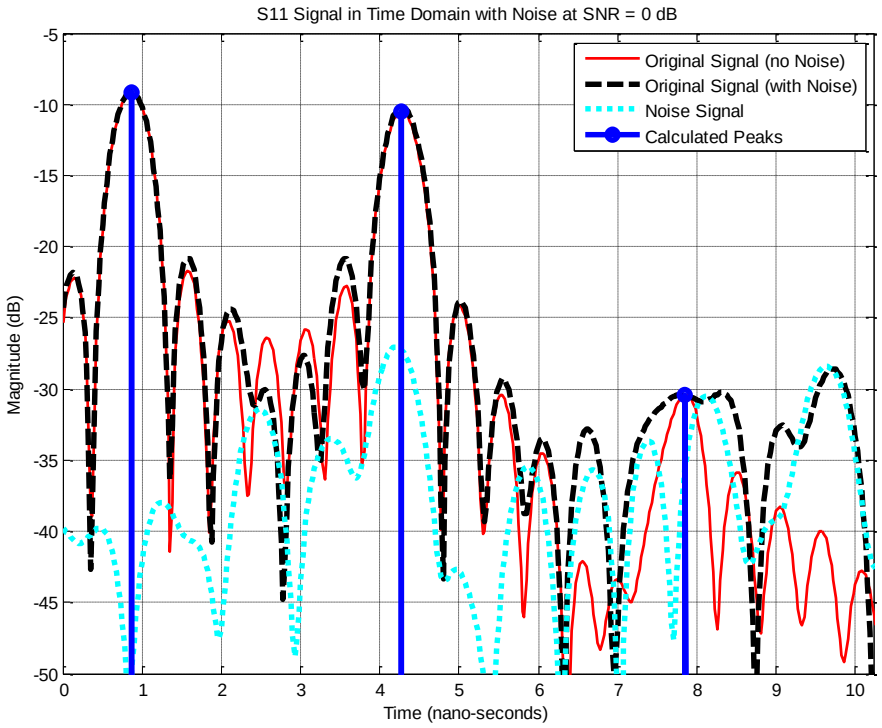

Figure V-19: Showing Effect of Added Noise on the Original Signal (SNR = 0dB)

Concerning the new proposed techniques of Superimposition in presence of noise, Figure V-21 shows both RSI-10 and NSI-6 techniques. The results still show a superiority of the NSI-6 over the RSI-10. However, it is noted that even though the narrowing effect of the NSI-6 technique is still there, it has actually been lessened. Furthermore, it is noticed that the height of the third main lobe is slightly distorted. However, unlike the Standard-IFFT, Standard-SI and Windowing functions, the positions of all three main lobes are still detectable.

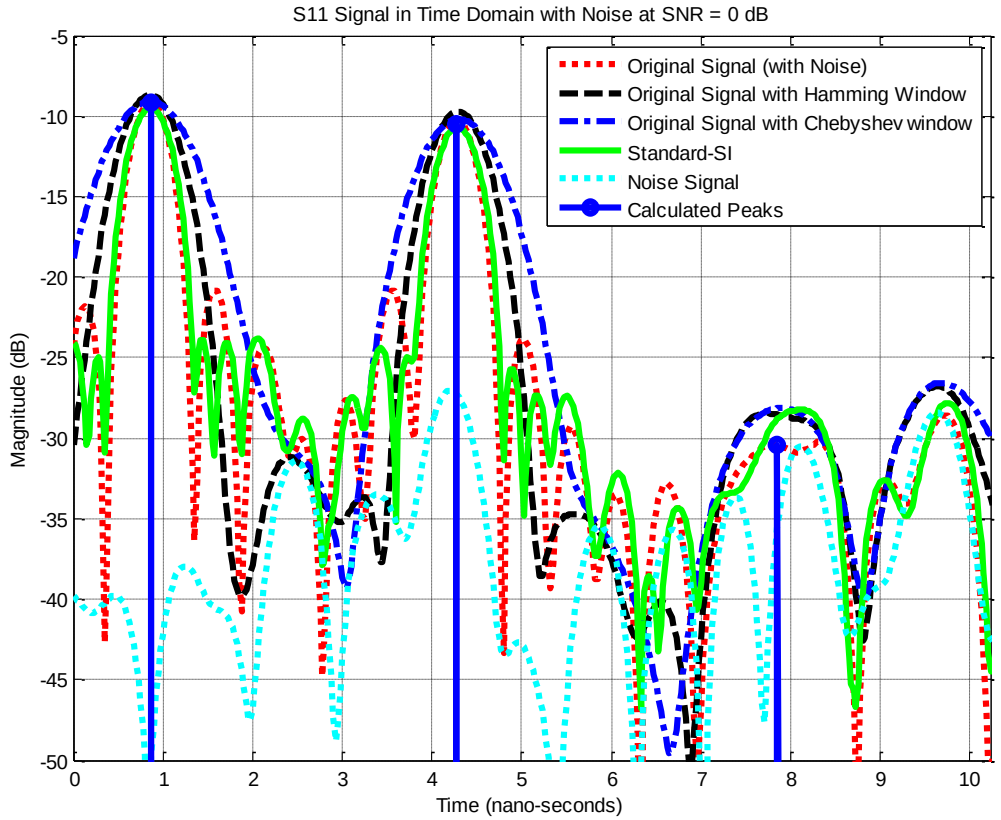

Figure V-20: Comparing Standard-SI with Windowing Functions (Hamming and Chebyshev) at SNR = 0dB

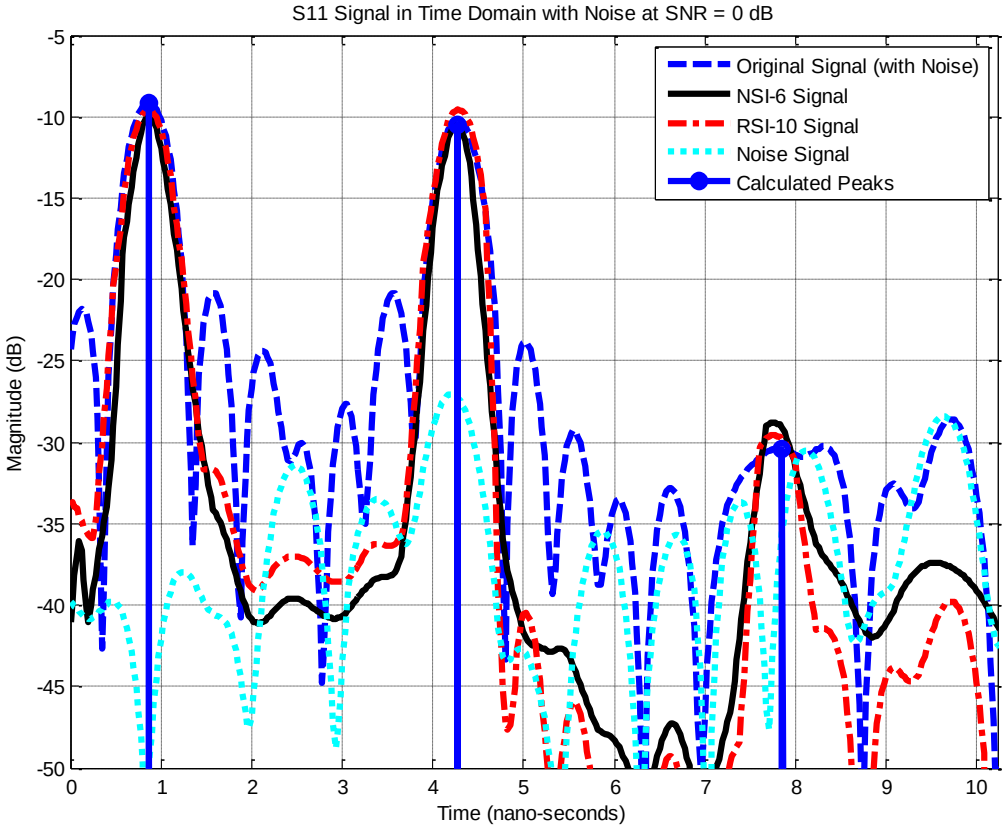

Figure V-21: Comparing Improved Superimposition Techniques (NSI-6 & RSI-10) in the presence of noise

Referring to Figure V-22 and Figure V-23 the SVA and Super-SVA techniques, are compared with NSI-6. It can be noticed that both of SVA and Super-SVA techniques, unlike the NSI-6, have failed to preserve the third main lobe and are clearly more susceptible to the introduction of false targets than the Superimposition techniques: NSI-6 and RSI-10.

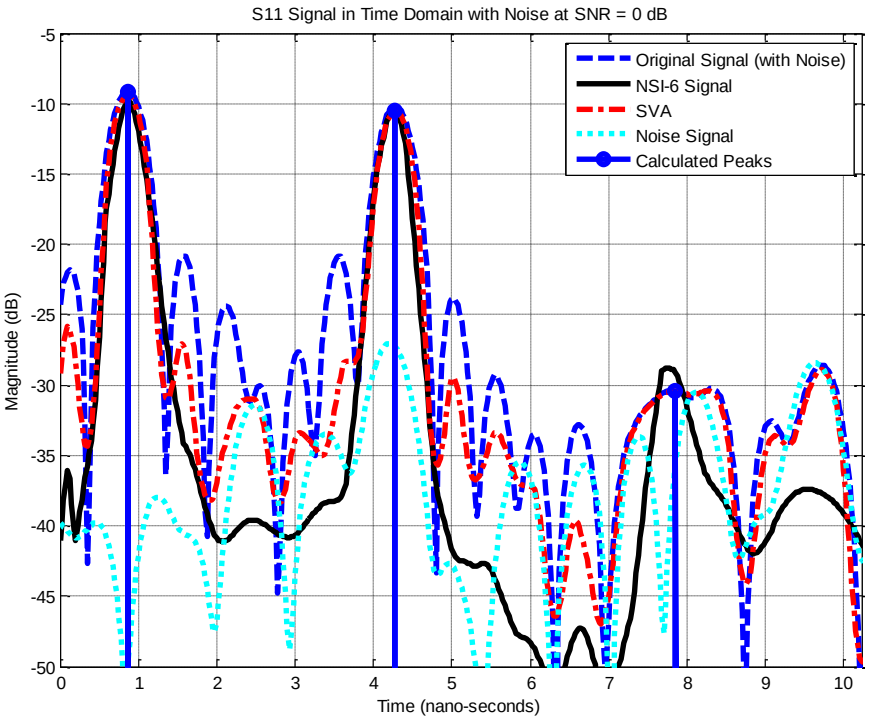

Figure V-22: Comparing SVA with NSI-6 technique in the presence of noise (SNR = 0dB)

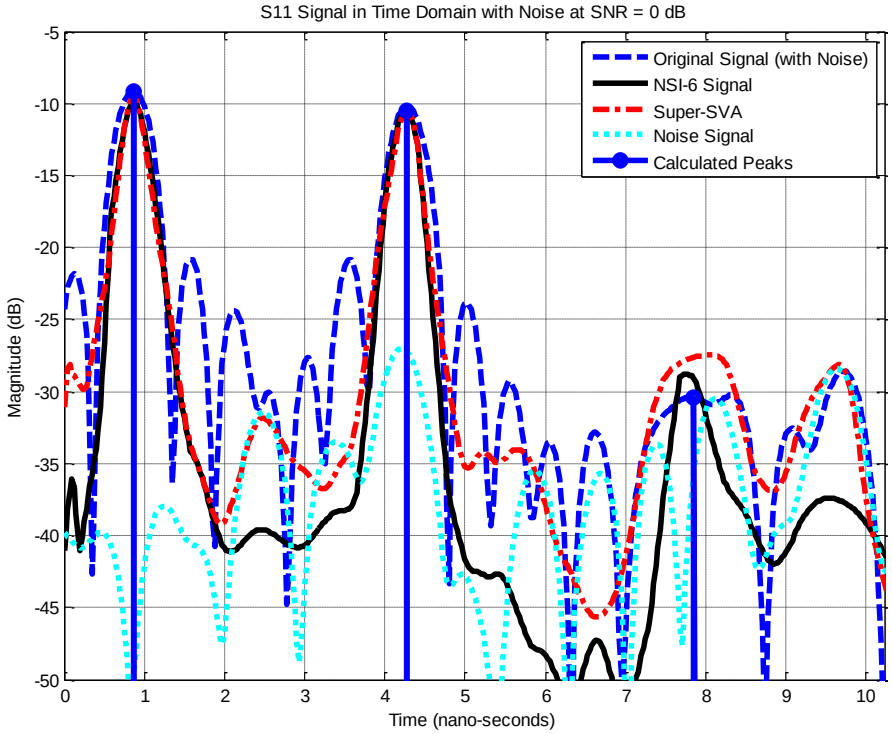

Figure V-23: Comparing Super-SVA with NSI-6 technique in the presence of noise (SNR =0dB)

The influence of noise on a signal can be reduced by averaging if the constant signal is measured in independent noise samples. Figure V-24 shows the comparison of Superimposition using RSI-10 technique with the average of 100 different noisy, and standard-IFFT transformed signals. The traces showing the median plus or minus the standard deviation are included to show the spread on the data and the reliability of the process under 100 independent noise traces. It is noticed that when using the standard-IFFT technique at 0dB SNR, it required 100 different measurements, with statistically independent noise samples, and 100 different FFT processes in order to achieve similar level of performance that is realized using 10 measurements and 10 FFT processes using the new RSI-10 technique.

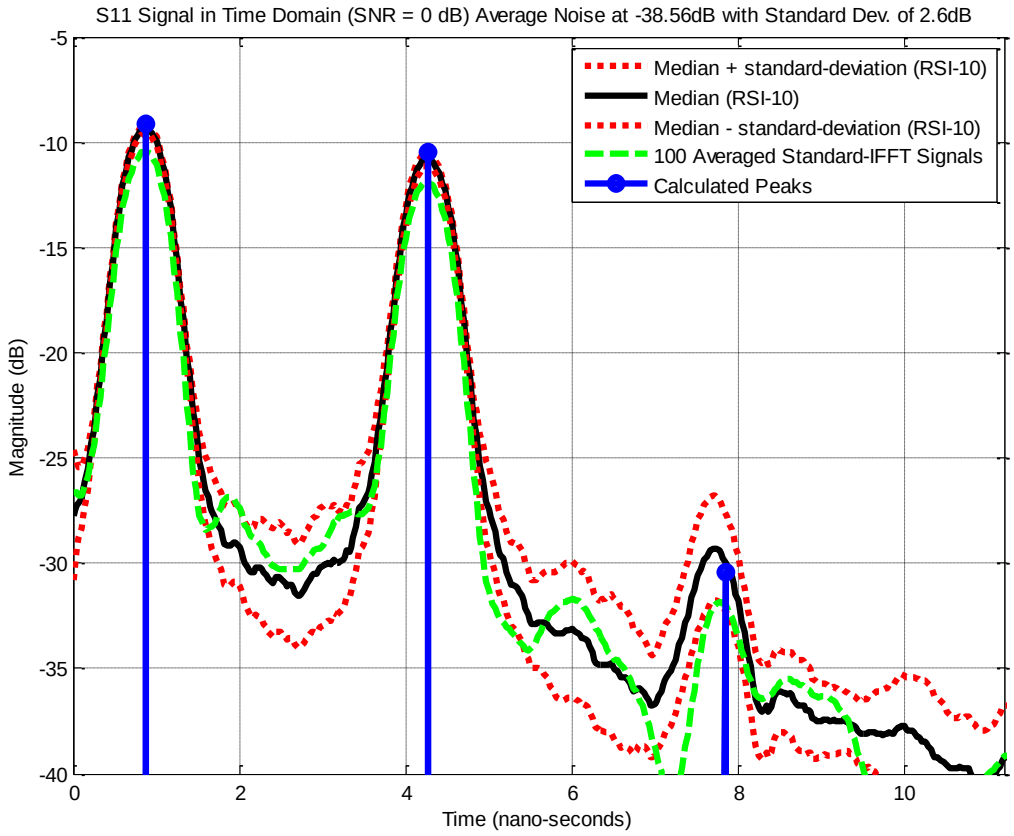

Figure V-24: Comparing RSI-10 with standard IFFT in presence of noise (SNR = 0dB)

ii. Simulating Added Noise to Beatty Standard with -10dB SNR

As the power of the added noise is increased, the SNR level is reduced to -10dB. In Figure V-25, the improved Superimposition techniques of RSI-10 and NSI-6 are compared again at with the new noise level where it can be noticed that the heights of the first two main lobes are slightly affected while the height of the third main lobe is considerably distorted. However, the position of the main lobes can still be detected.

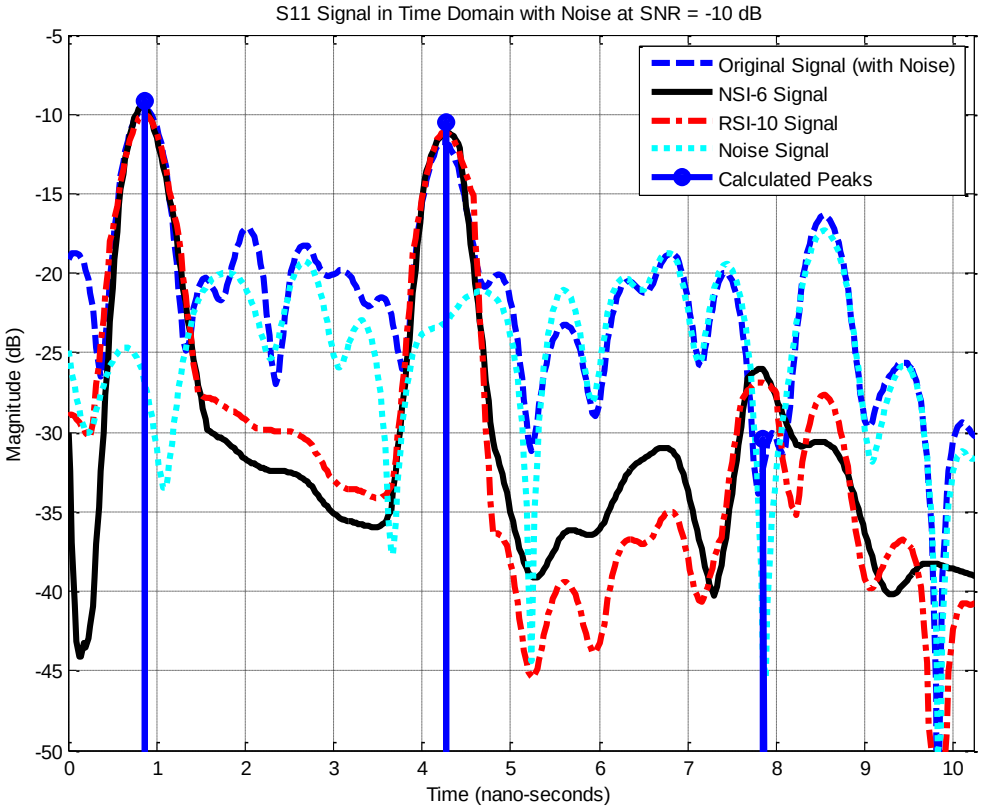

Figure V-25: Comparing Superimposition techniques (NSI-6, RSI-10) in the presence of noise (SNR = -10dB)

NSI-6 is compared with the SVA and Super-SVA in Figure V-26 and Figure V-27 respectively. In these figures the performance of both SVA and Super-SVA is significantly corrupted by the noise. Even though the positions of the first two main lobes are preserved, their height and width are distorted while the third main lobe is completely lost beyond detection due to false targets caused by the added noise.

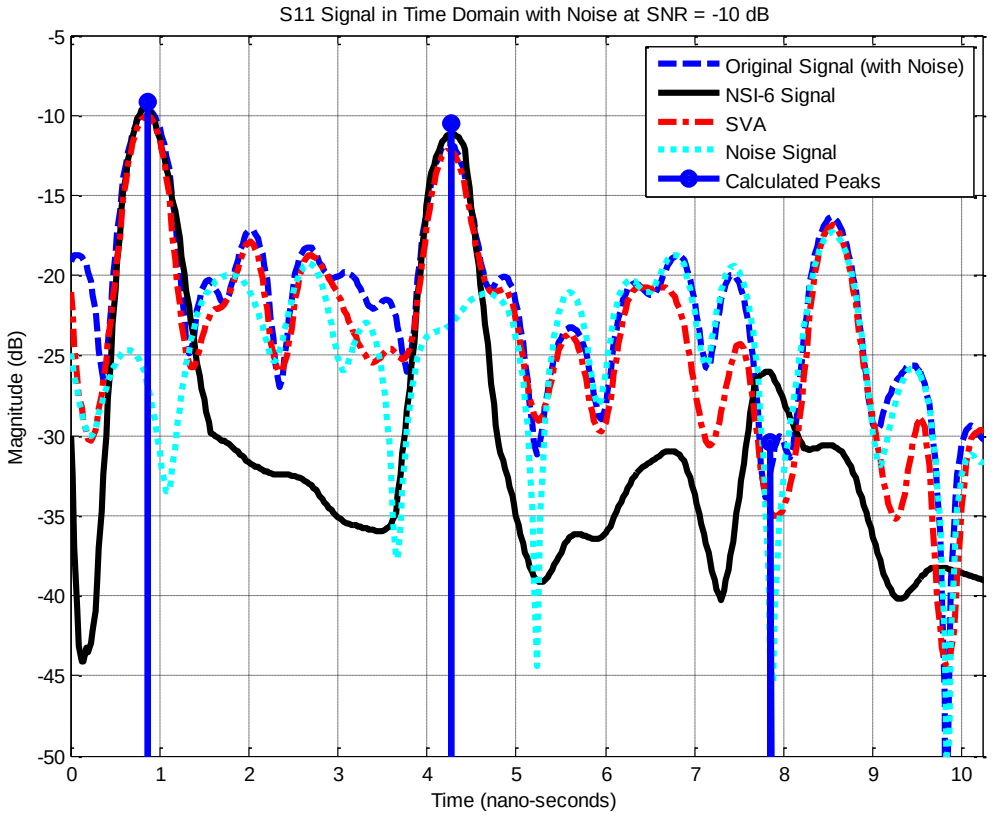

Figure V-26: Comparing SVA with RSi-10 technique in the presence of noise (SNR = -10dB)

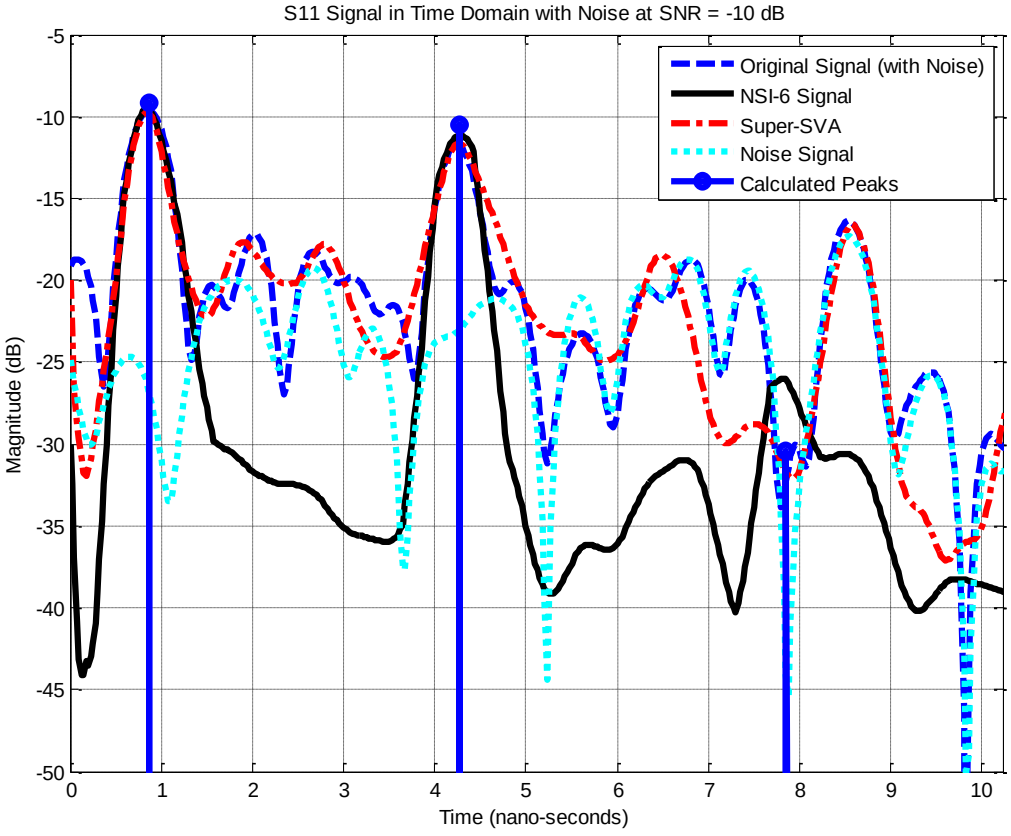

Figure V-27: Comparing Super-SVA with RSI-10 technique in the presence of noise (SNR = -10dB)

iii. Simulating Added Noise to Beatty Standard with -20dB SNR

The power of the noise signal is increased so that the SNR is now -20dB. Figure V-28 shows that the RSI-10 data is more distorted than the NSI-6. In the RSI-10 data, a noticeable spike at 7.8nsec has raised to the extent that it can be detected as a false target even in comparison with the first two authentic main lobes. On the other hand, NSI-6 still preserves the first two main-lobes even though their amplitudes are slightly changed, but the third main lobe, which is considered to be undetectable, is indicated by with the wrong amplitude, due to the high noise power, next to a false target that is shown at 6.3nsec. However, this false target doesn't have an effect on the detestability of the first two main lobes in terms of capability of identifying the true reflections from the false targets.

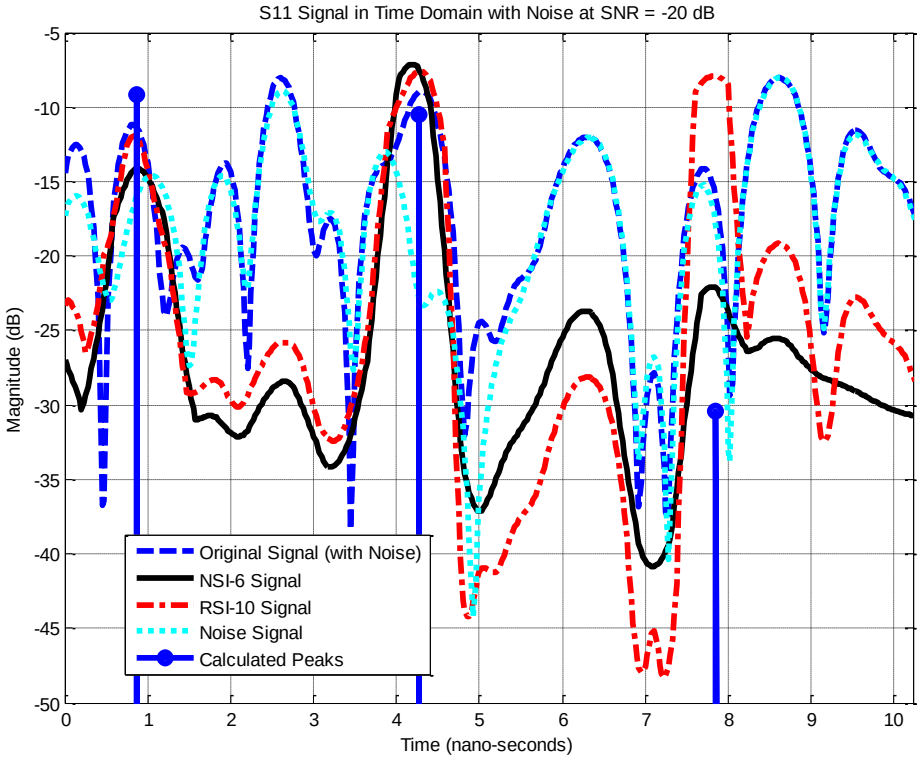

Figure V-28: Comparing Improved Superimposition techniques (NSI-6 and RSI-10) in the presence of noise (SNR = -20 dB)

Similarly, both SVA and Super-SVA, shown in Figure V-29 and Figure V-30, are significantly distorted with the presence of false peaks to the extent that they are both beyond the capability of identifying the true reflections. These results emphasize the superiority that the new techniques of Superimposition provide as oppose to the standard-IFFT technique and the more advanced techniques of SVA and Super-SVA in the presence of noise.

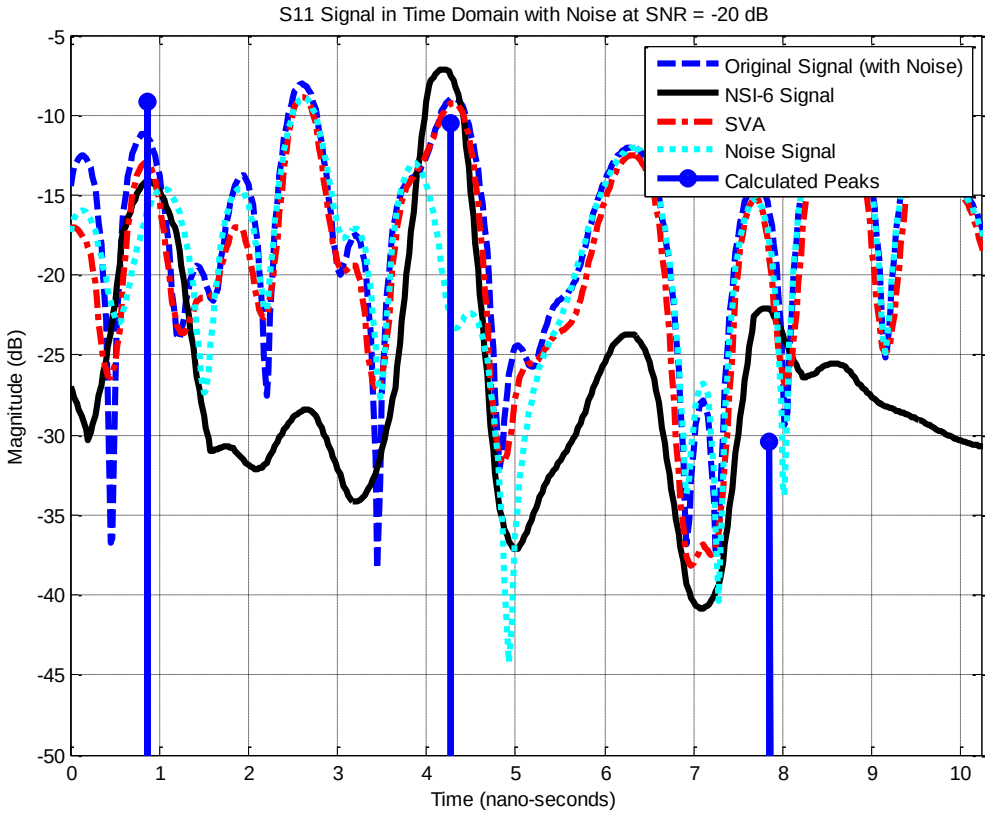

Figure V-29: Comparing SVA with RSI-10 technique in the presence of noise (SNR = -20 dB)

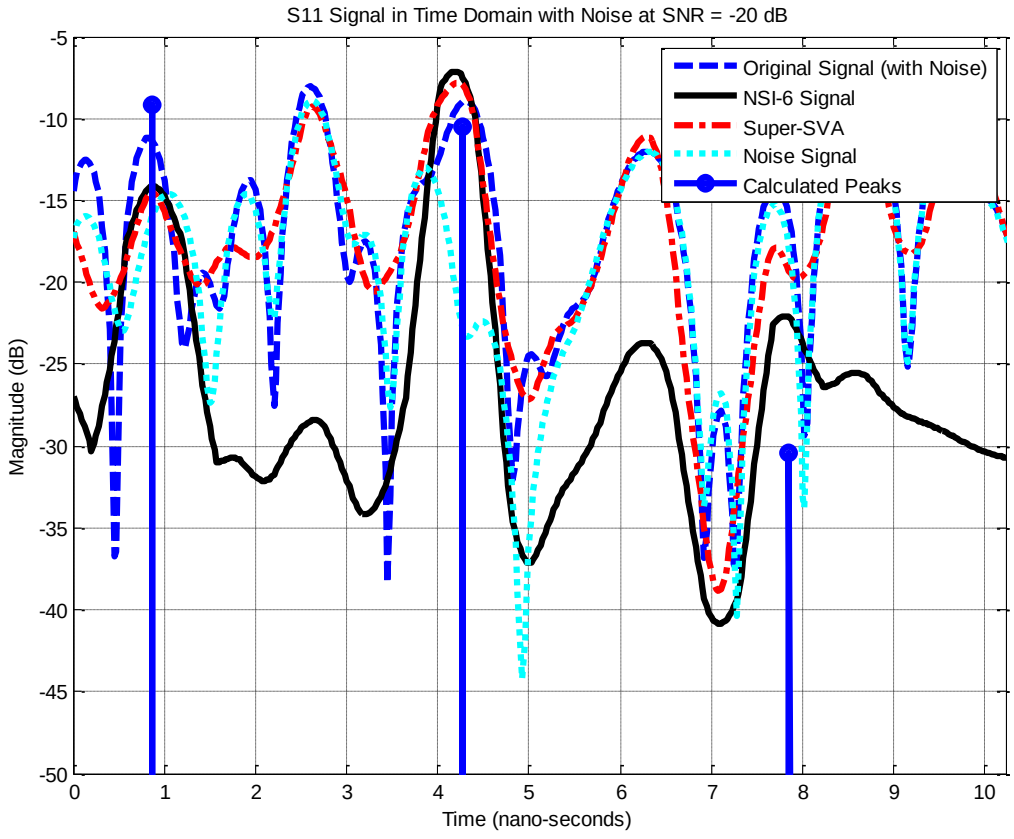

Figure V-30: Comparing Super-SVA with RSI-10 technique in the presence of noise (SNR = -20 dB)

As mentioned earlier, the influence of noise on a signal can be reduced by averaging, if the constant signal is measured in independent noise samples. Figure V-31 shows the comparison of Superimposition with the average of 850 different noisy, and IFFT transformed signals, which achieve similar signal levels to the NSI-6 performance. Clearly using the conventional technique at -20dB SNR, requires 850 different measurements, with statistically independent noise samples, and 850 different IFFT processes in order to achieve the same level of performance that is realized using six measurements and six IFFT processes using the new NSI-6 technique. Finally, as shown in Figure V-32, it is noticed that at -25dB SNR, even the NSI-6 is distorted beyond the ability to identify the true reflections.

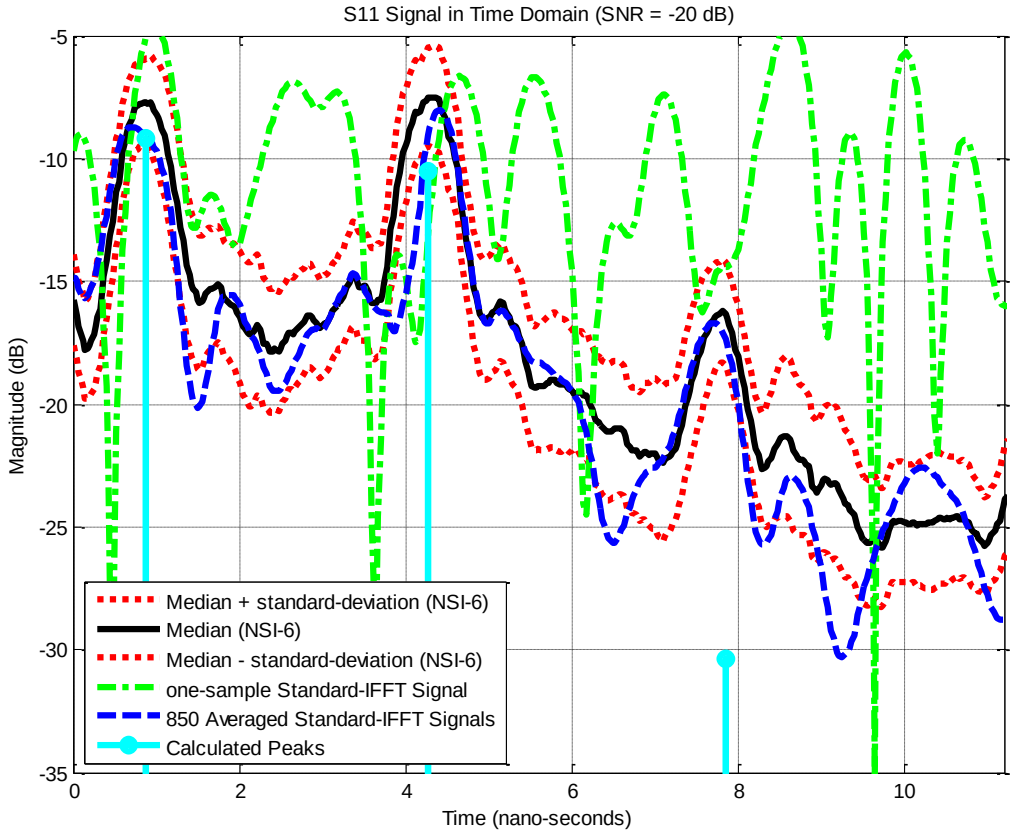

Figure V-31: Assessing NSI-6 technique robustness: comparing with standard-IFFT in presence of high levels of noise (SNR = -20dB)

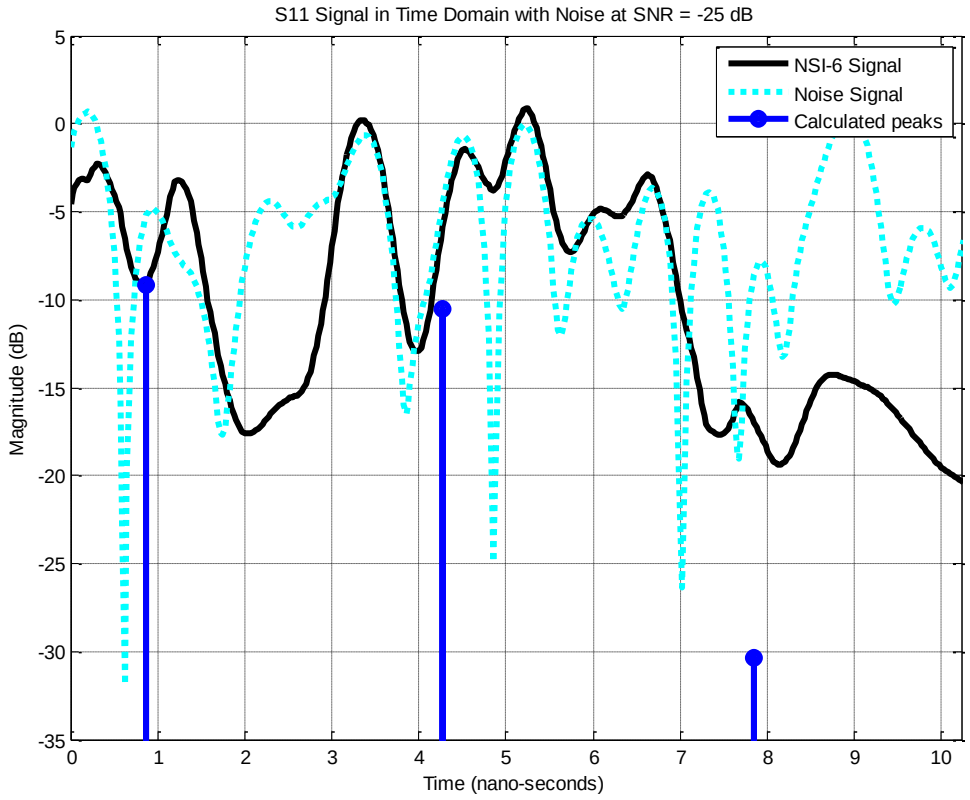

Figure V-32: Presenting performance of NSI-6 technique in very high level of noise (SNR = -25dB)

iv. Assessing the Effect of Noise on Signal Level

Results from the previous subsections raise an interesting question on the ability of the different techniques to combat the effect of noise on the signal. Table V-3 summarise the comparison between standard-IFFT, SVA, Super-SVA, RSI-10 and NSI-6 techniques in terms of signal level, which is the average level of the signal – with its peaks and nadirs, vs. SNR value. It is worth mentioning that the signal level has been taken over the whole measured signal and not only on the part shown in the figures presented in this chapter.

Table V-3: Comparing signal level vs. SNR for the different techniques.

SNR (dB)	Signal Average Level (dB)				
	Standard IFFT	SVA	Super SVA	RSI-10	NSI-6
0	-38.6	-42.3	-43.1	-49.6	-49.5
-10	-29.3	-30.2	-30.5	-42.2	-41.6
-20	-20.4	-20.9	-21.7	-30.2	-31.3

As the power of the noise increases, the average level of the signals, intuitively, increase as well because they get pushed up by the level of noise. However, it is noticed that SVA and Super-SVA techniques are giving nearly the same signal level as the original signal. On the other hand, the superimposition techniques are significantly more robust to the effect of noise as they are designed to suppress sidelobes with the noise contained in them.

9. Unsharp-Mask Sharpening Technique

Even though, sharpening techniques are not usually considered in such measurements, the mathematics of the unsharp-Mask sharpening technique has been applied to the Beatty Standard signal in order to observe the effect of this technique on the main-lobes and sidelobes of targets' signals. The sharpening technique examined in this thesis is using the Matlab built-in functions: "fspecial" and "imfilter". The trace representing the sharpening technique effect on the Original signal with the presence of only measured noise is presented in Figure V-33. It can be noticed that sharpening technique actually smoothes the sidelobes. Furthermore the cases of added noise levels of 0 dB SNR, -10 dB SNR and -20 dB SNR, which are shown in Figure V-34, Figure V-35 and Figure V-36 respectively. Due to the fact that the performance of the sharpening technique is highly correlated with the accuracy of the original signal, the sharpening technique actually degrades rapidly in the presence of noise.

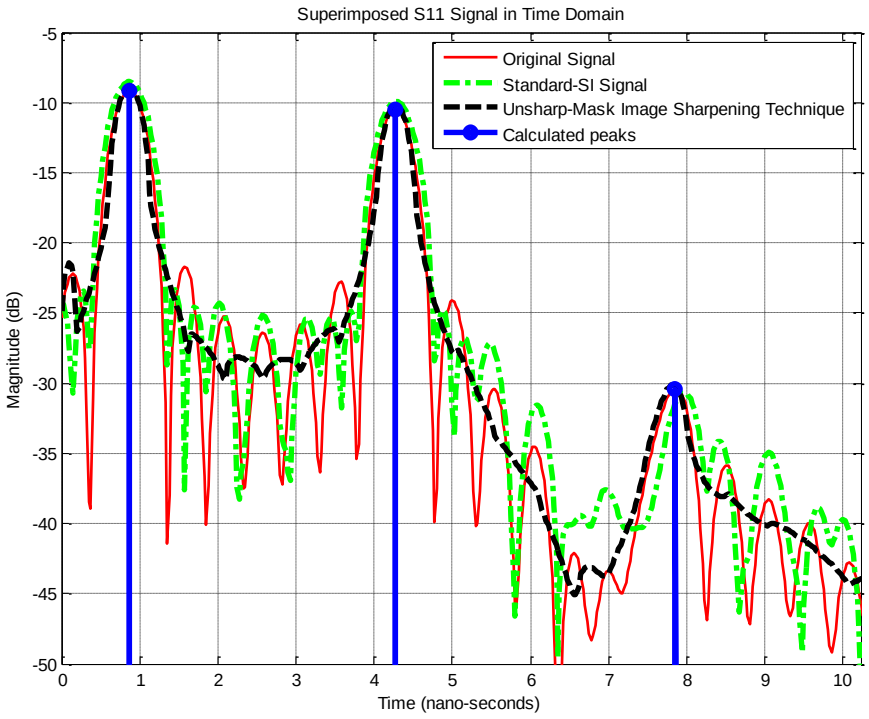

Figure V-33: Assessing Sharpening technique performance on measured signal in comparison with standard-SI

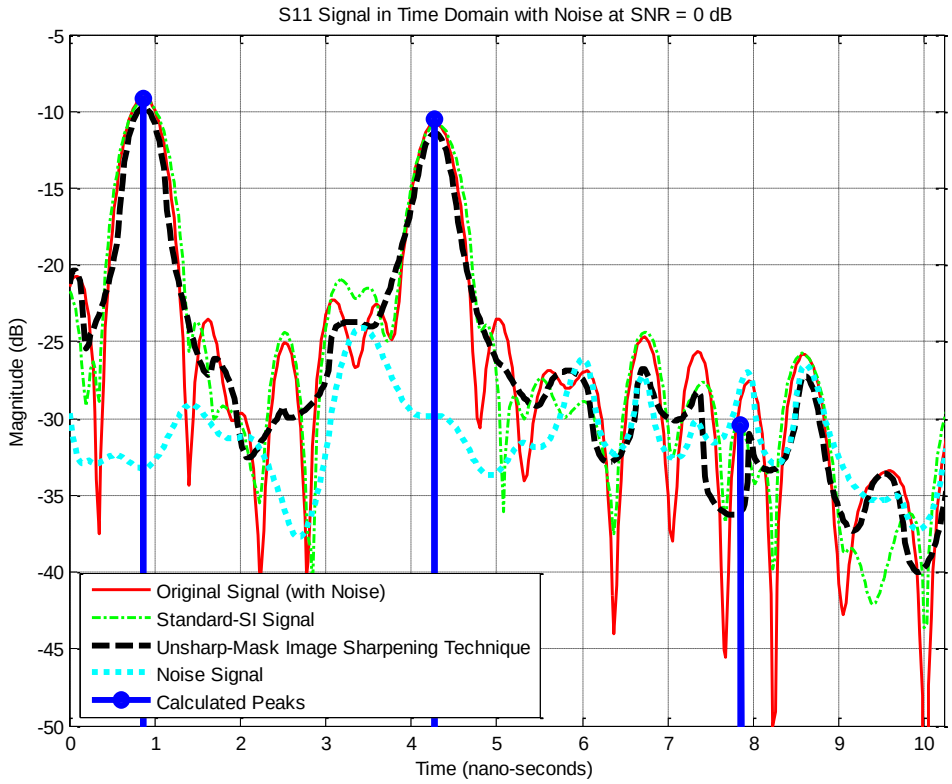

Figure V-34: Comparing Standard-SI with Sharpening technique in presence of noise (SNR = 0dB)

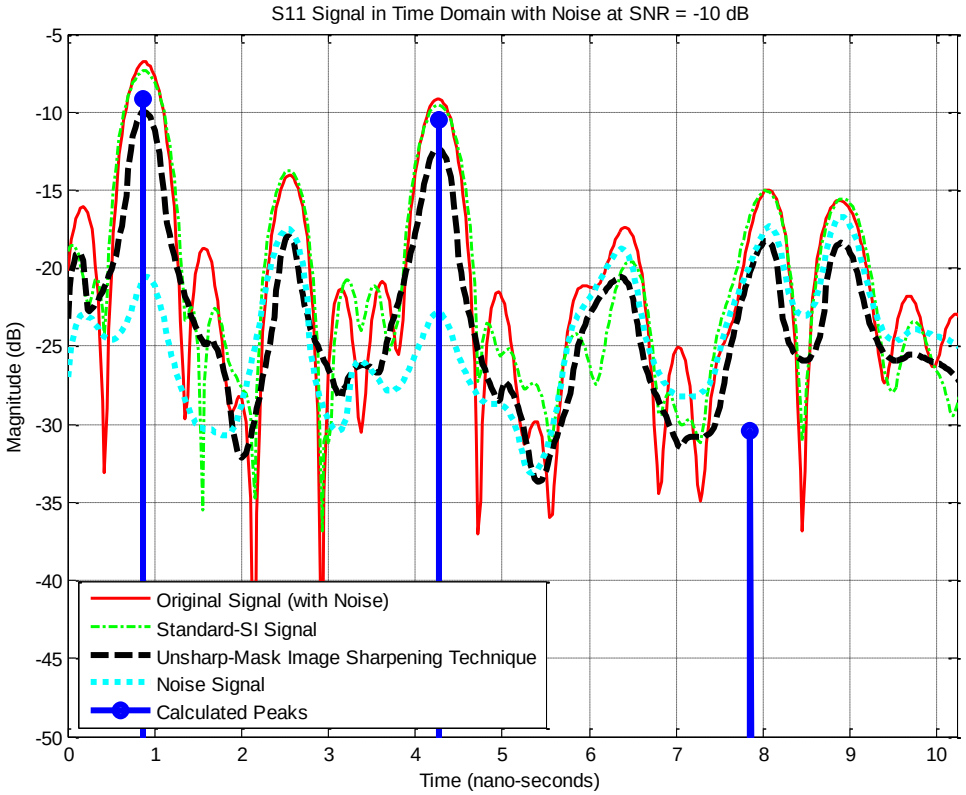

Figure V-35: Comparing Standard-SI with Sharpening technique in presence of noise (SNR = -10dB)

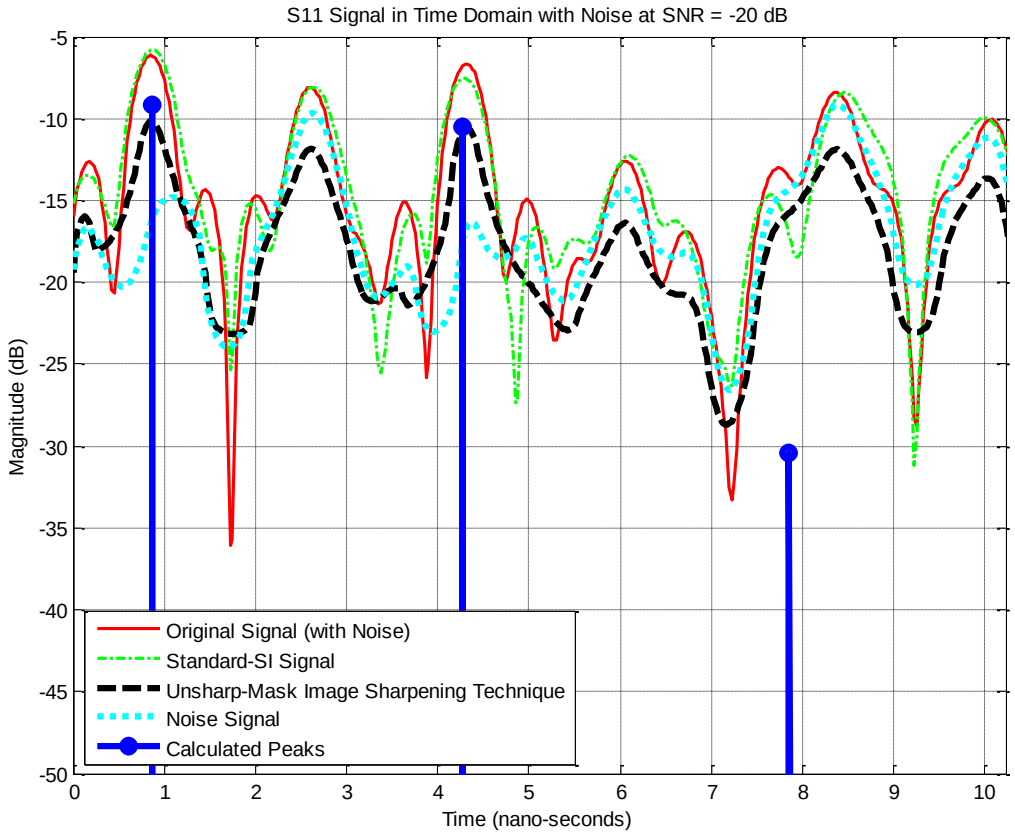

Figure V-36: Comparing Standard-SI with Sharpening technique in presence of noise (SNR = -20dB)

10. Ground Penetrating Radar Simulation and Measurement

Initial simulations, which are presented in [127], of two GPR target responses are performed and the outcome for a case where there are two targets that are positioned far from each other is illustrated in Figure V-37, where the second target produces a rather weaker response. The standard-IFFT calculation shows considerable sidelobe response where the second target is only recognisable as a slight disturbance to the side lobes. Applying a Hann window reduces the side lobes making the second target clearly identifiable. However the Hann window also broadens the main lobe causing a significant effect on resolution. The superimposed-IFFT using the RSI-8 technique also reduces sidelobes but with no increase in the width of the main lobe.

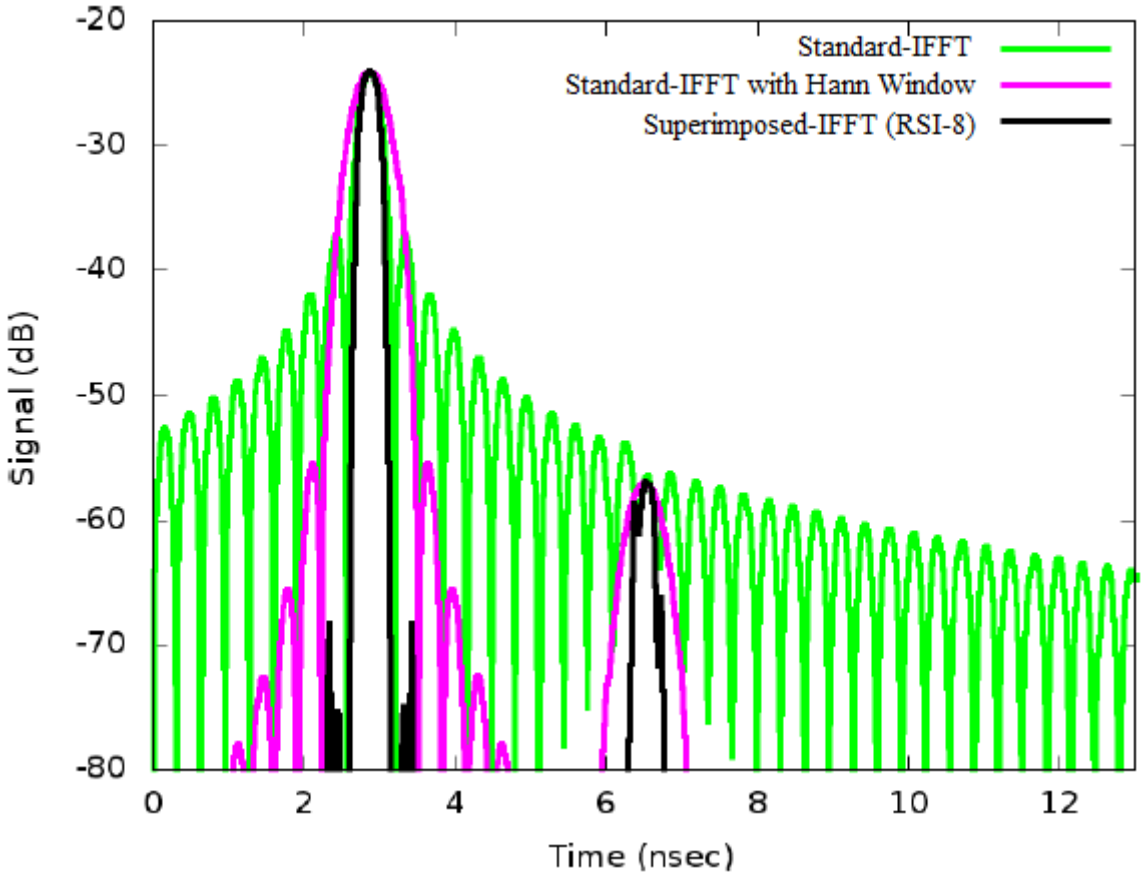

Figure V-37: Simulated responses from two targets. The second weaker target produces a minor influence on the Rectangular windowed analysis. The analysis of this research shows good resolution in time with very minor sidelobes.

Considering the effect of the width of the main lobe on resolution, Figure V-38 shows the case where the weaker second target is quite close to the first target. Again the second target produces a small disturbance in the side lobes of the standard-IFFT evaluation. In the Hann window case the sidelobes are greatly reduced, but the two targets merge into one main lobe that is wider than that for a single target. The superimposed-FFT using the RSI-8 technique of this research reduces the sidelobes and still presents two separate main lobes showing that the two targets are clearly resolved into two identifiable responses.

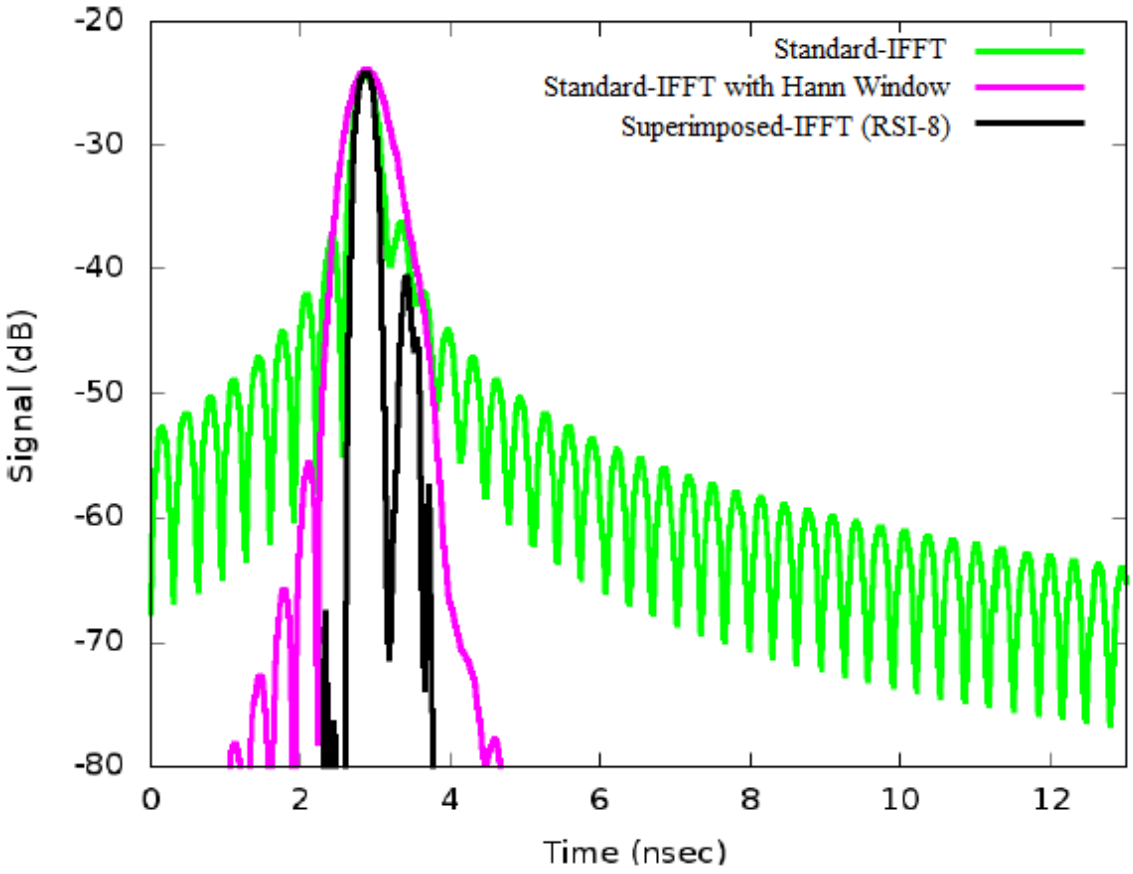

Figure V-38: Simulated responses from two closely spaced targets. The second target is hardly visible when using Rectangular or Hann windows, but RSI-8 produces discrimination of the two targets with almost no sidelobes.

In addition to the simulation, a real-life GPR image generated by superimposed-IFFT using RSI-8 technique, shown in Figure V-39, where data from a commercial GPR unit operating around 250 MHz, sampled every 2.3 cm as the unit moves over the suspected target has been processed. There is a clear indication of the target at a depth of about 1.2 m, which corresponded quite well with known records for this field. There are other responses, and it is not known if these are genuine reflecting objects as the ground has not been excavated to confirm what was buried.

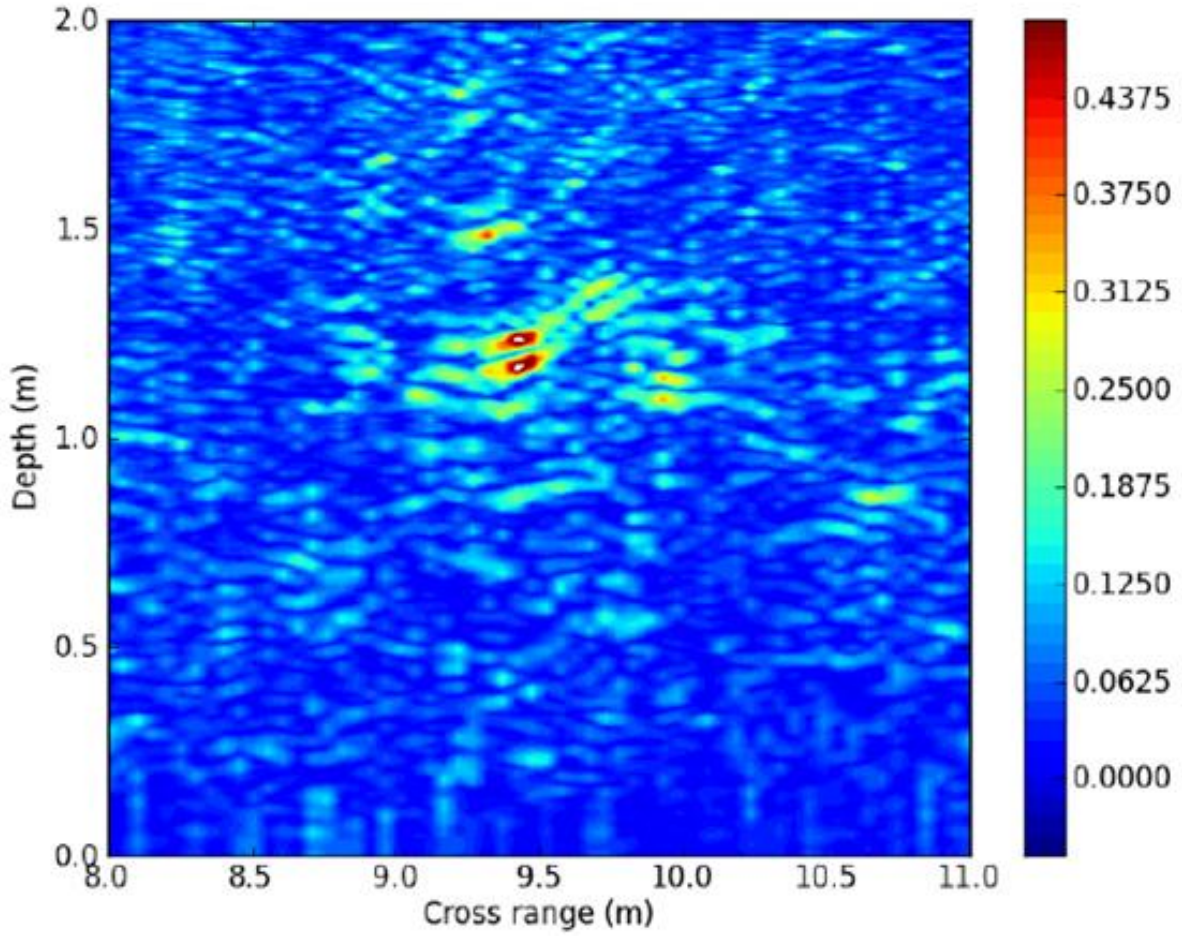

Figure V-39: Focussing of commercial GPR data taken around 250MHz over a pipe buried in a field. Main peak breaks into two peaks. Other peaks may be due to anomalies in the ground.

Figure V-40 shows the image formed of processed GPR data using standard-IFFT taken over a test site. In this case, metal pipes at cross ranges of 4.2 m and 5.2 m are known to be buried with an air filled plastic pipe in between at 4.6 m and deeper pipes at 5.7 m and 6.4 m. These deeper targets produced minor responses, while the two shallower metal pipes are quite visible. The air filled pipe in between the shallow metal pipes produces a response, but it is rather dominated by the responses from the metal pipes. Anyway, in both of these cases of real-life image formation from GPR measurements, the contrast in amplitude in the image field between targets and 'uniform' ground is not that great. The images were evaluated using permittivity data from other measurements for that site, and so are thought to be quite accurate. The data used was typical B-scan data with measurement points every 2.3 cm across the ground. The fill in away from the targets seems to be due to the fact that so many similar measures are used which nearly focus at positions near the targets.

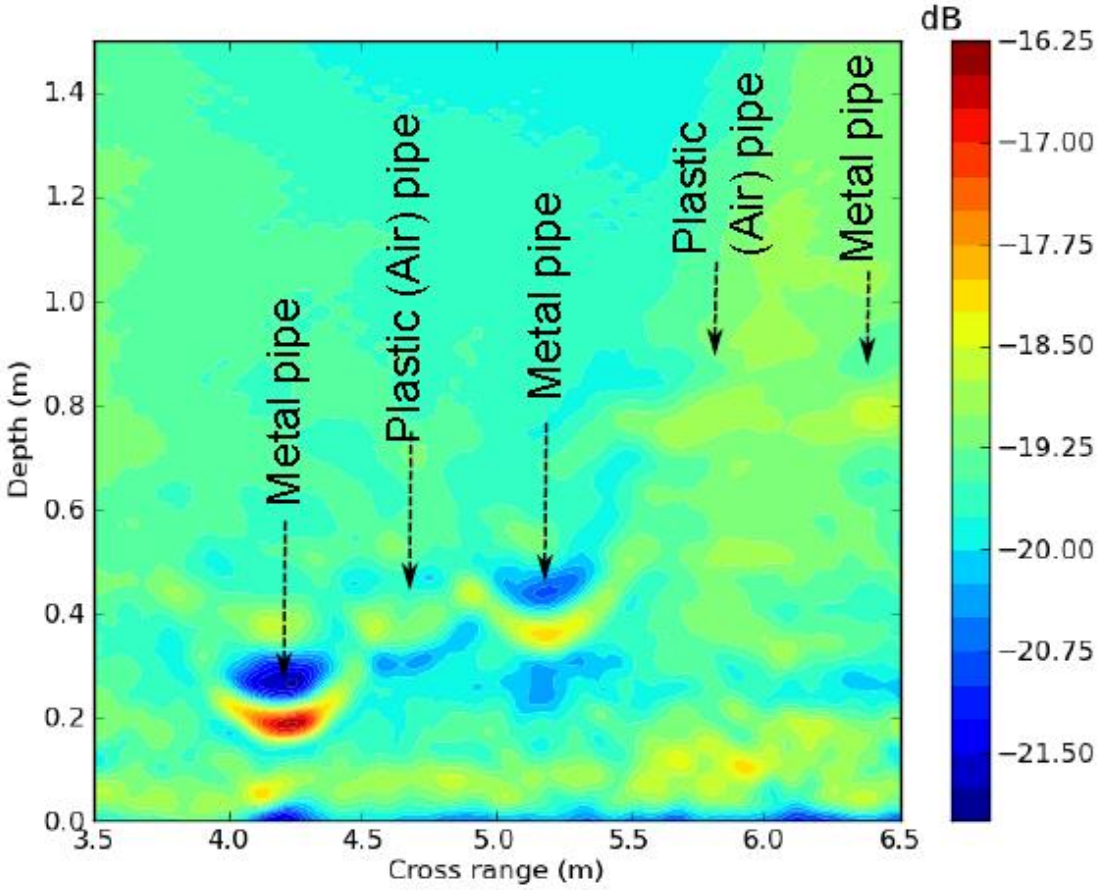

Figure V-40: Analysis of data from a commercial GPR operating around 250MHz, showing quite clear indication of two metal pipes at cross ranges of 4.2m and 5.2m. Some indication of the air filled plastic pipe at cross range of 4.6m, and the deeper pipes at 5.7m and 6.4m.

In many cases an accurate knowledge of permittivity may not be available. Using an approximate value results in a poorly focussed and low amplitude image using the normalisation scheme, NSI-6, while a high amplitude well focussed image is found with the correct permittivity. Generating images for several assumed permittivities over a $\pm 25\%$ range of permittivity around the true value, and summing the separate images gives the resultant image in Figure V-41 for a simulated example of four targets and just seven reception points spaced every 0.5 m over the target area. The targets are visible, but there is much extraneous response from the images generated by the incorrect permittivities. The image intensity and contrast maximise when the image is properly focussed with the true permittivity, and so provide an indication of the best image that is formed using the true permittivity. The best image in this example is shown in Figure V-42 where the four targets have been resolved to 'point targets' with about 40 dB suppression of off-target responses.

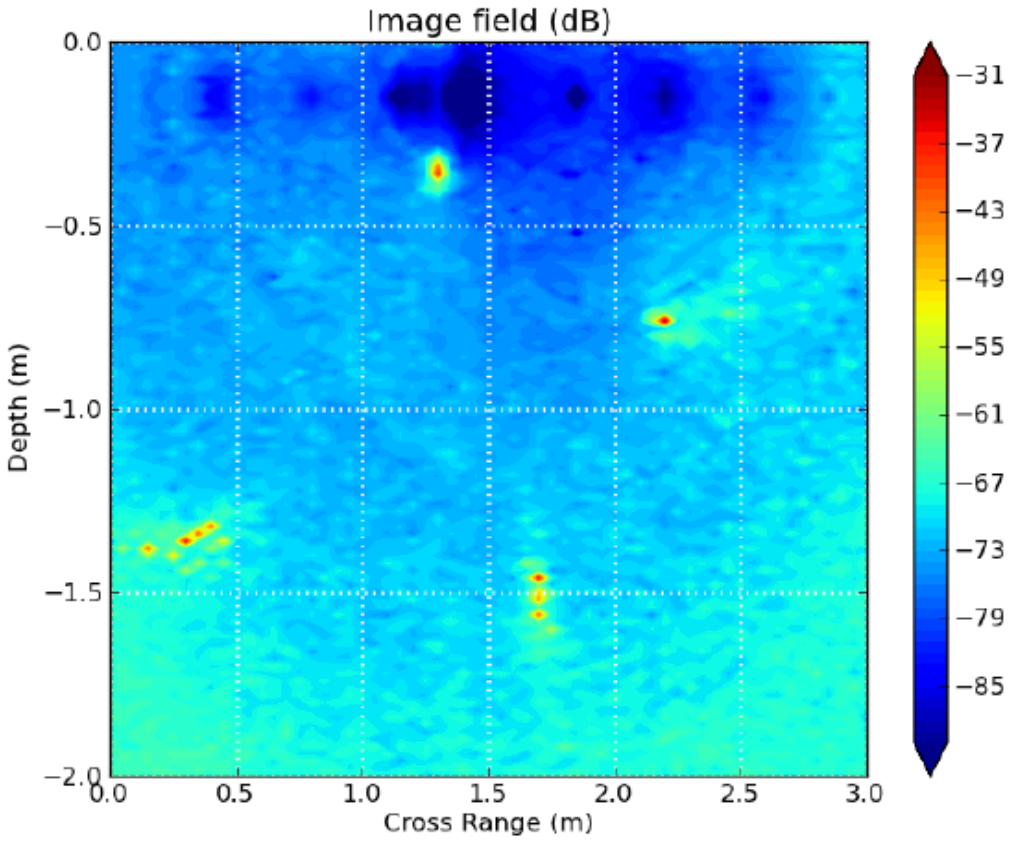

Figure V-41: Focussing of simulated FMCW GPR data over a bandwidth 100 MHz- 4 GHz when the permittivity is unknown and a ± 25% range is used around an estimate. The 4 targets are visible but there is a high level of extraneous response.

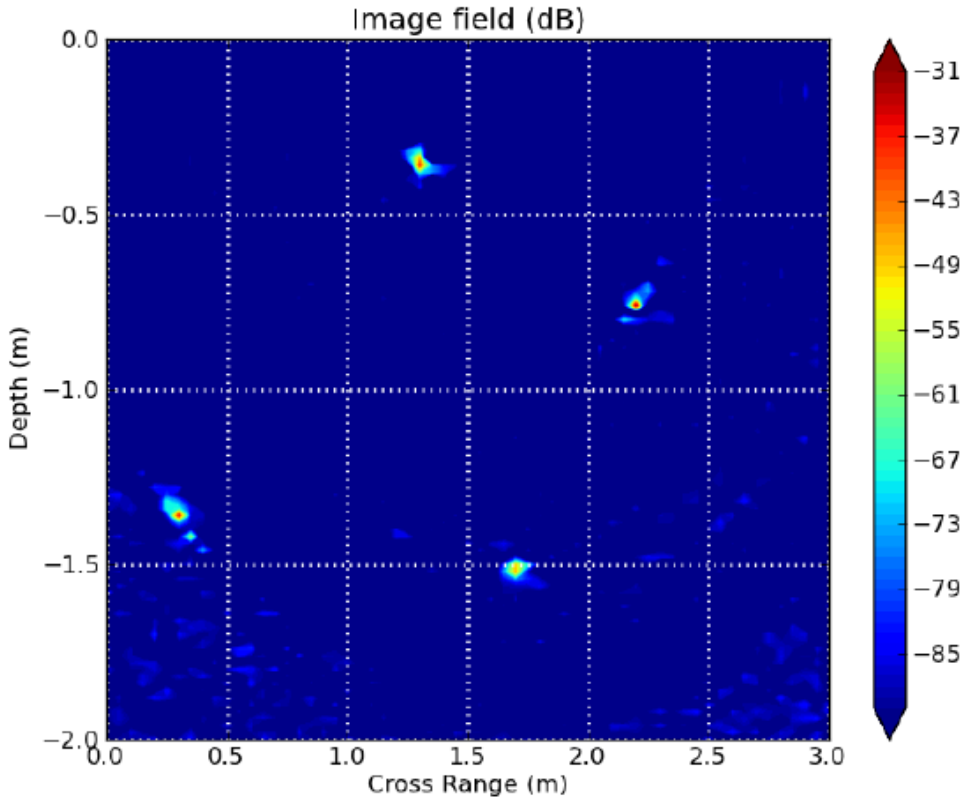

Figure V-42: Focussing of simulated FMCW GPR data over a bandwidth 100 MHz- 4 GHz data for 4 targets using what is identified as the best estimate of permittivity.

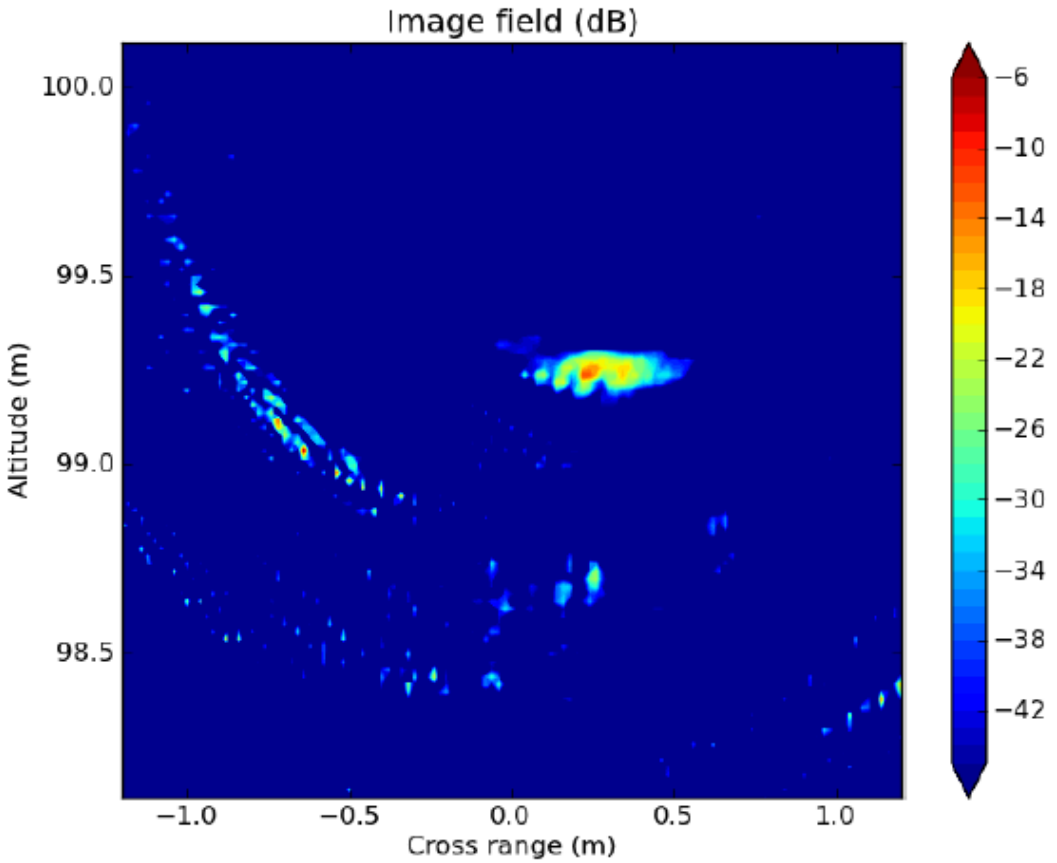

Figure V-43: Focussing of simulated FMCW GPR data over a bandwidth 100 MHz- 4 GHz data for 4 targets using what is identified as the best estimate of permittivity.

The superimposed-IFFT using NSI-6 technique has also been applied to data measured with an experimental SFCW GPR over an area of ground suspected to contain one buried pipe. Using a $\pm 25\%$ permittivity range around a permittivity estimate of $\varepsilon_r = 7.5$ gained from the B-scan from a commercial GPR measuring the same target a best estimate was obtained. The resulting image is shown in Figure V-43. The indication of best permittivity estimate of ε_r is less clear than in the previous simulated data, but it still provides a permittivity estimate over the range $\varepsilon_r = 7.3 \rightarrow 7.9$. The indicated target depth and cross range position agrees well with data from site plans and that from a commercial GPR.

11. Chapter Summary

In this Chapter, an Ansoft simulation is introduced and results are presented. In this simulation, NSI and RSI are thoroughly examined to find the most advantageous design in terms of the order N that is to use six signals for the Normalization technique (NSI-6) and ten signals for the Repetitive technique (RSI-10). The improved Superimposition technique of NSI-6 is shown to be superior to all other techniques of standard-IFFT, Hamming

Windowing Function, SVA and Super-SVA in all standard quality metrics that were used to assess the performance in terms of suppressing sidelobes and enhancing resolution with a relatively small increase in processing time when compared to standard-IFFT but it was still faster than the other techniques.

After that, Beatty Standard experiment is considered. The importance of Beatty Standard, which is real-life measurement (before adding the additional simulated noise), is that it has multiple reflectors with an emphasis on the significance of the third reflector being relatively lower in amplitude and more susceptible to noise. The measured data obtained from the experiment has been processed using conventional and superimposed frequency-time conversion. Results showed the superiority of the superimposition technique over conventional sidelobes suppressing techniques as it has shown minimal resolution loss, significant sidelobe reduction, and negligible distortion of peak positions from the original spectrum and enhanced resolution. Furthermore, when noise signals with different power values were added to the measured signal, the conventional techniques were highly affected and generated false targets while both of the improved techniques of Superimposed-IFFT RSI-10 and NSI-6 were more robust. Results showed that it required averaging 100 different measured signals using standard-IFFT to have the same level of performance of the RSI-10 technique at 0dB SNR. More to the point, at -20dB SNR when using standard-IFFT, 850 different measurements had to be taken with 850 different IFFTs that had to be computed while only six measurements with six IFFTs had to be done if using the improved Superimposed-IFFT technique of NSI-6. Additionally, the unsharp-mask sharpening technique has been applied to the Beatty Standard measured signal. These Beatty Standard results show that superimposed-IFFT techniques, especially that of NSI, have superior performance to the standard sidelobe suppression techniques and standard image sharpening technique.

Finally, GPR simulation and image formation using real-life GPR measurements, which are presented in [127], are studied in section 10. Results show that the superimposition technique is superior to the standard-IFFT scheme in terms of reducing the sidelobe levels while maintaining the width of the main lobe. In conjunction with the normalisation process, NSI-6, the sidelobes are almost eliminated and that the main lobe width is reduced.

Chapter VI: SAR Simulation & Image Formation

1. Introduction

The fundamentals of Synthetic Aperture Radar (SAR) are detailed in chapter 2, where it is highlighted that by using an active microwave system it is possible to generate images of a target. This chapter starts simulating a basic SAR system in order to evaluate the performance of the new proposed superimposition technique and compare it to the conventional standard-FFT technique. After that, a thorough in-depth performance analysis of real-life SAR images generated using various techniques in comparison with the SAR images generated using the proposed superimposition technique is conducted and assessed. It is worth mentioning that throughout this chapter all reference to Superimposition technique is referring to the FFT-based NSI-6 technique. The SAR signal processing algorithm used for the different techniques is based on the basic RDA signal processing block diagram, see Figure VI-1.

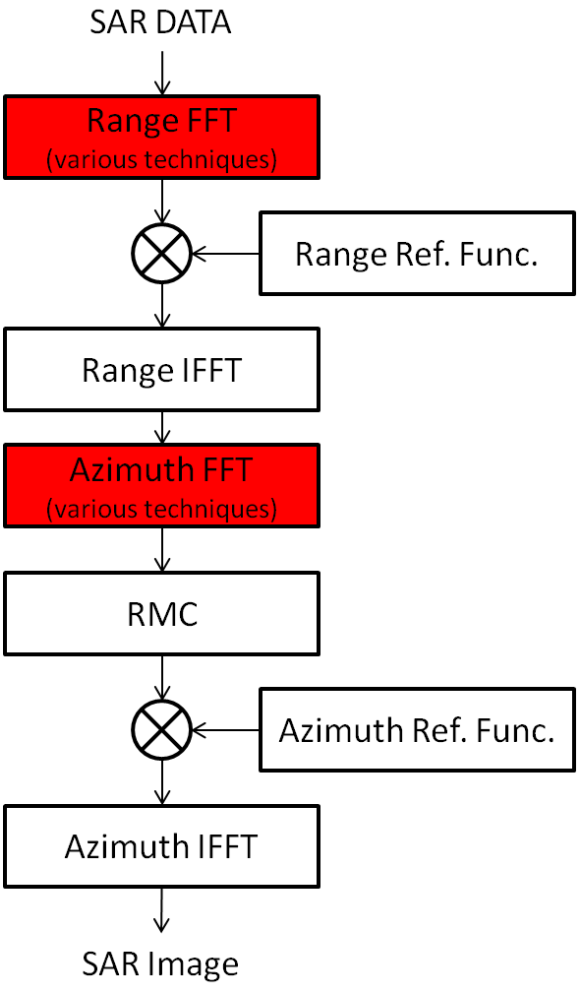

Figure VI-1: Basic RDA Signal Processing Block Diagram

In this chapter, real-life SAR data is processed to form SAR images using the different techniques for the Range and Azimuth FFT blocks. The techniques compared for these blocks are the standard-FFT, standard-FFT with Hann Windowing, NSI-6, SVA, Super-SVA. Standard image sharpening techniques are also compared in the analysis.

2. Simulation of Point Spread Function for SAR Model

The point-spread function (PSF) of an imaging system is also sometimes called the impulse response [113]. However, the term impulse response is usually reserved for linear time/space invariant systems [128]. PSF is an important characteristic in SAR systems since it is used to determine the correlation and sampling properties of the imagery. Furthermore, it is an important concept for describing the properties of both point and distributed targets and how they interplay, which is central in calibrating SAR for accurate measurements of the geophysical quantities known as RCS and the radar backscattering coefficient. Since a SAR system is spatially varying, the term point spread function (PSF) is used to describe the response of the SAR sensor to a particular reflector. The resolution limit of closely spaced reflectors in range is determined by the bandwidth of the transmitted signal and the resolution limit in azimuth is determined by the bandwidth of the induced azimuth signal, which is strongly dependent on the length of the physical antenna on the SAR sensor. The PSF of a SAR system is determined by these resolution limits and is limited by the physical attributes of the SAR sensor (i.e. antenna length) [116]. However, technically speaking, the PSF is a sinc-like function and produces the bright, star-like artefacts that are noticeable around strong reflectors in the focused image. A SAR system is simulated by generating a SAR signal for a single reflector. As the normalized pulse $s(t)$ is defined by:

$$s(t) = \frac{1}{\sqrt{\acute{t}}} Rect\left(\frac{t}{\acute{t}}\right) \quad \textbf{(Eq. VI-1)}$$

This signal is then demodulated and subjected to Range and Azimuth compression using matched filtering and Discrete Fourier Transformation. The transformation between time and frequency domain is performed by FFT and IFFT. The outcome of the simulation of a single point reflector using standard-FFT is presented in Figure VI-2. It can be noticed that the sidelobes actually spread far from the targeted main-lobe.

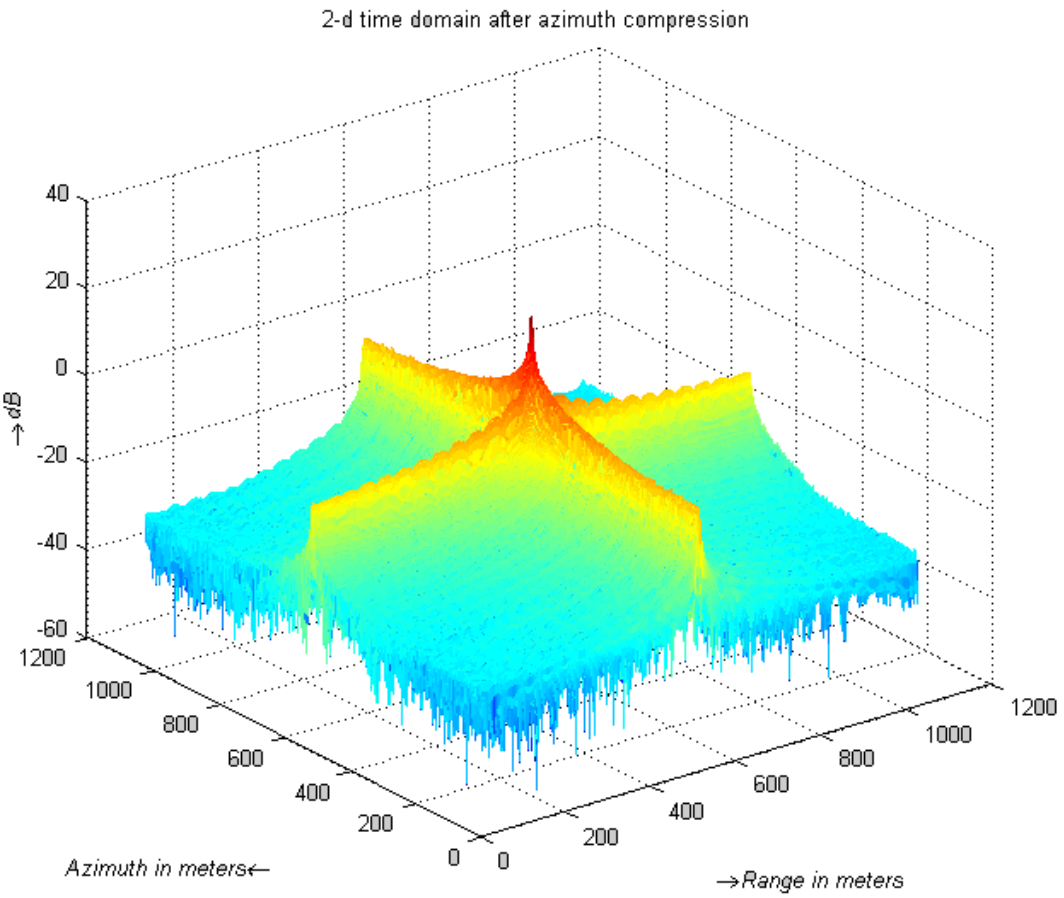

Figure VI-2: Spectrum Result of the Simulation of a single point reflector in SAR

Subsequently, Figure VI-3 and Figure VI-4 show the spectrum results of the PSF for standard-FFT and for NSI-6 respectively in 2D format in order to have a better assessment of the effect of both techniques on the level of sidelobes. It can be noticed that the spatial resolution has enhanced and that sidelobes have actually been suppressed more by using the NSI-6 technique when compared to the standard-FFT technique. The results show that the target's position and magnitude are preserved in both techniques. However, the sidelobes have been significantly suppressed by the NSI-6 technique. It can be noticed that the PSLR value for the outcome of standard-FFT is -13dB while for the NSI-6 outcome it's -21dB. More to the point, the sidelobes that are further from the target are down by nearly -20dB in the PSF using NSI-6 when compared to the PSF using standard-FFT. For ISLR measurements, the main-lobe and sidelobe areas of a SAR image of a point target are delimited by ellipses. The main-lobe is defined by a small elliptical area whereas the main-lobe plus sidelobe areas are limited by a bigger elliptic area. The dimensions of these ellipses are given by ($2\Delta x$, $2\Delta r$) for main-lobe and ($10\Delta x$, $10\Delta r$) for sidelobes as defined in subsection 4.iii of Chapter I. ISLR values for PSF using standard-FFT and NSI-6 technique are -6.69dB and -24.78dB respectively.

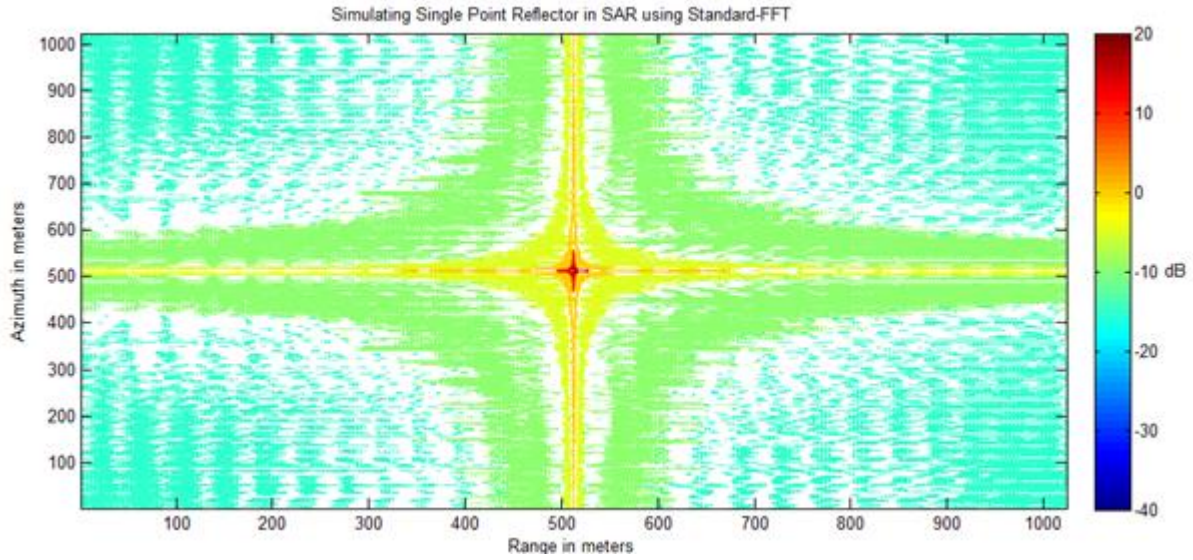

Figure VI-3: Point Spread Function using standard-FFT

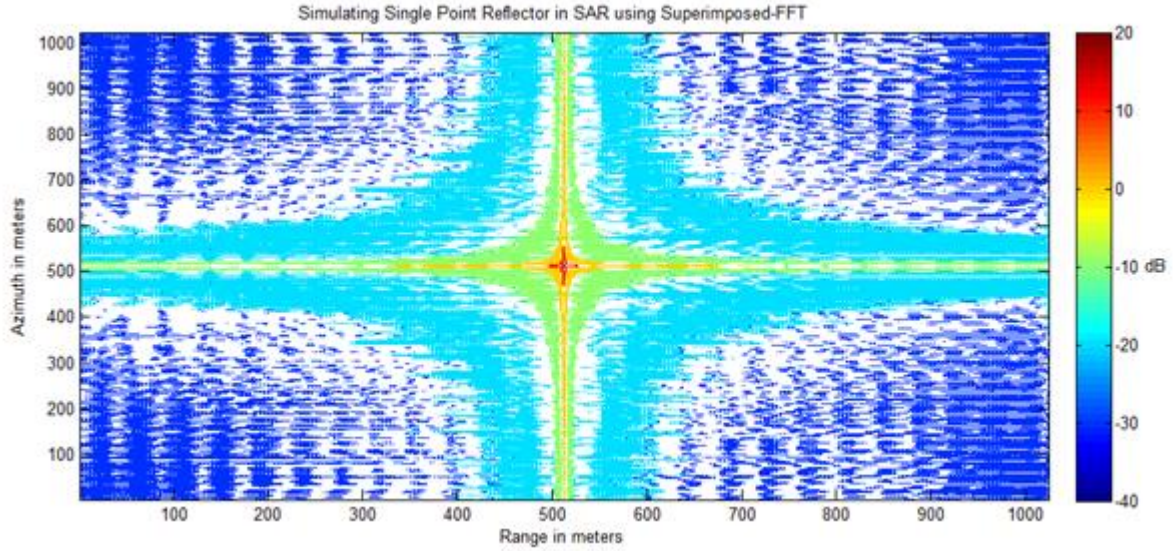

Figure VI-4: Point Spread Function simulation using Superimposed-FFT (NSI-6)

3. Simulation of Two Point Targets and Distributed Targets in SAR

This section discusses the results of a SAR simulation based on the basic RDA model discussed in subsection 9.*v* of Chapter 2. At first, a simulation of a response from two targets is performed using standard-FFT and NSI-6 techniques that are presented in Figure VI-5 and Figure VI-6, respectively. The results confirm the findings reported in the previous section in regard to the relation between each target and its sidelobes. Conversely, in terms of the effect of the accumulated sidelobe caused by the joint of sidelobes from the two different responses, the result of the standard-FFT technique shows that even though the two targets are positioned far apart, an accumulation of the sidelobes of the two responses has generated a new peak with magnitude of 17.4dB at the 600-metre point in range axis, which can be

falsely detect as a target. On the other hand, when the same simulation is performed using NSI-6 technique, the overlapping sidelobes from the two targets have accumulated to only 1.2dB, which is 16.2dB smaller than the standard-FFT technique.

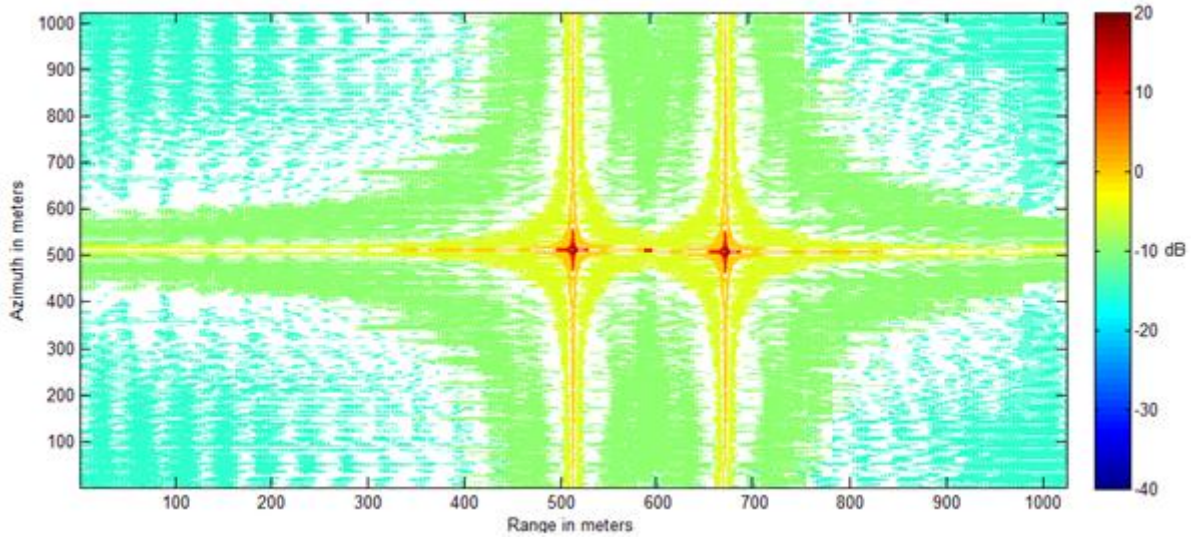

Figure VI-5: Simulation of two targets generated using standard-FFT

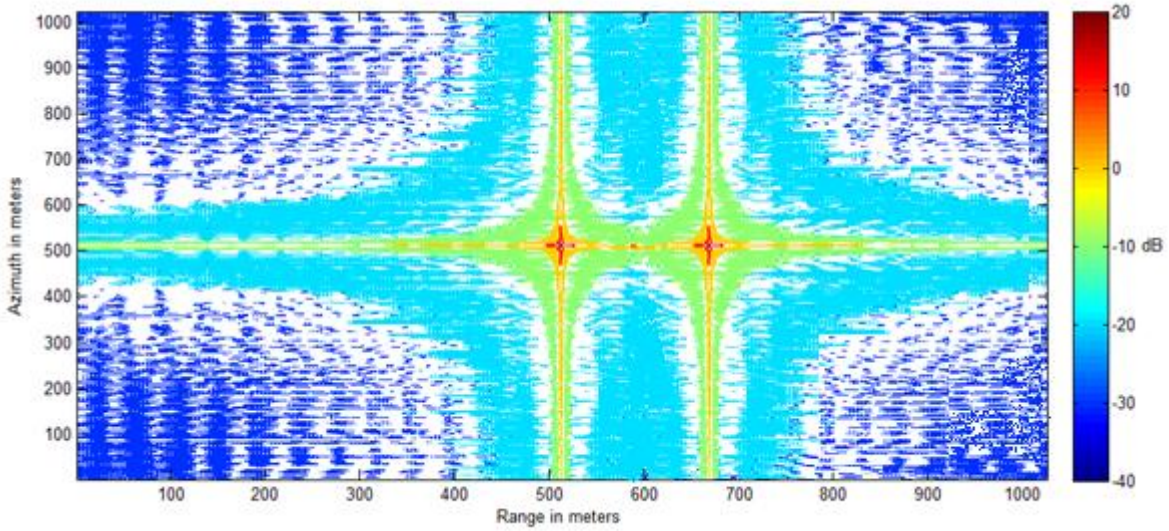

Figure VI-6: Simulation of two targets generated using Superimposed-FFT (NSI-6)

After that, using the same RDA-based SAR model, an extended target is simulated using both standard-FFT and NSI-6 techniques, results are presented in Figure VI-7 and Figure VI-8. Similar to the finding from the PSF analysis in section 2, the results show that the target's position, magnitude and shape haven't change in both techniques. Yet, in terms of sidelobe levels, NSI-6 technique shows clear superiority in suppressing sidelobes. The standard-FFT technique has a PSLR and ISLR values of -15.6dB and -9.3dB, respectively. While for the NSI-6 technique, PSLR and ISLR values are -23.2dB and -33.6dB respectively. Furthermore, the vast fluctuations in the sidelobes of the standard-FFT technique along axes away from main the extended target can be mistaken for individual point targets.

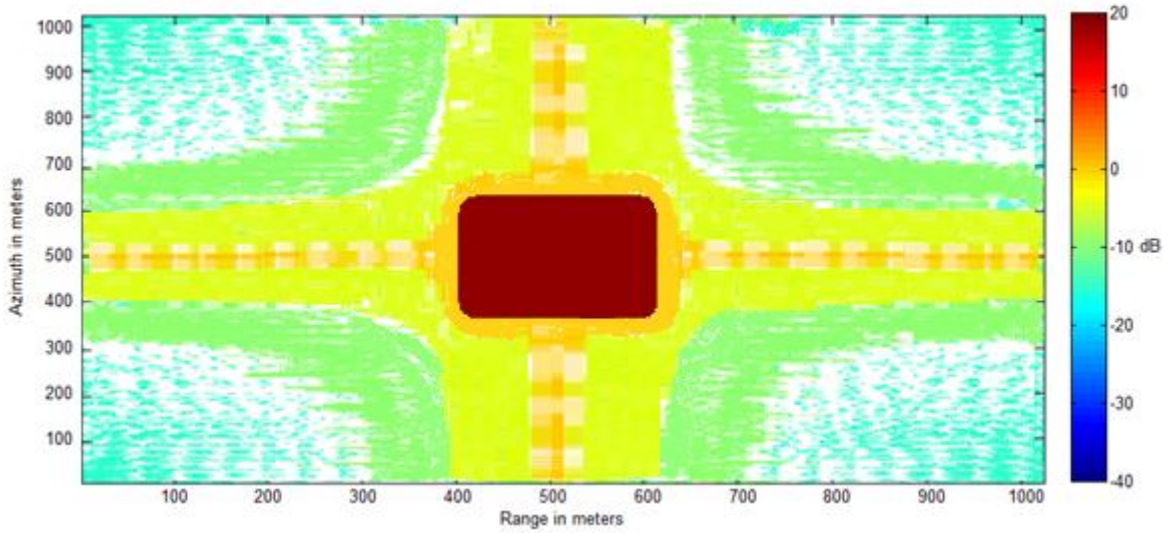

Figure VI-7: Simulation of an extended target using standard-FFT

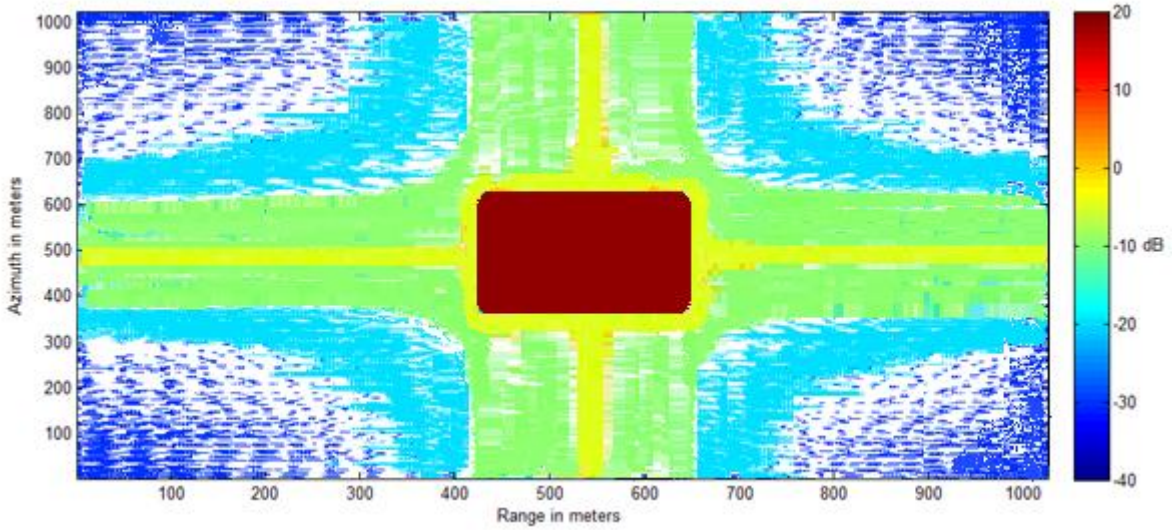

Figure VI-8: Simulation of an extended target using Superimposed-FFT (NSI-6)

4. Image Formation using Real-Life Spaceborne SAR

Real-life data for a spaceborne SAR image has been obtained from [4]. The data was acquired by the RADARSAT-2 mission of Canadian Space Agency in June 2002 for the Vancouver lower mainland. The scene shows water, farmland and a city area. This data is processed using Matlab Software (v. 2010a). First, Range compression is performed and the image is generated. After that, Azimuth compression is performed and the final image is gained, which has 245,830 pixels. The same system is processed using NSI-6 superimposition technique. Both SAR images formed using the standard-FFT and NSI-6 FFT are shown in Figure VI-9. It can be noticed that the focus of the image is enhanced due to suppressing the sidelobes causing a certain level of blurriness especially at the circled areas.

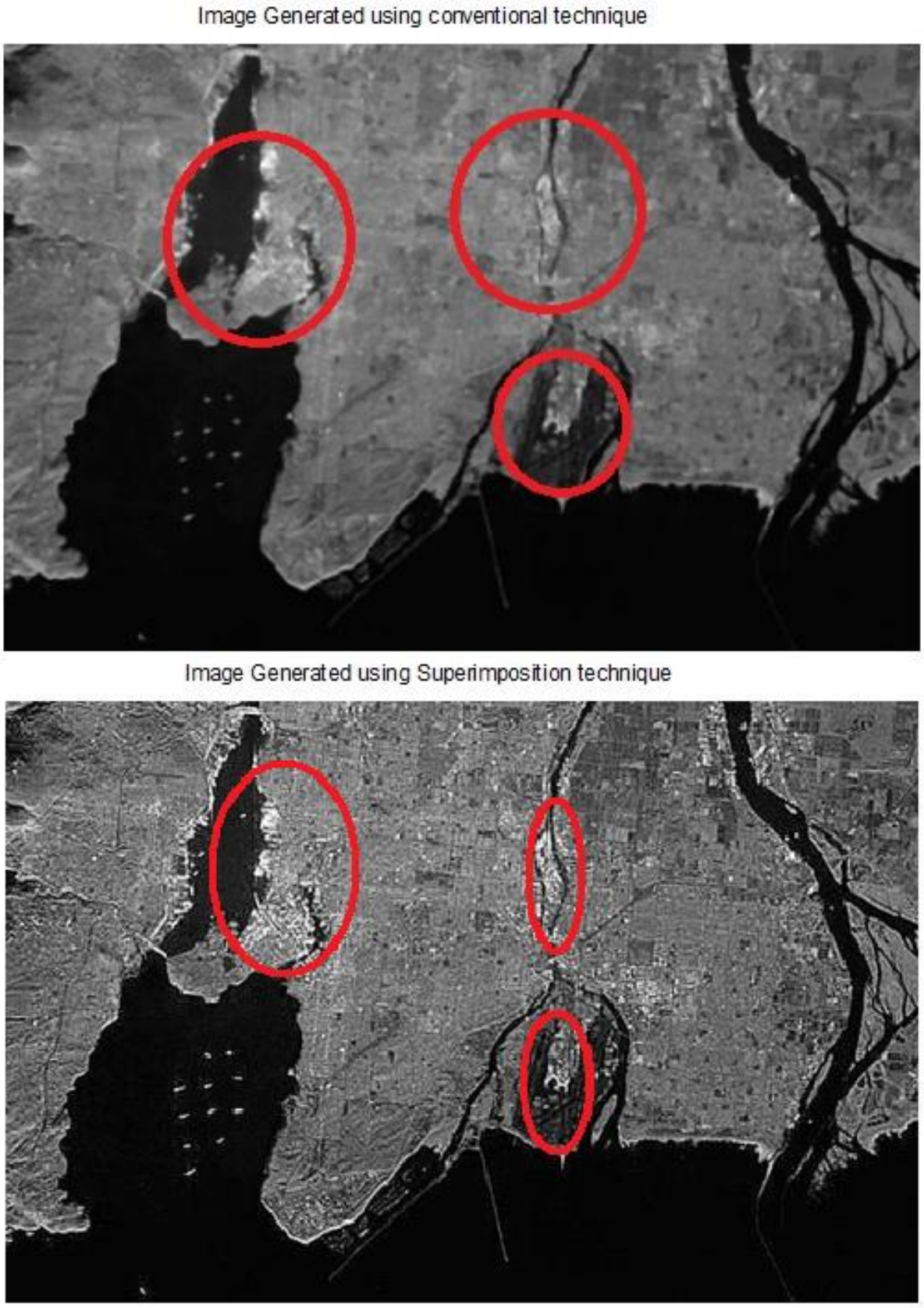

Figure VI-9: Comparing standard-FFT and NSI-6 techniques for Spaceborne SAR image

In order to give a better comparison for the two techniques, the upper-right circled area is expanded in Figure VI-10 presenting the outcome image of that area using standard-FFT and NSI-6 techniques. It can be clearly seen that the standard-FFT SAR image suffers from blurriness and the river sides seem faded with surrounding land especially in the upper part of the image, while the NSI-6 Image is much more focused and the river sides are more distinguishable. Furthermore, another part of the full SAR image is expanded, the constellation of the unidentified objects in sea are with some of the surrounding land areas in the lower-left part of the SAR image are presented in Figure VI-11 representing the SAR output image using standard-FFT and NSI-6 techniques respectively. Here, again, the line between land and sea areas is clearer and the SAR image is more focused in general in outcome of the NSI-6 technique when compared with the outcome of the standard-FFT.

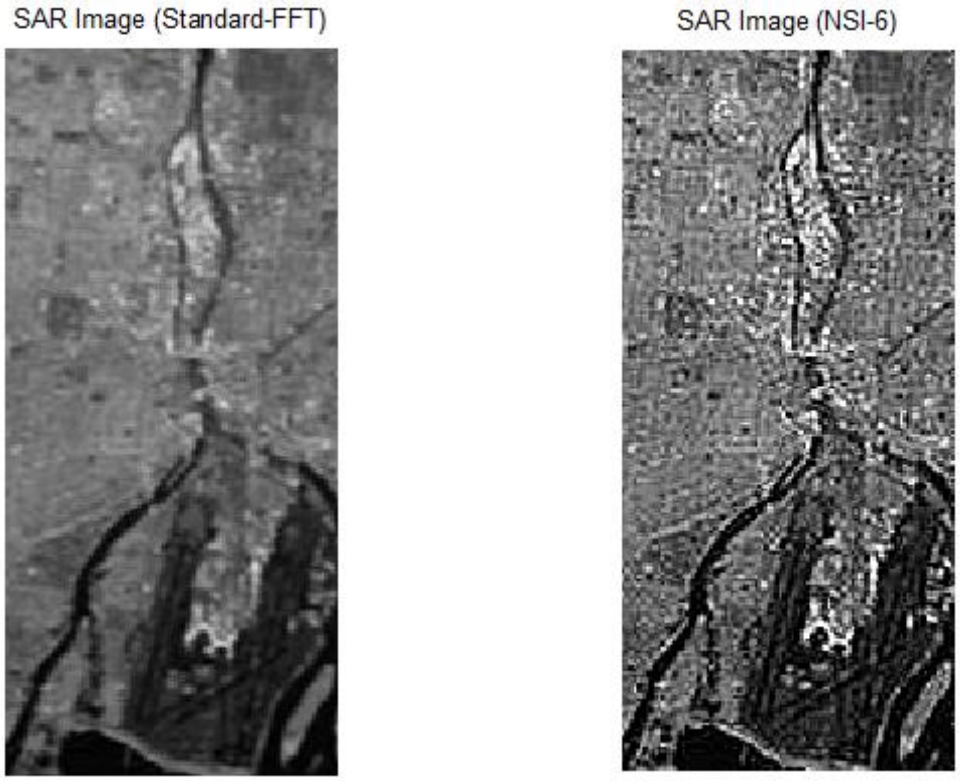

Figure VI-10: Comparing standard-FFT and NSI-6 techniques on an expanded part of the upper-right circled area of the Full SAR image

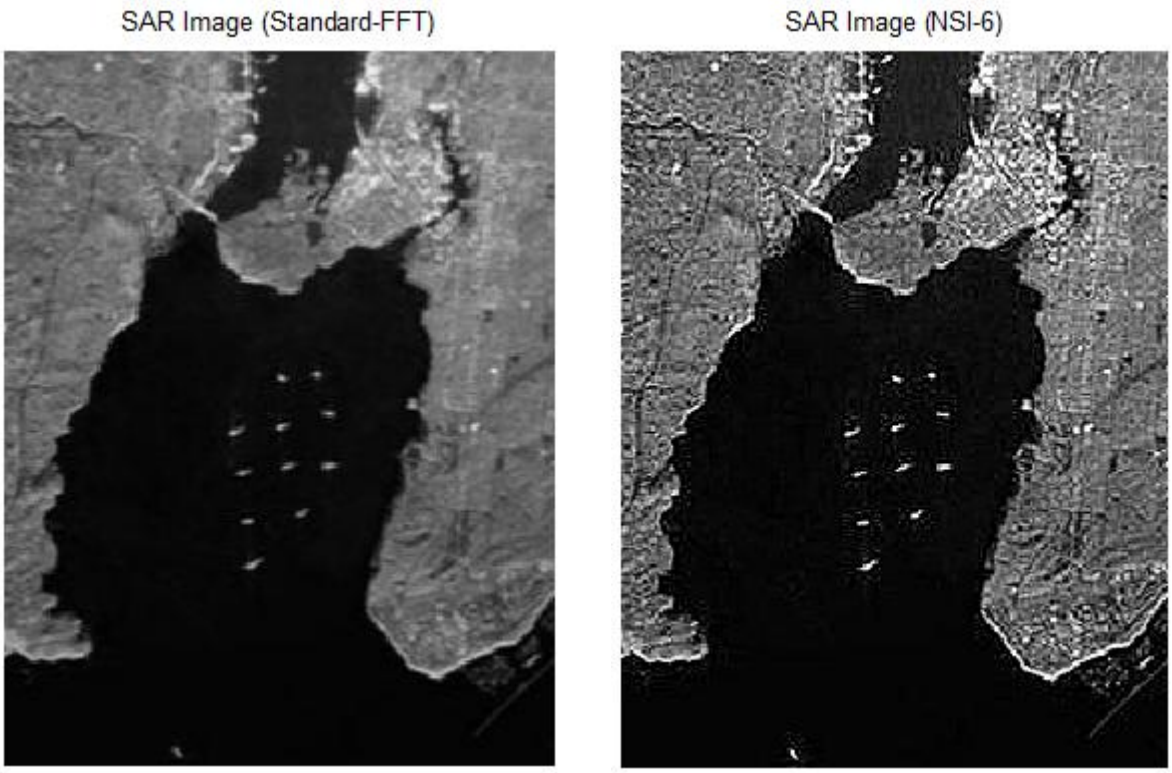

Figure VI-11: Comparing standard-FFT and NSI-6 techniques on an expanded part of the lower-left area of the Full SAR image

The average Mean-Square-difference per pixel between the images generated using standard-FFT and NSI-6 techniques is 26dB. This average Mean-Square difference gives an indication of the quantity of difference between the SAR image generated using the standard-FFT technique and the SAR image generated by the NSI-6 technique. However, in order to see how that change is taking place over the SAR image, an absolute difference image, from images generated by both standard-FFT and NSI-6 techniques, is generated and presented in Figure VI-12. The absolute difference image shows how a clear difference between the two images is at the edges of the different landscapes especially between see and land and along the rivers. Furthermore, it is also clear that areas with high intensity values, such as the areas circled in Figure VI-9 for both SAR images, have noticeable difference while the sea area shows no visible difference. However, a better look at the sea area using logarithmic scale images, shown and discussed in section 6 of this chapter, shows a notable difference of the sea area between the two images.

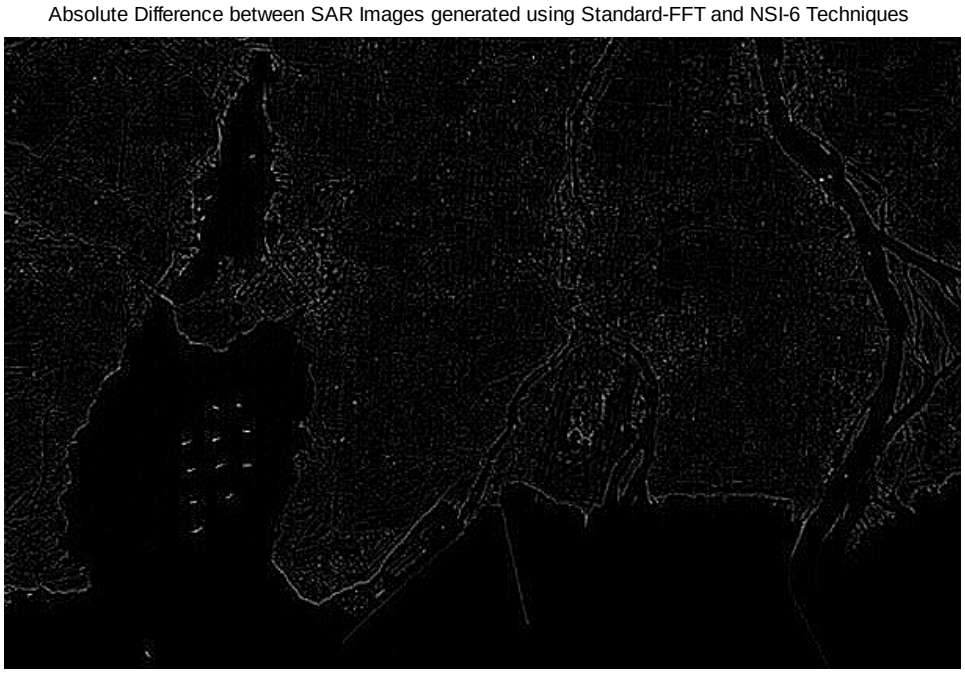

Figure VI-12: Absolute Difference Image of the SAR Images generated using standard-FFT and NSI-6 techniques

The SAR image formed using standard-FFT technique with Hann windowing function is presented in Figure VI-13. It can be noticed that the SAR image formed using standard-FFT technique with Hann windowing function is clearer than the standard-FFT SAR image, see Figure VI-9. Nevertheless, it is much more unfocused especially when compared to the SAR image generated using NSI-6 superimposition technique, see Figure VI-9. The average Mean-Square difference per pixel for the SAR image formed using standard-FFT with Hann windowing function from the original SAR image formed using the conventional standard-FFT technique is 16.2dB. And finally, Figure VI-14 and Figure VI-15, present the SAR images formed using SVA and Super-SVA techniques respectively. It can be noticed that visually they are as good as the NSI-6 SAR image. However, in terms of the average Mean-Square difference per pixel from the original image, SVA and Super-SVA are 18dB and 20.6dB respectively.

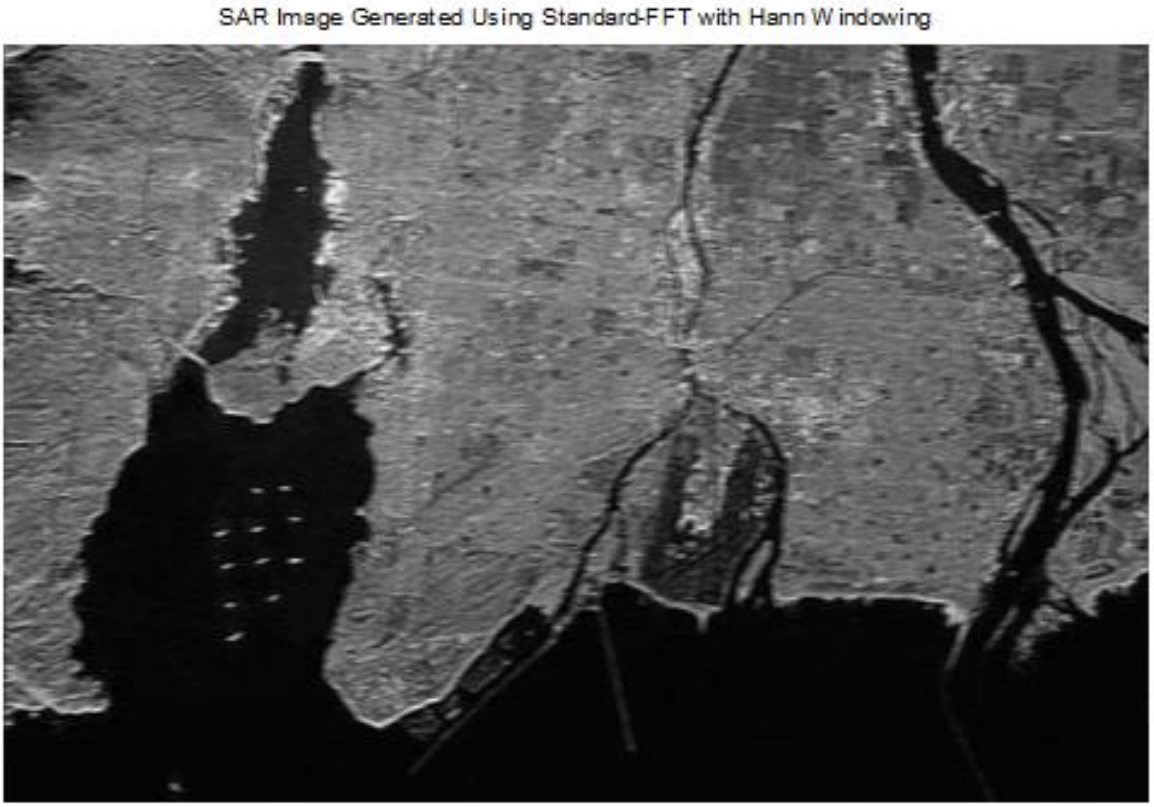

Figure VI-13: SAR Image formed using standard-FFT with Hann Windowing function

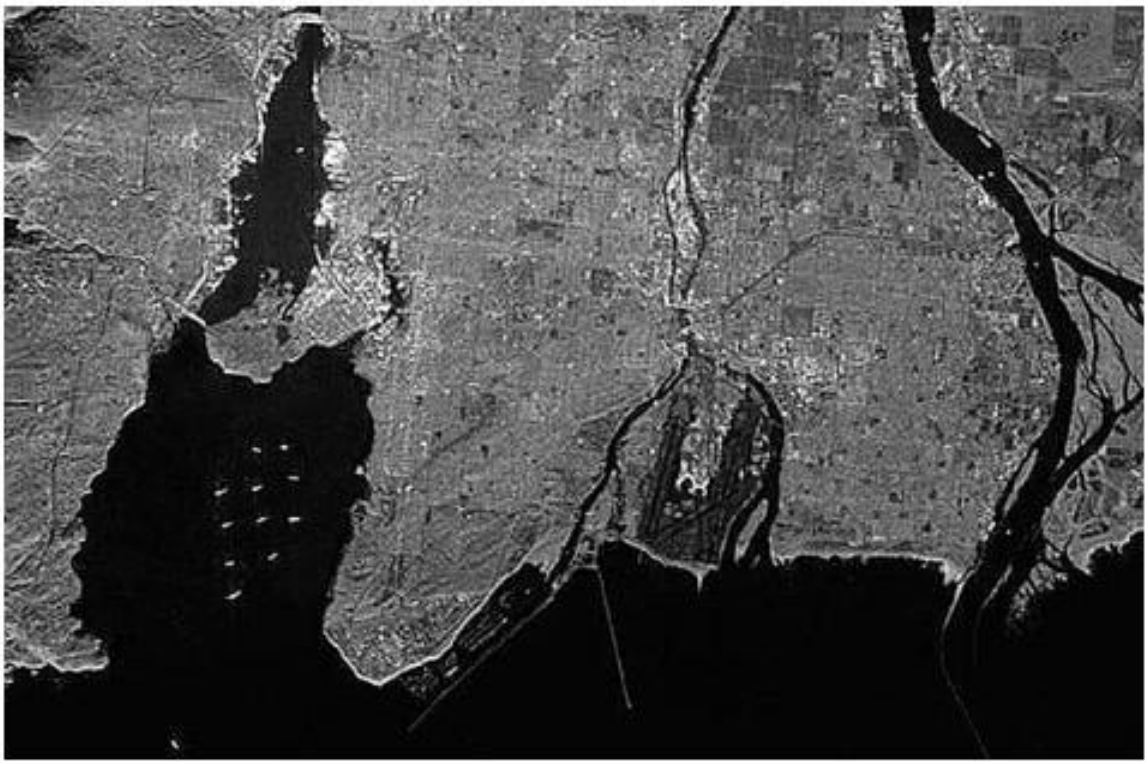

Figure VI-14: SAR Image formed using SVA technique

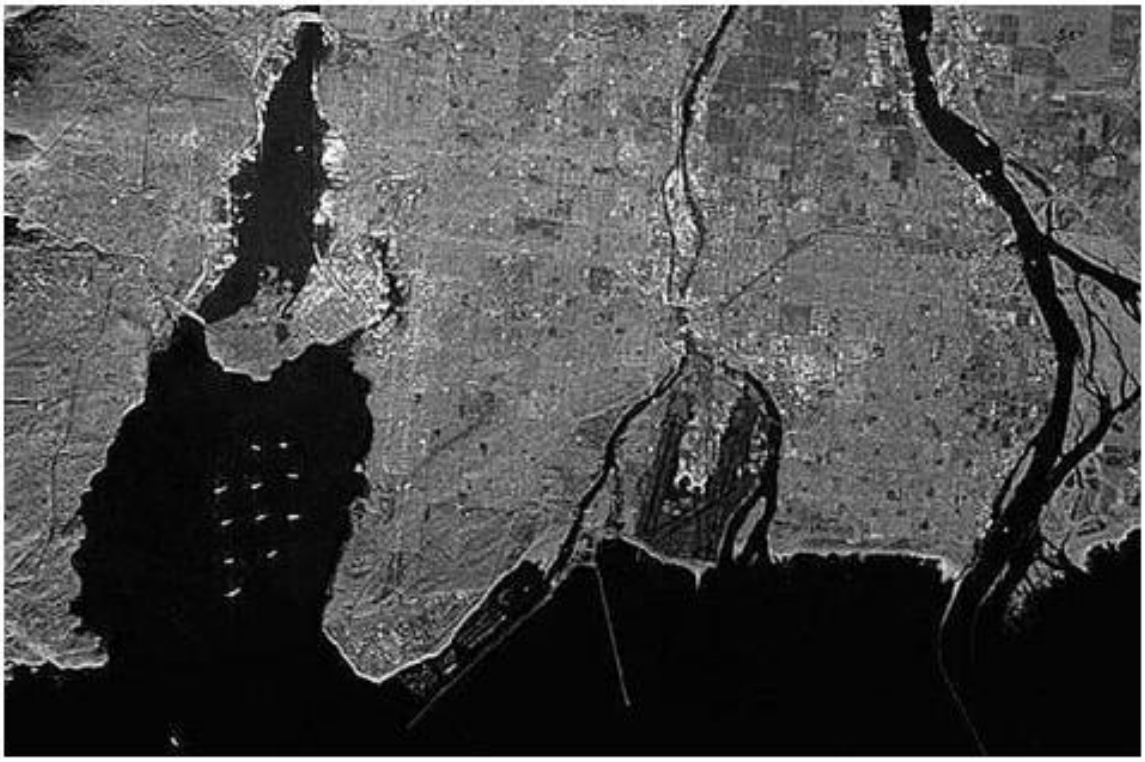

Figure VI-15: SAR Image formed using Super-SVA technique

5. Image Sharpening vs. Superimposition

One can argue that some image sharpening techniques can be applied to the SAR image to improve the focus of the image without the need for superimposition technique. Well, the sharpening technique adopted in this dissertation works by utilizing a slightly blurred version of the original image. This is then subtracted from the original to detect the presence of edges, creating the unsharp mask, which is effectively a high-pass filter. Contrast is then selectively increased along these edges using this mask — leaving behind a sharper final image [129]. When this sharpening technique is applied, using Matlab built-in functions: "fspecial" and "imfilter", the image in Figure VI-16 is obtained. The average Mean-Square-difference per pixel between the original and the sharpened images is 12.3dB.

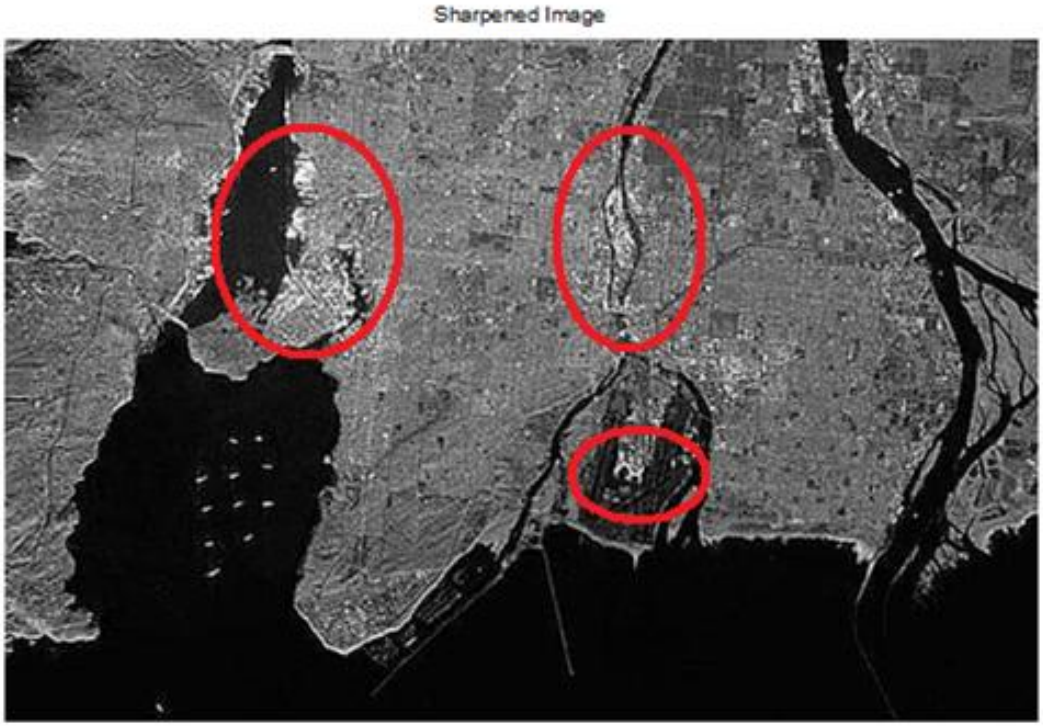

Figure VI-16: Sharpened Space-borne SAR Image

These results give an indication that both images generated using superimposition and sharpening techniques are close to each other visually and quantitatively. However, the sharpening technique doesn't enhance the resolution of the image. More to the point, the sharpening process only creates the appearance of a more pronounced edge rather than actually enhancing image resolution [130] while the superimposed technique deals with the problem on an early stage (i.e. image formation level) instead of waiting until the corruption has occurred and then dealing with it.

Besides, any sharpening technique can be added as a post-processing phase to the enhanced image. When the superimposed image is post-processed by the sharpening technique using the Matlab built-in functions described before, the quality of the final SAR image did slightly enhance, where the average Mean-Square difference per pixel between the original image and the post-sharpened superimposed image is 27.4dB. The post-sharpened superimposed image is presented in Figure VI-17. This result, when compared to applying only the sharpening technique as shown in Figure VI-16, gives an indication that applying the sharpening technique to SAR image formed using the superimposition technique produces a better quality image especially that the extra computation time required for applying the sharpening technique is almost negligible, 89 milliseconds.

Figure VI-17: Post-Sharpened superimposed image

A comparison between the SAR images formed using the different techniques in terms of Mean-Square Difference (MSD) per pixel with respect to the SAR image formed using the standard-FFT, the processing time and the memory space that is used by Matlab to hold and process the data used by each technique, as explained in section 3 of chapter 5, is presented in the following table:

Table VI-1: Summary of performance assessment of SAR images formed using the different techniques

Technique	MSD per pixel	Processing Time	Memory Required
Standard-FFT	Reference Image	0.91 sec	64.1 kB
Standard-FFT with Hann Window	16.2 dB	1.07 sec	64.93 kB
SVA	20.6 dB	14.8 sec	592.7 kB
Super-SVA	18.0 dB	9.66 sec	931.4 kB
NSI-6	26.0 dB	4.83 sec	312.9 kB
Standard-FFT with Sharpening	12.3 dB	0.99 sec	67.5 kB
NSI-6 with Sharpening	27.4 dB	4.94 sec	316.19 kB

6. Comparison of SAR Images in Logarithmic Scale

Based on the results from the previous two sections, a more accurate method of showing the differences, especially subtle ones around high intensity objects in the image, between the SAR images generated using standard-FFT and NSI-6 techniques is considered. The technique used is converting the intensity value at each pixel of the SAR images to logarithmic scale. Results presented in Figure VI-18, show that while SAR image generated using standard-FFT and standard-FFT with Hann Windowing Function have orange colour (i.e. intensity value of around 47dB) vastly spread over land areas, the SAR image generated using NSI-6 technique has the orange colour more limited and surrounded by yellowish colour (i.e. intensity value of 40dB). This means that high intensity objects are more distinguishable due to suppressed sidelobes and enhanced resolution. Furthermore, it is also noticed that sea area is more homogeneous in standard-FFT with Hann Windowing Function and NSI-6 SAR image than in standard-FFT SAR image due to sidelobe suppression and noise reduction features of the Superimposition technique. This observation isn't clear in the SAR images presented earlier in this chapter due to the subtle changes that were not noticeable until a logarithmic scaled image is used.

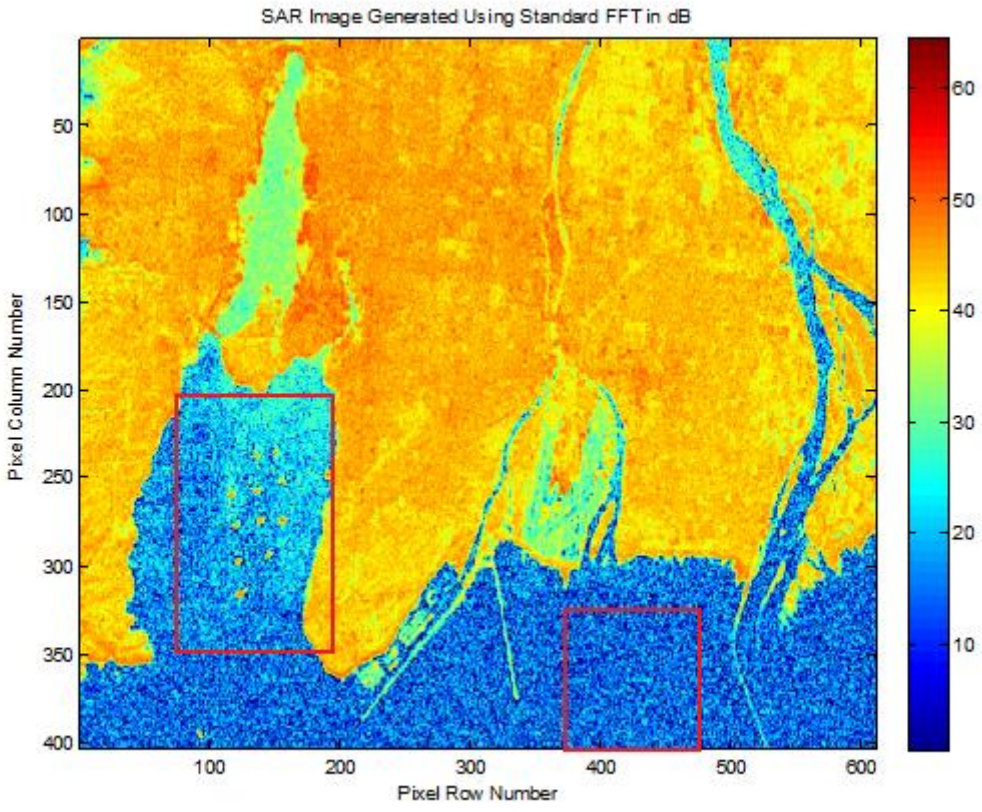

(a) SAR Image generated using standard-FFT technique in logarithmic scale (with expanded areas framed in red).

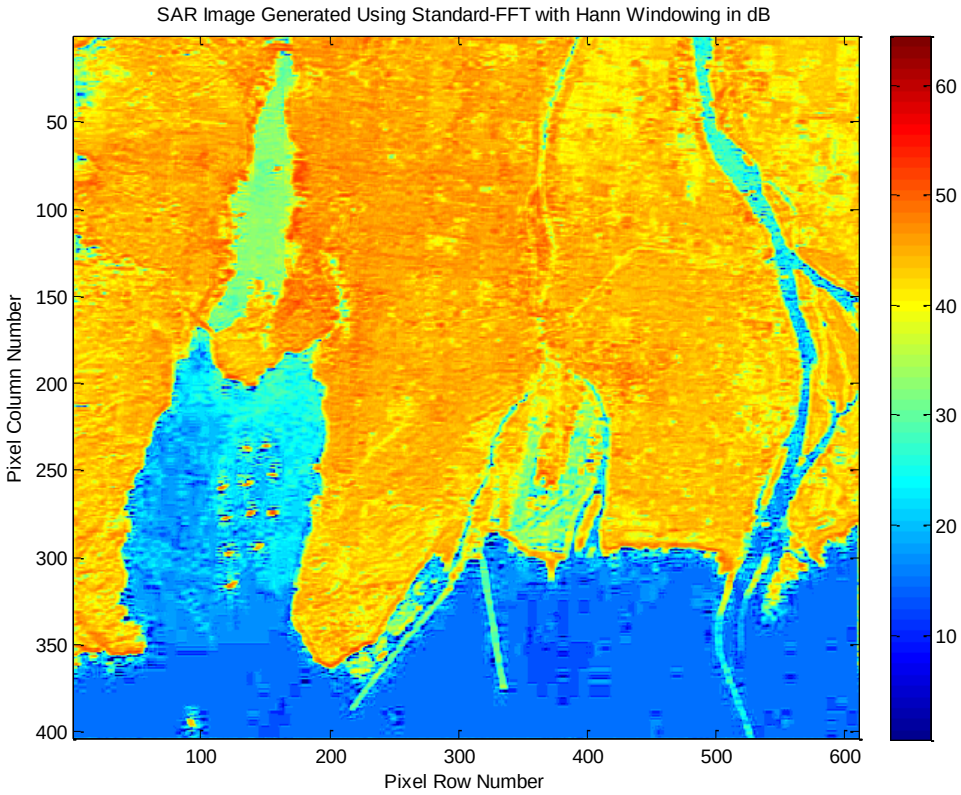

(b) SAR Image generated using standard-FFT with Hann Windowing function in logarithmic scale.

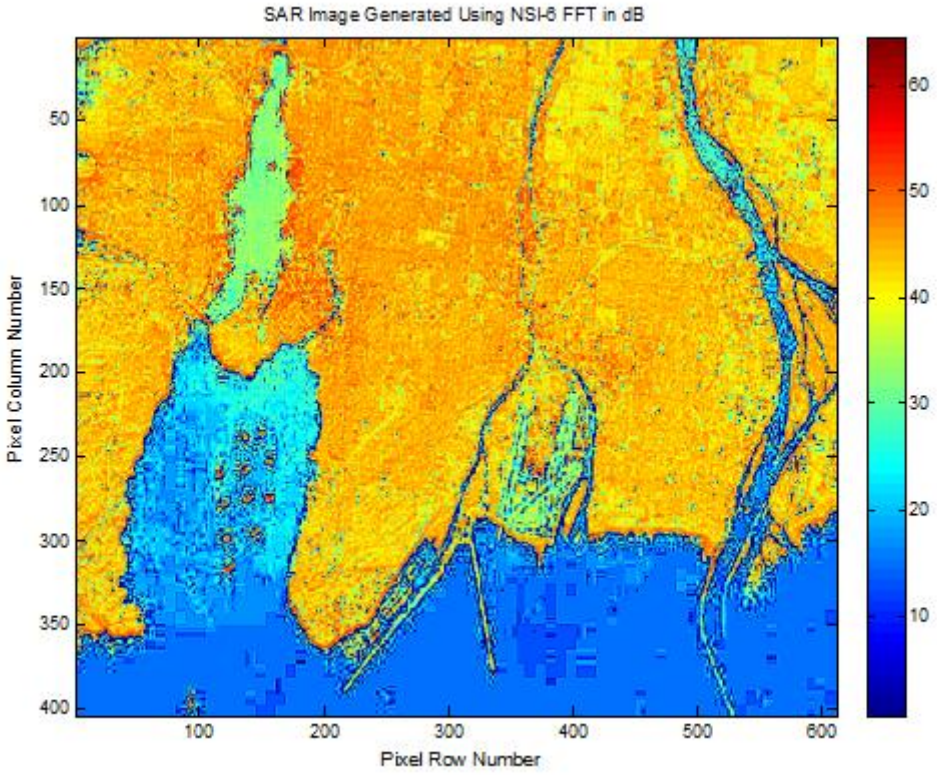

(c) SAR Image generated using NSI-6 technique in logarithmic scale.

Figure VI-18: Comparison of standard-FFT, standard-FFT with Hann Windowing and NSI-6 techniques in logarithmic scale SAR images.

A second observation that is noted is the clear line between land areas and water areas is observed in the SAR image generated using NSI-6 technique, on the other hand, this line in the SAR image generated using standard-FFT technique is blurred especially in areas where the water body is relatively small such as in the upper-left side of the SAR image where the small water area has a relatively high intensity value. More to the point, it is also noted that the constellation of the unidentified objects in the lower-left area of the SAR image is much more resolvable with clear edges. Expanded/zoomed images of that area, which is framed in red in Figure VI-18 (a), from SAR images formed using standard-FFT, standard-FFT with Hann windowing function and NSI-6 techniques are presented in Figure VI-19. It is clearly noticed in these expanded figures that, in the standard-FFT image, the edges of these high intensity-value objects gradually changes in colour to the low-intensity value of the surrounding sea, while in the NSI-6 image these edges are very sharp as the intensity value drops more than 30dB. In the standard-FFT with Hann windowing function case, the different objects in the constellation are expanded a little bit. The intensity value at the centre of the objects are still the same as in the NSI-6 image, however, the edges around these high intensity value objects are not as clear as in the NSI-6 image.

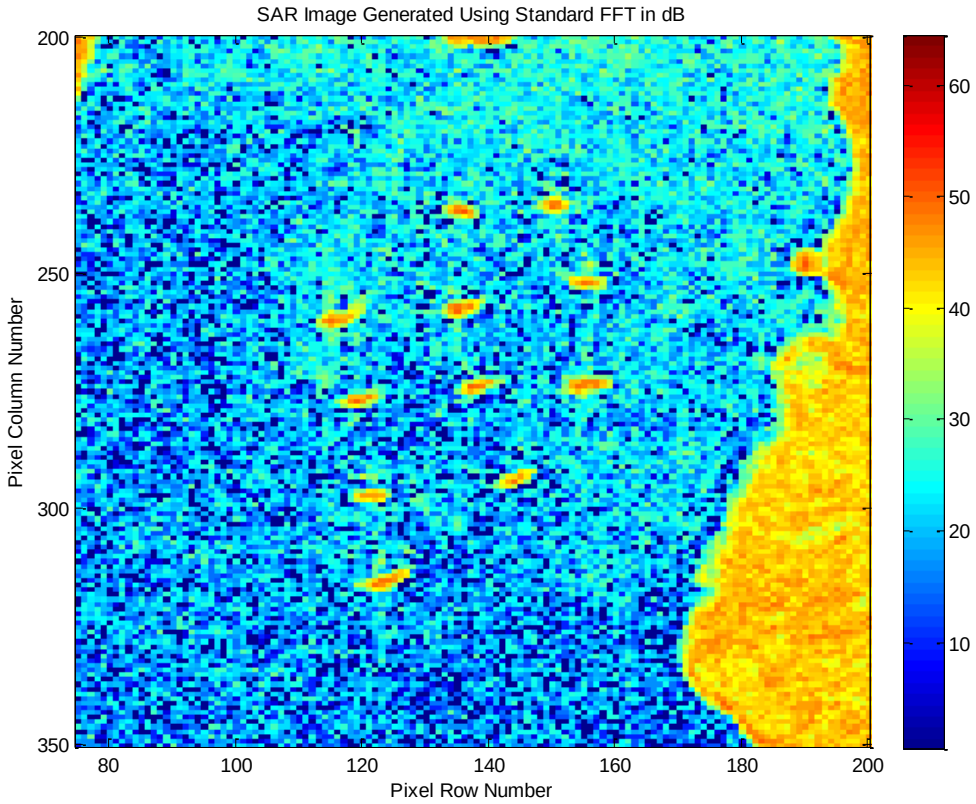

(a) Expanded area of SAR Image generated using standard-FFT techniques in logarithmic scale

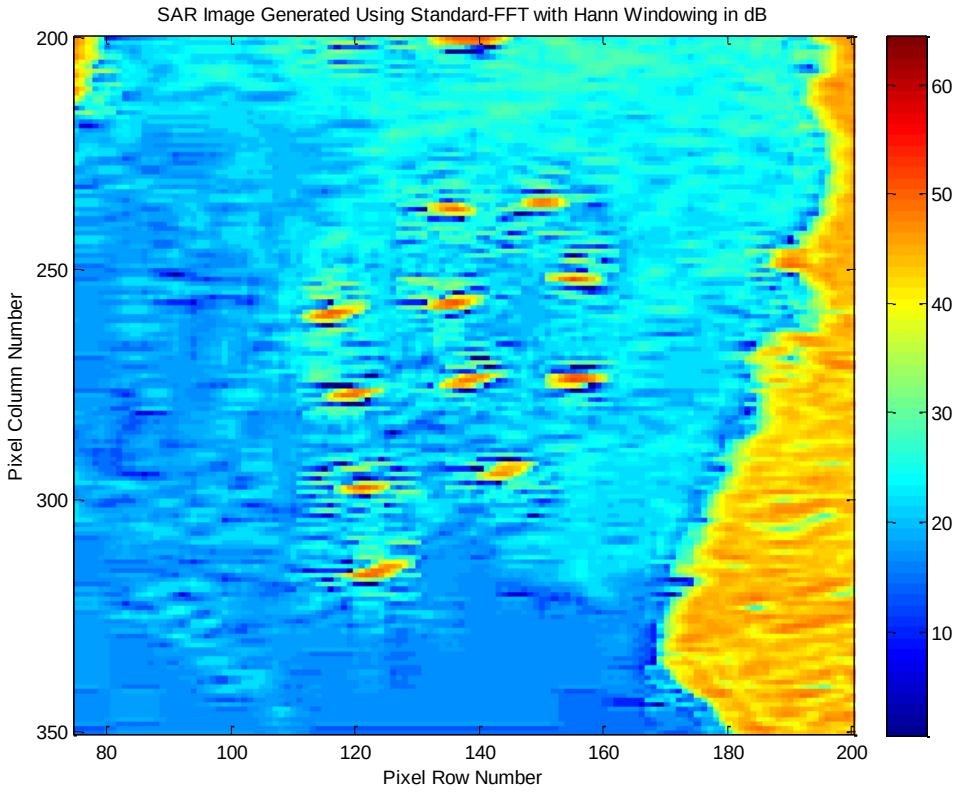

(b) Expanded area SAR Image generated using standard-FFT with Hann Windowing Function in logarithmic scale

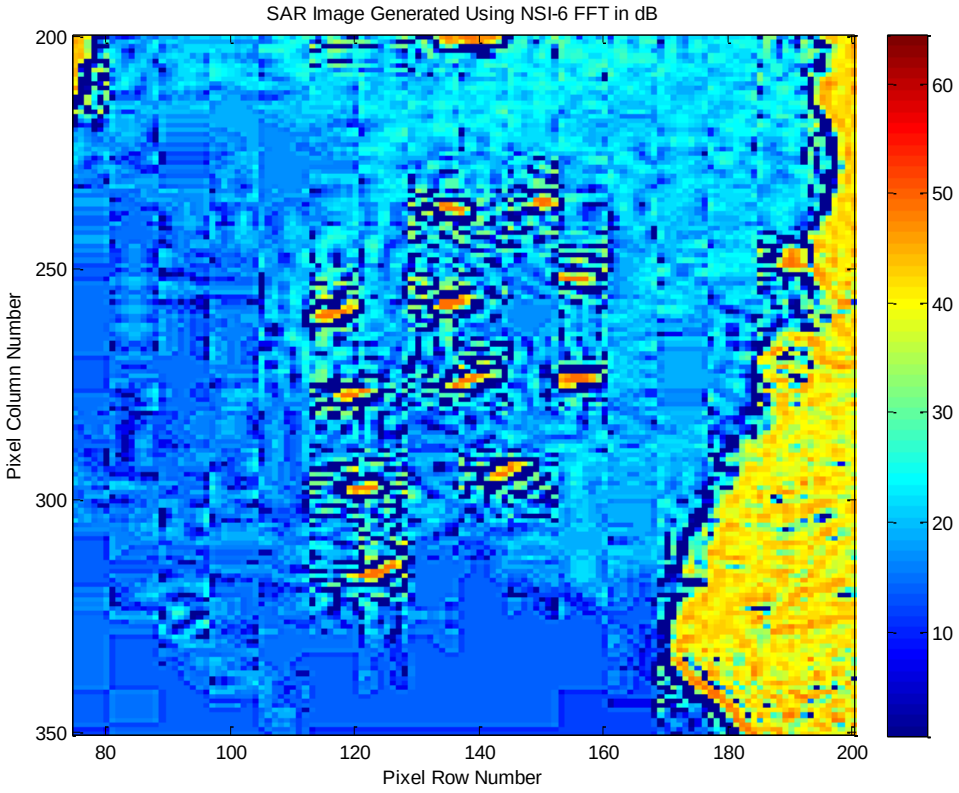

(c) Expanded area SAR Image generated using NSI-6 techniques in logarithmic scale

Figure VI-19: Comparing of standard-FFT, standard-FFT with Hann Windowing Functions and NSI-6 techniques by expanded SAR Images in logarithmic scale

Finally, Figure VI-20 (a) shows that the SAR image generated using the standard-FFT technique is highly speckled and what is supposed to be a homogeneous surface of water is formed as a heterogeneous image. On the other hand, the SAR images generated using the standard-FFT with Hann windowing function, Figure VI-20 (b), and the NSI-6 superimposition, Figure VI-20 (c), are both obviously enhancing the image and suppressing these side-effects with different levels of competence in favour of the superimposition technique. A summary of the average intensity value per pixel in decibel for sea area of 7171pixels (71 row-pixels, 101 column-pixels) in SAR image, which is framed in Figure VI-18 (a), formed using standard-FFT technique, standard-FFT with Hann windowing and superimposition NSI-6 technique is presented in the following table:

Table VI-2: Summary of Average Intensity value (dB) per pixel for sea area using the different techniques

Technique	Average Intensity per pixel
Standard-FFT	18.9 dB
Standard-FFT with Hann Window	13.6 dB
NSI-6	11.2 dB

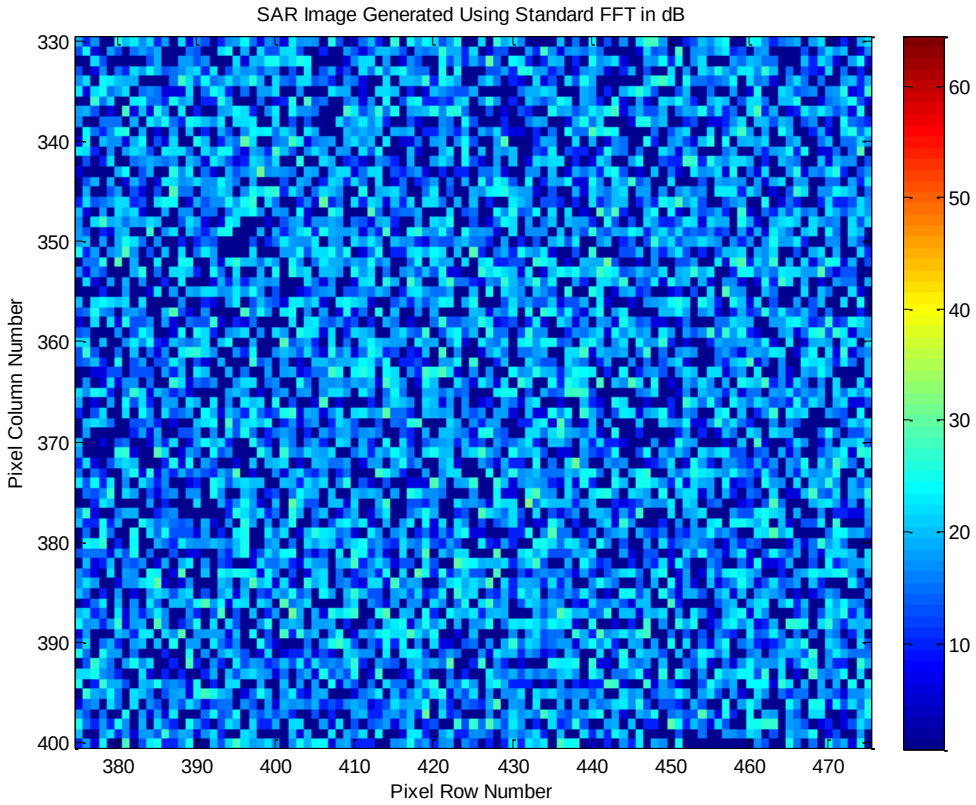

(a) Sea area of SAR Image generated using standard-FFT techniques in logarithmic scale

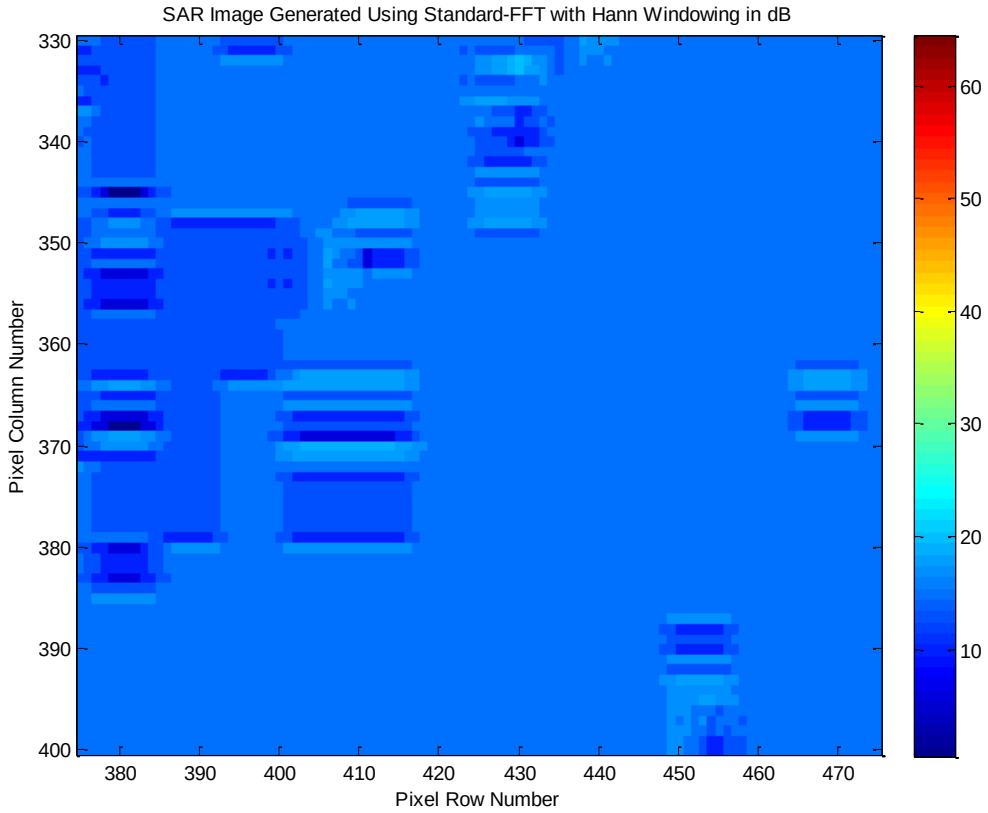

(b) Sea area of SAR Image generated using standard-FFT with Hann Windowing Function in logarithmic scale

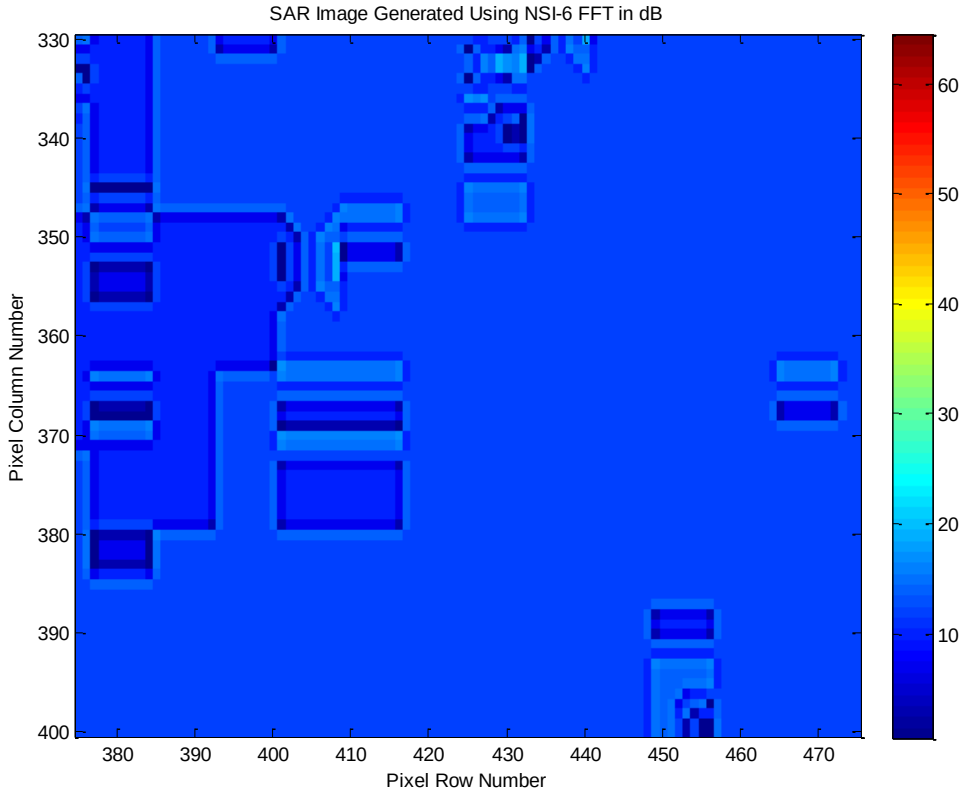

(c) Sea area of SAR Image generated using NSI-6 techniques in logarithmic scale

Figure VI-20: Comparing of standard-FFT and NSI-6 techniques on sea areas of SAR Images in logarithmic scale

7. Assessing SAR Images using Line Intensity Profile

Based on definition of line intensity profile presented in subsection 4.*v*. in Chapter I, three lines are been placed across three different areas in the SAR images generated using standard-FFT, standard-FFT using Hann windowing function and NSI-6 techniques, see Figure VI-21. The first line starts in a high-intensity land area, but then goes to low-intensity water area and then goes back to high-intensity land area where just next to the water a bright light representing to what seems to be a populated area is just at the edge next to water. In contrast, the second line starts in a low-intensity water area then goes through a high-intensity land area and then back to the water area where it runs through a very narrow high intensity objects and lines. Finally, the third line crosses a relatively narrow river with small land areas on both of its sides. Zoomed images showing the areas surrounding the three lines are presented in Figure VI-22 (a), Figure VI-23 (a) and Figure VI-24 (a).

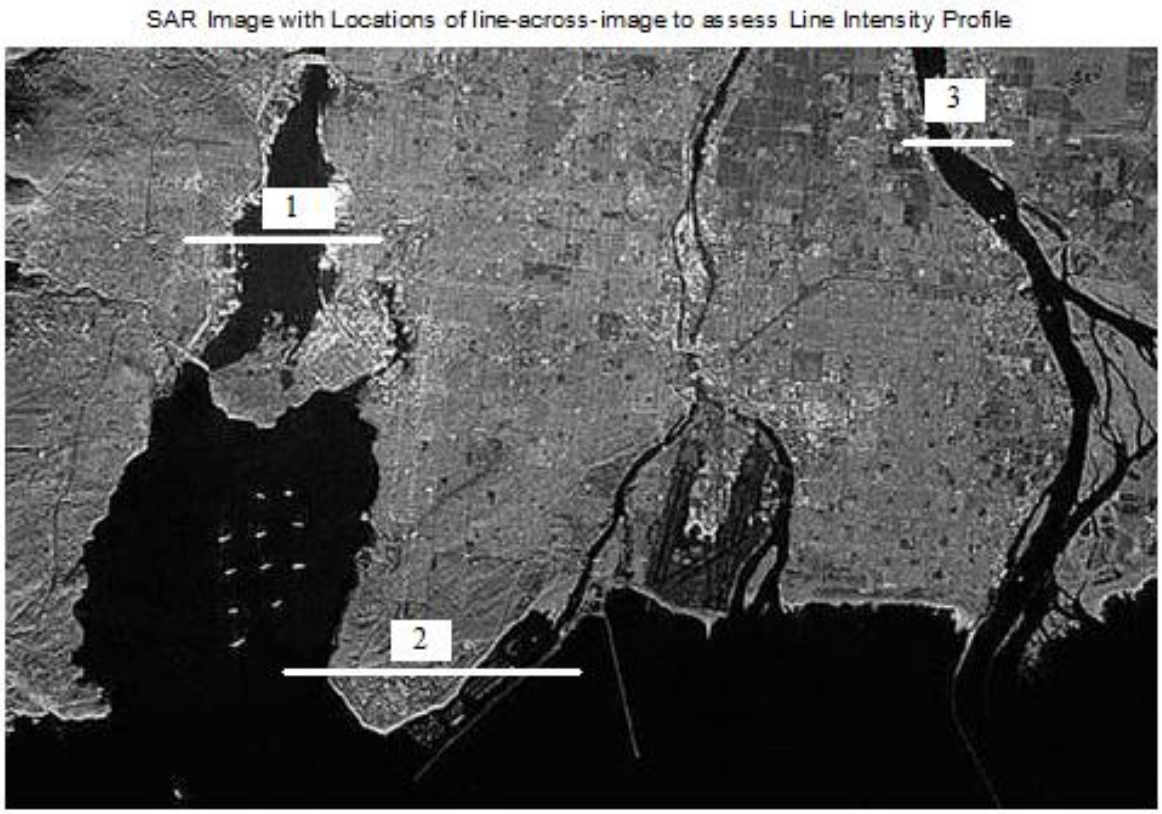

Figure VI-21: Showing the three Lines used for the line intensity profile analysis of SAR Images formed using standard-FFT, standard-FFT with Hann windowing and NSI-6 techniques

Traces of the line intensity profiles for the first line using the three techniques are presented in Figure VI-22 (b), the two traces of standard-FFT and NSI-6 techniques show that peak values and positions are relatively similar but with much more resolvability in NSI-

6. While the standard-FFT with Hann windowing function is worse in terms of resolution as the width of the peak values is extremely wide to the extent that it actually gives one peak pulse for a number of genuine pulses in the other techniques. However, at the low intensity area in the middle of the line, which is the sea area in the SAR image, it is, like the NSI-6 technique, smoother than the standard-FFT technique due the effect of suppressed sidelobes.

Figure VI-23 (b) shows the intensity profile traces for the second line of all the techniques, the NSI-6 outcome shows that it is preserving almost all main pulses that appear in the conventional technique of standard-FFT, except for very few that can't be verified to be genuine, with narrower and more resolvable peaks unlike the standard-FFT with Hann windowing function that has a very broad peaks causing the resolution to deteriorate noticeably. For the smooth low-intensity areas at both ends of the line, both NSI-6 and standard-FFT with Hann windowing function techniques combat the effect of the small sidelobes while the standard-FFT technique is obviously suffering from them.

Finally, results from the third intensity line profile traces shown in Figure VI-24 (b) support the findings from the outcome of the other two line intensity profile examination that NSI-6 is preserving most of the main peaks' position while enhancing their resolution in comparison to the standard-FFT technique. Interestingly, it is noted that the left side of the low-intensity areas is clearly sharper in NSI-6's line intensity profile as the line drops from high-to-low intensity at pixel number 487. The trace from the standard-FFT with Hann windowing function demonstrates a deteriorated resolution due to the broadened main peaks.

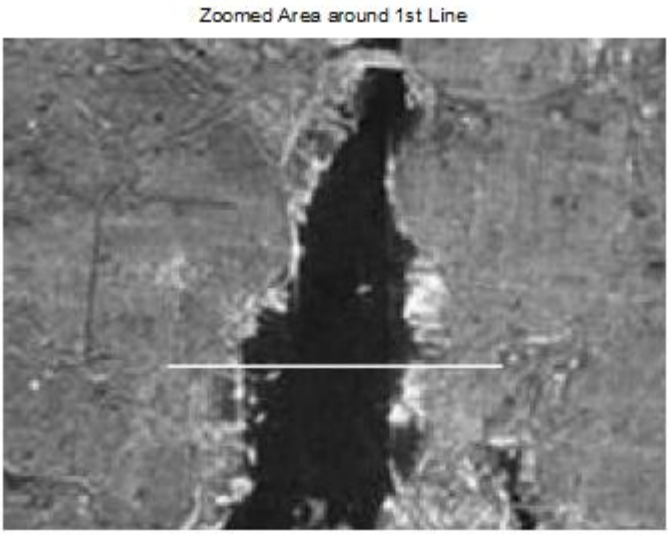

(a) Zooming of the area of the 1st line

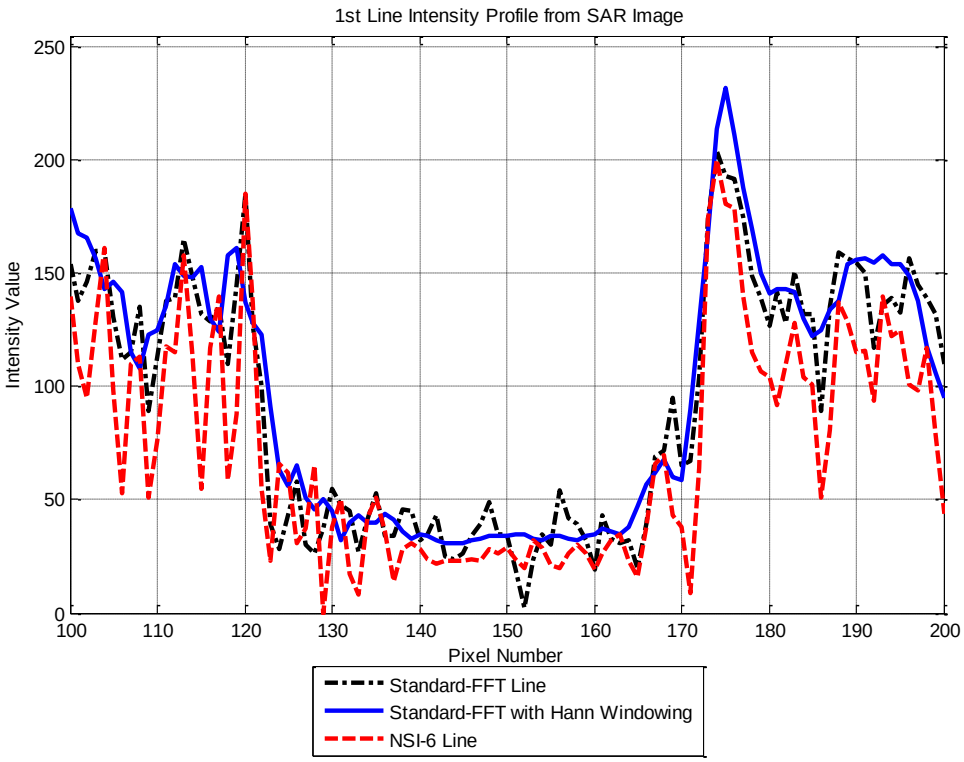

(b) Line Intensity Profile of the 1st line using all techniques

Figure VI-22: Line Intensity Profile of the 1st line as indicated in Figure VI-21

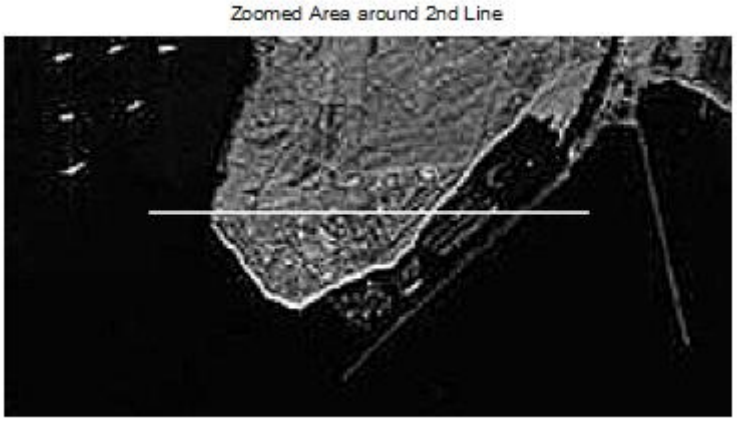

(a) Zooming of the area of the 2nd line

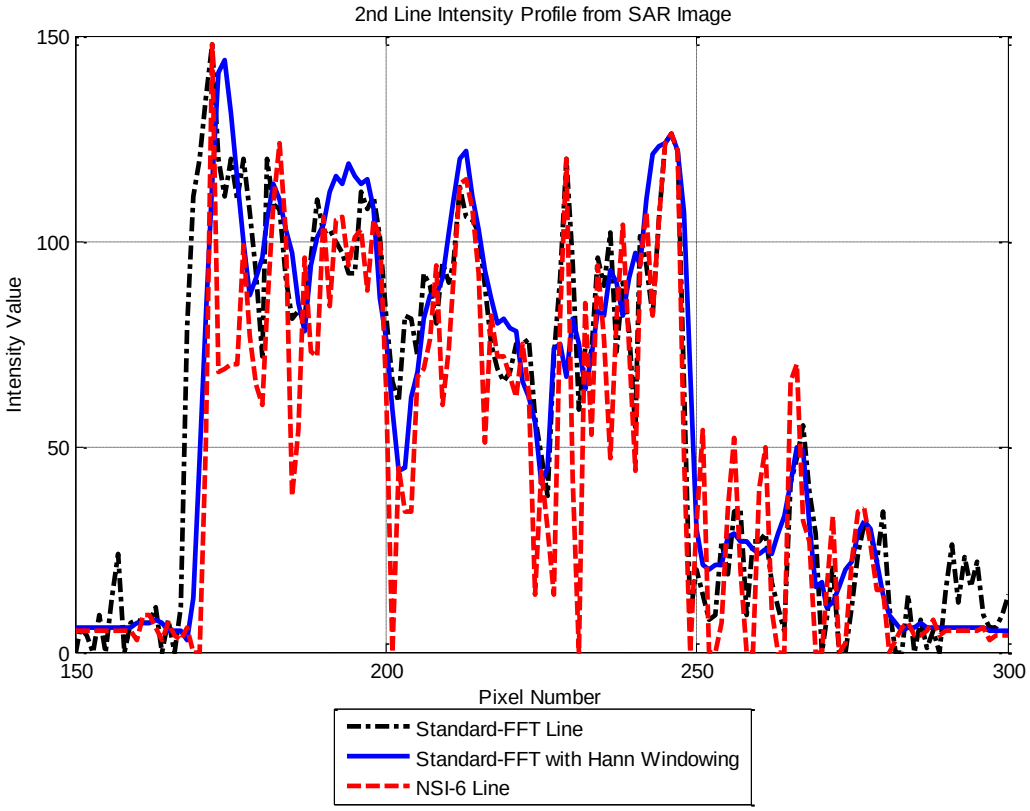

(b) Line Intensity Profile of the 2nd line using all techniques

Figure VI-23: Line Intensity Profile of the 2nd line as indicated in Figure VI-21

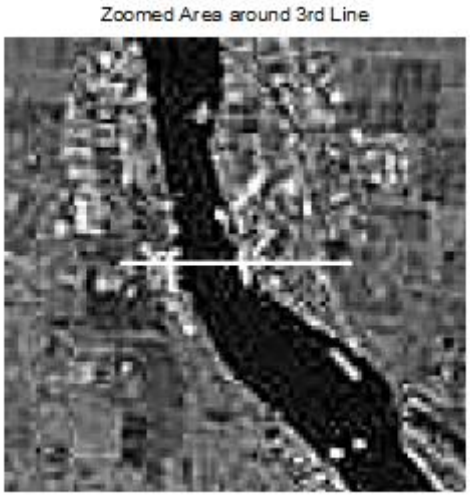

(a) Zooming of the area of the 3rd line

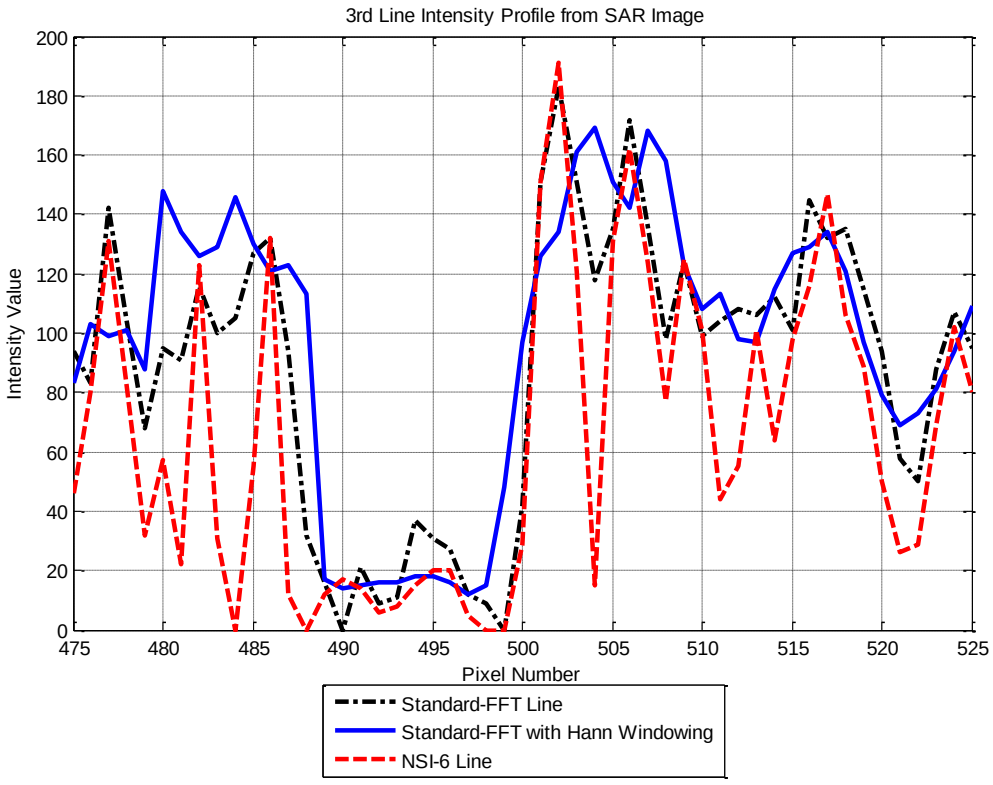

(b) Line Intensity Profile of the 3rd line for all techniques

Figure VI-24: Line Intensity Profile of the 3rd line as indicated in Figure VI-21

8. Chapter Summary

A brief overview of PSF and a simulation of a basic SAR model are presented at the beginning of this chapter to study the difference in performance between the standard-FFT and the newly proposed Superimposed-FFT technique of NSI-6 in terms of sidelobe reduction (i.e. PSLR and ISLR), NSI-6 is shown to be superior as sidelobe are suppressed by nearly 20dB in comparison with the standard-FFT outcome. A second simulation of two target points and a distributed target is presented in the following section for further analysis and comparison of the standard-FFT technique with the newly proposed NSI-6 technique. After that, a SAR image that contains different terrains and textures is generated from real-life SAR data acquired from [4] using the different techniques of standard-FFT, standard-FFT with unsharp-mask image sharpening technique, SVA, Super-SVA and Superimposed-FFT using NSI-6. Results showed that while the different techniques do have very similar performance visually, there is a noticeable difference of around 25dB in terms of Mean-Square difference between the different SAR images generated by the different techniques. Then, a more thorough comparative analysis of the conventional standard-FFT, the standard-FFT with Hann windowing function and the newly proposed superimposition technique, NSI-6, is performed using logarithmic-scale SAR images and line intensity profile analysis showing superiority of the superimposition technique in terms of both visual and quantitative analysis in suppressing sidelobes, combating noise, preserving main features and enhancing resolution.

Chapter VII: Summary and Future Work

1. Introduction

As the importance of SAR increased, so did the interest to enhance its performance and expand its abilities. This research work has generated novel enhancements to the image formation and image segmentation parts of the SAR system. This chapter summarizes the important elements of each chapter in this thesis and the contributions made to the SAR image formation and segmentation as part of this research work. Additionally, this chapter also extends some of the contributions and suggests ideas for the future work in SAR processing and other FFT-based applications and systems.

2. Summary of Thesis

The thesis started with Chapter I that introduced the research work, identified the drive behind the project and the major contributions and objectives set for this research work. Some main considerations for SAR design and a brief overview of quality metrics measurement techniques considered in this project are also briefly discussed.

In Chapter II, a comprehensive literature review of the SAR principles, polarimetry, geometry, operation modes and basic model with mathematical analysis of pulse compression and SAR imaging process and its characteristics along with a review of different image formation techniques showing their importance o on FFT/IFFT and a brief introduction to distributed targets is presented.

In Chapter III, a thorough review of sidelobe suppression techniques of MUSIC algorithm, SVA and Super-SVA techniques are presented. Additionally, an introduction to Superimposition was covered as well, which also included an overview of windowing functions. Finally, the new proposed techniques of improved superimposition using Repetitive Superimposition (RSI) and Normalized Superimposition (NSI) are being explained.

In Chapter IV, a basic SAR model is designed and simulated in order to establish a proof-on-concept and have a better understanding of the new improved Superimposed-FFT techniques of RSI and NSI in comparison with the some of the other conventional techniques.

A study on the performance of the new techniques showed a noticeable increase in sidelobe suppression, noise reduction, main-lobe's height and position preservation and resolution enhancement. Then a simulation of distributed targets is presented followed by an analysis of the performance of a point target against a distributed background.

In Chapter V, Ansoft simulation of an impedance step discontinuity on a network analyzer was presented. A more in-depth investigation on the best possible design for the improved Superimposed-FFT techniques was conducted and the results showed the RSI has finest performance when working with ten input signals (RSI-10), while NSI's performance is optimized when working with six input signals (NSI-6). These techniques were compared with standard-FFT, Standard-FFT with Hamming Window, SVA and Super-SVA techniques. RSI-10 proved to be superior to all conventional techniques except for the Super-SVA while the NSI-6 outperformed all conventional techniques including Super-SVA in sidelobe suppression and resolution enhancement. Finally, a quantitive comparison on the effect of the different techniques on the main-lobe width has been performed showing that NSI-6 is superior to all techniques and that even though RSI-10 is modestly outperformed by Super-SVA, RSI-10 actually needs one-tenth of the processing time required by Super-SVA. After that, measurements from the Beatty Standard experiment has been utilized for comparing the new proposed techniques of improved Superimposition with the following techniques: standard-FFT, standard-FFT with Hamming Window, standard-FFT with Chebyshev Window, SVA and Super-SVA. Results were in accordance with the findings of the Ansoft simulation in Chapter IV. After that, an AWGN has been added with different power values for the noise signals so that the SNR is set to be 0dB, -10dB and -20dB. Results showed that in the presence of high level of noise, conventional techniques were highly susceptible to false targets while the improved Superimposition techniques of RSI-10 and NSI-6 were more robust. Impressively, in order to produce the same level of performance produced by RSI-10 at 0dB SNR, 100 signals with independent noise samples were required to be averaged. Even more, at -20dB SNR it required averaging 850 signals generated using standard-FFT to have the same performance of the NSI-6 technique. In addition, image sharpening using unsharp-mask technique was also applied to the measured signal in order to have a comparison with the other techniques in terms of suppressing sidelobes and in order to have a visualization of its effect on a one-Dimensional signal.

Finally, in Chapter VI, a basic model for 2-D PSF in SAR system is introduced and simulated using both standard-FFT and NSI-6 techniques. Results showed that sidelobes were suppressed when using the NSI-6 technique by up to 20dB. This is followed by a second SAR simulation of multi-targets (two targets) and a distributed target. After that, a real-life SAR data of Vancouver lower mainland, which include different terrains and textures as it shows water, farmland and a city area, is used to form a SAR image by applying the different techniques of standard-FFT, NSI-6, SVA and Super-SVA techniques. However, since a ground truth is not available, the Mean-Square difference between the different images is calculated in order to have a quantitative analysis of these techniques. Furthermore, an in-depth study and analysis of the performance of the superimposition technique of NSI-6 in comparison with both the conventional technique of standard-FFT and the widely used technique of standard-FFT with Hann windowing function is conducted. An assessment of the final SAR image quality is studied quantitatively, using absolute difference and logarithmic scale version of SAR images, and qualitatively, using line intensity profile technique to examine images' sharpness and clarity.

3. Contribution of the Thesis

i. Summary of Contributions

This thesis has demonstrated research work in the areas of SAR image formation. The major novelties and contributions can be summarized by the two newly proposed techniques that are presented, analyzed and discussed in this thesis: 1) Repetitive Superimposition (RSI): this technique is more than simply repeating the superimposition over and over again, it is specifically designed so that each superimposition process have a zero-crossing points aligned with spikes of unwanted sidelobes that are near the targeted main-lobes. Furthermore, it utilized windowing functions in order to lower all sidelobes but still preserved the main-lobe's position and height. Then, it was optimized by limiting the number of repetition to give good results in the fastest processing time. 2) Normalized Superimposition (NSI): this technique took advantage of the normalization process that emphasizes similarities between the different superimposed signals. The similarities were designed to be on the peaks of the main-lobes, and therefore suppress other unwanted sidelobes.

ii. Publications

The following papers have been produced from the findings of this research work:

1. O. M. Abdul-Latif, S. R. Pennock, "**Enhancing SAR Image Formation Using Superimposed Fast Fourier Transformation**", 30th IEEE Geoscience and Remote Sensing Symposium IGARSS 2012, Munich, Germany, 22 - 27 July 2012.
2. S. R. Pennock, O. M. Abdul-Latif, C. H. J. Jenks, "**Improved GPR Image Focussing with Repetitive and Normalised Superimposition Techniques**", 15th International Conference on Ground Penetrating Radar, GPR 2014, Brussels, Belgium, June 30 – July 4, 2014.
3. O. M. Abdul-Latif, S. R. Pennock, "**Repetitive Superimposed Fourier Transform for Enhanced SAR Image Formation**", Submitted to the IEEE Transactions on Geosciences and Remote Sensing (TGRS-2014-00185) and still under review.
4. O. M. Abdul-Latif, S. R. Pennock, "**Normalized Superimposed Fourier Transform for Suppressing Sidelobes in Network Analyzer**", to be submitted to the IEEE Transactions on Microwave Theory and Techniques soon.

4. Future Work

Research outcome of this project shows that it can generate interesting improvements and innovations to existing FFT/IFFT-based systems where enhancing resolution, suppressing sidelobes and combating noise and distortion effects while maintaining desired peaks' position and magnitude is of interest. Still, there are many different research areas in the field of SAR image formation that were either only briefly mentioned in this dissertation or not addressed at all. For instance, researchers have found application for SAR in bathymetry, which is related to measuring the underwater bottom topography [131]. Even some subsurface features have been imaged by SAR, as the radar signals can penetrate into some materials such as dry sand [99]. All these different applications can be explored in order to have a better understanding of the SAR requirements and, hence, extend superimposition technique to have the best possible outcome.

Similarly, preliminary simulation of Ground Penetrating Radar with some real-life measurement is investigated in this dissertation. Results showed that by using the superimposition technique the images produced by migration stacking can be improved as the

basic data that is input into the migration is more clearly defined than from traditional FFT/IFFT evaluations. Furthermore, using the normalisation process described here rather than simple averaging in the migration stacking even clearer images of simple targets have been observed. Evaluating a set of images with a range of assumed permittivity values can produce a composite image in which the targets can be discerned. Monitoring the intensity and/or sharpness of the image gives the best quality measure of the image when the true permittivity is used. This gives another method of identifying the permittivity of the ground, and identifies the best image of the ground. Results showed that in simple single target cases, superimposition has been seen to be effective. However, the reliability of the approach on measured data has yet to be fully assessed.

References

(Referenced are generated by M.S. Word's "Citations & Bibliography" feature using the IEEE 2006 Reference Standard)

[1] W. G. Carrara, R. S. Goodman and R. M. Majewski, Spotlight Synthetic Aperture Radar: Signal Porcessing Algorithms, Boston: Artech House, 1995.

[2] M. I. Skolnik, Introduction to Radar Systems, 3rd Edition ed., New York: McGraw-Hill, 2001.

[3] Rosemount Inc., "Basic Principles of Radar," Rosemount Inc., Chanhassen, MN 56317 USA, 1999.

[4] I. G. Cumming and F. H. Wong, Digital Processing of Synthetic Aperture Radar Data: Algorithms and Implementations, Norwood, MA: Artech House Inc., 2005.

[5] J. J. Daniels, R. Roberts and M. Vendi, "Ground Penetrating radar for the detection of liquid conaminants," *Journal of Applied Geophysics,* vol. 33, pp. 195-207, 1995.

[6] M. Soumekh, Synthetic Aperture Radar Signal Processing, USA: Hohn Wiley & Sons Inc., 1999.

[7] "What is SAR," [Online]. Available: http://www.sandia.gov/radar/whatis.html. [Accessed 25 November 2010].

[8] F. T. Ulaby, R. K. Moore and K. Fung, Microwave Remote Sensing: Active and Passive, vol. I, Addison-Wesley, 1981.

[9] W. Hardin, 2000. [Online]. Available: http://www.spie.org/app/sar/~Hardin/. [Accessed 28 April 2004].

[10] J. S. Pottier and E. Lee, Polarimetric Radar Imaging: From Basics to Applications, CRC Press, 2009.

[11] J. C. Curlander and R. N. MchDounough, Synthetic Aperture Radar, Systems and Signal Processing, New York: John Wiley & Sons, 1991.

[12] E. O. Brigham, The Fast Fourier Transform and its Application, Englewood Cliffs, NJ: Prentice-Hall, 1988.

[13] M. Yaagoubi, G. Neveux, D. Barataud, T. Reveyrand, J. M. Nebus, F. V. Verbeyst, F. Gizard and J. Puech, "Time-Domain Calibrated Measurements of Wideband Multisines Using a Large-Signal Network Analyzer," *IEEE Transactions on Microwave Theory and Techniques,* vol. 56, no. 5, pp. 1180-1192, May 2008.

[14] H. M. Jol, Ground Penetrating Radar: Theory and Applications, Oxford: Elsevier, 2009, pp. 106-107.

[15] K. Nagai, "A new Synthetic Aperture Focussing Method for Ultrasound B-scan Imaging by FT," *IEEE Transactions on Ultrasound* , vol. 32, pp. 531-536, 1985.

[16] M. O'Donnel and L. J. Thomas, "Efficient Synthetic Aperture Imaging from a Circular Aperture with Possible application to Catheter-based Imaging," *IEEE Transactions on Ultrasound,* vol. 39, pp. 366-380, 1992.

[17] A. Bellettini and M. Pinto, "Theoratical Accuracy of Synthetic Aperture Sonar Micronavigation," *IEEE Journal of Oceanic Engineering,* vol. 27, no. 4, pp. 780-789, 2002.

[18] Candadian Space Agency, "RADARSAT-2 Data and Products © MacDONALD, DETTWILER AND ASSOCIATES LTD (2008) – All Rights Reserved. RADARSAT is an official mark of the Canadian Space Agency," MDA Corporation, 2008. [Online]. Available:

http://gs.mdacorporation.com/SatelliteData/Radarsat2/SampleDataset.aspx. [Accessed 2011].

[19] I. Tsang, J. A. Kong and R. T. Shin, Theory of Microwave Remote Sensing, New York: Wiley-Interscience, 1985.

[20] R. E. Blahut, "Theory of Remote Surveillance Algorithms," *Radar and Sonar Journal*, vol. I, no. 32, 1991.

[21] J. T. Pulliainen, K. Heiska, J. Hyyppa and M. T. Hallikainen, "Backscattering Properies of boreal forests at the C- and X- bands," *IEEE Tansaction on Geoscience and Remote Sensing*, vol. 32, no. 5, pp. 1041-1050, 1994.

[22] A. Gandhe and I. J. Gupta, "Comparison of various enhanced radar imaging techniques," *Algorithms for Synthetic Aperture Radar Imaging*, vol. 3370, pp. 250-260, April 1998.

[23] Envisat ASAR Cal/Val Team, "Quality measurements definition for SAR," ESA, March 2002.

[24] A. Marinez and J. Marchand, "SAR Image Quality Assessment," in *Revista Asociacion Espanola de Teledeteccion*, 1993.

[25] X. Lu and H. Sun, "Parameter Assessment for SAR Image Quality Evaluation System," in *1st Asian and Pacific Conference on Synthetic Aperture Radar (APSAR2007)*, 2007.

[26] P. Granceschitte and R. Lanari, "Wide Angle SAR Processor and their qulity assessment," in *IGARSS 91*, 1991.

[27] J. Guignard, "Final Acceptance of the MDA Software SAR Processor," *IEEE Transactions on Geoscience and Remote Sensing*, vol. 43, no. 3, 2005.

[28] B. Jahne, Image Processing for Scientific Applications, CRC Press L.L.C, 1997.

[29] K. Lukin and P. Vyplavin, "Integrated Sidelobe Ratio in Noise Radar Received," in *19th International Radar Symposium*, Warsaw, Poland, 2012.

[30] H. Maitre, Processing of Synthetic Aperture Radar (SAR) Images, Hoboken, NJ: John Wiley & Sons, 2013.

[31] A. Mittal, A. K. Moorthy and A. C. Bovik, "Blind/Referenceless Image Spatial Quality Evaluator," Austin, Texas, 2011.

[32] R. C. Gonzalez, R. E. Woods and S. L. Edding, Digital Image Processing using Matlab, Upper Saddle River, New Jersey: Pearson Prentice Hall, 2004.

[33] A. C. Bovik, The Essential Guide to Image Processing, 2nd ed., San Diego, California: Elsevier, 2009.

[34] R. N. McDonough and J. C. Curlander, Synthetic Aperture Radar: Systems and Signal Processing, New York: John Wiley & Sons Inc., 1991.

[35] A. G. Stove, "Linear FM-CW Radar Techniques," *IEE Proc. Part F Radar Signal Process*, vol. 139, no. 5, pp. 343-350, 1992.

[36] S. O. Piper, "FMCW Linearizer Bandwidth Requirements," in *IEEE National Radar Conference*, 1991.

[37] A. Meta, P. Hoogeboom and L. P. Lighthart, "Non-Linearity Correction in FMCW SAR," in *IEEE International Geoscience and Remote Sensing Symposium*, Denver, CO, USA, 2006.

[38] M. Edrich, "Design Overview and Flight Test Results of the Miniaturized SAR Sensor MISAR," in *European Radar Conference*, Amsterdam, 2004.

[39] M. Vossiek, P. Heide, M. Nalezinski and V. Magori, "Novel FMCW radar system concept with adaptive compensation of phase errors," in *European Microwave Conference*, Prague, 1996.

[40] Z. Zhu, W. Yu, X. Zhang and X. Qiu, "A Correction Method to Distortion in FMCW Imaging

System," in *IEEE Aerospace Electronics Conference*, Dayton, USA, 1996.

[41] J. A. Richards, Remote Sensing with Imaging Radar, New York: Springer, 2009.

[42] HP Advanced Technology, "Radar Technology: Use of Radar Technology in Imaging Systems," 2014. [Online]. Available: http://www.hp-adtec.de/pages/en/projects/radar-technology-terahertz-technology.php?lang=EN. [Accessed 15 August 2014].

[43] E. Dich and M. Christensen, "SAR Antenna Design for Ambiguity and Multipath Suppression," vol. III, no. 29, 1993.

[44] M. Bell and J. S. Daba, "Statistics of the Scattering Cross-Section of a Small Number of Random Scatterers," vol. 43, no. 8, pp. 773-783, 1995.

[45] J. S. Daba, "Scattering Statistics of Doppler Faded Acoustic Signals Using Speckle Noise Models," Lviv, West Ukraine, 2003.

[46] S. R. Cloude, "The Characterization of Polarimetric effects in EM Scattering," 1986.

[47] C. Baker and D. Belcher, "Hybrid Strip-map/spotlight SAR," *IEE Colloquium on Radar and Microwave Imaging*, vol. 2, pp. 1-7, November 1994.

[48] A. K. Fung, Microwave Scattering and Emission Models and Their Applications, Boston, MA, USA: Artech House, 1994.

[49] W. D. Jakowatz, D. Yocky, B. Bray and J. Richards, "Comparison of algorithm for use in real-time SAR image formation," *SPIE*, no. 5427, pp. 108-120, 2004.

[50] Y. K. Chan and V. C. Koo, "An Introduction to Synthetic Aperture Radar (SAR)," *Progress in Electromagnetics Research*, vol. 2, pp. 27-60, 2008.

[51] K. C. Ho, Y. T. Chan and R. Inkol, "A digital quadrature demodulation system," *IEEE Trans. on Aerospace and Electronic Systems*, vol. 32, no. 4, pp. 1218-1227, 1996.

[52] G. F. Stickley, D. A. Noon, M. Cherniakov and I. Longstaff, "Stepped-Frequency Ground Penetrating Radard," *Journal of Geophysics*, vol. 43, pp. 259-269, March 2000.

[53] D. Brandwood, Fourier Transforms in Radar and Signal Processing, London: Artech House, 2003.

[54] J. C. Jan, Digital signal filtering: analysis and restoration, London: Institute of Electrical Engineering, 2000.

[55] V. Chen and H. Ling, Time-Frequency Transforms for Radar Imaging and Signal Analysis, London: Artech House, 2002.

[56] K. Nagai, "A new synthetic aperture focusing method for ultrasonic B-scan imaging by FT," *IEEE trans Son. Ultrason.*, vol. 32, no. 4, pp. 531-536, 1985.

[57] European Space Agency, "SAR Handbook," European Space Research and Technology Centre (ESTEC), 2007.

[58] J. Wang and X. Liu, "Automatic Correction of Range Migration in SAR Imaging," *IEEE Geoscience and Remote Sensing Letters*, vol. VII, no. 2, pp. 256-260, April 2010.

[59] J. K. Jao, "Theory of Synthetic Aperture Radar Imaging of a Moving Target," *IEEE Transactions on Geoscience and Remote Sensing*, vol. 39, no. 9, pp. 1984-1992, Septemeber 2001.

[60] S. Martin, An Introduction to Ocean Remote Sensing, Cambridge: Cambridge University Press, 2012, p. 415.

[61] M. Xing, Y. Wu, Y. D. Zhang, G.-C. Sun and Z. Bao, "Azimuth Resampling Processing for Highly Squinted Synthetic Aperture Radar Imaging with Several Modes," *IEEE Transactions*

on Geoscience and Remote Sensing, pp. 4339-4352, July 2014.

[62] J. S. Lee, "Speckle Suppression and Analysis for Synthetic Aperture Radar Images," *Journal of Optical Engineering*, vol. 25, no. 5, pp. 636-643, May 1986.

[63] J. S. Daba and M. R. Bell, "Segmentation of speckled images using a likelihood random field model," *Proceedings of World Academy of Science, Engineering and Technology, Vol. 2*, pp. 321-325, 2005.

[64] F. Qiu, J. Berglund, J. Jensen, P. Thakkar and D. Ren, "Speckle Noise Reduction in SAR imagery using a Local Adaptive Median Filter," *GIScience and Remote Sensing*, vol. III, no. 41, pp. 244-266, 2004.

[65] A. Lopes, E. Nezry, R. Touzi and H. Laur, "Structure Detection and Statistical Adaptive Speckle Filtering in SAR Images," *International Journal of Remote Sensing*, vol. 14, no. 9, pp. 1735-1758, 1993.

[66] RSI, "RADARSAT Data Products Specifications," RADARSAT International, Richmond, British Columbia, 2000.

[67] B. Tso and P. M. Mather, Classification Methods for Remotely-Sensed Data, London: Taylor & Francis, 2001.

[68] P. M. Mather, Computer Processing of Remotely-Sensed Images: An Introduction, 2nd ed., Chichester: John Wiley & Sons, 2001.

[69] Z. Shi and K. O. Fung, "A Comparison of Digital Speckle Filters," in *Proceedings of the International Geoscience and Remote Sensing Symposium (IGARSS)*, 1994.

[70] J. S. Lee, "Digital Image Enhancement and Noise Filtering by use of Local Statistics," *IEEE Transaction on Pattern Analysis and Machine Intelligence*, vol. II, pp. 165-168, 1980.

[71] D. T. Kuan, A. A. Sawchuck, T. C. Strand and P. Chavel, "Adaptive Noise Smoothing Filter for Images with Signal-Dependent Noise," *IEEE Transaction on Pattern Analysis and Machine Intelligence*, vol. 7, no. 2, pp. 165-177, 1985.

[72] D. T. Kuan, A. A. Sawchuck, T. C. Strand and P. Chavel, "Adaptive Restoration of Images with Speckel," *IEEE Transaction on Acoustic Speech and Signal Processing*, vol. 35, no. 3, pp. 373-383, 1987.

[73] V. S. Frost, J. A. Stiles, K. S. Shamugan and J. C. Hotzman, "A Model for Radar Images and its Application to Adaptive Digital Filtering of Multiplicative Noise," *IEEE Transaction on Pattern Analysis and Machine Intelligence*, vol. 4, pp. 157-166, 1982.

[74] D. C. Munson, J. D. O'Brien and W. K. Jenkins, "A tomographic formulation of Spotlight-mode synthetic aperture radar," no. 71, 1983.

[75] W. K. Jenkins and M. D. Desai, "Convolution backprojection image reconstruction for spotlight mode synthetic aperture radar," *IEEE Transactions on Image Processing*, pp. 505 - 517, 1992.

[76] M. Slaney and A. C. Kak, Principles of Computerized Tomographic Imaging, New York: IEEE Press., 1988.

[77] T. G. Feeman, The Mathematics of Medical Imaging: A Beginners's Guide, Springer, 2010.

[78] D. C. Munson and H. Choi, "Direct-Fourier reconstruction in tomography and synthetic aperture radar," *International Journal of Image Systems and Technology*, no. 9, pp. 1 - 13, October 1998.

[79] W. Carrara, R. Goodman and R. Majewski, "Compariosn of polar formatting and backprojection algorithms for SAR image formation," *SPIE*, no. 62370H, pp. 203-212, 2006.

[80] S. Lockwood, A. Brown and H. Lee, "Backward Propagation Image Reconstruction Techniques for Bistatic Synthetic Aperture Radar Imaging System," *IEEE*, pp. 110-115, 2001.

[81] C. W. Therrien, Discrete Random Signals and Statistical Signal Processing, Englewood Cliffs, NJ: Prentice-Hall, 1992.

[82] S. R. Degraaf, "SAR imaging via modern 2-D spectral estimation methods," *IEEE Transactions on Image Processing*, vol. 7, no. 5, pp. 729-761, May 1998.

[83] D. C. Munson and J. A. C. Lee, "Spatially variant apodization for image reconstruction from partial Fourier data," *IEEE Transaction on Image Processing*, vol. 9, no. 11, pp. 1914-1924, November 2000.

[84] G. R. Benitz, "High-definition vector imaging," *Lincoln Laboratory Journal*, vol. 10, no. 2, pp. 147-170, 1997.

[85] J. H. McClellan, Parametric Signal Modeling, J. S. L. a. A. V. Oppenheim, Ed., Englwood Cliffs, NJ: Prentice-Hall, 1988, pp. 1-57.

[86] I. J. Gupta, M. J. Beals and A. Moghaddar, "Data extrapolation for high resolution radar imaging," *IEEE Transactions on Antennas and Propagation*, pp. 1540-1545, 1994.

[87] D. C. Munsoon Jr and E. A. Ullman, "Support-Limited Extrapolation of offset Fourier data (synthetic aperture radar)," in *IEEE International Conference on Acoustics, Speech and Signal Processing*, 1986.

[88] J. A. C. Lee, O. Arikan and D. C. Munson Jr, "Formulation of a general imaging algorithm for high-resolution synthetic aperture radar," in *IEEE International Conference on Acoustics,Speech and Signal Processing*, 1996.

[89] C. L. Logan, "An Estimation-Theoretic Technique for Motion-Componstated Synthetic Aperture Array Imaging," MIT , 2000.

[90] X. Giganet, "Satellite Image Segmentation and Classification," 2004.

[91] S. P. Lutrell, "Prior Knowledge and object reconstruction using the best linear estimate technique," *Optica Acta*, pp. 703-716, 1985.

[92] S. M. Delves, G. C. Pryde and S. P. Lutrell, "A super-resolution algorithm for SAR images," *Inverse Problems*, pp. 681-703, 1988.

[93] C. J. Oliver and S. P. Lutrell, "Prior Knowledge in synthetic aperture radar processing," *Journal of Physics (applied physics)*, pp. 333-356, 1986.

[94] B. Borden, "Maximum entropy regularization in inverse synthetic aperture radar imagery," *IEEE Transactions on Signal Processing*, vol. 4, no. 40, pp. 969-973, April 1992.

[95] B. Borden, "Regularization of noisy ISAR images containing extended features," *IEEE Transactions on Image Processing*, vol. 8, no. 1, pp. 124-127, January 1999.

[96] A. T. Bajkova and B. R. Frieden, "Bayesian corss-entropy reconstruction of complex images," *Applied Optics*, vol. 2, no. 33, pp. 219-226, January 1994.

[97] A. T. Bajkova and B. R. Frieden, "Entropic reconstruction of complex images," *Optics Communications*, vol. 5, no. 102, pp. 515-522, 1993.

[98] F. B. Duh and C. F. Juang, "Radar Pulse Compression for Point Target and Distributed Target," *Journal of Information Science and Engineering*, no. 23, pp. 183-201, 2007.

[99] D. J. Daniels, "Surface penetrating radar," *Electronics and Communication Engineering Journal*, pp. 165-182, August 1996.

[100] C. Ozdemir, S. Demirci and E. Yigit, "Practical Algorithms to Focus B-scan GPR Images:

Theory and Application to Real Data," *Progress in Electromagnetics Research B,* vol. VI, pp. 109-122, 2008.

[101] C. Rappaport, "Accurate Determination of Underground GPR Wafefront and B-Scan Shape," *IEEE Transactions on Geoscience and Remote Sensing,* vol. 45, no. 8, pp. 2429-2454, August 2007.

[102] G. Angiulli, D. De Carlo and T. Isernia, "A comarative study of different strategies to focus GPR images collected from archaeological investigations along the basilian monks," in *14th International Conference on Ground Penetrating Radar*, Shanhai, China, 2012.

[103] L. Zhou and Y. Su, "GPR imaging with RM algorithm in layered medium," *IEEE Geoscience and Remote Sensing Letters,* vol. VIII, no. 5, pp. 934-938, 2011.

[104] J. Daniels, R. Roberts and M. Vendi, "Ground Penetrating radar for the detection of liquid conaminants," *Journal of Applied Geophysics,* vol. 33, pp. 195-207, 1995.

[105] E. Yigit, S. Demirci and C. Ozdemir, "On the imaging applications of Ground Penetrating Radar," in *International Symposium on Electromagnetic Theory*, Berlin, Germany, 2010.

[106] G. Cui, L. Kong and J. Yang, "A back-projection algorithm to stepped-frequency synthetic aperture through-the-wall radar imaging," in *1st Asian and Pacific Conference on Synthetic Aperture Radar (APSAR)*, 2007.

[107] Y. Kim, L. Jofre, F. De Flaviis and M. Feng, "Microwave reflection tomographic array for damage detection of civil structures," *IEEE Transactions on Antenna and Propagation,* vol. 51, pp. 3022-3032, 2003.

[108] D. J. Daniels, D. J. Gunton and H. F. Scott, "Introduction to subsurface radar," *Proc. Radar and Signal Processing,* pp. 135-f, 1988.

[109] F. Harris, "On the Use of Windows for Harmonic Analysis with the Discrete Fourier Transform," *Proceeding of the IEEE,* vol. 66, pp. 51-83, 1978.

[110] C. Dolph, "A Current Distribution for Broadside Arrays which Optimizes the Relationship between Beam Width and Sidelobe Levels," *Proceeding of the IRE,* vol. 34, pp. 333-348, 1946.

[111] J. Kaiser and R. Schafer, "On the use of the window for spectrum analysis," *IEEE Transactions on Acoustics, Speeh and Signal Processing,* vol. 28, pp. 105-107, 1980.

[112] M. O'Donnel and L. J. Thomas, "Efficient synthetic aperture imaging from a circular aperture with possible application to catheter-based imaging," *IEEE Trans. Ultrason. Ferroelec. Freq. Contr.,* vol. 39, pp. 366-380, 1992.

[113] M. Karaman, P. C. Li and M. O'Donnell, "Synthetic aperture imaging for small scale systems," *IEEE Trans. Ultrason. Ferroelec. Freq. Contr,* vol. 42, pp. 429-442, 1995.

[114] M. Daraman and M. O'Donnell, "Subaperture processing for ultrasonic imaging," *IEEE Trans. Ultrason. Ferroelec. Freq. Contr.,* vol. 45, pp. 126-135, 1998.

[115] F. M. Dickey, L. A. Romero and A. W. Doerry, "SAR Window Functions: a review and analysis," SANDIA National Laboratories, Albuquerque, New Mexico, 2002.

[116] P. Thompson, M. Nannini and R. Scheiber, "Target separation in SAR image with the MUSIC algorithm," in *Geoscience and Remote Sensing Symposium, IGARSS 2007.*, 2007.

[117] S. S. Yoon and M. G. Amin, "High-Resolution Radar Imaging using MUSIC algorithm," *IEEE Tansactions on Antennas and Propagation,* no. 56, pp. 1763-1774, 2008.

[118] Z. She, D. A. Gray, R. E. Bogner, J. Homer and I. D. Longstaff, "Three-Dimensional space-borne SAR imaging with multiple pass processing," *International Journal of Remote Sensing,* no. 23, pp. 4357-4382, 25 November 2010.

[119] W. Jiang, S. Pennock and P. Shepherd, "A Robust W-MUSIC algorithm for GPR target detection in the presence of noise," in *Radar Conference 2009*, 2009.

[120] R. J. Dallair and C. H. Stankwitz, "Spatially Variant Apodization". United States Patent 5,349,359, 1994.

[121] X. Wu, Y. Wang, S. Li and C. Liu, "A Stable realization of apodization filtering applied to noise SAR and SAR range sidelobe suppression," 2012. [Online]. Available: http://asp.eurasipjournals.com/content/2012/1/112. [Accessed 2012].

[122] P. Zhang, J. Shang and R. Yang, "A New algorithm improving SAR resolution based on SVA," Guillin, China, 2009.

[123] A. Maida, S. Pennock and P. Shephered, "Improving ground penetrating Radar Signal analysis through FFT Superimpostion," in *IEEE Antennas and Propagation Society International Symposium*, Washington, USA, 2005.

[124] L. Smith, Z. Gratz and S. Bousquet, The Art and Practice of Statistics, Belmont, CA: Wadsworth Cengage Learning, 2008.

[125] F. T. Ulaby and C. Elachi, Radar Plarimetry for Geoscience Applications, Norwood, MA: Artech House, 1990.

[126] J. Taylor, Scattering Theory, New York: Wiley, 1972.

[127] S. R. Pennock, O. M. Abdul-Latif and C. H. J. Jenks, "Improved GPR Image Focussing with Repetitive Normalised Superimposition Techniuqe (Accepted Paper)," in *15th International Conference on Ground Penetrating Radar*, Brussels, 2014.

[128] R. Tolimieri and L. Auslander, "Characterizing the Radar Ambiguity Functions," *IEEE Trans. on Information theory*, no. 30, pp. 832-836, 1984.

[129] R. Fisher, S. Perkins, A. Walker and E. Wolfart, "Hypermedia Image Processing Reference," 2003. [Online]. Available: http://homepages.inf.ed.ac.uk/rbf/HIPR2/featops.htm. [Accessed 2010].

[130] W. K. Pratt, Digital Image Processing, Wiley, 1991.

[131] R. Romeiser, O. Hirsch and M. Gade, "Remote Sensing of Surface Currents and Bathymetric Features in teh German Bighty by Along-Track SAR interferometry," in *Proc. Int. Geoscience and Remote Sensing Symposium*, Honolulu, HI, USA, July 2000.

[132] A. Suksmono, E. Bharata and A. Lestari, "Compressive Stepped-Frequency Continuous-Wave Ground-Penetrating-Radar," *IEEE Geoscience and Remote Sensing Letters*, vol. 7, no. 4, pp. 665-669, October 2010.

Appendix A: SAR Image Parameters

1. Vancouver SAR Image (1)

The RADARSAT-2 raw data (which was acquired by the Canadian Space Agency on June 16, 2002) for the high resolution scene of Vancouver lower mainland shown in Chapter 6 is obtained from [4]. The scene shows water, farmland and city. The relevant parameters of the scene are listed in the following table:

Parameter	Value
Sampling Rate	*32.317 MHz*
Pulse Bandwidth	*30.111 MHz*
Pulse Centre Frequency	*0 MHz*
Range FM rate	*0.72135 MHz/μs*
Data window start time	*6.5956 ms*
Pulse duration	*41.74 μs*
Number of samples in replica	*1349*
Number of samples per echo line	*9280*
Radar Frequency	*5.300 GHz*
Radar Wavelength	*0.05657 m*
Pulse repetition frequency	*1256.98 Hz*
Effective radar velocity	*7062 m/s*
Azimuth FM rate	*1733 Hz/s*
Doppler centroid	*-6900 Hz*
Spacecraft heading	*344.49 degrees*
Platform latitude	*48.36 degrees*
Platform longitude	*229.29 degrees*
Satellite orbit radius	*7,189,029 m*
Local Earth sphere radius	*6,390,524 m*
Incidence angle at near-range	*38.64 degrees*
Incidence angle at mid-range	*40.15 degrees*
Incidence angle at far-range	*41.61 degrees*

Appendix B: Other Publications by the Author

1. Journal Papers:

1. J. Dubois and O. Abdul-Latif, "Least Square-SVM Detector for Wireless BPSK in Multi-environmental Noise," International Journal of Applied Mathematics and Computer Sciences, ISSN 1307-6906, Vol. 1, No. 4, pp. 207-212, 2004.

2. J. Dubois and O. Abdul-Latif, "A Novel SVM-Based OOK Detector in Low SNR Infrared Channels", Transactions on Engineering, Computing, and Technology, ISSN 1305-5313 (currently PWASET, ISSN 1307-6884), Vol. 7, pp. 244-247, 2005.

3. J. Dubois and O. Abdul-Latif, "Improved M-ary Signal Detection Using Support Vector Machine Classifiers," Transactions on Engineering, Computing, and Technology, ISSN 1305-5313 (currently PWASET, ISSN 1307-6884), ISSN 1307-6884, Vol. 7, pp. 264-268, 2005.

4. J. Dubois and O. Abdul-Latif, "Detection of Ultrasonic Images in the Presence of a Random Number of Scatterers: A Statistical Learning Approach," Transactions on Engineering, Computing, and Technology, ISSN 1305-5313 (currently PWASET, ISSN 1307-6884), Vol. 7, pp. 326-329, 2005.

5. J. Dubois and O. Abdul-Latif, "SVM-Based Detection of SAR Images in Partially Developed Speckle Noise," Transactions on Engineering, Computing, and Technology, ISSN 1305-5313 (currently PWASET, ISSN 1307-6884), Vol. 7, pp. 321-325, 2005.

6. J. S. Daba and O. Abdul-Latif, "Least Square-SVM Detector for Wireless BPSK in Multi-environmental Noise," Transactions on Engineering, Computing, and Technology (currently Proceedings of World Academy of Science, Engineering and Technology), ISSN 1307-6884, Vol. 3, Issue 2, pp. 181-186, 2006.

2. Conference Papers:

1. S. R. Pennock, O. M. Abdul-Latif, C. H. J. Jenks, "Improved GPR Image Focussing with Repetitive and Normalised Superimposition Techniques", 15th International Conference on Ground Penetrating Radar, Brussels, Belgium, June 30 – July 4, 2014.

2. O. M. Abdul-Latif, S. R. Pennock, "Enhancing SAR Image Formation Using Superimposed Fast Fourier Transformation", 30th IEEE Geoscience and Remote Sensing Symposium IGARSS 2012, Munich, Germany, 22 - 27 July 2012.

3. O. M. Abdul-Latif, P. R. Shepherd, S. Pennock, "Optimum TDoA/AoA Data Fusion Positioning System for Team-Sport Players", Conference on Advances in Computational Tools for Engineering Applications (ACTEA2009) July 15-17, 2009 Notre Dame University, Lebanon.

4. O. M. Abdul-Latif, P. R. Shepherd, S. Pennock, "Transmission Power Vs. BER in UWB Telecommunication System", 5th GCC IEEE Conference, Kuwait, March, 2009.

5. O. M. Abdul-Latif, P. R. Shepherd, S. Pennock, "Effect of Multiple Access Interferers on UWB system Performance", IFIP Wireless Days, Dubai, UAE, November 2008.

6. J. Daba and O. M. Abdul-Latif, "Novel Diversity Combining in OFDM-Based MIMO Systems," American Conference on Applied Mathematics at Harvard, Cambridge, MA, USA, March 2008.

7. R. Ayoubi, J. P. Dubois, O M. Abdul-Latif, "FPGA Implementation of a Novel Receiver Diversity Combining Technique for Wireless SIMO Systems", ICSPC07, International Conference of Signal Processing for Communication 2007, Dubai, UAE, Nov 2007.

8. O. M. Abdul-Latif, P. R. Shepherd, S. Pennock, "TDoA/AoA Data Fusion for Enhancing Positioning in an Ultra Wideband System", ICSPC07, International Conference of Signal Processing for Communication 2007, Dubai, UAE, Nov 2007.

9. O. M. Abdul-Latif, P. R. Shepherd, S. Pennock, “Transmission Range of an UWB positioning System”, Workshop of Signal Processing and Applications, Sharjah, UAE, March 2007.

10. O. M. Abdul-Latif, J. P. Dubois, “LS-SVM Detector for RMSGC Diversity in SIMO Channels”. ISSPA 2007, 20th International Symposium on Signal Processing and its Applications, Sharjah, UAE, Feb, 2007.

11. O. M. Abdul-Latif, J. P. Dubois, “LS-SVM Detector for RMSGC Diversity in SIMO Channels”. ISSPA 2007, 20th International Symposium on Signal Processing and its Applications, Sharjah, UAE, Feb, 2007.

12. J. P. Dubois and O. M. Abdul-Latif, “Least Square-SVM Detector for Wireless BPSK in Multi-environmental Noise”. MMSE2006, 3rd International Conference on Mathematical and Computational Methods in Science and Engineering, Czech Republic, Aug. 2006.

13. J. P. Dubois, O. M. Abdul-Latif, “SVM-Based Detection of SAR Images in Partially Developed Speckle Noise”. WEC2005, 5th World Enformatika Conference on Signal Processing, Czech Republic, Aug. 2005.

14. J. P. Dubois, O. M. Abdul-Latif, “A Novel SVM-Based OOK Detector in Low SNR Infrared Channels”. International Conference on Signal Processing, Czech Republic, Aug. 2005.

15. J. P. Dubois, O. M. Abdul-Latif, “Improved M-ary Signal Detection using Support Vector Machine Classifiers”. ICSP2005, International Conference on Signal Processing, Czech Republic, Aug. 2005.

16. J. P. Dubois, O. M. Abdul-Latif, “Detection of Ultrasonic Images in the Presence of a Random Number of Scatterers: A Statistical Learning Approach”. WEC2005, 5th World Enformatika Conference on Signal Processing, Czech Republic, Aug. 2005.